Additive-free thick $Li_4Ti_5O_{12}$ and $LiFePO_4$ electrodes for high energy density lithium-ion batteries

by

Carmen de la Torre Gamarra

A dissertation submitted by in partial fulfillment of the requirements for the degree of Doctor of Philosophy in

Materials Science and Engineering

Universidad Carlos III de Madrid

Advisors:

Alejandro Várez Álvarez
Belén Levenfeld Laredo

Tutor:

Alejandro Várez Álvarez

October, 2019

ACKNOWLEDGEMENTS

Durante la realización de esta tesis doctoral he tenido la oportunidad de estar rodeada de muchas personas, tanto dentro como fuera del ámbito científico. Algunas me han ayudado con mi trabajo, con otras he compartido muy buenos momentos y muchas se han convertido en grandes amistades. Pasado este periodo puedo asegurar que de todas ellas he aprendido algo y que, de alguna forma, esta tesis está hecha con trocitos de cada una de esas personas. Por eso en estas páginas quisiera dedicar unas palabras de agradecimiento y cariño a todas ellas y transmitirles que, al fin y al cabo, han sido la parte más importante de esta tesis.

Primeramente, quisiera dar las gracias a mis directores de tesis, Belén y Alejandro, por confiar en mí desde que llegué a la Universidad Carlos III. Gracias por todo el tiempo dedicado durante estos años y sobre todo por la ilusión que habéis puesto en este trabajo. Aprecio mucho la libertad que me habéis dado para investigar en diferentes temas y las facilidades para colaborar y conocer a otros muchos científicos. Ha sido un placer trabajar con vosotros.

A Mariu, muchas gracias por todo lo que has hecho tanto por mi trabajo como por mí en este periodo. Gracias por tu generosidad, gran parte de lo que he aprendido en esta tesis me lo has enseñado tú y muchos de los resultados obtenidos son gracias a ti. Has sido la mejor compañera de trabajo que podría haber tenido y una gran amiga.

A todos los compañeros con los que he coincidido del grupo de “Síntesis y procesado de materiales”, profesores, doctorandos y alumnos de grado y máster, gracias por vuestra ayuda, por el buen ambiente de trabajo y por todo lo que he aprendido con vosotros. Quisiera agradecer especialmente a Jean-Yves su colaboración en este trabajo, sus ideas han sido de gran utilidad.

Gracias también a todo el personal del Departamento de Ciencia e Ingeniería de Materiales e Ingeniería Química de la Universidad Carlos III de Madrid, profesores, personal investigador, personal administrativo y técnicos, por la ayuda y compañerismo. Especialmente a Cristina, por su ayuda en microscopía y difracción de rayos-X.

A continuación quisiera agradecer la colaboración de algunos científicos y grupos de investigación ajenos a la Universidad Carlos III pero que, sin duda, han sido imprescindibles para el desarrollo de esta tesis. Así mismo quisiera agradecer a la Universidad Carlos III de Madrid y al Instituto Álvaro Alonso Barba por la financiación para la realización de mis estancias predoctorales.

A José Manuel Amarilla, del Instituto de Ciencia de Materiales de Madrid, gracias por tu implicación en este trabajo, por hacer las medidas de las primeras celdas y animarnos para empezar este proyecto.

A Esteban Urones, del Centro Nacional de Microscopía Electrónica, su colaboración con medidas en microscopía de transmisión electrónica.

To professor Stefano Passerini from HIU (Ulm) for giving me the opportunity to join his amazing group and the fruitful discussions. Also, to Giovanni Battista Appetecchi, thanks so much for your kind treatment and all the time dedicated to my work, it was a pleasure to work with you. Special thanks to Alberto, Ulderico, Adele, and Maider for all the help during my stays and also to Guk-Tae for his collaboration. In general, to all the group Electrochemistry for batteries, for all the good moments we shared inside and outside work, which was an experience I will never forget.

I would like to thank especially to Ulderico and Adele for the nice moments we spent together. You were my family during my time in Ulm and I will never forget all the travels we did. We are true survivors.

From ICMPE-CNRS (Paris), thanks to Jean-Pierre Pereira-Ramos for accepting me in his group and, including Barbara Läik, thanks for the time dedicated to train me and the effort put into my work, I learnt so much. I would like to mention also Rita, Nicolas and Gladys for their kindness. Thanks to all of you for all the nice moments we shared.

Me gustaría dedicar unas palabras muy especiales para mis amigos de París Diego y Miguel. Gracias a vosotros viví una de mis mejores experiencias y nunca olvidaré el vínculo tan especial que creamos. Gracias por todo lo que vivimos juntos.

Quisiera mandar todo mi cariño a mis amigos más cercanos. Para ello, me gustaría empezar con las que son unas de mis personas favoritas, mis amigos de Toledo, la base de todo y mi segunda familia: Queen, Porres, Koala, Inés, Mari, Lindi, Pablo, Gusi, Lucía, Guio y Pentente. Gracias por ser tan desiguales y auténticos. Sois inspiración para mí.

Para mis tres grupos de amigos de Químicas. Pese a haberos conocido en momentos diferentes, todos me habéis aportado mucha felicidad durante estos años. Me siento muy afortunada de contar con vosotros. A las que primero conocí, María, Cris, Nerea, Laura y Ana, gracias por estar siempre unidas y mantener esta bonita amistad. A mis compañeros de los martes de vinos, Adri, Pelu y Rafa, por compartir los momentos más divertidos y también las intensas tardes de estudio. A Lidia y Alicia, por entenderme tan bien y estar siempre a mi lado. A mi gran amiga Rebeca, por las risas que nos echamos y nuestros encuentros esporádicos. A Eli, Ope, Sandra y Belén, gracias por haberme recibido con los brazos abiertos y por nuestros maravillosos viajes. Gracias también a Nacho, Daniel y Javi, por todos los buenos momentos.

A mis amigos del colegio mayor, Eva, Bego, Irene y Jose, gracias por esa convivencia tan especial y por seguir presentes. A Espe y Eu, por ser tan geniales.

A mis compañeros de máster, Diana, Karina, Gleidys, Lidia, Marta y Eric, gracias por vuestro apoyo y por la amistad que hemos creado. Por convertiros en algunas de las personas más influyentes durante mi tesis. Muchas gracias por vuestros infinitos consejos, vuestra empatía y el cariño que me habéis dado en todos estos años.

A todos mis amigos del Departamento de Materiales. Gracias por hacer de cada día de trabajo una alegría. Con vosotros todo ha sido mucho más fácil. A Mariola, María José, Ana, Paula, Mariu, Belén, Tere y Nieves, mil gracias por los buenísimos momentos durante las comidas, en los despachos y en los laboratorios. También fuera de la universidad, ya fuera de fiesta o en la montaña, gracias al grupo de Materialitos: Alberto, Raquel, Andrea F., Sergio, Freddy, Amaya, Estela, Edu, Cate, Andrea A., Borja, Andrés, Morena, Carol, Lucía, María N., Sara, Jorge, María F., Javi, Pedro, Sara L.B., Andrea G. y Guille. Gracias también a "las charlies" por los divertidos entrenamientos dentro y fuera de la pista. Por supuesto siempre me acordaré de ti, Raúl, desde lo más alto de la Maliciosa.

Y a ti, Cris, que has sido una de mis mayores motivaciones durante esta tesis, gracias por tu paciencia, por estar siempre a mi lado y por los momentos tan bonitos que me haces vivir.

Por último, quisiera agradecer a toda mi familia, la de Madrid, Granada, Alemania y Zaragoza, por todo su apoyo durante estos años. Especialmente a mis padres, a los que tengo que agradecer todo lo que tengo y lo que soy. Gracias por inculcarme la curiosidad científica que ambos tenéis, por ayudarme y apoyarme siempre que lo he necesitado y por quererme y respetarme tal y como soy. Esta tesis está dedicada a vosotros.

A mis padres, por su amor, respeto y dedicación
a la Ciencia

PUBLISHED AND SUBMITTED CONTENT

Published articles:

- M.E. Sotomayor, C. de la Torre-Gamarra, W. Bucheli, J.M. Amarilla, A. Varez, B. Levenfeld, J.-Y. Sanchez, *Additive-free $Li_4Ti_5O_{12}$ thick electrodes for Li-ion batteries with high electrochemical performance*, J. Mater. Chem. A. 6 (2018) 5952–5961.
doi: 10.1039/C7TA10683A.

This publication is partially included as part of the Thesis, in Chapter 3.
I contributed directly to this publication since I carried out the experiments, participated to discussion of the results and contributed to the final manuscript.
The material from this source included in this Thesis is not singled out with typographic means and references.

- M.E. Sotomayor, C. de la Torre-Gamarra, B. Levenfeld, J.-Y. Sanchez, A. Varez, G.-T. Kim, A. Varzi, S. Passerini, *Ultra-thick battery electrodes for high gravimetric and volumetric energy density Li-ion batteries*, J. Power Sources. 437 (2019) 226923.
doi: 10.1016/j.jpowsour.2019.226923.

This publication is partially included as part of the Thesis, in Chapter 3.
I contributed directly to this publication since I carried out some experiments and participated to discussion of the results.
The material from this source included in this Thesis is not singled out with typographic means and references.

Submitted articles:

- C. de la Torre-Gamarra, M.E. Sotomayor, J.-Y. Sanchez, B. Levenfeld, A. Varez, B. Läik, J.-P Pereira-Ramos, *Self-supported additive-free LFP/C thick electrodes produced by powder extrusion moulding as cathode for Li-ion batteries with high areal capacity*. (To be submitted to ChemSusChem).

This publication is partially included as part of the Thesis, in Chapter 3.
I contributed directly to this publication since I carried out the experiments, participated to discussion of the results and contributed to the final manuscript.
The material from this source included in this Thesis is not singled out with typographic means and references.

Conferences:

- C. de la Torre Gamarra, M.E. Sotomayor, B. Levenfeld, A. Varez, B. Laïk, J-P. Pereira-Ramos, Self-supported binder-free LFP/C thick electrodes produced by Powder Extrusion Molding as cathodes for Li-ion batteries, *XV Congreso Nacional de Materiales-I Iberian Meeting on Material Science, Salamanca (España),4-6 Julio 2018*. ***Oral presentation.***

- J-Y. Sanchez, M.E. Sotomayor, C. de la Torre-Gamarra, C. Martinez-Cisneros, J-M. Amarilla, B. Levenfeld, A.Varez, Thick LTO ceramic electrodes: processing and performances, *16th International Symposium on Polymer Electrolytes, Yokohama (Japón), 24-29 Junio 2018.* ***Poster.***

- J-Y. Sanchez, M.E. Sotomayor, C. de la Torre-Gamarra, W. Bucheli, J.M. Amarilla, A. Várez, B. Levenfeld, New Additive-Free Sintered LTO Negatives: Towards Solid-State Batteries Endowed with High Areal Capacity?, *35th Annual International Battery Seminar and Exhibit, Fort Lau-derdale (Estados Unidos), 26-29 Marzo 2018.* ***Poster.***

- M.E. Sotomayor, C. de la Torre-Gamarra, W. Bucheli, J.M. Amarilla, A. Várez, B. Levenfeld, J.Y. Sanchez, Moldeo por extrusión de polvos de $Li_4Ti_5O_{12}$ para ánodos en baterías de ion-litio, *XIII Reunión Nacional de Electrocerámica, Cuenca (España), 21-23 Julio 2017*. ***Oral presentation.***

OTHER RESEARCH MERITS

Publications:

- C. de la Torre-Gamarra, G.B. Appetecchi, U. Ulissi, A. Varzi, A. Varez, S. Passerini, $Na_3Si_2Y_{0.16}Zr_{1.84}PO_{12}$-ionic liquid hybrid electrolytes: An approach for realizing solid-state sodium-ion batteries?, J. Power Sources. 383 (2017) 157–163. doi: 10.1016/j.jpowsour.2017.12.037.

- Egaña, M. Tardío, C. de la Torre-Gamarra, A. Várez, E. Cantelar, J.E. Muñoz Santiuste, Spectroscopy and Judd-Ofelt analysis of Er^{3+} ions in $Li_5La_3Nb_2O_{12}$ garnet-type ceramic powder, J. Lumin. 202 (2018) 232–238. doi: 10.1016/j.jlumin.2018.05.068.

- Egaña, C. de la Torre Gamarra, M. Tardío, A. Várez, J.E. Muñoz-Santiuste, Structural, morphology and luminescence study of Er^{+3}-doped garnet-type $Li_5La_3Nb_2O_{12}$ electrolytes as a potential new phosphor, Ceram. Int. 44 (2018) 18969–18977. doi: 10.1016/j.ceramint.2018.07.136.

- C. de la Torre-Gamarra, M. Woszczak, B. Levenfeld, A. Varez, E. García-González, E. Urones-Garrote, V. Di Noto, Interplay between humidity, temperature and electrical response of a conductivity sensor based on a La_2LiNbO_6 double perovskite, J. Mater. Chem. A. 6 (2018) 5430–5442. doi:10.1039/c7ta09496e.

Conferences:

- C. de la Torre-Gamarra, M. Woszczak, A. Várez, E. García-González, AR. West, The Double Perovskite La_2LiNbO_6: A New Humidity Sensor, *XXII Solid State Ionics,Padua (Italia), 18-23 Junio 2017.* ***Poster.***

- A. Engaña, M. Tardío, C. de la Torre-Gamarra, A. Varez, E. Cantelar, F. Cussó, V. Lavín, J.E. Muñoz Santiuste, Spectroscopy of Er3+ ions in $Li_5La_3Nb_2O_{12}$ garnets, *19th International - Conference on Dynamical Processes in Excited States of Solids. Paris (Francia), 17-22 Julio 2016.* ***Poster.***

- C. de la Torre-Gamarra, M. Woszczak, A. Várez, E. García-González, AR. West, Study of the influence of humidity and temperature on the electrical properties of the perovskite-type phase $LiLa_2NbO_6$ with possible application as humidity sensor, *XIV Congreso Nacional de Materiales, Gijón (España), 8-10 Junio 2016*. ***Oral presentation.***

- C. de la Torre-Gamarra, M. Woszczak, A. Várez, E. García-González, AR. West, Estudio del efecto de la influencia de la temperatura y la humedad en las propiedades eléctricas de la perovskita doble $LiLa_2NbO_6$: un nuevo sensor de humedad, *Jornadas de Jóvenes Investigadores del Instituto de Cerámica y Vidrio, CSIC, Madrid (España), 5 Julio 2016*. ***Oral presentation.***

- C. de la Torre-Gamarra, A. Varez, J. Sanz, I. Sobrados, Study of the Li_2CO_3 excess on the electric properties of the garnet-type Li ionic conductor $Li_5La_3Nb_2O_{12}$, *4th International Conference European Ceramic Society, Toledo (España), 22-25 Junio 2015.* ***Oral presentation.***

- M. J. Martínez Morlanes, C. de la Torre-Gamarra, C. del Río Bueno, B. Levenfeld, A. Várez, Synthesis and characterization of hybrid sulfonated polisulfone/TiO_2(B) nanowires membranes for their application in fuel cells, *Advances in Materials and Processing Technologies Conference, Madrid (España), 14-17 Diciembre 2015.* ***Poster.***

- C. de la Torre-Gamarra, M.E. Sotomayor, A. Varez, J. Sanz, I. Sobrados, Study of the Li_2CO_3 excess in electric properties of the garnet-type Li ionic conductor $Li_5La_3Nb_2O_{12}$, *LIV Annual Congress of Ceramics and Glass Spanish Society, Badajoz (España), 19-22 Noviembre 2014*. ***Poster.***

CONTENTS

Abstract

The growing development of renewable energies and electric vehicles in the most advanced societies requires new lithium-ion batteries with higher energy density and safety than the commercial ones. This is a significant challenge for the scientific community. The problem can be addressed by developing new materials or using new alternative technologies, leading to a reduction in the total cost and increase the energy density of the battery. Recently, increasing electrode thickness is gaining attention, as the associated reduction of inactive components (current collectors, porous separator) results in both gravimetric and volumetric capacity improvements as well as cost savings.

In this Thesis, novel additive-free thick $Li_4Ti_5O_{12}$ (LTO) and $LiFePO_4$ (LFP) electrodes for high energy density lithium-ion battery applications are obtained. Powder Extrusion Moulding (PEM) technology is employed for producing (LTO) and (LFP) electrodes of ~ 500 μm thickness. On the other hand, LTO electrodes of ~ 250 μm thickness are manufactured by Tape Casting (TC). These technologies are completely different than the conventional methods used in electrode manufacturing, and they were selected for being widely used in the industry since they are easily scalable and relatively cheap. Furthermore, all the compounds used during the processes were commercial, including LTO and LFP powders.

The different steps of PEM and TC processes were optimized in order to obtain defect-free electrodes. In the case of LTO, a reducing atmosphere (Ar/H_2 gas flow) was used during the thermal treatments, which allowed to the incomplete decomposition of the binder, leaving some conductive carbon in the electrode, and to the partial reduction of Ti^{4+} to Ti^{3+}. These two facts allow to obtain an electrode with enough conductivity and also to avoid the use of extra carbon additives. For LFP, a controlled inert atmosphere (N_2 gas flow) was used to prevent the oxidation of the carbon coating already present in the starting powder. A systematic study of the sintering process and the thermal stability of LTO and LFP was carried out, analysing the effect of the temperature on the structure and microstructure of the electrodes. In the case of LTO, the effect of the sintering atmosphere (air, N_2 or Ar/H_2 for LTO) was also studied. For that, X-ray diffraction, electronic microscopy (SEM, TEM) and density measurements were employed. In general, the obtained electrodes present a high porosity (8-35 %), which is beneficial for good contact with the electrolyte.

The electrochemical properties of the additive-free LTO and LFP electrodes were tested by chronopotentiometry in lithium half cells. The cycling performance of the electrodes was analysed and, in the case of LFP, the effect of the processing, electrolyte density and sintering temperature in the capacity of the electrode was studied. Both LTO and LFP electrodes exhibit a very high

volumetric capacity (~ 300 mA·h/cm^3) compared to conventional composite ones. Finally, a lithium-ion battery with LTO and LFP (obtained by PEM) as anode and cathode, respectively, and a commercial liquid electrolyte was tested. For that, a liquid electrolyte was used. The cell presented an excellent performance at the C-rate of C/12, simulating a typical day-night charge/discharge cycle, and reaching an energy density of 488 W·h/l after 50 cycles.

The novel thick electrodes obtained in this work paves the way for the development of low-cost stationary energy storage systems, which could be integrated into smart grids. The main advantage of this thick electrodes is that they do not require binders either the addition of conductive materials for their use. By eliminating these additives, the battery energy density is raised, the safety is improved (increasing the working temperature range), and the cost is reduced.

Resumen

Actualmente, el desarrollo de nuevas baterías de ion-litio con mayor densidad energética y seguridad que las comerciales, es un importante reto para la comunidad científica. Actualmente, el aumento del espesor de los electrodos está siendo muy investigado, ya que permite reducir la cantidad de componentes inactivos (como colectores de corriente y separadores porosos), dando lugar a un aumento de la capacidad tanto gravimétrica como volumétrica del electrodo y a una reducción del coste. Por lo tanto, en este trabajo se obtienen nuevos electrodos gruesos y libres de aditivos de $Li_4Ti_5O_{12}$ (LTO) y $LiFePO_4$ (LFP) con aplicaciones en baterías de ion-litio de alta densidad energética.

La tecnología de Moldeo por Extrusión de Polvos se usa para producir electrodos de LTO y LFP de ~ 500 µm de espesor. Por otro lado, electrodos de LTO de ~ 250 µm de espesor se fabrican mediante colado en cinta. Estas tecnologías son totalmente diferentes a los métodos convencionales de fabricación de electrodos y fueron seleccionadas por ser ampliamente utilizadas en la industria, ya que son fácilmente escalables y relativamente baratas. Además, todos los compuestos usados durante el procesado, incluidos los polvos de LTO y LFP, son productos comerciales.

Las diferentes etapas de cada uno de los dos procesos se optimizaron para obtener electrodos libres de defectos. En el caso del LTO, se ha utilizado una atmósfera reductora durante los tratamientos térmicos lo que permite la descomposición incompleta del sistema ligante, dejando una pequeña cantidad de carbono residual en el electrodo y la reducción parcial de Ti^{4+} a Ti^{3+}. La combinación de estos dos factores hace que el electrodo tenga una conductividad eléctrica adecuada y no sean necesario añadir carbono. En el caso del LFP, se ha usado una atmósfera inerte con el objetivo de evitar la oxidación del recubrimiento de carbono que ya estaba presente en el polvo de partida. Se ha hecho un estudio sistemático de la sinterización y de la estabilidad térmica de LTO y LFP analizando el efecto de la temperatura en la estructura y microestructura de los electrodos. En el caso del LTO, también se estudió el efecto de la atmósfera (aire, N_2 y Ar/H_2). Para ello se utilizaron las técnicas de difracción de rayos-X, microscopía electrónica y medidas de densidad. En general, los electrodos obtenidos presentan una alta porosidad (8-35 %), lo que resulta ser positivo para asegurar un buen contacto con el electrolito.

Las propiedades electroquímicas de los electrodos libres de aditivos se midieron por cronopotenciometría en semi celdas de litio. Se analizó el comportamiento de los electrodos durante sucesivos ciclos de carga y descarga y, en el caso del LFP, se estudió el efecto del procesado, la temperatura de sinterización y la viscosidad del electrolito en la capacidad del electrodo. Tanto los

electrodos de LTO como los de LFP muestran capacidades por unidad de volumen muy altas (~ 300 $mA \cdot h/cm^3$) comparados con los electrodos convencionales. Finalmente, se preparó una batería de ion-litio utilizando electrodos obtenidos mediante moldeo por extrusión, de LTO y LFP como ánodo y cátodo, respectivamente y electrolito líquido comercial. La batería muestra un excelente comportamiento para velocidades de carga y descarga de C/12, simulando un típico ciclo día-noche, y alcanzando, incluso después de 50 ciclos, una densidad energética de 488 W·h/l.

Los nuevos electrodos obtenidos en este trabajo abren el camino al desarrollo de sistemas de almacenamiento de energía estacionario de bajo coste que podrían ser integrados en redes eléctricas inteligentes. Las principales ventajas de estos electrodos gruesos es que no necesitan aglomerantes ni la adición de carbono conductor para su utilización. Mediante la eliminación de estos aditivos, la densidad energética de la batería aumenta, la seguridad mejora (incrementando el intervalo de temperatura de trabajo) y se reduce el coste.

Chapter 1

Introduction

1.1. From fossil fuels to more sustainable energies

Since the electrification and technological evolution derived from the Industrial Revolution, how people move and generate goods has changed. This has led to an increase in per capita energy consumption, which is becoming more dramatic, as world population grows. Nowadays, energy production is mainly based on the combustion of fossil fuels (oil, coal or gas), which produce highly contaminating gases with significant climate change risks. Moreover, fossil fuels are not geographically evenly distributed, and often deposits' location does not coincide with where exploitation takes place. These are only some of the main issues that we are currently facing for energy production and distribution. To address them, one possible solution is to develop and introduce alternative energy sources, which are based on affordable, sustainable and accessible energy resources (green energy) [1]. In this context, renewable energies technologies are excellent solutions, as they are virtually unlimited and environmentally friendly. Between them, solar and wind-power energies are among the most promising and widespread energy sources. However, they are inherently intermittent. Thus, a transition from a fossil-fuels based system to a renewable energy economy needs efficient energy storage systems (ESS) as a bridge between energy generation and energy consumption.

Unfortunately, currently we only have capacity for storing a minimum part of the energy consumed worldwide and most of this energy is stored in pumped hydroelectric plants, which have very low energy density [2]. Besides, cost per cycle, safety, maintenance, mobility and ease of use must be considered for developing alternative EES. There are other options for storing energy such as compressed air, batteries, fuel cells, flow batteries, solar fuels, superconducting magnetic ESS, capacitors and supercapacitors, flywheels or thermal ESS. Between them, lithium-ion batteries (LIBs), considered a developed technology, are desirable candidates for both mobile and stationary applications mainly due to their high coulombic efficiency and high energy and power densities (Figure 1. 1) [3].

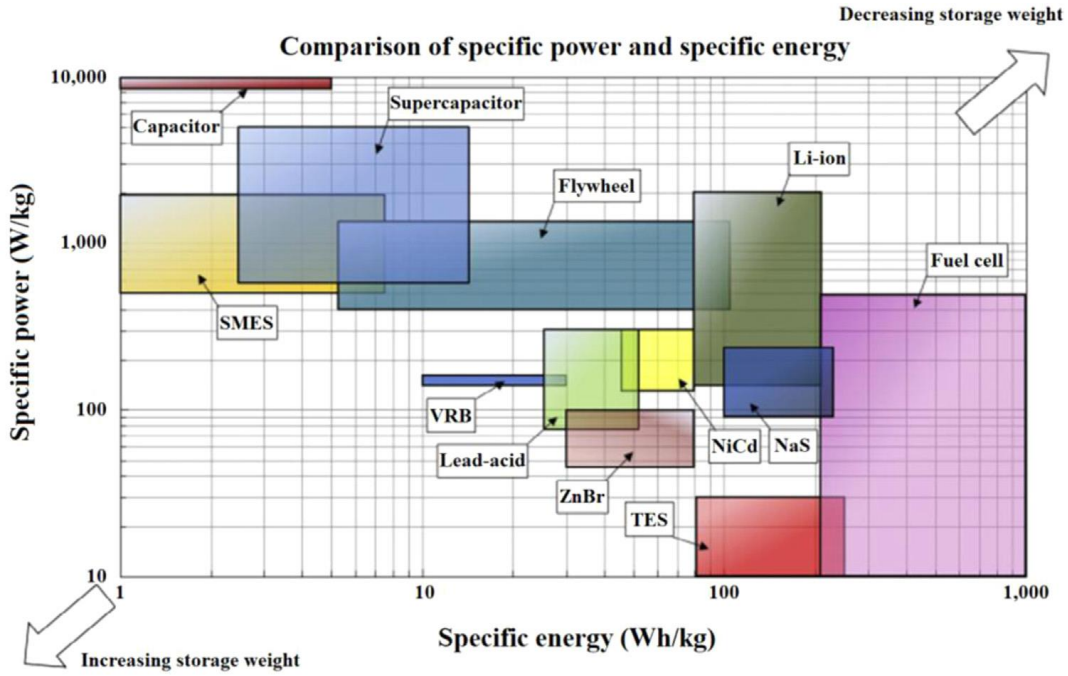

Figure 1. 1. Comparison of specific energy and specific power for several energy storage systems. The acronyms refers to: SMES (superconducting magnetic energy storage), VRB (vanadium redox battery), ZnBr (zinc-bromine battery) and TES (thermal energy storage) [4]**.**

Even though they are still under development for large-scale applications, LIBs could be integrated into a smart green grid to properly manage the electricity production and demand (Figure 1. 2) [5]. More importantly, LIBs are the ESS of choice for electric vehicles (EVs), which can also be included in smart grids to reduce the emission of greenhouse gases. EVs, however, are still not widely adapted, mainly due to the limited driving range of the car between charges. For this reason, further development of LIBs is required in terms of energy and power density [6]. Besides, it is not only about power and energy; cost, safety and reliability are particularly important aspects to be considered for new battery generations [7]. Therefore, the interest in developing LIBs has been increasing from the last decades and it will most probable be a very relevant research topic during the next years.

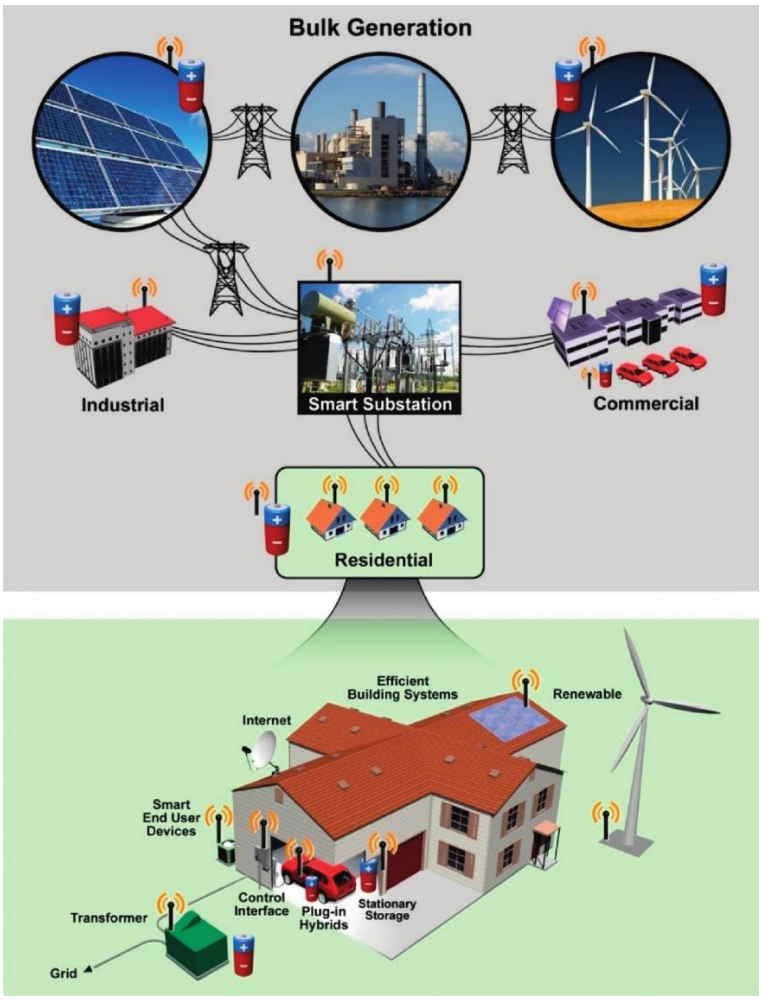

Figure 1. 2. Schematic representation of energy storage system integrated into a smart grid with renewable energy power generation [5]**.**

Besides the attractiveness of lithium-ion batteries, cost reduction and safety improvements are the main challenges to widespread their commercialization for EVs and large-scale energy storage applications. From one side, the low relative abundance of materials and the high cost of battery manufacturing are the main contributions to the total energy production cost. By designing cheaper electroactive materials and moving to more efficient processing, the total cost of battery production can be significantly decreased [2]. On the other side, safety can be improved by using active materials with higher thermal stability and reducing the presence of flammable and thermally unstable compounds in the electrode.

1.2. Lithium-ion batteries

1.2.1. Fundamentals

A lithium-ion battery is an ESS which uses electrochemical reactions to generate power, which means that chemical energy is converted in electrical energy. A battery is usually composed of several cells, connected in parallel and/or in series to provide the required capacity and voltage, respectively. Each cell consists of two electrodes separated by an electrolyte. Once the electrodes are connected through an external electrical circuit, the reactions occur spontaneously and simultaneously in both electrodes generating power. The potential difference between the electrodes is the cell voltage and it is directly correlated to the delivered energy [8]. Despite the term battery usually defines a system in which several cells are assembled, it is conventionally used to refer the final device even if it only contains a single cell, and so it will be used in this Thesis manuscript.

A lithium-ion battery is a rechargeable (or secondary) battery. The operation of a conventional lithium-ion battery is mainly based on the reversible insertion of lithium cations in the cathodic and anodic active materials. During the discharge of a battery, the oxidation of the anode active material releases lithium cations, which diffuse to the cathode, and electrons, which are conducted to the external circuit. At the same time, the cathode active material receives lithium ions and electrons and is reduced to compensate for the charge. Copper and aluminium foils are used in contact with the anode and cathode, respectively, as current collectors. On the other hand, during battery charge, energy is applied to force the lithium ions migration to the anode (the charge process is not spontaneous) [9]. A diagram of the discharge/charge of a lithium-ion cell is shown in Figure 1. 3.

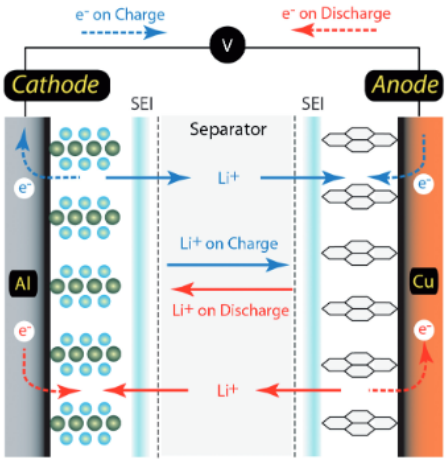

Figure 1. 3. Schematic representation of the discharge/charge process of a lithium-ion battery. Adapted from [10].

In a LIB, each material is characterized by a specific quantity of charge storage capability, which is called capacity. It is usually expressed in A·h and can be normalized by weight, volume or mol. The theoretical capacity of the material (normalized by weight) can be derived from Faraday's law, and it represents the amount of charge that can be stored by the material in exam. Considering the Faraday's constant, the charge of 1 mol of electrons corresponds to 96485.3329 C. Thus, considering the number of electrons involved in an intercalation reaction, the theoretical coulombic capacity ($Q_{theoretical}$) for an electrode can be calculated by:

$$Q_{theoretical}\ (mA \cdot h \cdot g^{-1}) = \frac{n \cdot F}{3600 \cdot M_w}$$

Where n is the number of electrons in the reaction, F the Faraday constant and M_w the molecular weight of the active material.

As the active material mass is obtained from the electrode weight, the specific current applied for charging or discharging the battery can be calculated. The current applied is usually expressed as C-rate. At a C-rate of C/10 or 1C the battery is discharged (or charged) in 10 h or 1 h, respectively. To calculate the C-rate, the theoretical capacity of the material is employed.

Thus, the specific capacity ($mA \cdot h \cdot g^{-1}$) of the electrode (also called gravimetric capacity) is calculated from the total sum of the current that is transferred to the electrode during the charge/discharge:

$$Q = \int_{t_1}^{t_2} I\ dt$$

In the same way, if it is considered the current that flows at a certain voltage U (typically the average voltage) during the experiment time, the specific energy ($W \cdot h \cdot kg^{-1}$) is obtained:

$$E = \int_{t_1}^{t_2} I \cdot U(t)\ dt$$

However, the specific power of the cell ($W \cdot kg^{-1}$) is obtained by multiplying the output voltage by the specific current. Notice that the voltage depends now on the state-of-charge (SOC) of the battery:

$$P = V(Q) \cdot I$$

Analogously to mass, these parameters can be converted to their corresponding volumetric capacity, energy and power by considering the density of the material.

The coulombic efficiency of the cell (C_{eff}) is usually given, as it provides information about the reversibility of the charge/discharge process:

$$C_{eff}\ (\%) = \frac{Q_{discharge}}{Q_{charge}} x\ 100$$

The cycling stability and the lifetime of a cell is determined by the number of charge/discharge cycles for which the capacity retention is higher than 80 %. The capacity retention is the ratio of the discharge capacity of a cycle $n + y$ to the discharge capacity of cycle n, which usually is the first cycle or the cycle following the formation stage.

$$C_{eff}\ (\%) = \frac{Q_{discharge}\ (cycle\ n + y)}{Q_{discharge}\ (cycle\ n)} x\ 100$$

1.2.2. Electrodes for lithium-ion batteries

Secondary lithium batteries were born in the 1970s when the idea of using intercalation compounds as the active material of the positive electrode began to be explored. In a first approach, a lithium foil was used as the negative material and an intercalation compound as the positive one (lithium-metal batteries). Despite the very high specific capacity of lithium metal (3860 mA·h/g), it was found that dendrites grow at the metal surface resulting in serious safety problems [8]. To overcome the safety concern, the use of intercalation compounds for both positive and negative electrodes was proposed [11] leading to the as-known lithium-ion batteries.

In the following sub-chapters, a general overview of the most used negative and positive electrodes for commercial LIBs is presented. As $Li_4Ti_5O_{12}$ and $LiFePO_4$ are the active materials used in this work, they are explained with more details.

1.2.2.1. Anodes

For the last 20 years, graphite has been the most employed negative material for LIBs due to its high specific capacity (372 mA·h/g), high volumetric capacity, low average voltage, good thermal stability and good electronic conductivity between others. However, graphite presents some disadvantages. It undergoes moderate volumetric expansion/contraction during charge/discharge of the battery, which can result in the peeling off of the active material from the current collector and thus battery deterioration. Besides, the low and flat working voltage profile (between 0.1 and 0.2 V vs. Li^+/Li) makes difficult to identify the end-of-charge, which may result

in an overcharge of the battery and a safety hazard. An important drawback of a battery containing graphite as the negative electrode is the irreversible capacity loss during the first charge due to the formation of a passivation layer on the electrode surface, called solid-electrolyte interface (SEI). This layer is formed as soon as a negative potential is applied to a carbon electrode immersed in an electrolyte. The SEI acts as a solid electrolyte between the electrode and the liquid electrolyte, preventing the anode from corrosion or dissolution. Thus, it is essential for a successful operation and safety of a LIB [12].

Other negative materials, such as lithium alloys, have recently attracted attention due to their high specific capacities (e.g. 3579 mA·h/g for silicon). However, these materials generally suffer from massive expansion during lithiation-delithiation processes (e.g. 280 % for Si), which is their main drawback and limits their application [13].

In this context, the spinel-type $Li_4Ti_5O_{12}$ (LTO), is a good alternative to graphite as it is considered a zero strain material, that is, the volume expansion during lithiation/delithiation is negligible (0.2 %) compared to that of graphite (10 %), ensuring a high cycling stability and long operation life [14]. Because the two-phase mechanism during battery cycling, LTO presents a flat discharge/charge profile, cantered at 1.55 V vs. Li^+/Li and its theoretical specific capacity is 175 mA·h/g considering that each mol of $Li_4Ti_5O_{12}$ can accommodate 3 mol of Li^+:

$$Li_4Ti_5O_{12} + 3Li^+ + 3e^- \rightleftarrows Li_7Ti_5O_{12}$$

During lithiation, the lithium ions move from the 8a to the 16c sites (Figure 1. 4) and, when all 16c sites are occupied, a rock salt type structure is formed, corresponding to the composition $Li_7Ti_5O_{12}$ (Figure 1. 4). The empty 8a sites facilitate lithium diffusion through 16c→8a→16c pathways [15].

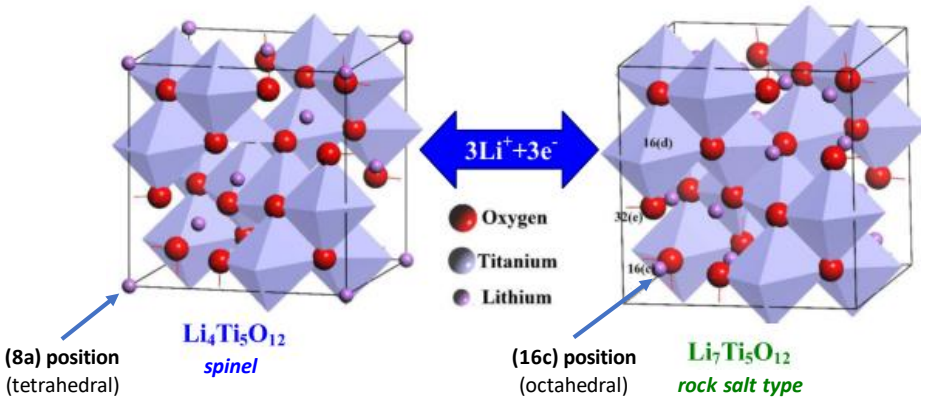

Figure 1. 4. Structure of $Li_4Ti_5O_{12}$ and $Li_7Ti_5O_{12}$. Adapted from [16]

LTO has recently attracted considerable attention due to the minimum chance of SEI formation and dendritic growth, which enhances its rate capability and safety. However, LTO exhibits a very low electronic conductivity (~ 10^{-7} - 10^{-8} S/cm) [17,18] and low lithium-ion diffusion coefficient (~ 10^{-8} - 10^{-13} cm^2/s) [19], which limits its capacity and rate performance. To solve this problem, doping is used to increase the electronic conductivity and lithium diffusion of LTO particles accompanied by a carbon coating for enhancing the electronic conductivity between LTO particles [20]. The carbon coating of LTO particles is a very effective method not only for improving the electrical conductivity of the material but also for acting as a barrier to the contact between the LTO particles and the carbonated electrolytes, preventing gassing (CO, CO_2 and H_2 evolution) derived from the electrolyte decomposition [21]. Another approach for increasing the lithium diffusion coefficient is to reduce the particle size and consequently shorten the diffusion length. Many works have used nanoparticles to obtain LTO materials with high rate performance [22].

1.2.2.2. Cathodes

The current commercial cathode materials for LIBs and their characteristics (specific/volumetric capacities and average voltage) are collected in Table 1. 1. The different materials and their main advantages and limitations are described in this section, [14], [23,24].

Table 1. 1. Features of the modern commercial cathode materials for lithium-ion batteries (crystal structure, specific and volumetric capacities and average voltage). Data were taken from [14]**.**

Crystal structure	Compound	Theoretical/experimental specific capacity (mA·h/g)	Average voltage (V)
Layered	$LiCoO_2$	274/148	3.8
	$LiNi_{1/3}Mn_{1/3}Co_{1/3}O_2$	280/160	3.7
	$LiNi_{0.80}Co_{0.15}Al_{0.05}O_2$	279/199	3.7
Spinel	$LiMn_2O_4$	148/120	4.1
Olivine	$LiFePO_4$	170/165	3.4

$LiCoO_2$ (LCO) was firstly proposed by G.B. Goodenough in 1980 [25] and used by Sony to produce the first commercial LIB in the 1990s. Since then, it has been the most widely used positive material for LIBs. It was very attractive due to its relatively high theoretical specific and volumetric capacities. However, its high cost (due to the relatively low abundance of Co), low

thermal stability, and relatively low practical specific capacity are the main reasons for its limited application, nowadays. In order to overcome LCO limitations, isostructural materials with LCO were proposed: $LiMnO_2$ and $LiNiO_2$.

$LiMnO_2$ was presented as a substitute to LCO due to its high thermal stability and safety. However, its cycling performance is not satisfactory, mainly due to the phase transition it undergoes during lithium insertion/extraction [26]. In order to enhance its specific capacity and structure stability, Ni and Co are added to the composition, resulting in $LiNi_xMn_yCo_{1-x-y}O_2$ (NMC). This material has a higher capacity than LCO and similar working voltage, also with a lower cost because of the reduction of Co. It presents a good compromise between energy and power density which makes it be one of the most popular positive materials for current commercial high power LIBs, including EVs [27]. The subscripts of the formula are usually called by their atomic ratios. Thus, for example, $LiNi_{0.5}Mn_{0.3}Co_{0.2}O_2$ is known as NMC-532. An exception is $LiNi_{1/3}Mn_{1/3}Co_{1/3}O_2$, which is known as NMC-111 (referred to x = y = 1/3). The electrochemical performance and thermal properties of NMC depends on its composition [28].

On the other hand, $LiNiO_2$, despite presenting similar theoretical specific capacity than LCO, is not favourable as Ni^{2+} ions tend to substitute Li^+ sites during synthesis and lithium extraction, blocking the Li diffusion pathways [29]. To overcome this problem, the partial substitution of Ni by Co and the addition of Al results in the reduction of the cationic disorder and the improvement of the thermal stability. As a result, $LiNi_{0.80}Co_{0.15}Al_{0.05}O_2$ (NCA) was developed with outstanding energy and power densities, and it has been successfully implemented in the EVs industry.

Another commercial cathode material is $LiMn_2O_4$ (LMO). It benefits from the relatively low cost of Mn, high power density and high safety which makes it have a place in the market for high power tools and even for some EVs models. Nonetheless, it presents low stability during cycling due to side reactions with the electrolyte and Mn dissolution [30] and has the lowest specific capacity between the commercial cathode materials.

$LiFePO_4$, firstly proposed by Goodenough *et al.* as a positive material for Li-ion batteries [31], has attracted much attention due to its fairly low cost and environmentally benignity (low toxicity). Furthermore, it has high structural stability, (contributing to long battery life), and high power density.

LFP exhibits a flat charge/discharge voltage profile at 3.5 V, within the electrochemical stability window of commercial electrolytes, which minimizes the decomposition of typical liquid electrolytes [32]. The theoretical capacity of LFP is 170 mA·h/g according to:

$$LiFePO_4 \rightleftarrows FePO_4 + Li^+ + e^-$$

Eventually, it is considered the safest cathode material, presenting a very high thermal stability and preventing O_2 evolution and thermal runaway. The high structural stability of LFP is explained by its crystalline structure (Figure 1. 5). PO_4 tetrahedra are zigzagged along [010] direction and alternating a-c planes. These tetrahedra serve as a bridge between the FeO_6 octahedra of adjacent planes by sharing one edge with FeO_6 and two edges with LiO_6, which gives great stability to the structure due to the strong P-O covalent bond.

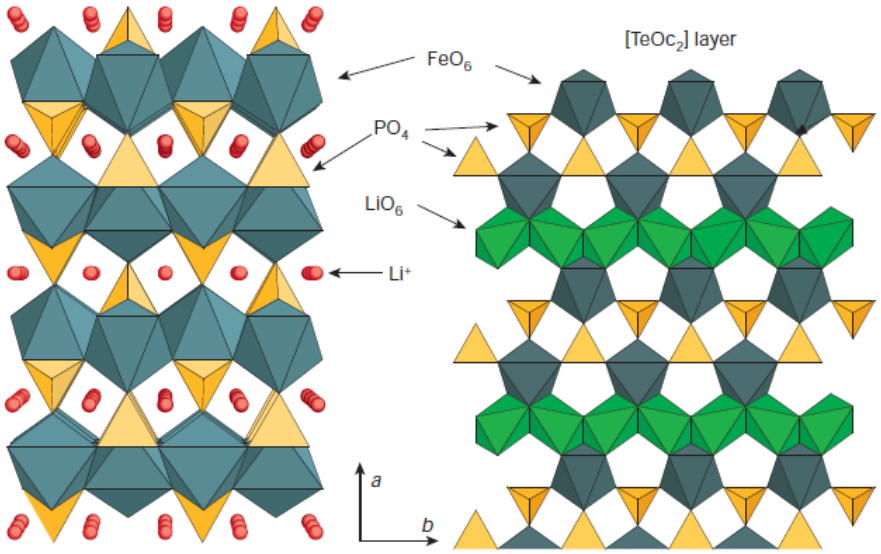

Figure 1. 5. Crystal structure of $LiFePO_4$ along the [001] direction. On the left image, the octahedra FeO_6 (in bluish-green) and tetrahedra PO_4 (in yellow) framework is represented, with Li ions in red. On the right image, the LiO_6 octahedra are represented in green. Image were taken from [33].

Lithium motion in LFP mainly occurs through the 1D channels along the c axis direction [32]. During lithium insertion and extraction in the discharge-charge processes of a battery, the structural stability of LFP is excellent due to the volume restriction for the movement of the lithium atoms in the structure. Therefore, the volume difference between $FePO_4$ and $LiFePO_4$ is only 6.8% [34], which explains its excellent cyclability. As a consequence of this restriction for the ion movement, however, the lithium diffusion coefficient (D) in $FePO_4$ and $LiFePO_4$ is very low (10^{-16}-10^{-13} cm^2/s) [35–37].

To give a general overview, Figure 1. 6 shows a spider chart of the main characteristics of the different commercial cathode materials. A score is provided for each feature so that "1" means the poorest performance and "5" the best one. It can be observed that NCA and NMC present high power and energy density, which justifies their widespread use in EVs [6]. However, safety associated to the risk of thermal runaway is a significant concern [38]. For LCO, as mentioned before, the main drawback is its low safety and high cost. On the other side, LMO is a good option in terms of power density and safety, but its stability is very poor and has a very low energy density. LFP presents an excellent performance in terms of power density, safety, stability and cost. Indeed, the main disadvantage of LFP lies in its lower energy density compared with other cathode materials. This is not due to its specific capacity (170 mA·h/g), among the highest ones, but to its average potential (3.5 V). Currently, experimental and commercial LFP cathodes achieve specific capacities close to the theoretical one (Table 1. 1). Therefore, the theoretical maximum specific energy is already reached.

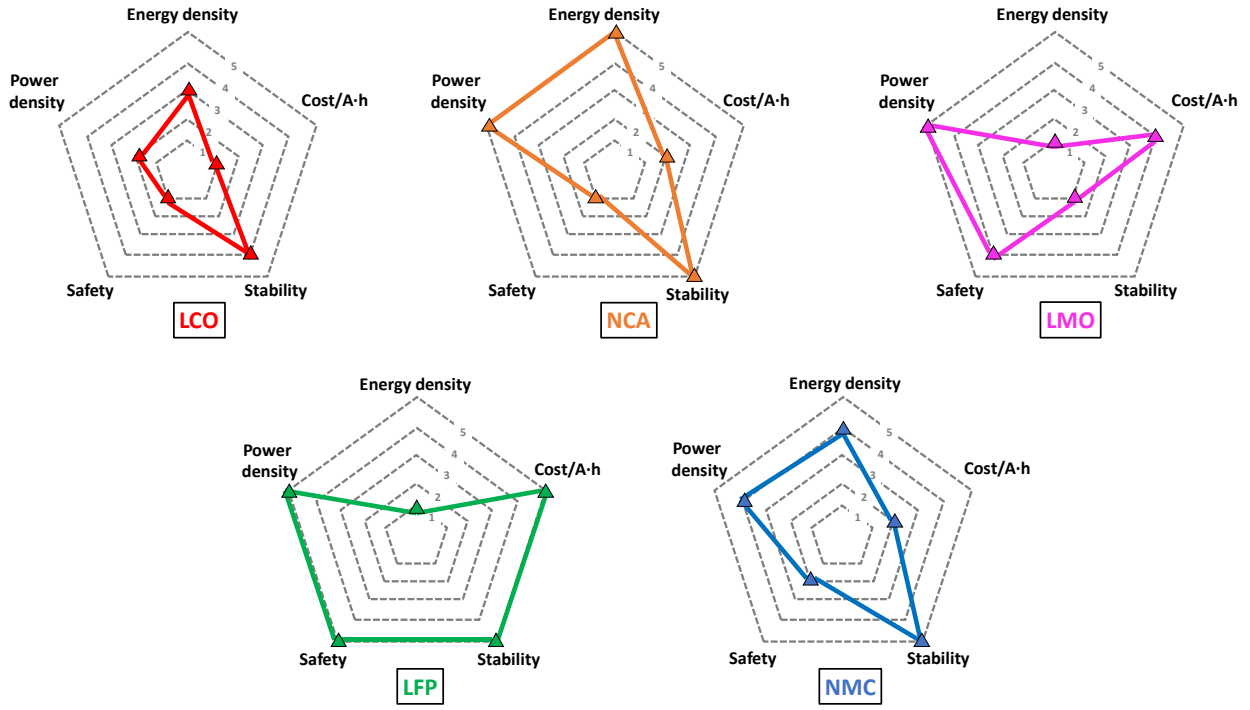

Figure 1. 6. Main challenges of cathode materials for lithium-ion batteries. The worst performance is scored as "1" and the best as "5". Created from data of [6].

1.2.3. Conventional electrode manufacturing

The different steps involved in the assembly of conventional LIBs are described in this section [8].

The active materials for the anode and cathode are selected according to the final application of the battery. The preparation of both electrodes is very similar. First, a conductive agent (usually acetylene black, carbon black) is added to the powder to improve the electrical conductivity, and it may also mitigate the dilatation and contraction of the particles during lithium insertion and extraction. Then, a binder is added as plasticizer to favour the manipulation of the electrode. One of the most common binders is polyvinylidene fluoride (PVDF). However, it is dangerous for humans and the environment and, moreover, the expensive, toxic and flammable N-N-methylpirrolydone (NMP) is used to dissolved it [39]. Next, the active material, carbon additive and dissolved binder are mixed and deposited on an aluminium foil (for the cathode) or copper foil (for the anode) usually by casting, coating or printing. After this, the film is calendared to reduce the porosity and, finally, they are cut to the desired dimensions. Finally, alternate films of anode and cathode with a porous separator between them are stacked or rolled depending on the cell configuration (Figure 1. 7) and then the case is filled with the electrolyte. Usually, a period between 12 and 24 hours is required for complete electrolyte wetting. Then, the so-called formation process occurs, by which an electronically passivation film forms at the electrolyte/electrode interface, known as the solid electrolyte interface (SEI).

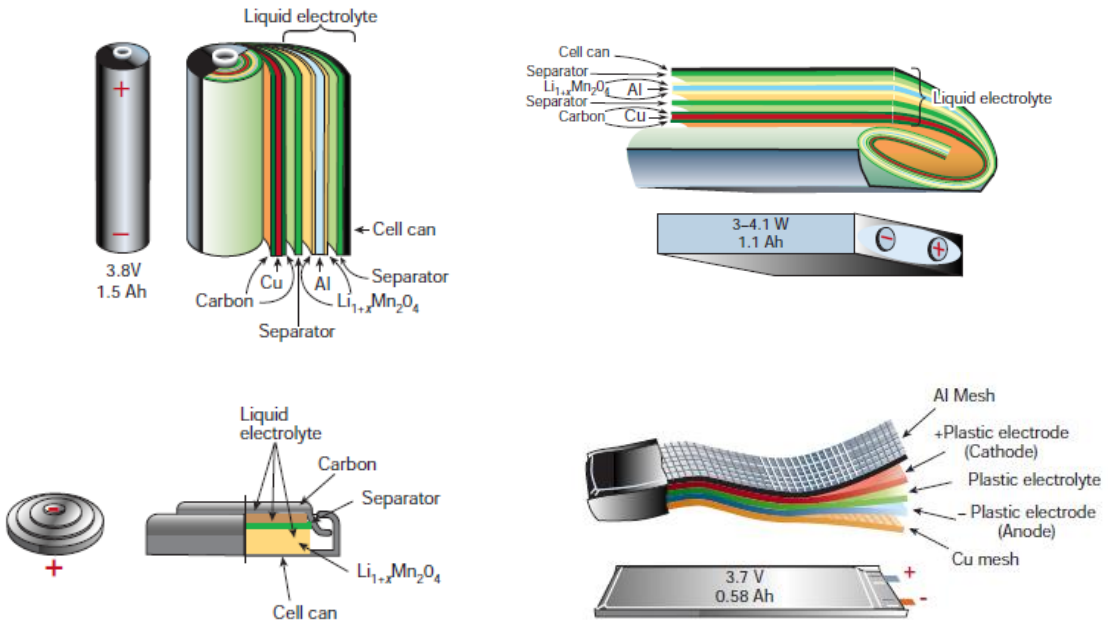

Figure 1. 7. Configurations for Li-ion batteries with different shapes and their components [33]**. In these examples, $Li_{1-x}Mn_2O_4$ is the positive active material and carbon the negative one.**

1.3. Beyond conventional lithium-ion batteries: thick electrodes and all solid-state batteries

Since the past two decades, commercial lithium-ion batteries have achieved typical specific energies of ~250 W·h/kg and maximum energy densities of 690 W·h/l (see Table 1. 2) [40]. However, this still cannot satisfy the increasing demand for higher energy and power densities of large-scale energy storage and electric vehicles. Furthermore, the use of flammable, thermally unstable and corrosive organic liquid electrolytes of conventional batteries can lead to serious safety problems [41]. As a result, new manufacture of LIBs with higher energy density and safety toward lower cost are urgently needed.

Table 1. 2. Theoretical and practical specific energy and energy density of commercial lithium-ion batteries [40].

Li-ion battery	Theoretical specific energy (W·h/kg)	Specific energy in 18650-size LIBs (W·h/kg)	Theoretical energy density (W·h/l)	Energy density in 18650-size LIBs (W·h/l)
$C/LiCoO_2$	420	206	1597	530
$C/LiNi_{1/3}Mn_{1/3}Co_{1/3}O_2$	450	210	1561	530
$C/LiNi_{0.80}Co_{0.15}Al_{0.05}O_2$	470	265	1597	690
$C/LiMn_2O_4$	330	132	1146	340
$C/LiFePO_4$	370	126	1126	325

LIBs cost strongly depends on the electrodes' chemical composition, but the non-active components (carbon additives, binders, separators and current collectors), which represent about half of the weight of the total battery, play an important role [33]. For this reason, a major LIB cost-cutting measure lies in the increase of electrodes' areal capacity [42], which involves using much thicker electrodes than those employed in the current commercial batteries (usually no more than 100 μm thickness [43]). In addition, the removal of electrical inactive components leads to an increase of both gravimetric and volumetric energy densities. Figure 1. 8 represents a conventional electrode configuration, where thin anode and cathode are stacked, against a thick electrode configuration. By a rough calculation, if the electrode thickness is increased from 25 to 200 μm, the inactive components can be reduced from 45 to 12 wt. % with the corresponding increased of active material (from 56 to 88 wt.%) [44].

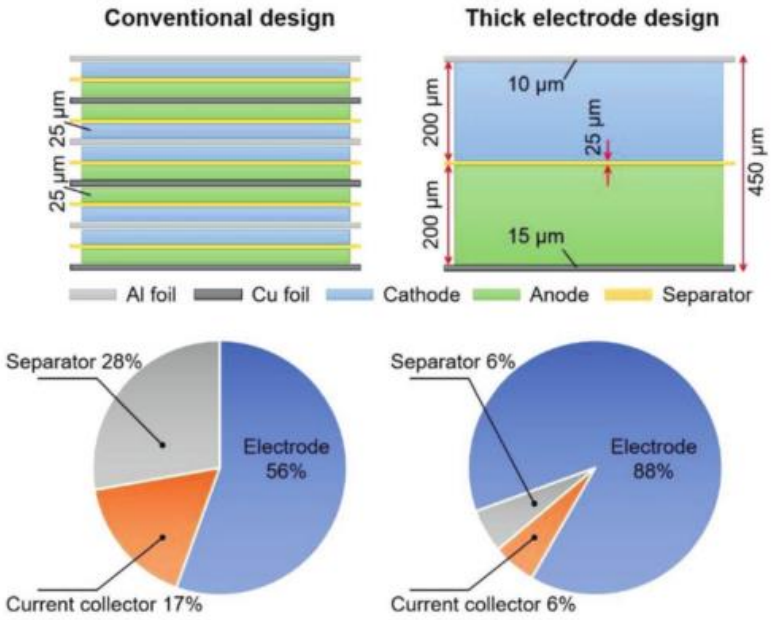

Figure 1. 8. Schematic representation of the battery component's ratios using conventional thin electrodes with stacking configuration and thick electrode (200 µm thickness) configuration. The percentages of the separator, the current collector and the electrode are expressed in weight %, the tap density of both anode and cathode was assumed to be 3.2 g·cm^{-3}, and the packing thickness was not considered [44].

A good alternative to the current commercial LIBs using thick electrodes is the so-called all solid-state batteries (ASSBs) in which, instead of a porous separator soaked in a liquid electrolyte, a solid-state electrolyte (SSE) is employed. Despite solid electrolytes usually commonly exhibit lower ionic conductivities than liquid electrolytes, in the past years significant improvements have been achieved and, currently, some SSEs can reach conductivities up to ~10^{-2} S·cm^{-1} [45], even higher than conventional organic liquids. One of the main advantages of all solid-state batteries is their high safety due to the substitution of combustible organic solvents by a solid electrolyte. Moreover, the highly cost solvents are avoided, and the time associated to drying, electrolyte wetting and SEI formation is not consumed. Besides, the use of solid electrolytes permits designing batteries with higher energy densities due to (1) the wider working voltage range of solid electrolytes (up to 5 V) compared to organic liquid electrolytes and (2) the possibility of using large specific capacity electrodes, such as lithium metal [46].

Even if the all solid-state strategy seems to be a promising solution for developing high density safe lithium-ion batteries, ASSBs still face great challenges, such as (i) the high impedance of the electrode/electrolyte interface, (ii) the poor mechanical stability of the electrode/electrolyte interface due to volume changes of the electrodes during charging/discharging and (iii) the substantial increase in the thickness of composite electrodes frequently results in cracking and

delamination. Furthermore, an efficient and homogeneous transfer of electrons and ions through their entire volume must be guaranteed in order to avoid the performance decay of the cells (iv) new processing methods are needed to reduce their high manufacturing cost and allow their commercialization [47]. In an attempt to address the challenges associated with thick electrodes design, several approaches have been proposed.

One attractive solution is using the additive manufacturing process, which allows designing electrodes with variable geometries. For that, a slurry containing the active material is added layer by layer. Thus, thick LTO (200, 450, 820 μm) [48] and LFP (1500 μm) [49] electrodes have been recently produced by 3D printing. These electrodes exhibit relatively high areal capacities (4.8 $mA \cdot g \cdot cm^{-2}$ at 0.2C for LTO and 7.5 $mA \cdot g \cdot cm^{-2}$ for LFP at 0.1C). However, the presence of additives and binders in the printable inks reduces the gravimetric and volumetric electrode capacities and limits the thermal stability of the electrode.

Further approaches in which binders and carbon additives are eliminated could improve the electrochemical performance of the battery and allow to operate at higher temperatures in which most of the binders are unstable, hence increasing the safety of the battery. Recently, binder-free LTO and LFP ceramic electrodes (1 mm thickness) with high areal capacity (20 $mA \cdot h/cm^{-2}$) and highly porous (40 %) were fabricated by Spark Plasma Sintering (SPS), and a templating approach, using NaCl, and its subsequent removal by water [50]. The main drawbacks of this fabrication methodology (not discussed in the paper) are *(i)* the plausible ion-exchange reaction occurring, *i.e.,* Li^+ by H^+ (water) and/or Na^+ (NaCl), as a consequence of being in contact with NaCl aqueous solution, and *(ii)* the questionable industrial scale-up of the SPS process.

The preparation of ceramic composites is also a common way of increasing the electrode thickness. In this context, Kanno *et al.* reported thick composite electrodes based on $LiCoO_2$ (600 μm) as cathode material and graphite as anode material with large areal capacity (15.7 $mA \cdot h/cm^2$) [51]. The composite electrodes were constituted by a mixture of glassy electrolyte (GE), and active electrode materials. Consequently, high capacity was achieved at the expense of weight increase. The weight increase is due to the high amount of electrolyte in the composite electrodes (36 and 54 wt. % of GE in cathode and anode respectively). However, they are limited to the use of electrolytes and electrodes that do not react with each other at the sintering temperature. Furthermore, there are better alternatives to electrode materials than the toxic and costly LCO.

Although in the past years it is rapidly growing, the production of thick electrodes is still an unexplored field compared to, for example, the development of new active materials. However, the importance of new methods to obtain thick electrodes is being recognized, mainly focusing in avoiding the use of costly and toxic solvents, reducing the amount of inactive components and increasing the energy density of the battery. Thus, in this Thesis, new processing methods for the manufacturing of additive-free electrodes with high volumetric capacities are proposed.

1.4. Bibliography

[1] S. Chu, A. Majumdar, Opportunities and challenges for a sustainable energy future, Nature. 488 (2012) 294–303. doi:10.1038/nature11475.

[2] D. Larcher, J.M. Tarascon, Towards greener and more sustainable batteries for electrical energy storage, Nat. Chem. 7 (2015) 19–29. doi:10.1038/nchem.2085.

[3] H. Chen, T.N. Cong, W. Yang, C. Tan, Y. Li, Y. Ding, Progress in electrical energy storage system: A critical review, Prog. Nat. Sci. 19 (2009) 291–312. doi:10.1016/j.pnsc.2008.07.014.

[4] G. Zubi, R. Dufo-López, M. Carvalho, G. Pasaoglu, The lithium-ion battery: State of the art and future perspectives, Renew. Sustain. Energy Rev. 89 (2018) 292–308. doi:10.1016/j.rser.2018.03.002.

[5] Z. Yang, J. Zhang, M.C.W. Kintner-Meyer, X. Lu, D. Choi, J.P. Lemmon, J. Liu, Electrochemical energy storage for green grid, Chem. Rev. 111 (2011) 3577–3613. doi:10.1021/cr100290v.

[6] X. Zeng, M. Li, D. Abd El-Hady, W. Alshitari, A.S. Al-Bogami, J. Lu, K. Amine, Commercialization of Lithium Battery Technologies for Electric Vehicles, Adv. Energy Mater. 1900161 (2019) 1–25. doi:10.1002/aenm.201900161.

[7] B. Dunn, B. Dunn, H. Kamath, J. Tarascon, Electrical energy storage for the gridfor the Grid : A Battery of choices, Sci. Mag. 334 (2011) 928–936. doi:10.1126/science.1212741.

[8] C. Julien, A. Mauger, A. Vijh, K. Zaghib, Lithium Batteries: Science and Technology, Springer, 2016. doi:10.1007/978-3-319-19108-9.

[9] D. Liden, T. Reddy, eds., Handbook of batteries, 3rd editio, McGraw-Hill, 2004.

[10] B.J. Landi, M.J. Ganter, C.D. Cress, R.A. DiLeo, R.P. Raffaelle, Carbon nanotubes for lithium ion batteries, Energy Environ. Sci. 2 (2009) 638–654. doi:10.1039/b904116h.

[11] M.B. Armand, Intercalation electrodes, in: Mater. Adv. Batter., NATO CONFERENCE SERIES, 1980: pp. 145–161.

[12] E. Peled, S. Menkin, Review - SEI: Past, present and future, J. Electrochem. Soc. 164 (2017) A1703–A1719. doi:10.1149/2.1441707jes.

[13] M.N. Obrovac, V.L. Chevrier, Alloy negative electrodes for Li-ion batteries, Chem. Rev. 114 (2014) 11444–11502. doi:10.1021/cr500207g.

[14] N. Nitta, F. Wu, J.T. Lee, G. Yushin, Li-ion battery materials: Present and future, Mater. Today. 18 (2015) 252–264. doi:10.1016/j.mattod.2014.10.040.

[15] C.P. Sandhya, B. John, C. Gouri, Lithium titanate as anode material for lithium-ion cells: A review, Ionics (Kiel). 20 (2014) 601–620. doi:10.1007/s11581-014-1113-4.

[16] T.F. Yi, S.Y. Yang, Y. Xie, Recent advances of $Li_4Ti_5O_{12}$ as a promising next generation anode material for high power lithium-ion batteries, J. Mater. Chem. A. 3 (2015) 5750–5777. doi:10.1039/c4ta06882c.

[17] B. Yan, M. Li, X. Li, Z. Bai, J. Yang, D. Xiong, D. Li, Novel understanding of carbothermal reduction enhancing electronic and ionic conductivity of $Li_4Ti_5O_{12}$ anode, J. Mater. Chem. A. 3 (2015) 11773–11781. doi:10.1039/c5ta00887e.

[18] M. Wilkening, R. Amade, W. Iwaniak, P. Heitjans, Ultraslow Li diffusion in spinel-type structured $Li_4Ti_5O_{12}$ - A comparison of results from solid state NMR and impedance spectroscopy, Phys. Chem. Chem. Phys. 9 (2007) 1239–1246. doi:10.1039/b616269j.

[19] B. Zhao, R. Ran, M. Liu, Z. Shao, A comprehensive review of $Li_4Ti_5O_{12}$-based electrodes for lithium-ion batteries: The latest advancements and future perspectives, Mater. Sci. Engeenering R. 98 (2015) 1–71. doi:10.1099/00221287-128-9-2165.

[20] C. Lin, B. Ding, Y. Xin, F. Cheng, M.O. Lai, L. Lu, H. Zhou, Advanced electrochemical performance of $Li_4Ti_5O_{12}$-based materials for lithium-ion battery: Synergistic effect of doping and compositing, J. Power Sources. 248 (2014) 1034–1041. doi:10.1016/j.jpowsour.2013.09.120.

[21] Y.B. He, B. Li, M. Liu, C. Zhang, W. Lv, C. Yang, J. Li, H. Du, B. Zhang, Q.H. Yang, J.K. Kim, F. Kang, Gassing in $Li_4Ti_5O_{12}$-based batteries and its remedy, in: Sci. Rep., 2012. doi:10.1038/srep00913.

[22] M.J. Armstrong, C. O'Dwyer, W.J. Macklin, J.D. Holmes, Evaluating the performance of nanostructured materials as lithium-ion battery electrodes, Nano Res. 7 (2014) 1–62. doi:10.1007/s12274-013-0375-x.

[23] G.E. Blomgren, The development and future of lithium ion batteries, J. Electrochem. Soc. 164 (2017) A5019–A5025. doi:10.1149/2.0251701jes.

[24] B.L. Ellis, K.T. Lee, L.F. Nazar, Positive electrode materials for Li-Ion and Li-batteries, Chem. Mater. 22 (2010) 691–714. doi:10.1021/cm902696j.

[25] K. Mizushima, P.C. Jones, P.J. Wiseman, J.B. Goodenough, Li_xCoO_2 ($0<x\leq1$): A new cathode material for batteries of high energy density, Solid State Ionics. 15 (1980) 783–789. doi:10.1016/0167-2738(81)90077-1.

[26] P. He, H. Yu, D. Li, H. Zhou, Layered lithium transition metal oxide cathodes towards high energy lithium-ion batteries, J. Mater. Chem. 22 (2012) 3680–3695. doi:10.1039/c2jm14305d.

[27] T. Placke, R. Schmuch, G. Hörpel, R. Wagner, M. Winter, Performance and cost of materials for lithium-based rechargeable automotive batteries, Nat. Energy. 3 (2018) 267–278. doi:10.1038/s41560-018-0107-2.

[28] H.J. Noh, S. Youn, C.S. Yoon, Y.K. Sun, Comparison of the structural and electrochemical properties of layered $Li[Ni_xCo_yMn_z]O_2$ (x = 1/3, 0.5, 0.6, 0.7, 0.8 and 0.85) cathode material for lithium-ion batteries, J. Power Sources. 233 (2013) 121–130. doi:10.1016/j.jpowsour.2013.01.063.

[29] A. Rougier, P. Gravereau, C. Delmas, Optimization of the composition of the $Li_{1-z}Ni_{1+z}O_2$ electrode materials: Structural, magnetic, and electrochemical studies, J. Electrochem. Soc. 143 (1996) 1168–1175. doi:10.1149/1.1836614.

[30] G. Xu, Z. Liu, C. Zhang, G. Cui, L. Chen, Strategies for improving the cyclability and thermo-stability of $LiMn_2O_4$-based batteries at elevated temperatures, J. Mater. Chem. A. 3 (2015) 4092–4123. doi:10.1039/c4ta06264g.

[31] A.K. Padhi, K.S. Nanjundaswamy, J.B. Goodenough, Phospho-olivines as Positive-Electrode Materials for Rechargeable Lithium Batteries, J. Electrochem. Soc. 144 (1997) 1188–1194. doi:10.1684/agr.2014.0700.

[32] L.-X. Yuan, Z.-H. Wang, W.-X. Zhang, X.-L. Hu, J.-T. Chen, Y.-H. Huang, J.B. Goodenough, Development and challenges of $LiFePO_4$ cathode material for lithium-ion batteries, Energy Environ. Sci. 4 (2011) 269–284. doi:10.1039/C0EE00029A.

[33] J.M. Tarascon, M. Armand, Issues and challenges facing rechargeable lithium batteries, Nature. 414 (2001) 359–67. doi:10.1038/35104644.

[34] A.S. Andersson, B. Kalska, L. Häggström, J.O. Thomas, Lithium extraction/insertion in $LiFePO_4$: An X-ray diffraction and Mössbauer spectroscopy study, Solid State Ionics. 130 (2000) 41–52. doi:10.1016/S0167-2738(00)00311-8.

[35] H. Liu, C. Li, H.P. Zhang, L.J. Fu, Y.P. Wu, H.Q. Wu, Kinetic study on $LiFePO_4$/C nanocomposites synthesized by solid state technique, J. Power Sources. 159 (2006) 717–720. doi:10.1016/j.jpowsour.2005.10.098.

[36] X.C. Tang, L.X. Li, Q.L. Lai, X.W. Song, L.H. Jiang, Investigation on diffusion behavior of Li^+ in $LiFePO_4$ by capacity intermittent titration technique (CITT), Electrochim. Acta. 54 (2009) 2329–2334. doi:10.1016/j.electacta.2008.10.065.

[37] P. Paolo, M. Lisi, D. Zane, M. Pasquali, Determination of the chemical diffusion coefficient of lithium in $LiFePO_4$, Solid State Ionics. 148 (2002) 45–51.

[38] A. Mauger, C.M. Julien, Critical review on lithium-ion batteries: are they safe? Sustainable?, Ionics (Kiel). 23 (2017) 1933–1947. doi:10.1007/s11581-017-2177-8.

[39] D. Bresser, D. Buchholz, A. Moretti, A. Varzi, S. Passerini, Alternative binders for sustainable electrochemical energy storage-the transition to aqueous electrode processing and bio-derived polymers, Energy Environ. Sci. 11 (2018) 3096–3127. doi:10.1039/c8ee00640g.

[40] K.M. Abraham, Prospects and limits of energy storage in batteries, J. Phys. Chem. Lett. 6 (2015) 830–844. doi:10.1021/jz5026273.

[41] X. Feng, M. Ouyang, X. Liu, L. Lu, Y. Xia, X. He, Thermal runaway mechanism of lithium ion battery for electric vehicles: A review, Energy Storage Mater. 10 (2018) 246–267. doi:10.1016/j.ensm.2017.05.013.

[42] G. Patry, A. Romagny, S. Martinet, D. Froelich, Cost modeling of lithium-ion battery cells for automotive applications, Energy Sci. Eng. 3 (2014) 71–82. doi:10.1002/ese3.47.

[43] D.L. Wood, J. Li, C. Daniel, Prospects for reducing the processing cost of lithium ion batteries, J. Power Sources. 275 (2015) 234–242. doi:10.1016/j.jpowsour.2014.11.019.

[44] Y. Kuang, C. Chen, D. Kirsch, L. Hu, Thick Electrode Batteries: Principles, Opportunities, and Challenges, Adv. Energy Mater. 1901457 (2019) 1–19. doi:10.1002/aenm.201901457.

[45] N. Kamaya, K. Homma, Y. Yamakawa, M. Hirayama, R. Kanno, M. Yonemura, T. Kamiyama, Y. Kato, S. Hama, K. Kawamoto, A. Mitsui, A lithium superionic conductor, Nat. Mater. 10 (2011) 682–686. doi:10.1038/nmat3066.

[46] S. Xia, X. Wu, Z. Zhang, Y. Cui, W. Liu, Practical Challenges and Future Perspectives of All-Solid-State Lithium-Metal Batteries, Chem. 5 (2019) 753–785. doi:10.1016/j.chempr.2018.11.013.

[47] J. Schnell, T. Günther, T. Knoche, C. Vieider, L. Köhler, A. Just, M. Keller, S. Passerini, G. Reinhart, All-solid-state lithium-ion and lithium metal batteries – paving the way to large-scale production, J. Power Sources. 382 (2018) 160–175. doi:10.1016/j.jpowsour.2018.02.062.

[48] C. Liu, F. Xu, Y. Liu, J. Ma, P. Liu, D. Wang, C. Lao, Z. Chen, High mass loading ultrathick porous $Li_4Ti_5O_{12}$ electrodes with improved areal capacity fabricated via low temperature direct writing, Electrochim. Acta. 314 (2019) 81–88. doi:10.1016/j.electacta.2019.05.082.

[49] J. Wang, Q. Sun, X. Gao, C. Wang, W. Li, F.B. Holness, M. Zheng, R. Li, A.D. Price, X. Sun, T.K. Sham, X. Sun, Toward High Areal Energy and Power Density Electrode for Li-Ion Batteries via Optimized 3D Printing Approach, ACS Appl. Mater. Interfaces. 10 (2018) 39794–39801. doi:10.1021/acsami.8b14797.

[50] R. Elango, A. Demortière, V. De Andrade, M. Morcrette, V. Seznec, Thick Binder-Free Electrodes for Li–Ion Battery Fabricated Using Templating Approach and Spark Plasma Sintering Reveals High Areal Capacity, Adv. Energy Mater. 8 (2018) 1–8. doi:10.1002/aenm.201703031.

[51] Y. Kato, S. Shiotani, K. Morita, K. Suzuki, M. Hirayama, R. Kanno, All-Solid-State Batteries with Thick Electrode Configurations, J. Phys. Chem. Lett. 9 (2018) 607–613. doi:10.1021/acs.jpclett.7b02880.

Objectives

The main objective of this work is to prepare additive-free thick electrodes with application in high energy density lithium-ion batteries.

$Li_4Ti_5O_{12}$ (LTO) and $LiFePO_4$ (LFP) powders are selected as negative and positive active materials, respectively, based on their *(i)* outstanding cyclability, *(ii)* safety, *(iii)* environmentally friendly nature, *(iv)* almost zero-strain behaviour and *(v)* relatively low cost.

To produce the electrodes, as alternatives to conventional electrode manufacturing, two processing methods will be proposed: *(a)* Powder Extrusion Moulding (PEM) and *(b)* conventional Tape Casting (TC) followed by a sintering step. We have selected these technologies because they are fast near-net-shape, easily scalable and relatively cost-effective manufacturing methods to produce thick electrodes. Both methods result in a sintered ceramic electrode with no additives (binders, extra conductive carbon). PEM will be used to obtain LTO and LFP electrodes (~ 500 µm thickness), and TC will be employed to produce LTO electrodes (~ 250 µm thickness).

The electrodes will be tested separately in lithium half cells (using lithium as the negative electrode). Finally, the additive-free LTO and LFP electrodes produced by PEM will be tested together in a full cell configuration to obtain a lithium-ion battery with high energy density.

Chapter 2

Characterization techniques

2.1. X-Ray Diffraction (XRD)

XRD is a highly useful technique for identifying crystalline materials and determining the different phases present in a mixture. By a fingerprint method, the phases can be easily identified, and the unit cell parameters calculated. Besides that, Rietveld refinement method can be employed to obtain, between others, the unit cell parameters, atomic positions and occupancies with high accuracy by comparing the experimental pattern with a theoretical one, calculated from a standard model [1].

In this work, powder XRD was used for identifying the crystalline phases present in the materials under study for determining the unit cell parameters of the main phases. The samples were analysed by powder XRD using a Philips X'Pert-MPD with Cu Kα radiation in the 2θ range from 10° to 120° at a scanning step rate of 0.02°. A step time of 0.5 s was used for routine experiments and 7 s for structural refinement. Voltage and current intensity were 40 kV and 40 mA, respectively. For Rietveld refinement, the program *Fullprof Suite* was employed [2].

2.2. Electron microscopy

2.2.1. Scanning Electron Microscopy (SEM)

SEM is a widely employed technique for inspection and characterization of either organic or inorganic materials. The electrons are accelerated by a potential up to 30 kV and they interact with the sample, producing different kinds of phenomena. With a constant electron dose, the dispersed energy is scattered from different deepness of the material, as is shown in Figure 2. 1.

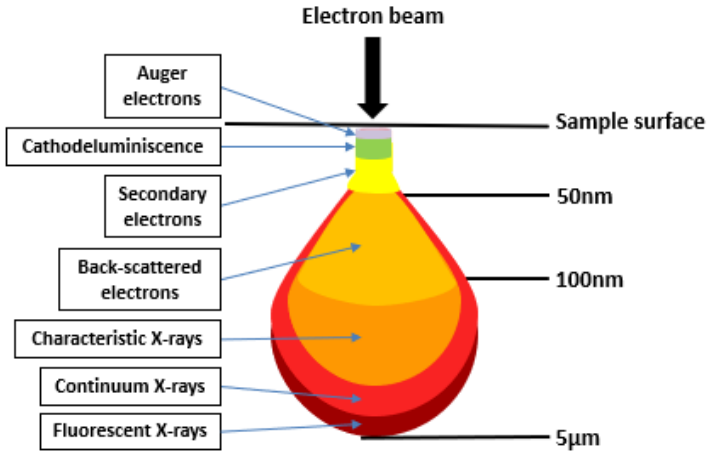

Figure 2. 1. Interaction volume between electron beam and sample and phenomena type generated in a Scanning Electron Microscope.

Inelastic scattering produces secondary electrons (SE), coming from the surface of the material, which provides morphological information. Elastic scattering gives back-scattered electrons (BSE) from deeper areas of the material and their intensity is proportional to the atomic number of the specimen, so compositional and topographical information are obtained from the resulting image. Eventually, X-rays are generated from relaxation processes of internal electronic transitions and provide data of elemental composition semiquantitatively by Energy-Dispersive Spectroscopy (EDS) [3].

During this study, the surface examination of the samples was performed, and, in some cases, cross-section images of the materials were taken in order to study the inside of the sample. The composition of some materials was investigated by EDS. In addition, an EDS mapping analysis was performed on some samples in order to check the homogeneous distribution of the different elements in the material.

The SEM equipment employed in this work was a TENEO-FEI Field Emission Scanning Electron Microscope (FESEM) equipped with an EDS X-ray analyser DX-4 detector. A Circular Backscattered (CBS) type detector was used for BSE and an Everhart-Thornley Detector (ETD) for SE. The working voltage was in the range from 5 to 10 kV. For a better inspection of polymeric materials, the samples were coated with Au using a sputtering equipment.

2.2.2. Transmission Electron Microscopy (TEM)

A transmission electron microscope uses much higher acceleration voltage than a scanning electron one (up to 300 kV). This allows decreasing the wavelength of the electrons and thus reaching atomic resolution. Detailed structural examination is possible throughout high magnification and high-resolution imaging. This technique also permits the investigation of crystalline structures, chemical compositions or specimen orientations.

In this work, TEM was employed for evidencing the presence of carbon coatings on the surface of LTO and LFP particles. For the sample preparation, the powder material was suspended in acetone, and the suspension was dropped in a copper grid which contains a porous polymer matrix. In this manner, the powder particles are collected in the polymer matrix. Before introducing the sample in the microscope, it was inspected using an optical microscope in order to check the presence of powder particles and their distribution. The microscope was a JEOL JEM 3000F operating at a potential of 300 kV and equipped with an INCA Energy EDS X-Ray analyser.

2.3. Differential Scanning Calorimetry (DSC)

DSC is a thermoanalytical technique in which the changes of a material heat capacity with temperature are recorded as changes in heat flow. It allows the detection of thermal transitions such as glass transitions, melting, curing and phase changes.

In this work, DSC was employed for identifying the melting temperature of the polymers employed as binder components for powder extrusion moulding. This information is very important for the design of the extrusion and debinding processes.

DSC experiments were performed in a Perkin Elmer Diamond calorimeter under a dry N_2 flow. The sample under study was located into a hermetically closed aluminium pan and the heat changes are compared with an empty crucible as reference. Before measuring, the materials were heated from 30 to 180 °C at 10 ºC·min^{-1} and cooled down to room temperature at the same rate in order to remove the thermal history of the polymer and hence, to be able to compare between them. Then, the samples (of approximately 15 mg) were heated again in the same conditions to 180 ºC. Peak temperatures and melting enthalpies were determined from the second scan.

2.4. Thermogravimetric Analysis (TGA)

TGA experiments are employed to measure the variation in mass of a sample with the temperature or time using a purge gas to control the sample environment. For variable temperature measurements, temperature is increased at a constant rate. The results can provide information about loss of solvent or water, oxidation/reduction reactions or decompositions. Depending on the target of the experiment, the variables that can be controlled are the atmosphere (O_2, N_2 or a combination of both), the heating and cooling rate, the time at a constant temperature and the initial and final temperatures.

In the case of this work, TGA was employed for different tasks: *(1)* to determine the decomposition temperature range of polymers and, consequently, for designing the heating cycles in different steps of the process, and *(2)* to study the thermal stability of different components.

The equipment was a Perkin Elmer TGA Pyris1 analyser using air or N_2 as working atmosphere. The temperature range was 30 to 600 °C and the heating rate was 10 °C/min. Polymeric samples were measured under N_2 atmosphere, while ceramics were studied under air. The mass amount of each sample analysed was between 10 and 20 mg.

2.5. Density measurements

2.5.1. Helium pycnometry

Helium pycnometry allows calculating the so-called theoretical density of a powder. This value, which is also known as true density, is usually taken as a reference of the maximum density that can be obtained after processing the material. Thus, the helium pycnometric density, or theoretical density, should be very close, but always lower, to the crystallographic density.

In this work, helium pycnometry was used for determining the theoretical density of the starting materials and for measuring the homogeneity of feedstocks for powder extrusion moulding.

The pycnometer was a Micrometrics AccuPyc 1330. After calibration, the average cell volume and expansion volume were 11.369 and 9.310 cm^3, respectively. The measurement was performed for three times using different fractions of each material. Then, the average value was calculated.

2.5.2. Archimedes method

The Archimedes method is employed for calculating the density of a compact material and it is especially useful for porous samples. As open and close pores are included in the density value, the total porosity of the sample is calculated by the difference between the theoretical and the Archimedes densities.

The sample weight is measured both immersed in water and at open air. For porous materials a lacquer is used as a pore sealant, preventing water from penetrating into the pores. Considering the Archimedes principle, the density can be calculated by using the following equation:

$$\rho = \frac{m_{dry}}{\frac{m_{sealed} - m_{immersed}}{\rho_{water}} - \frac{m_{sealed} - m_{dry}}{\rho_{lacquer}}}$$

where:

ρ is the calculated density of the sample (g/cm^3).

m_{dry} is the mass of the dry sample (g).

m_{sealed} is the mass of the sample sealed with the lacquer (g).

$m_{immersed}$ is the mass of the sample sealed with the lacquer and immersed in water (g).

ρ_{water} is the density of water (at working temperature conditions).

$\rho_{lacquer}$ is the density of the lacquer.

As the materials tested in this work are porous, a lacquer (density of 1.1 g/cm^3) was used as sealant agent. The measurement was repeated in three different samples of the same material and the average value was given.

2.6. Elemental carbon determination

The technique is based on the combustion of the sample and detection of the carbon released as CO_2 using an infrared detector. The amount of carbon dioxide is calculated by detecting the reduction in the level of energy that reaches the detector. The rest of the infrared energy is prevented from reaching the detector by a narrow bandpass filter [4].

During the development of this work, elemental carbon analysis was used for determining the carbon content of LTO and LFP samples at the different steps of the processing.

A Carbon/Sulfur Determinator (LECO CS-200 instrument) was used. In all cases, the sample weight was approximately 1 g, and the measurement was repeated five times for each batch, calculating the average value. For 1 g of material, the equipment can determine the carbon content in the range between 4 and $3.5 \cdot 10^{-4}$ ppm, with a precision of 2 ppm.

2.7. Particle size analyser

The particle size distribution of a powder can be measured by using a particle size analyser based on the dispersion of a laser beam that impacts the sample. For that, the powder particles are suspended between a laser beam and a detector and the light dispersed by the particles is collected and used for calculating their size.

The particle size and its distribution of commercial LTO and LFP powders was determined using a by a Malvern Mastersizer 2000. The experiments were carried out in dry conditions.

2.8. Rheology

2.8.1. Powder extrusion moulding rheology

Rheology experiments are crucial for determining the ability of a feedstock to be extruded. The technique allows registering pressure measurements at variable shear rates and temperatures and transducing it to viscosity. The best option to obtain the rheological curve of a thermoplastic feedstock is to use a capillary rheometer, at shear rates between 10 and 10^4 s^{-1}, reproducing the conditions found during moulding and extrusion processes. The instrument is equipped with a thermally controlled cylinder, in which the temperature is controlled by two thermo-couples (temperature control $\pm$ 0.1 °C). The feedstock is heated up to the melting temperature of the binder and forced by a piston to flow through a capillary. Under conditions of steady-state flow, the pressure drop and volumetric flow rate are measured, and the shear stress and shear rate can be determined to finally obtain the viscosity. Figure 2. 2 represents the feedstock flowing through a capillary rheometer and the different parts of the instrument.

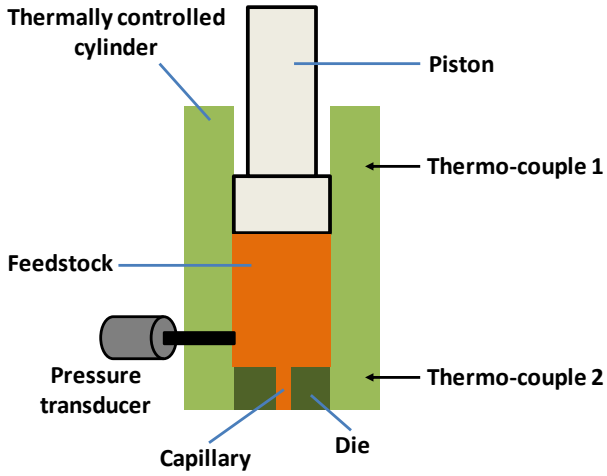

Figure 2. 2. Schematic representation of a capillary rheometer.

In our case, a Haake Rheocap capillary rheometer with a die of 30 mm length and 1 mm diameter was employed for maintaining a constant length/diameter ratio of 30. When the ratio length/diameter is equal or higher than 30, pressure corrections accounting for the elastic character of the polymers are not necessary. The viscosity was measured in the range of shear rates between 100 and 10000 s^{-1} and at temperatures between 160 and 190 °C (temperature control of $\pm$ 1 °C). The pressure transducer used in this investigation works in the range 0-1400 bar.

2.8.2. Tape casting rheology

In order to analyse the flow behaviour of a slurry and check its suitability for tape casting, rheological measurements are commonly done. One of the most used experiments consists in applying a variable shear rate while measuring the viscosity variation. For this, a parallel plate rheometer is employed. This equipment consists of two parallel discs. One of them is fixed (the bottom one) and the other one rotates (the top one). The slurry is poured between the two plates and the torque is measured in the rotating disk at different shear rates.

In this work, the viscosity of different LTO slurries was measured using a HAAKE Viscotester iQ from Thermo Scientific with a parallel plate geometry and profiled surfaces. A gap of 1 mm was fixed between the disks. The amount of slurry used for the measurement was enough for covering all the disk surface and to be retained in between the disks without flowing out. The viscosity was obtained by controlling the shear rate from 1 to 300 s^{-1}.

2.9. X-Ray Photoelectronic Spectroscopy (XPS)

XPS is a powerful technique for measuring the elemental composition of the surface of a material. It is based on the irradiation of the surface of a sample by X-ray photons and the detection of the emitted photoelectrons and Auger radiation. As the electron binding energy is characteristic of each element, the technique allows to determine the atomic species present in a material. Moreover, the high utility of the technique comes from the fact that the chemical environment of the atoms produces a shift in the binding energies of the electrons, being possible to determine the atomic environment and oxidation state. It must be highlighted that XPS is a surface technique and, even if the X-ray photons can penetrate a few microns, only the electrons from the first 10 nm of the sample thickness can reach the detector without losing kinetic energy and being trapped.

In this work, LTO electrodes prepared by powder extrusion moulding were investigated by XPS in order to determine the presence of Ti^{3+}.

An aluminium monochromatic source (K_a = 1486.6 eV) was used and a Phoibos 150 spectrometer was employed as detector. High resolution scans were acquired at high power (200 W), using a pass energy of 20 eV with an energy step of 0.1 eV. Data analysis was carried out with CasaXPS program, using Shirley-type function for the background and a function 70 % Gauss- 30 % Lorentz for the profile. The limit of detection of the Ti2p band considering the employed equipment is 0.38 at. % (relative sensitivity factor of 7.9).

2.10. Impedance Spectroscopy (IS)

Impedance is the ability of a circuit element to resist the electrical current flow. The Ohm's law defines the resistance as the ratio between voltage and current. However, this is limited to one circuit element (the ideal resistor), the resistance is independent of frequency and the alternating current (AC) voltage and current through a resistor are in phase. However, real systems contain elements with much more complex behaviour and, for that, impedance is used instead of resistance. In impedance measurements, potential with constant amplitude and variable frequency is applied, and the resulting current is measured. The excitation potential is usually small (10-100 mV) in order to obtain a response at the same frequency than the excitation signal but shift in phase (pseudo-linear behaviour) [5]. By impedance measurements, information about capacitance and resistivity can be obtained. This information can be associated with a specific phenomenon that occurs in the electrochemical cell. Resistors accounts for all the resistive contributions of the cell, such as electronic or ionic movement either in the bulk or interfaces of the different materials. On the other hand, the double-layer capacitance due to the charge accumulation in the interfaces is represented by a capacitor.

IS is a powerful technique for analysing the dynamics of charge in the bulk or interface of liquid and solid materials, which makes it be an excellent tool for research on materials to be used in a battery. IS provides information about capacitive behaviour, diffusion-limited reactions and electrochemical reactions.

As the electronic conductivity of an electrode is a crucial parameter for its electrochemical performance in a Li-ion battery, the impedance of the manufactured LTO and LFP electrodes was measured to determine their conductivities at room temperature. For that, a gold paste was painted on both sides of the samples as blocking electrodes. The paint was spread on one surface of the material and dried at 150 °C for 5 min after painting the other side. Then the samples were treated at 800 °C for 30 min to fix the paint to the surface of the ceramics. A home-made cell was used for measuring the impedance (see Figure 2. 3).

The equipment was an Impedance/Gain-Phase analyser SI 1260 (Solartron, UK) coupled with an Electrochemical Interface analyser SI 1287. The amplitude of the voltage applied was 100 mV and the measurements were recorded in the frequency range between 0.1 Hz and 10 MHz.

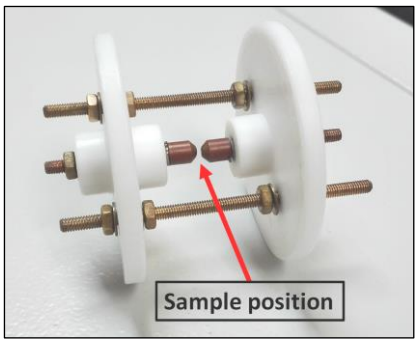

Figure 2. 3. Home-made cell for impedance measurements at room temperature.

2.11. Chronopotentiometry

Chronopotentiometry is one of the most employed techniques for batteries electrochemical characterization. It consists on applying a constant current to an electrode and detect the changes at its interface, which causes a potential response that is recorded during time. Thus, during the discharge of the battery, a negative current is applied, and the current is reversed to positive for charging the battery when the cut-off voltage is reached or after a defined time. In this manner, several cycles can be measured to study the cycling performance of the cell. Charge/discharge voltage-time profiles of the redox active materials (either the cathodic or anodic material) can be analysed to obtain some key parameters as specific capacity, energy and power, efficiency and cycling stability. Typically, the specific capacity (Q in $mA \cdot h \cdot g^{-1}$) of the material is reported for comparison with others and compared to the theoretical one.

Ideally, the measured potential of the cell should be equal to the Open Circuit Voltage (OCV), i.e. the one measured when no current is applied and in a relax state. In this condition, all the chemical energy stored in the material would be converted into electric energy. However, as soon as the circuit is closed and current flows through the electrode, potential losses occur due to polarization effects. These effects consume part of the energy, which is lost as heat. The potential dependency on the discharge rate is represented in Figure 2. 4. Polarization is composed by three phenomena [6].

(1) Ohmic polarization (IR loss): it is due to the internal impedance of the electrode, which is the sum of the resistances of the different components of the cell. The higher the current, the higher the ohmic polarization. Only at very low currents the working potential approximates the OCV. Also, poor contact between the current collector and the working

electrode can produce bad current distribution along the electrode surface and hence increase the impedance in some parts and, consequently, the ohmic polarization.

(2) Activation (or charge transfer) polarization: it is associated to the electrochemical reaction kinetics, specifically to the exchange of electrons (charge transfer). In practice, it is affected by several parameters, such as temperature, applied current, electrochemically active species concentration, reaction constants (material dependent, e.g. activation energy).

(3) Concentration (or diffusion) polarization: it is a result from the concentration gradients between reactants and products at the electrode surface and inside the material, due to the mass transfer. The thickness of the electrode in ceramic materials is the main limitation for good diffusion. Therefore, in thick electrodes, porosity must be enhanced to counter for concentration polarization.

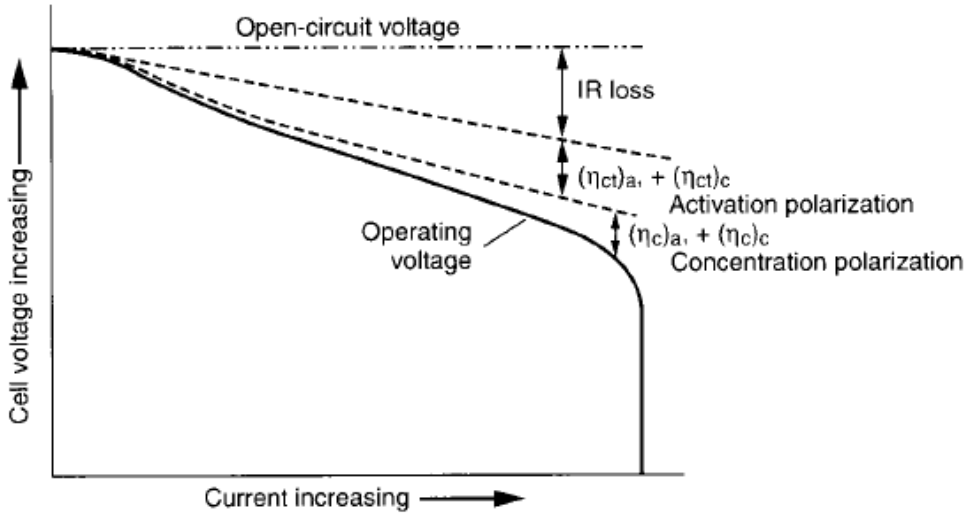

Figure 2. 4. Representation of the cell polarization while increasing current [6]**.**

For chronopotentiometry measurements, different cell configurations can be used by employing two or three electrodes cells.

A two-electrodes cell consists of a working electrode (WE), which is the material under investigation, and a counter electrode (CE). The potential is measured between these two electrodes. This configuration simulates real conditions of a commercial cell, where no reference electrode is available. When testing materials to be applied in lithium batteries, the counter electrode is usually lithium metal.

On the other hand, a three-electrode configuration has an additional reference electrode (RE) among which no current flows, allowing to measure the potential of the WE and CE, minimizing polarization effects. As the potential of the positive and negative electrodes can be evaluated separately, this configuration provides a deeper understanding of the electrochemical processes that occur in the material.

In this work, two-electrode cell configurations were employed (Swagelock cell and coin cell type CR2032). The specific conditions for chronopotentiometry measurements carried out for each material are specified in their corresponding chapter (see experimental procedure in Chapters 3 and 4).

2.12. Bibliography

[1] A.R. West, Solid State Chemistry, 2nd edition, John Wiley & Sons, Chichester, 2014.

[2] J. Rodríguez-Carvajal, Fullprof Program: Rietveld Pattern Matching Analysis of Powder Patterns, Grenoble, ILL, 1990, Phiysica B. 192 (1993) 55–69.

[3] D. Newbury, D. Joy, C. Lyman, P. Echlin, E. Lifshin, J. Michae, J. Goldstein, D. Newbury, D. Joy, I. Charles, Scanning Electron Microscopy and X-Ray Microanalysis, 3rd edition, Kluwer Academic/Plenum Publishers, New York, 2003.

[4] L. Corporation, CS-200 Carbon / Sulfur Determinator. Instruction Manual, (2003).

[5] J.R. Macdonald, Impedance Spectroscopy Theory, Experiment and Applications, Wiley Interscience, 2015.

[6] D. Liden, T. Reddy, Handbook of batteries, 3rd edition, McGraw-Hill, 2004.

Chapter 3

Additive-free thick $Li_4Ti_5O_{12}$ and $LiFePO_4$ electrodes manufactured by Powder Extrusion Moulding

3.1. INTRODUCTION TO THERMOPLASTIC POWDER EXTRUSION MOLDING

3.1.1. General description

Powder Extrusion Moulding (PEM) is a processing technology for shaping 2-D pieces of ceramic or metallic powders. It is a close variant of Powder Injection Moulding (PIM) and combines the advantages of polymer extrusion moulding with those of conventional powder technologies. Both PIM and PEM processes use a combination polymeric and organic compounds (binder) with an inorganic powder to form a mixture (feedstock) that can be moulded. After shaping the feedstock, the binder is removed (debinding step), and the ceramic/metal is sintered. PIM and PEM technologies allow obtaining three-dimensional and bidimensional samples, respectively, with exceptionally good shape control. These processes are also cheap, easily scalable at the industrial level and automatable, which makes them very productive and widely employed [1].

3.1.2. Powder extrusion moulding steps

In Powder Extrusion Moulding, the success of the process is based on the control and optimization of several steps. The process begins with the selection of the appropriate raw materials, which consist of ceramic or metallic powders, a binder system based on thermoplastic polymers and some additives to improve flow. The powder (usually between 45 and 65 vol. %) is mixed with the binder under proper conditions to obtain a homogeneous feedstock, which is fed to the extruder. During the extrusion, the so-called “green part” is obtained. This part already has the desired shape, but still contains the binder that must be removed. The debinding step can be performed in different ways, being the thermal debinding the most employed one. After the debinding, the so-called “brown part” is obtained. Due to the absence of binder, this part is very porous and presents low mechanical stability. Eventually, the brown part is densified by sintering obtaining the desired final properties of the material. Figure 3. 1 shows a schematic representation of the different steps of the process.

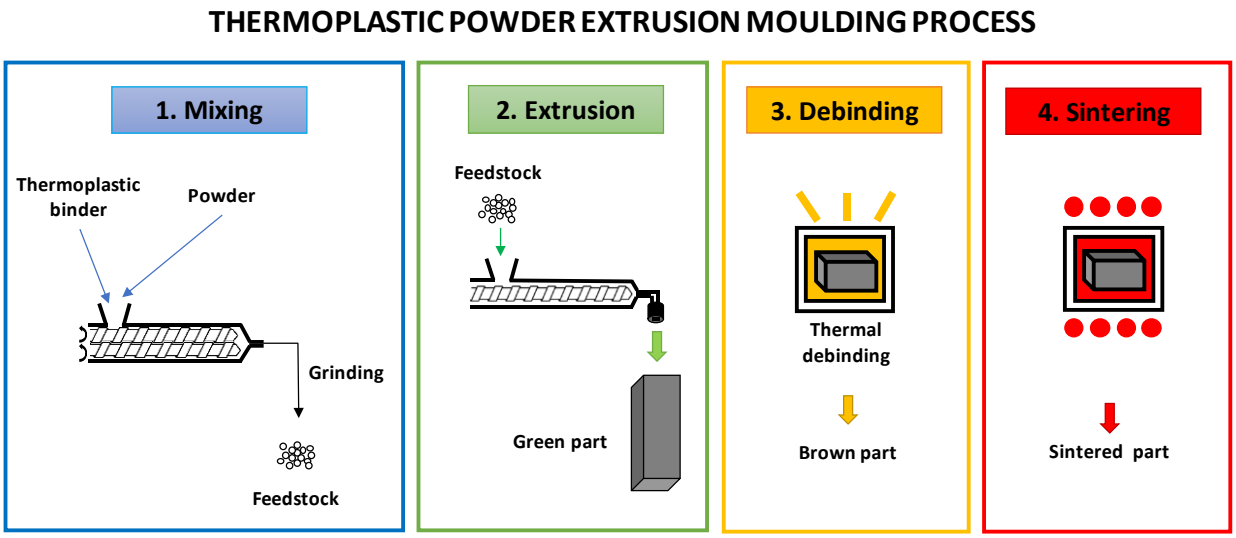

Figure 3. 1. Powder extrusion moulding process steps.

3.1.2.1. Powder and binder selection

In powder extrusion moulding, the selection of appropriated powder and binder as well as the optimization of the powder-binder composition are critical to ensure the success of the process.

In order to check the suitability of a powder for PEM, a deep characterization is recommended. This includes analysing its composition, particle size distribution, morphology, density and surface chemistry (including coatings). In principle, spherical-shape powders with a low tendency to agglomerate are desired in order to avoid particle orientation. Moreover, a wide particle size distribution favours the packing of the particles to reach a high-density material [2].

The binder, which is responsible for the flowability of the feedstock, is usually a mixture of organic and polymeric compounds. Usually, thermoplastic systems are classified according to their main component. The most common main components are polypropylene (PP), polyethylene (PE), ethyl vinyl acetate (EVA) and polymethyl methacrylate (PMMA), between others [2]. Minor additives are normally added to modify the viscosity and to improve the powder-binder interaction. Low molecular weight compounds are usually employed for reducing the viscosity of the feedstock and easing the moulding. Between them, paraffin wax is one of the most widely used [3].

3.1.2.2. Mixing

During the mixing step, powder and binder must be properly mixed to obtain a homogeneous feedstock. For that, a specific mixing equipment (such as a rotor blade mixer or a screw extruder) is used. The mixture is heated until the binder melts, but without reaching its degradation temperature, under shear forces that favour the mixture of powder and binder. In this step, the powder loading, the homogeneity and the rheological properties must be controlled to obtain an appropriate feedstock.

3.1.2.2.1. Powder loading

The viscosity of the feedstock rises with the powder volume fraction (powder loading). The Critical Powder Volume Concentration (CPVC) is the maximum powder volume percentage in which the powder particles are in contact between each other and all the free volume is filled by the binder. If the system has a binder excess, the material is more susceptible to defects formation, while, if the powder loading is too high, some voids are created between the particles, preventing the contact with the binder.

The CPVC depends on the binder composition and the powder characteristics. In such a way, the CPVC has to be estimated for each specific powder-binder system and for that, torque and viscosity measurements are commonly employed.

3.1.2.2.2. Homogeneity

A homogeneous feedstock is necessary to avoid phase separation during the extrusion process, to minimize geometry distortion during debinding and to favour the sintering. Temperature and shear stress applied during mixing are the most influent parameters in homogeneity. In general terms, the higher the shear stress the more homogeneous the feedstock is.

3.1.2.2.3. Rheological properties

The ability of a feedstock to be extruded is usually analysed by rheological measurements, in which the shear stress τ (Pa), defined as the resistance of a substance to flow per area unit, is measured at different shear rates $\dot{\gamma}$ (s^{-1}). Shear stress and shear rate are proportionally related by the viscosity η (Pa·s), following the so-called Newtonian behaviour:

$$\tau = \eta \cdot \dot{\gamma}$$

The rheological behaviour of a mixture is directly related to its viscosity, which is characteristic of the system at a given shear rate.

However, when the relation between shear stress and shear rate is not linear, the fluid is called non-newtonian and the viscosity depends on the shear stress. One of the most common models for non-newtonians fluids is the power law model proposed by Ostwald and De Waele [4,5]:

$$\tau = \eta \cdot \dot{\gamma}^{n}$$

where η is the viscosity, k the consistency index, $\dot{\gamma}$ the shear rate and n the power index. When n is lower than 1, the mixture presents a pseudoplastic behaviour, and the viscosity decreases when the shear rate increases. The value of n indicates the degree of sensitivity of viscosity with the shear rate. The lower the value of n the more sensitive is the viscosity to the shear rate.

For pseudoplastic fluids, viscosity is only influenced by the shear rate. In PEM, these fluids are employed to favour the flow of the feedstock through the extruder. In this manner, the viscosity of the feedstock decreases when it encounters high shear rates inside the extruder and increases when the material comes out from the extrusion nozzle, allowing to retain the nozzle shape.

The viscosity dependence with the temperature must also be studied, in order to optimize the temperature profile along the extrusion barrel and to control the flow of the feedstock. Normally, thermoplastic binders are often used, and they follow an Arrhenius-type equation:

$$\eta(T) = \eta_0 e^{E_a / RT}$$

where E_a is the flow activation energy, η_0 is the viscosity at a reference temperature T and R is the ideal gas constant.

3.1.2.3. Extrusion

For the extrusion process, two kind of extruders can be used: piston extruder (or ram extruder) and screw extruder [2]. As the viscosity of the feedstock depends on the operating temperature, both systems are thermally controlled.

In the first case, the feedstock fills a cylinder and it is forced, by means of a piston, to flow through a nozzle with a hole with the desired shape. Its main advantages are that it allows applying high pressures and the small number of moving parts permits minimizing sample contamination and tool wear.

A screw extruder, which is the most commonly used in PEM, consist in a barrel with a rotating screw inside. The ground feedstock is fed into the feeding zone and is then transported by the screw to the melting zone, in which the thermoplastic system melts allowing the flow of the mixture. The feedstock moves until the end of the barrel, where it comes out of the nozzle with a specific cross-section geometry, for example circular or rectangular. Figure 3. 2 includes a picture of a single-screw extruder and a schematic representation of the main parts of the equipment.

During extrusion, the screw rotation rate and the barrel profile temperature are optimized in order to obtain the green parts. Moreover, the cooling rate of the extruded part can be increased by water immersion.

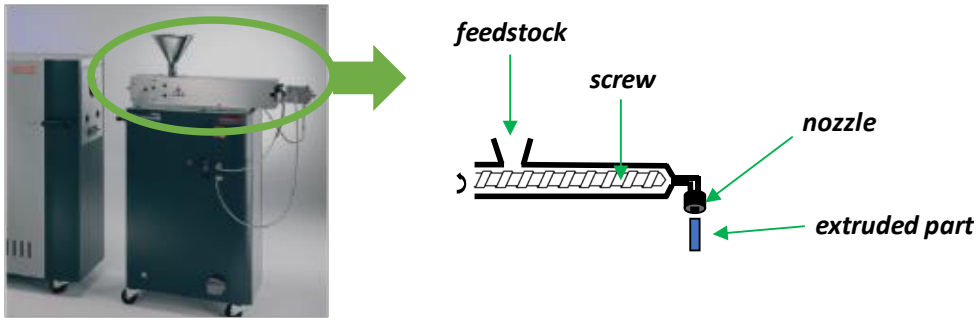

Figure 3. 2. Picture of a Haake Rheomex OS Single Screw Extruder (left) and schematic representation of the different parts of the extruder (right).

3.1.2.4. Debinding

The debinding process is a critical step in thermoplastic powder extrusion moulding to avoid defects in the final pieces. There are different types of debinding: catalytic debinding, debinding using supercritical fluids, solvent debinding and thermal debinding. Between them, the thermal debinding is the most commonly used for thermoplastic binders.

During a thermal debinding, temperature gradients and pressure rise inside the specimen may cause cracks. Moreover, debinding thermal cycles are usually very long, as the heating rates must be slow for minimizing bloating and blistering [2]. However, if some binder components are previously removed, internal channels are formed in the material, making easier the evacuation of the gases produced during the polymer thermal decomposition.

An option to create an open porous structure in the sample is to use a solvent debinding stage before the thermal debinding. For that, the ceramic green parts are immersed in a solvent which dissolves one of the components of the binder, which usually are low molecular weight

compounds such as waxes. The removal of these components provides the creation of interconnected channels, favouring the evacuation of the gases coming from the subsequent decomposition of the rest of the binder components [6,7]. In the solvent debinding, an appropriate solvent must be selected, and immersion time and temperature are optimized.

Moreover, multicomponent systems are beneficial for the thermal debinding, especially if their components present very different degradation temperatures, which allows removing them progressively. The thermal debinding is designed based on the decomposition temperature of the binder components that remain in the material. The heating rates programmed during the thermal cycle are critical to avoid cracks and defects in the brown parts.

3.1.2.5. Sintering

The sintering step consists in the densification of a powder by applying a heat treatment below the melting point of the material. During sintering, the main driving force of the process is the reduction of the surface energy, which can be principally due to *(1)* coarsening, the decrease of the total surface area as a consequence of grain growth and/or *(2)* densification, the removal of solid/vapor interfaces creating grain boundaries followed by grain growth, which densifies the material. These two mechanisms can occur simultaneously or one of them can dominate over the other. If the coarsening process is faster, both grains and pores become larger with the sintering time. On contrary, if the densification dominates, the pores decrease in size and the material shrinks [8,9].

Figure 3. 3 represents the three main stages of the sintering process. In the *initial stage* (Figure 3. 3-(a)), the contact between particles increases by neck growth. Relative densities of approximately 65 % can be reached during this step. The *intermediate stage* (Figure 3. 3-(b)) consists in the mass diffusion between particles, producing the formation of an open porous structure that leads to the creation of grain boundaries. During this stage, the material can densify from 65 to 90 % with respect to the theoretical density. Eventually, in the *final stage* (Figure 3. 3-(c)), some pores are isolated, and the densification rate of the materials is very low. However, the mobility of pores and grains is high, leading to possible pore and grain growth [9].

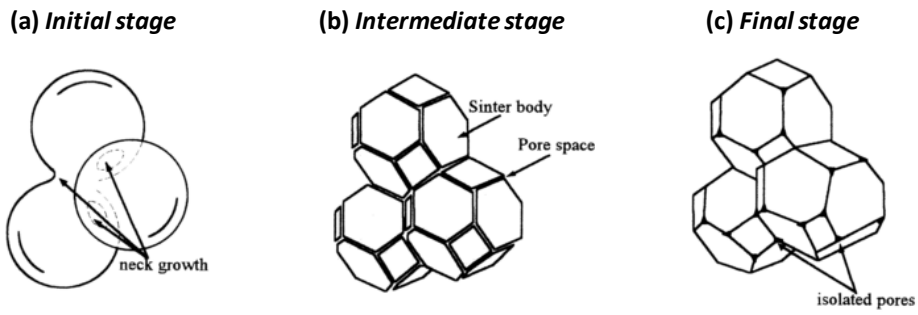

Figure 3. 3. Schematic representation of different stages during sintering. The initial stage is represented by spherical particles in tangential contact. During the intermediate stage the particles coalesce acquiring a dodecahedral shape creating pore channels at the grain edges. In the final stage isolated pores are located in the edge corners. Image adapted from [9]**.**

The optimization of the different parameters involved in the sintering process is fundamental to control the final properties of the sintered parts. Between them, heating and cooling rates, sintering time and temperature or sintering atmosphere are the most critical ones.

3.1.3. Powder extrusion moulding applications

One of the advantages of powder extrusion moulding is the capability of obtaining materials with different geometries, such as rods, tubes or prisms. Regarding to the applications, many different materials have been manufactured by PEM, such as metals (hard-metals [10], alloys [11] or stainless steel [12]) and ceramics (Si_3N_4 [13] or yttria-stabilized zirconia and ceria doped with gadolinium oxide [14]).

The possibility of producing ceramics with different porosities claims a lot of interest in the research field of Solid Oxide Fuel Cells (SOFCs), in which high porosity is desired to favour gas diffusion. For example, Sotomayor *et al.* successfully produced 430L stainless steel supports with different porosities by controlling the powder loading and sintering conditions [15]. Moreover, the porosity can be promoted by the use of pore formers. For example, corn starch [16] or PMMA [17]. On the other hand, Arias *et al.* studied the influence of the particle size distribution in the porosity and final properties of Ni-YSZ microtubes [18].

However, no one, to the best of our knowledge, has investigated the production of ceramic electrodes for lithium-ion batteries by PEM yet. However, our group has a well-recognized experience in PEM technology [12,15–18] and we recently patented the use of this method for the production of lithium-ion batteries electrodes [19].

3.2. OBJECTIVES

The aim of the present study is to *(1)* obtain additive-free $Li_4Ti_5O_{12}$ (LTO) and $LiFePO_4$ (LFP) electrodes with high thickness using the Powder Extrusion Moulding (PEM) technology and *(2)* prepare a full cell using the obtained LTO and LFP electrodes as anode and cathode, respectively, in order to obtain a high energy density lithium-ion battery.

For the manufacturing of LTO and LFP thick electrodes by PEM, the different steps in which the process consists will be optimized. Firstly, composition, particle size distribution morphology, microstructure and density of both LTO and LFP (starting powders) will be investigated. Then, the binder components will be thermally characterized, and the feedstock composition selected according to torque and rheological measurements. Once the homogeneous feedstock is extruded, a debinding step will be designed based on the decomposition temperatures of the binder components. Eventually, LTO and LFP layers will be sintered to obtain the additive-free electrodes. Structural, microstructural and electrical characterization of sintered LTO and LFP layers will be carried out to investigate the effect of sintering temperature and atmosphere in the final properties of the electrodes. The optimum additive-free LTO and LFP electrodes will be tested firstly separately in lithium half cells and finally, both electrodes will be tested together using a full cell configuration.

3.3. EXPERIMENTAL

3.3.1. Materials

3.3.1.1. $Li_4Ti_5O_{12}$ and $LiFePO_4$ powders

Commercial $Li_4Ti_5O_{12}$ (LTO) and $LiFePO_4$ (LFP) powders were both provided by Linyi Gelon Lib Co. LTD. It is important to underline that the $LiFePO_4$ powder presents a carbon coating and the total carbon content is 1.8 wt. % according to the specifications given by the provider.

3.3.1.2. Binder system

The binder system employed for powder extrusion moulding is a thermoplastic multicomponent system that consists in a mixture of polypropylene (PP), paraffin wax (PW) and stearic acid (SA). This system has been successfully used for PEM purpose in our laboratory previously. The molecular structure of each material is represented in Figure 3. 4.

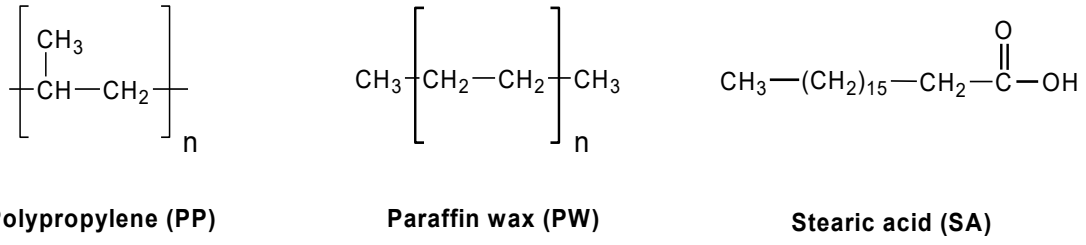

Figure 3. 4. Molecular structure of polypropylene (PP), paraffin wax (PW) and stearic acid (SA).

The selected *Polypropylene* (Isplen PP 090 G2M, Repsol-YPF) acts as the backbone polymer of the binder, providing strength to the system. Its molecular weight (M_w) is in the range 100000-150000 and the polymer presents a flow index of 55 g·10 min^{-1} (ISO 1133:2011, 230 °C/2.16 kg).

The *Parafin Wax* (Panreac, 99%) provides flowability by decreasing the viscosity of the binder compared to that of single polypropylene. This wax is a petroleum derivative formed by linear saturated hydrocarbon chains with variable length (n = 18-50) and few ramifications.

The *Stearic Acid* (Panreac, 99%) is the surfactant agent and acts also as a lubricant helping to unstick from the extruder screw and cavities. The polar extreme of the chain presents high affinity for the powder surface, while the low polarity one is compatible with the binder system. In this manner, SA improves the contact between the powder and the binder.

3.3.2. Production of $Li_4Ti_5O_{12}$ and $LiFePO_4$ electrodes by powder extrusion moulding

In this section, the different steps involved in LTO and LFP powder extrusion moulding are described. As the experimental procedure is analogous for both LTO and LFP materials, a common description of the process for both powders is given as follows.

3.3.2.1. Feedstock preparation and characterization

In order to mix the ceramic powder with the binder system and to optimize the powder loading, a pair roller rotor blade Haake Rheocord 252p mixer was employed. The equipment records the torque value during the mixing time. The chamber temperature was programmed at 180 °C and the mixing was carried out at a speed of 40 r.p.m. for 40 min, including the addition of the different components. The mixture total mass was calculated for filling the 70 % of the chamber volume with respect to its maximum capacity (69 cm^3). Figure 3. 5 shows a picture of the rotor blades inside the mixer chamber.

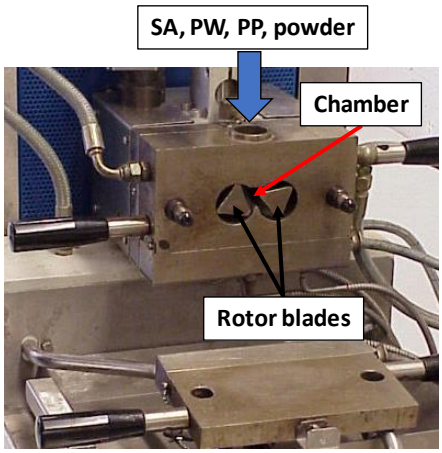

Figure 3. 5. Rotor blade mixer chamber of a Haake Rheocord 252p mixer.

Different mixtures were prepared by varying the powder/binder volume ratio. In all cases, the relative volumes of PP, PW and SA in the binder were maintained. The binder composition used in this work was optimized in previous studies [20] and was 50 vol. % of PP, 46 vol. % of PW and 4 vol. % of SA.

Table 3. 1 summarizes the volume percentage of the different components for the prepared mixtures. The mixtures were characterized in order to optimize the powder loading and to study their rheological properties for a good performance during the process.

Table 3. 1. Prepared mixtures and relative amounts of their components in volume percentage.

Component	Volume %						
Powder (LTO or LFP)	50.00	51.00	52.50	55.00	56.50	58.00	60.00
PP	25.00	24.50	23.75	22.50	21.75	21.0	20.00
PW	23.00	22.54	21.85	20.70	20.01	19.32	18.40
SA	2.00	1.96	1.90	1.80	1.74	1.68	1.60

3.3.2.1.1. Homogeneity

The evolution of torque with mixing time offers information about the homogeneity and viscosity of the mixture. When the torque remains constant with mixing time, the steady-state torque (τ), which is a first indicator of homogeneity, is reached. However, complementary experiments can be developed to ensure a good feedstock homogeneity.

First, the change in viscosity with time at a constant shear rate was measured for different mixtures. Feedstocks with same composition prepared in a rotor blade mixer and in a twin-screw extruder were measured and compared. A constant viscosity value with time is expected for homogeneous feedstocks, while the presence of heterogeneous parts in the mixtures would provoke viscosity variations. Secondly, the pycnometric density of three different fractions of the most homogeneous feedstock was measured and compared with the density value calculated from the relative volume fractions of each component and its respective density. If no material loss or degradation occur during the process, both density values should be equal. In addition, a low standard deviation of the average density value would indicate a good homogeneity while a high standard deviation implies a heterogeneous distribution of the powder within the binder. However, it must be considered that this is a qualitative approach.

3.3.2.1.2. Critical Powder Volume Concentration (CPVC)

Feedstocks with powder loadings very close to the CPVC have high viscosities as a consequence of the friction between the powder particles. For this reason, the optimal loading is considered to be between 2 and 5 vol. % lower than the CPVC [21].

Although there are several methods for estimating the CPVC, in this work a combination of torque and rheological measurements is employed for approaching the optimal powder loading of the feedstocks.

3.3.2.1.3. Rheological characterization

In order to determine the ability of the feedstocks to be extruded, a deep rheological characterization was performed. As the binder behaves as a thermoplastic material, a capillary rheometer was used to measure the feedstock viscosity in a wide shear rate range and at different temperatures.

3.3.2.2. Preparation of optimized feedstock

First, the LTO and LFP powder loadings were optimized. A twin-screw extruder (Haake Rheomex) is used to obtain big quantities of feedstock. The twin-screw extruder can reach shear rates much higher than those of the rotor blade mixer, leading more homogeneous mixtures. Moreover, the extrusion allows obtaining big quantities of mixture by a continuous process, while the mixer chamber has a limited capacity. Thus, for preparing the optimized feedstocks an extrusion profile temperature of 160/165/170 °C for LTO and 170/175/180 °C for LFP was programmed and a speed of 70 r.p.m. was used. The materials were passed through the extruder three times to obtain homogeneous feedstocks.

3.3.2.3. Extrusion

To obtain LTO and LFP thick electrodes, the feedstocks were ground for feeding a single-screw extruder. The extrusion process was done vertically through two different home-designed nozzles of 6 mm width and 0.5 or 1 mm thickness. A schematic representation of the 0.5 mm thickness nozzle is shown in Figure 3. 6-(a). The extruder machine (Figure 3. 6-(b)) was a Haake Rheomex OS Single Screw Extruder with four heating areas along the barrel from the feeder to the nozzle in which the temperature can be programmed individually. The barrel temperature profile was optimized and fixed to 170/175/185/155 °C and 175/178/182/185ºC for LTO and LFP, respectively. Green extruded electrodes of LTO and LFP of 0.5 and 1 mm of thickness were obtained.

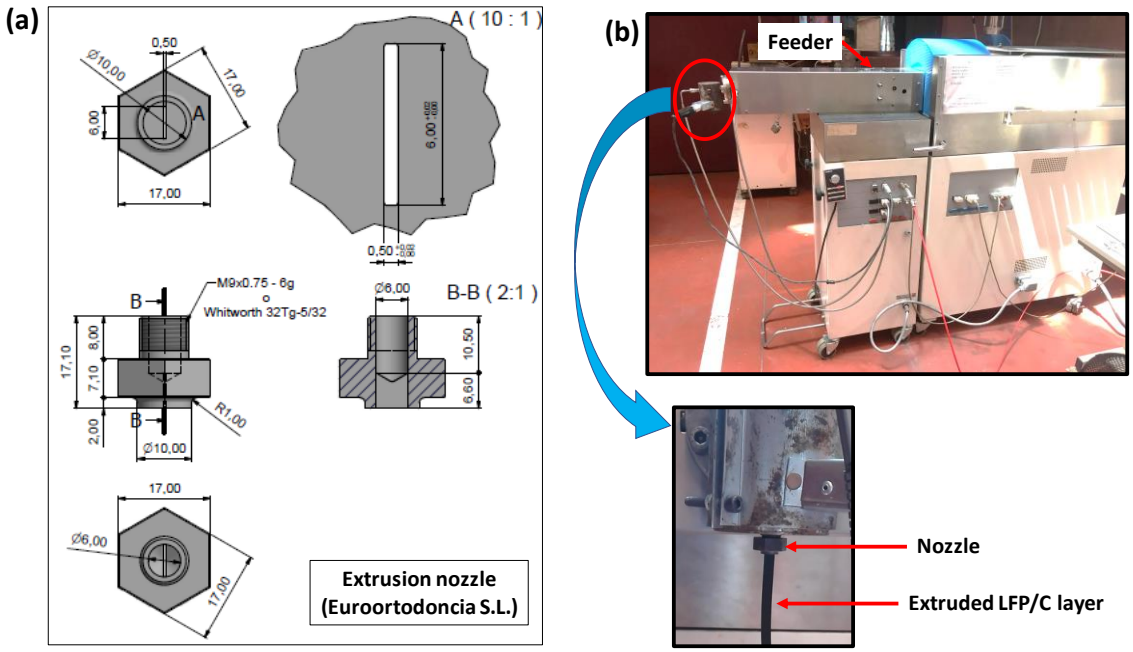

Figure 3. 6. (a) Home-design extrusion nozzle of 0.5 mm thickness. (b) Single-screw extruder machine for LTO and LFP films extrusions.

3.3.2.4. Debinding

In this work the debinding was performed in two steps: (1st) solvent debinding and (2nd) thermal debinding.

The solvent debinding was carried out by immersing the green electrodes in n-heptane for dissolving the binder components of lower molecular weight (SA and PW). The weight difference related to the initial mass of the sample was plotted against the immersion time. Thus, the extracted SA and PW at a certain immersion time t ($m_{t_{(SA+PW)}}$) was calculated as:

$$m_{t_{(SA+PW)}} = \frac{m_{i_{sample}} - m_{f_{sample}}}{m_{i_{(SA+PW)}}}$$

where $m_{i_{sample}}$ is the initial mass of the sample (t=0), $m_{f_{sample}}$ the mass of the sample after immersing for a specific time and $m_{i_{(SA+PW)}}$ the initial mass of SA and PW.

The design of the thermal cycle was based on TGA experiments of the binder components and the optimized feedstocks. A furnace Goceram GD-DC-50 was used for the thermal debinding. For LTO three different batches of samples were prepared in air, N_2 and Ar/H_2 (5 vol. % H_2). For LFP, the process was carried out in N_2 atmosphere. After the debinding process, the carbon content of the extruded layers was measured.

3.3.2.5. Sintering

The sintering process was optimized on the basis of density and shrinkage measurements. In all cases, a horizontal tubular furnace Carbolite STF 15/75/450 was employed and the heat treatment was performed under the same atmosphere used in the debinding process for each batch of samples. The heating and cooling rates were 2 °C/min and 5 °C/min, respectively. LTO electrodes were sintered at 900, 950, 1000, 1050 and 1100 °C for 1 h, while LFP was sintered at 600, 650, 700, 750, 800 and 850 °C for 2 h. In the case of LFP, the samples were covered with the commercial LFP powder (the layers were buried in the powder) for preventing oxidation due to eventual oxygen impurities of the N_2 gas.

3.3.3. Electrochemical performances of sintered electrodes in lithium half cells

3.3.3.1. $Li_4Ti_5O_{12}$ electrodes

The electrochemical properties of the LTO-extruded sintered electrodes were evaluated in collaboration with Instituto de Ciencia de Materiales de Madrid (ICMM-CSIC).

The samples under study were compared with a conventional composite electrode composed of 80 wt. % of the starting commercial LTO powder, 10 wt. % of carbon black (Super-P, TIMREX) and 10 wt. % of polyvinylidene fluoride (PVDF) and processed by the doctor-blade procedure. The maximum thickness of the cast electrodes was 110 μm and the mass loading was 9.4 mg/cm^2. In the case of the extruded electrode, the mass loading was 138 mg/cm^2 (475 μm thickness) and a nickel grid was used as current collector in order to improve the contact with the sample and hence the current density distribution.

The electrolyte was $LiPF_6$ 1M dissolved in EC:DMC (1:1 vol.%) (UBE) and a glass fibre separator (BSF80, Whatman) was used.

The cell assembly was done in a glovebox (H_2O and O_2 < 0.1 ppm) using a coin cell type CR2032 with lithium metal foil as reference and counter electrodes and the material under study as working electrode.

Galvanostatic measurements were carried out using a Biologic VMP3 multichannel tester with current densities of C/24, C/12 and C/8 from a potential of 1.0 V to 2.7 V.

3.3.3.2. $LiFePO_4$ electrodes

The electrochemical performances of the LFP-extruded cathodes were tested at Institut Chimie et Materiaux Paris-Est (ICMPE) of Centre National de la Recherche Scientifique (CNRS) in Paris (France), in collaboration with "Gruope d'Electrochimie et Spectroscopie des Matériaux" (GESMAT).

The extruded cathodes were self-supported and consisted only in a sintered piece of 500 µm thickness with a surface of (0.14) cm^2, with a mass loading of 86 mg/cm^2. In this case only two filters were employed as separators in order to reduce the thickness of the cell. The extruded cathodes were tested and compared with a composite electrode in which the starting LFP powder was the active material. Thus, the composite consisted in 80 wt. % of active material, 7.5 wt. % of acetylene black, 7.5 wt. % of graphite and 5 wt. % of Teflon as binder agent. This mixture was pressed on a stainless-steel grid (14 mm diameter) using 8 $tons/cm^2$ of pressure. The mass loading was 24 mg/cm^2. For cell assembly, three glass microfiber filters (Whatman GF/F) were used as separator.

Two electrolytes were employed, both using a solution 1M of $LiClO_4$ in *(a)* propylene carbonate (PC) or *(b)* propylene carbonate (PC), ethylene carbonate (EC) and dimethyl carbonate (DMC) (1:1:1 vol.%). In all the cases 150 µl were used.

Coin cells type CR2032 were assembled inside a glovebox (H_2O and O_2 < 0.1 ppm), using a lithium foil as reference and counter electrode and the LFP-extruded material or the composite reference as working electrode.

A Biologic VMP3 multichannel tester was employed for the galvanostatic tests. The measurements were performed at different current densities (from C/20 to C/2) in the potential range from 2 to 4 V and 2 to 4.5 V vs. Li^+/Li at a temperature of 20 °C.

The impedance of the cells was measured using a three-electrode cell in which a lithium wire and a gold wire acted as reference and counter electrodes, respectively. The lithium wire was in a separated compartment from the gold wire. Both electrodes were immersed together with the working LFP extruded electrode in an electrolyte 1M of $LiClO_4$ in PC/EC/DMC (1/1/1 vol.). The impedance was measured between $8 \cdot 10^4$ and $2 \cdot 10^{-3}$ Hz using an excitation signal of 5.7 mV. The measurements were carried out when the equilibrium potential was reached, considering a variation less than 1 mV during 1 h.

3.3.4. Electrochemical performances of a lithium-ion battery with extruded $Li_4Ti_5O_{12}$ and $LiFePO_4$ electrodes

The electrochemical behaviour of a full cell, consisting of an LTO-extruded layer as negative electrode and a LFP-extruded layer as positive electrode, was investigated. The work was carried out at Helmholtz Institute Ulm (HIU) in Ulm (Germany) in the group "Electrochemistry for batteries".

Firstly, the electrochemical performance of Li-LTO and Li-LFP was evaluated by using a two-electrode Swagelok-type cell. The sintered electrodes, which presented a surface of 0.25 cm^2, were vacuum dried for 12 h at 120 ºC. The mass loading was 110 mg/cm^2 for the LTO electrode and 90 mg/cm^2 for the LFP electrode.

The electrolyte was a 1M solution of $LiPF_6$ in ethylene carbonate (EC) and dimethyl carbonate (DMC) in a weight ratio 1:1. A Whatman GF/A glass fibre film was employed as separator and a carbon felt was used as current collector.

The cell assembly was carried out in a glove box with O_2 and H_2O content below 1 ppm.

The battery cycler was a Maccor 4000 and the experiments were performed at 20 ºC using a constant current of C/24 during the first two cycles and C/12 for the following ones (1C = 170 $mA \cdot g^{-1}$). The voltage range (vs. Li^+/Li) for LTO and LFP half-cells was 1.0 - 2.0 V and 2.6 - 4.0 V, respectively, and 1.0 – 2.8 V for the full-cell.

3.4. RESULTS

3.4.1. Characterization of starting materials

3.4.1.1. $Li_4Ti_5O_{12}$ and $LiFePO_4$ starting powders

3.4.1.1.1. Carbon content and its distribution

For $Li_4Ti_5O_{12}$ and $LiFePO_4$ materials, carbon coating is one of the most critical features to achieve the necessary electronic conductivity and hence obtain suitable electrochemical properties to be used as active materials in battery applications. Moreover, the distribution of carbon in the material is important for obtaining a homogeneous current distribution.

The carbon content of the starting powders was measured by elemental carbon analysis resulting in a negligible carbon content for LTO (less than 0.05 wt. %) and 1.70 ± 0.01 wt. % for LFP. The results are in good agreement with the values supplied by the manufacturer (zero for LTO and 1.8 ± 0.3 wt. % for LPF).

In order to analyse the carbon distribution and morphology on LTO and LFP particles, TEM analysis was conducted. In Figure 3. 7 it can be appreciated that both LTO and LFP present high crystallinity. LFP presents a homogeneous layer surrounding the crystalline particle, which is identified as amorphous carbon because of the characteristic contrast in the edge of the crystal [22]. This well-distributed carbon film around the ceramic particles is beneficial for obtaining a continuous pathway for the electrons motion throughout the electrode. As observed in the image, the thickness of the carbon coating is around 2 nm. According to previous studies [23], a thin layer between 1 and 2 nm is enough to supply electronic connectivity to the electrochemical active surface of the material, and a higher amount of carbon may introduce a barrier to the lithium diffusion and electrolyte penetration. Hence, during the processing of the LFP powder, special care must be taken to preserve the integrity of the amorphous carbon film over LFP particles.

On the other hand, LTO particles, as expected, do not present any carbon coating. As no electronic conductivity is expected, a specific strategy will be employed during the processing of the LTO material in order to improve electronic conductivity.

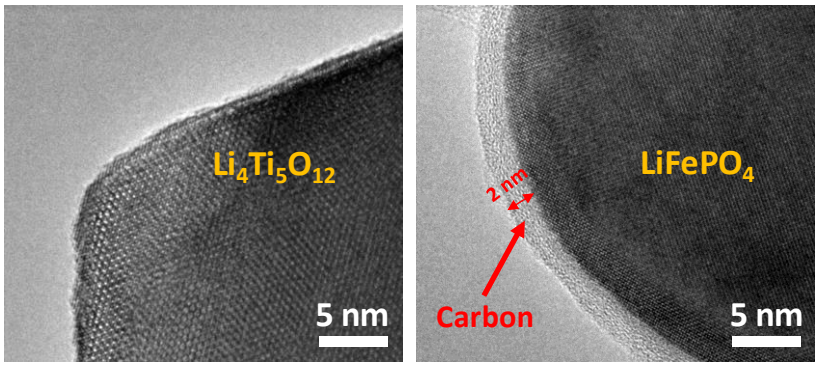

Figure 3. 7. TEM images of $Li_4Ti_5O_{12}$ and $LiFePO_4$ particles from the corresponding starting powders.

3.4.1.1.2. Particle size distribution and morphology

The powders' morphology was examined by SEM, using secondary electrons. In Figure 3. 8 (left) it can be observed that both LTO and LFP particles present irregular shape, high agglomeration and a relatively wide distribution of particle size (1-3 µm).

The particle size distribution was quantitatively measured by using a particle size analyser. The measurement determines the volume percentage of particles with a specific diameter and the percentage of particles with less than a specific diameter, represented as cumulative frequency. Figure 3. 8 (right) shows the particle size distribution for LTO and LFP powders. In both cases, a bimodal particle size distribution is observed. The two maximums are centred in 1.4 and 207 µm for LTO and 1.1 and 256 µm for LFP. However, a higher quantity of small particles is measured for LFP than for LTO, and the presence of agglomeration is more significant for LTO than for LFP. All these observations are in good agreement with the SEM images.

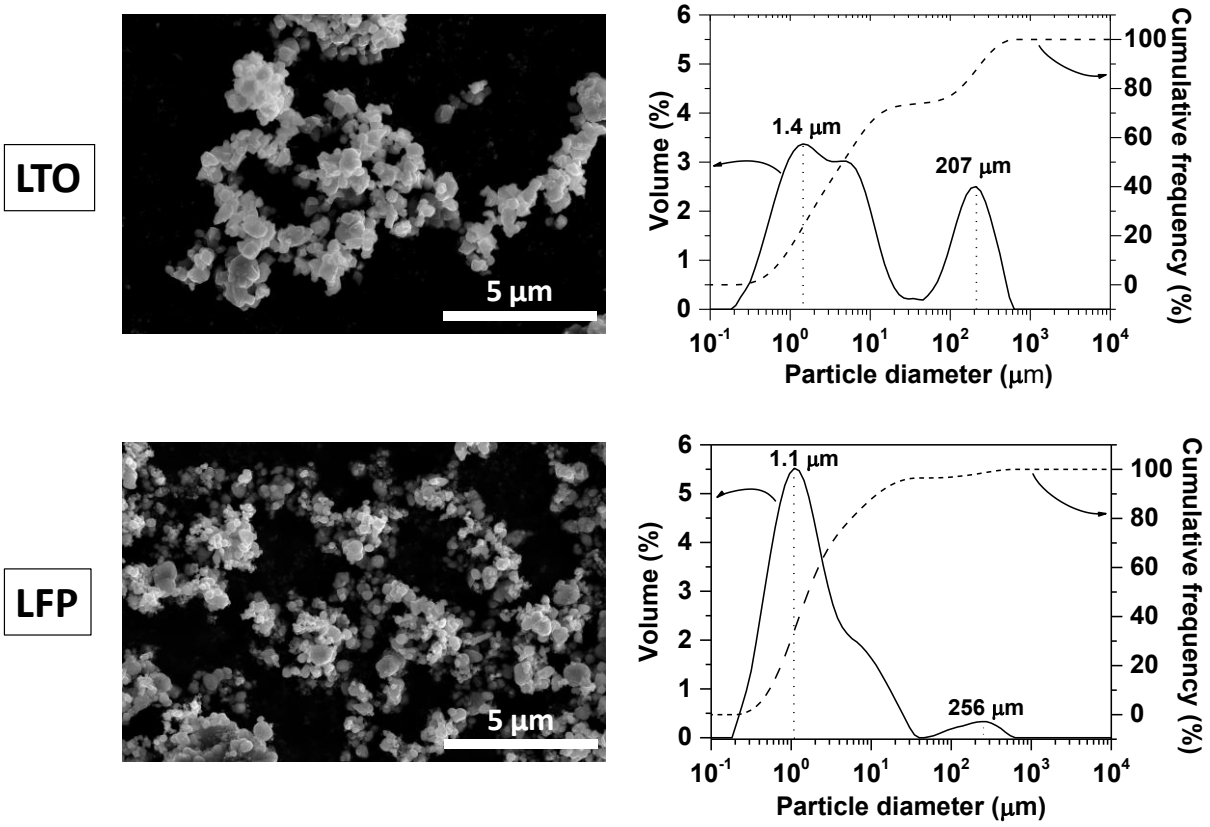

Figure 3. 8. Secondary electrons SEM image (left) and particle size distribution of starting $Li_4Ti_5O_{12}$ and $LiFePO_4$ powders (right).

Powders with wide particle size distributions are easier to pack, as the small particles can occupy the void volume between the bigger ones. Thus, for obtaining high packing densities, a powder with a wide particle size distribution and big particles would be desirable. However, a very wide particle size distribution could provoke the collapse of the piece during the debinding step.

The S_w parameter, which indicates the width of the particle size distribution, is calculated from the following equation:

$$S_w = \frac{2.56}{\log\left(\frac{d_{90}}{d_{10}}\right)}$$

For each powder, d_{90}, d_{50}, d_{10} values are acquired from the graphs and, using these data, the parameter S_w is obtained (Table 3. 2).

The value d_x indicates the diameter value for a given "x" (volume percentage) and indicates the "x" percentage of particles with a diameter lower than d_x. For example, for LTO, d_{50} is 4.6, which means that 50 vol. % of particles have less than 4.6 µm of diameter. In this manner, the

values collected in Table 3. 2 show that bigger LTO particles are measured in comparison with LFP ones. The main difference between LTO and LFP powders comes from the volume percentage of agglomerates. The much higher d_{90} value for LTO than for LFP indicates the more significant agglomerate presence in LTO powders.

On the other hand, this difference does not have a relevant effect on S_w. The lower the S_w parameter, the higher the particle size distribution width and, consequently, the easier the package of the powders. It is considered that S_w value close to 2 represent easy moulding powders [1]. The results for S_w show that both powders would be easily moulded and hence they are appropriate for powder extrusion moulding.

Table 3. 2. Particle size distribution parameters for $Li_4Ti_5O_{12}$ and $LiFePO_4$ powders.

Powder	d_{90} (µm)	d_{50} (µm)	d_{10} (µm)	S_w
$Li_4Ti_5O_{12}$	241.4	4.6	0.8	1.0
$LiFePO_4$	12.3	1.6	0.5	1.8

3.4.1.1.3. Energy dispersive spectroscopy and X-ray diffraction

The elemental composition of the as-received LTO and LFP powders was studied by Energy Dispersive Spectroscopy (EDS) using a scanning electron microscope equipped with an Energy-Dispersive X-ray (EDX) detector. The resulting spectra are reported in Figure 3. 9. In the case of LFP, peaks corresponding to the elements that compose the material (Fe, P, O and C) were identified. However, for LTO, apart from the expected elements (Ti and O), a signal identified as Al was observed and a relative weight of 1.7 % was measured. The origin of the Al is uncertain but could be attributed to LTO powder contamination during the synthesis process probably due to the use of alumina refractory crucibles or grinding instruments. In our case, as EDS is a surface technique, most of the measured aluminium content is expected to come from synthesis contamination and the Al presence inside LTO particles should be much lower than 1.7 wt. %

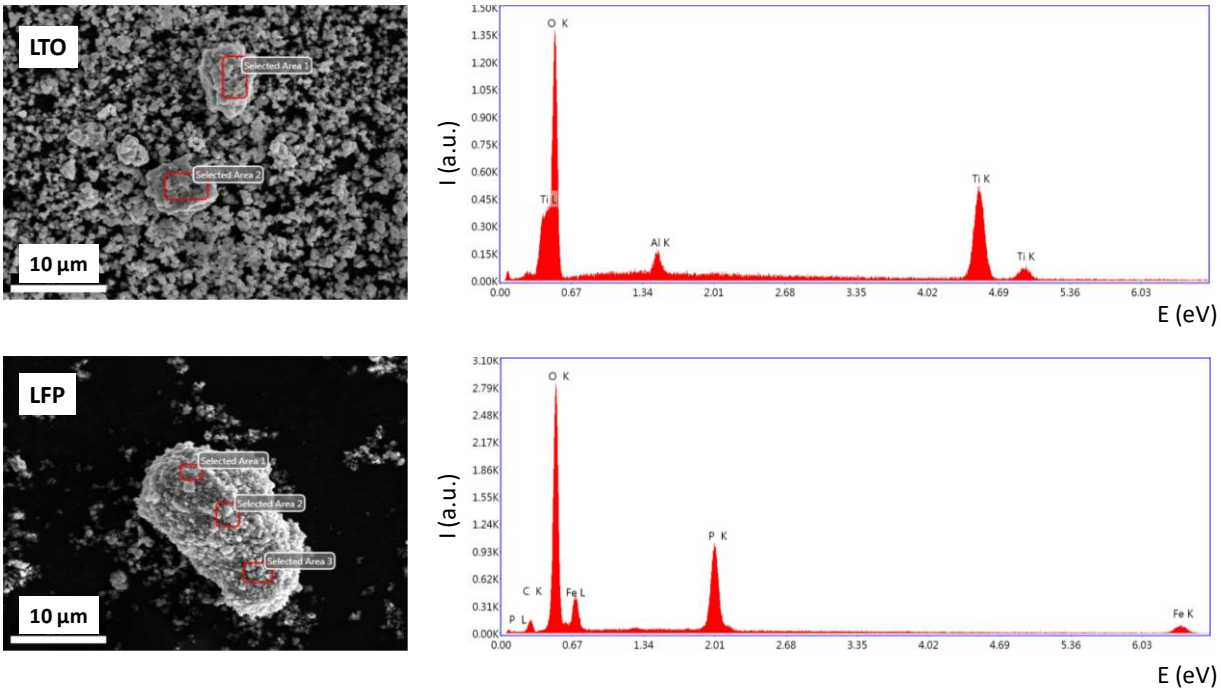

Figure 3. 9. SEM images of LTO and LFP powders and the corresponding EDS spectra of the marked areas.

The possible presence of secondary phases was studied by powder XRD. Figure 3. 10 shows x-ray diffraction patterns of LTO (left) and LFP (right) powders. In both cases, the diffraction maxima were identified with the corresponding diffraction planes (hkl) of pure $Li_4Ti_5O_{12}$ (JCPDS #40-0207) and $LiFePO_4$ (JCPDS #40-1499), respectively. LTO was indexed in a cubic spinel-type structure with space group Fd-3m. No secondary phases were identified in the XRD pattern. On the other hand, LFP crystallizes in an orthorhombic system with olivine-type structure based on the Pnma space group. No secondary phases are observed, and carbon identification is not possible due to its small quantity in the phase and its amorphous structure.

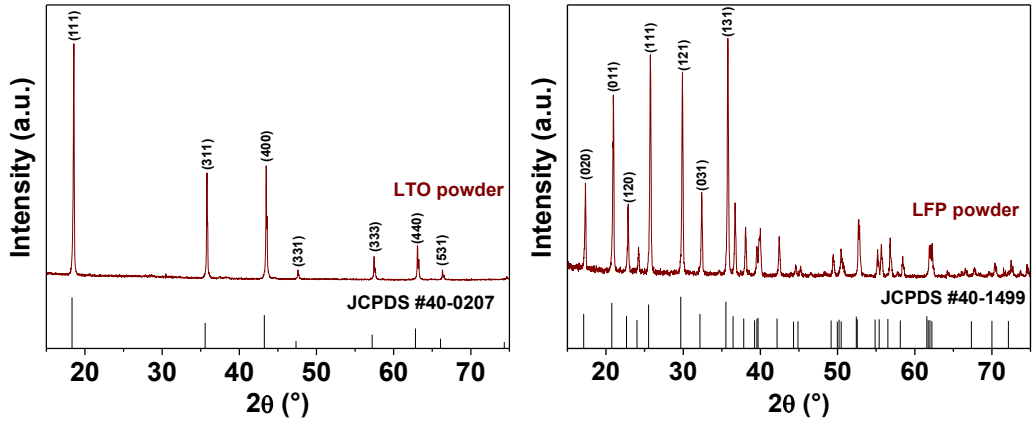

Figure 3. 10. X-ray diffraction patterns of $Li_4Ti_5O_{12}$ (left) and $LiFePO_4$ (right) powders and their corresponding reference pattern JCPDS #40-0207 and #40-1499, respectively.

As the commercial LTO powder presents a small quantity of Al (1.7 wt. %), its presence may affect LTO structural and electrical properties. In octahedral coordination, the ionic radius of Al^{3+} (0.53 Å) is smaller than that of Ti^{4+} (0.605 Å) or Li^{+} (0.74 Å), so a partial substitution of Ti or Li by Al may occur. This chemical substitution could produce oxygen vacancies, which would increase the ionic conductivity of the material. This fact improves the electrochemical performance of the electrode, reaching higher initial discharge capacity and rate capability than $Li_4Ti_5O_{12}$ [24,25]. Despite the presence of aluminium in the acquired LTO powder could result beneficial for the electrochemical performance of the final anode, high aluminium contents can lead to the formation of a secondary phase, identified as $LiAlO_2$ [26]. In order to study the effect of Al in the structure of LTO, the X-ray diffraction pattern was analysed by the Rietveld's method using the Fullprof Suite program [27] and considering a partial substitution of x=0.27 in $Li_4Ti_{5-x}Al_xO_{12}$ according to the Al quantity detected by EDS and considering that all the aluminium detected is in the LTO structure. On the other hand, the XRD refinement of LFP was also done using the same method.

The parameters of LTO and LFP were successfully refined by using the space groups Fd-3m (Nº 227) and Pnma (Nº 62), respectively, considering the atomic positions given by Leonidov *et al.* for LTO [28] and Rousse *et al.* for LFP [29] (see Supplementary information-Table S3. 1). A summary of the structural parameters obtained from the Rietveld analysis of LTO and LFP powder XRD patterns is collected in Supplementary information-Table S3. 2 and the diffraction patterns of the refinement are illustrated in Supplementary information-Figure S3 .1.

In the case of LTO, the calculated cell parameter (8.3305(7) Å) is slightly lower than that reported in the literature for $Li_4Ti_5O_{12}$ (8.354 Å) [28]. This is attributed to a partial substitution of Ti by Al. Related to the position in which Al is substituted, there is some controversy in the literature between the 8a position for Li and the 16d position for Ti. In this work, the XRD patterns of $Li_4Ti_{5-x}Al_xO_{12}$ (x=0.25) and $Li_{4-x}Al_xTi_5O_{12}$ (x=0.25) were simulated (see Supplementary information-Figure S3.2). However, no changes in the relative intensities of the diffraction maxima were observed, which indicates that the XRD results are not sensitive to the occupancies. Anyway, in the literature it is reported that independently of the position in which the substitution occurs, the cell parameter decreases [30,31]. For LFP, the cell parameters refined in the present study are a = 10.3210(2) Å, b = 6.0002(3) Å and c = 4.6897(2) Å. The calculated parameters show good agreement with those reported in the literature, varying less than 0.05 Å when compared with refined data from neutron diffraction [32].

3.4.1.1.4. Density

The pycnometric density of LTO and LFP powders was measured and the results were compared with the crystallographic density obtained from the Rietveld analysis carried out for the XRD patterns (Table 3. 3). In both cases the values obtained by the two different methods are similar. However, as expected, the pycnometric density is slightly lower than the crystallographic one due to the presence of defects in the crystalline structures. Hence, the pycnometric density is considered the maximum one that can be obtained, and normally it is referred as theoretical density.

Table 3. 3. Theoretical and crystallographic densities of LTO and LFP powders.

Material	**Density (g/cm^3)**	
	Helium pycnometry (Theoretical)	Rietveld Refinement (Crystallographic)
$Li_4Ti_5O_{12}$	3.49 ± 0.01	3.531
$LiFePO_4$	3.57 ± 0.01	3.607

3.4.1.2. Binder system

The characterization of the binder components was carried out by means of DSC and TGA. Melting temperatures of the binder components were determined by DSC experiments, while decomposition temperature ranges were estimated by TGA. In Figure 3. 11, the DSC and TGA curves of each component are included. The melting temperatures were identified in the DSC curves as endothermic peaks. For PP and SA, a single endothermic peak was observed at 164 and 73 ºC, respectively, while PW present two endothermic peaks at 32 and 53 ºC. The first peak corresponds to a solid-solid transition from hexagonal to orthorhombic structure of PW [33], while the second one is related to the melting process of the crystals. On the other hand, the decomposition temperature ranges were determined from the temperature in which the weight loss starts (T_1) until the end of the weight loss (T_2). Table 3. 4 collects the melting temperature, the decomposition temperature range and the pycnometric density of each binder component.

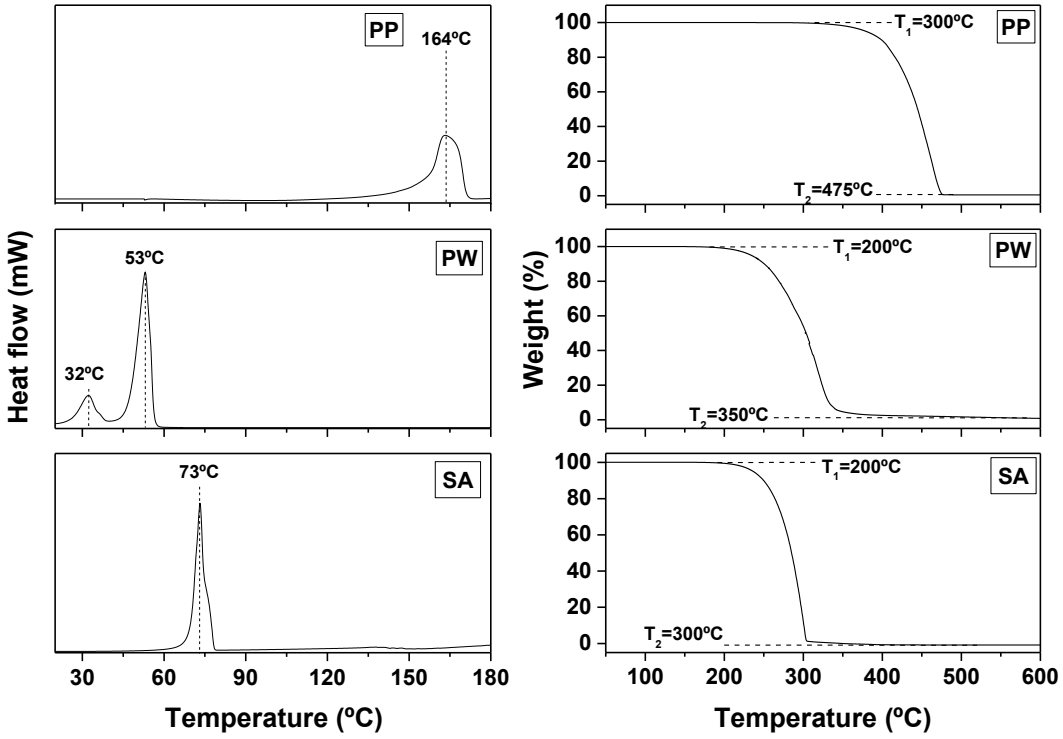

Figure 3. 11. DSC (left) and TGA curves (right) for polypropylene (PP), paraffin wax (PW) and stearic acid (SA).

Table 3. 4. Pycnometric density, melting temperature, onset temperature, offset temperature and decomposition temperature range of PP, PW and SA.

Component	Pycnometric density ($g \cdot cm^{-3}$)	Melting temperature (°C)	Decomposition temperature range (°C)
Polypropylene (PP)	0.89 ± 0.01	164	300-475
Paraffin wax (PW)	0.91 ± 0.01	53	200-350
Stearic acid (SA)	1.01 ± 0.01	73	200-300

The decomposition of the three components takes place in different temperature ranges, which will allow designing a thermal debinding cycle which ensures their progressive removal. From the melting temperatures of PP, PW and SA and the corresponding decomposition temperature range, the mixing temperature was selected as 180 ºC in order to guarantee the melting of all binder components without degradation of any of them.

3.4.2. $Li_4Ti_5O_{12}$ electrodes

3.4.2.1. Feedstock characterization

The different prepared LTO-feedstocks were characterized in terms of homogeneity and the Critical Powder Volume Concentration (CPVC). For that, torque, viscosity and density measurements were carried out.

3.4.2.1.1. Torque measurements

The mixing torque, which corresponds to the effort required by the rotor blade mixer, is an indicator of the viscosity of the powder-binder mixture. So, the homogeneity of the mixture is estimated by the variation of the mixing torque over a period of time. Torque curves for mixtures with different powder loadings are plotted in Figure 3. 12-(a). At the beginning of mixing process, small portions of binder components are added in the following order: polypropylene, paraffin wax and stearic acid. Subsequently, powder is progressively incorporated into the mixture, while an increment of torque is registered due to a bad distribution of the powder within the binder. When all the powder is added, the torque started decreasing until reaching a constant value, called the steady state (τ), which indicates a good mixture homogeneity. In this work, τ is calculated as the average torque values in the last 5 minutes of mixing for all mixtures except the one with 60 vol. % of LTO, which does not reach the steady state torque, indicating poor homogeneity. In Figure 3. 12-(b), τ values are plotted against different powder loadings. In the graph, two regions are clearly distinguished. In the first one, below 55 vol. % of LTO, the steady-state toque remains almost constant. In the second region, however, a pronounced increase of the steady-state torque occurs while increasing the powder loading.

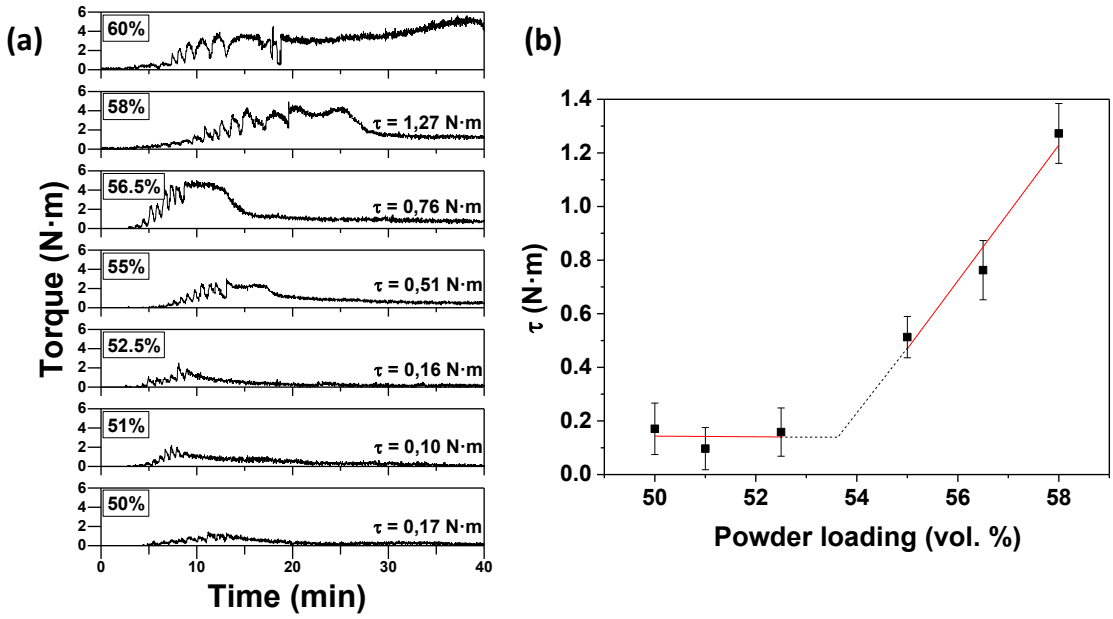

Figure 3. 12. (a) Torque against mixing time for mixtures with different LTO vol.%. (b) Steady-state toque variation with LTO powder charge.

It must be underlined that, in all cases, τ remains almost constant for low powder loadings, as there is enough binder to cover all the ceramic particles and reduce the friction between them. However, an abrupt growth occurs when a certain powder loading is reached, caused by the friction between the powder particles because the too low binder content.

This behaviour was observed before in mixtures of other ceramic powders prepared in our laboratory using the same mixing equipment and procedure. Figure 3. 13 collects the results of τ for different powder loadings of $Li_4Ti_5O_{12}$ prepared in this work (d_{10}=0.8, d_{50}=4.6 and d_{90}=241.4 μm), NiO-YSZ (d_{10}=0.3, d_{50}=1.1 and d_{90}=14.3 μm) [18] and alumina (d_{10}=0.8, d_{50}=45.0 and d_{90}=170.0 μm) [7]. Comparing different particle diameters of a given powder, in the case of Ni-YSZ it was reported that the steady-state torque increases with the particle diameter [18]. Thus, the difference in τ between the feedstocks could be related in principle with their particle size distribution. However, the relation between the particle size distribution and the steady-state torque is not clear. Also, the particle morphology and the binder composition can affect the torque response of the system.

For determining the CPVC different criteria can be used, and no standard criteria was found in the literature. In powder injection moulding, some authors determine the CPVC from the point in which the slope sharply changes, and the optimal loading is considered to be between 2 and 5 vol. % lower than the CPVC [1,34]. In our case, we think the CPVC could be considered as a

region and not a single value. Feedstocks with slightly different powder loadings located in the slope change region can all be suitable for being extruded. For the feedstocks prepared previously in our laboratory, the optimal solid loading was 65 vol. % for Ni-YSZ and 58 vol. % for alumina. In this manner, and based on our previous experience, we propose that the CPVC is slightly higher than the powder loading value at the inflection point of the τ graph. Thus, a powder loading of 55 vol. % was selected as the CPVC for LTO feedstocks.

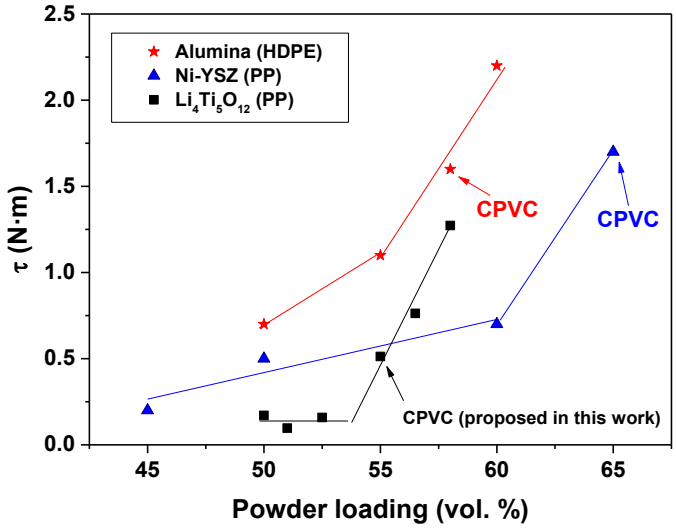

Figure 3. 13. Steady-state torque (τ) variation with powder loading for feedstocks of alumina and Ni-YSZ powders [7,18] and LTO feedstocks prepared in this work.

3.4.2.1.2. Homogeneity

The homogeneity of the feedstock is an important feature which influences the different parts of the process as well as the final properties of the sintered samples. The presence of agglomerates influences the flow behaviour of the feedstock and may cause defects in the sintered bodies. A homogeneous feedstock with no segregation between the powder and the binder is desired. Thus, to evaluate the homogeneity of the prepared feedstocks, viscosity and density experiments were performed.

As the agglomerates can influence the viscosity of a mixture, a homogeneous feedstock should have constant viscosity during mixing time. The viscosity variation with the time of three different feedstocks prepared in a rotor blade mixer was measured. The measurements were carried out at the extrusion temperature (180 ºC) and at a constant shear rate of 1000 s^{-1}, which is a typical shear rate value usually reached in PEM process, as mentioned before. Figure 3. 14-(a) shows the results for feedstocks with 50, 55 and 58 vol. % of powder loading. As the polymeric binder cannot surround perfectly all the particles, the viscosity increases with the powder loading as a

consequence of the higher friction between the powder particles. For the feedstock with the lowest powder loading (50 vol. %), the viscosity remains constant with the mixing time, indicating a good homogeneity. On the other hand, for higher powder contents the viscosity changes during the measurement, which can be explained by the presence of powder agglomerates in the feedstocks. This means that during mixing, these agglomerates are not broken, and this phenomenon is more significant in the mixtures with high powder loadings. From these results, it can be deduced that using a rotor blade mixer employed for preparing the feedstocks results in a not completely homogeneous mixing of powder and binder. In addition, torque measurements using the rotor blade mixer resulted to be not sensitive enough to determine the presence of agglomerates in a mixture and reaching the steady-state torque is not always enough to demonstrate a good mixture homogeneity. Consequently, this experiment shows approximately the maximum powder loading admitted by the system.

To improve the mixing of the powder within the binder and to reach a good feedstock homogeneity, a twin-screw extruder was employed for preparing the feedstock. The evolution of viscosity with the time for the feedstock with 55 vol. % of powder loading is displayed in Figure 3. 14-(b). It can be observed that the viscosity remains constant during the time, indicating a high homogeneity. This is attributed to the high shear rates that the feedstock encounters inside the extruder, which led to a more homogeneous powder distribution within the binder, reducing the agglomerates.

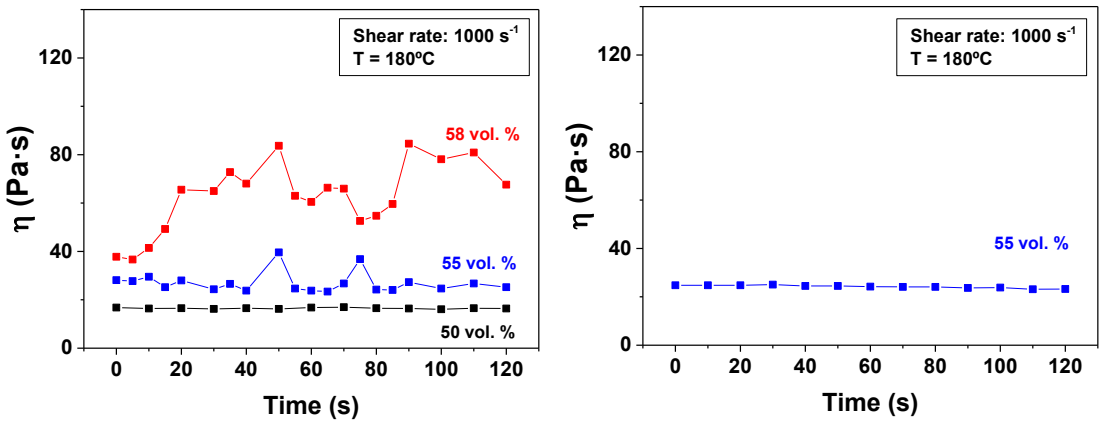

Figure 3. 14. Variation of viscosity with time for feedstocks with (a) 50, 55 and 58 vol. % of LTO prepared in a rotor blade mixer and (b) 55 vol. % of LTO prepared in a twin-screw extruder. The experiments were carried out at 180 ºC and at a constant shear rate of 1000 s^{-1}.

The homogeneity of the feedstock prepared in the twin-screw extruder was also analysed by measuring its density on a helium pycnometer, resulting in 2.346 ± 0.002 g/cm^3, while the

theoretical density, obtained by the mixture rule and the theoretical density of each component, is 2.380 g/cm^3. This fact indicates that no significant feedstock compositional change occurred during the mixing step, keeping the ratio between the different components. Moreover, the low standard deviation indicates that the different fractions (at least three) of feedstock have very similar density and, hence, the feedstock is homogeneous.

According to these results, the twin-screw extruder was selected for preparing a homogeneous feedstock of 55 vol. % of LTO, which will be used for obtaining extruded layers.

3.4.2.1.3. Rheological characterization

A rheological characterization of a feedstock is crucial to determine its ability to be extruded and allows to calculate useful parameters such as flow index or activation energy, can be calculated. However, due to the poor homogeneity of the feedstocks prepared in the rotor blade mixer, a high dispersion of the values in the viscosity curves was obtained, not being possible to fit the data and calculate the rheological parameters. Figure 3. 15 shows the difference in the rheological curves of two different feedstocks of same composition prepared separately in a rotor blade mixer and in a twin extruder. By using the mixer, erratic data were obtained at the different temperatures, with random variations of viscosity in the shear rate interval. On the other hand, when the extruder is used for mixing, the viscosity decreases with the shear rate following the power law model proposed by Ostwald and De Waele [4,5] and previously mentioned:

$$\eta = k\,\dot{\gamma}^{n-1}$$

As the viscosity decreases with the shear rate, the feedstock presents a pseudoplastic behaviour, which is the most convenient for extrusion process since *(i)* the viscosity decreases with the shear rate, which is higher when feedstock is forced to pass through the nozzle and *(ii)* the viscosity increases when the shear rate ceases, that is, when the feedstock get out of the extrusion nozzle, allowing to maintain the geometry of the layer. Furthermore, all the values are lower than 1000 Pa·s between 100 and 2000 s^{-1}. These values are considered as a reference for a successful PIM process and in our specific case of powder extrusion moulding the maximum shear rates encountered in the twin-screw extruder is around 1800 s^{-1} [35].

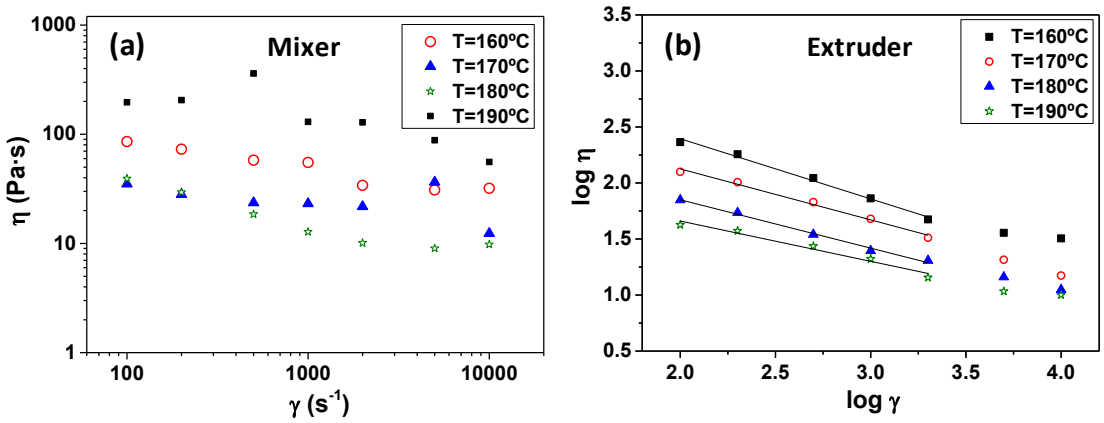

Figure 3. 15. Evolution of viscosity with shear rate at different temperatures for feedstocks with 55 vol. % of LTO prepared (a) in a rotor blade mixer and (b) in a twin-screw extruder.

As the viscosity of the different feedstocks follow the Ostwald and De Waele power law model, the power law index was obtained from the slope of linear regression of the logarithmic representation of the viscosity *versus* the shear rate between 100 and 2000 s^{-1}. The corresponding linear fittings are plotted in Figure 3. 15-(b). The preparation of several feedstocks with different powder loadings using a twin-screw extruder was not practicable in this work due to the large amount of material needed for loading the extruder equipment. Therefore, the rheological characterization was done only for the feedstock of 55 vol. % of LTO prepared in the twin-screw extruder.

The calculated power indexes at each temperature are collected in Table 3. 5. It is observed that n increases with the temperature, which means that the feedstock at high temperatures is less pseudoplastic. Comparing with other feedstocks prepared with similar binder formulation, such as injected YSZ [20] or Ni-YSZ [18], the n value of LTO-feedstock is higher, which indicates it is less sensitive to shear rate.

Table 3. 5. Calculated power law indexes of 55 vol. % LTO feedstock for temperatures between 160 and 190 ºC. The regression coefficients of the linear fittings are also indicated in brackets.

T (ºC)	160	170	180	190
n	0.46	0.55	0.57	0.64
(R)	(0.986)	(0.992)	(0.995)	(0.988)

The variation of viscosity with the temperature is also important in extrusion process because fluctuation of temperature during extrusion takes place, producing stress concentration in the extruded part, resulting in cracking, distortion and other kind of defects. As previously

mentioned, the viscosity in a thermoplastic system displays an Arrhenius-type dependence with temperature, following the equation:

$$\eta(T) = \eta_0 e^{E_a / RT}$$

where E_a is the flow activation energy, η_0 is the viscosity at a reference temperature T and R is the gas constant. As seen in Figure 3. 15-(b), the viscosity decreases with the temperature, which is explained by: *(1)* the viscosity of the binder decreases with temperature, due to a higher mobility of the polymeric chains and *(2)* the thermal expansion of the binder, reduces the contact between the powder particles [1]. The activation energy (E_a), calculated from the linear fit of ln η *versus* 1/T for viscosity values between 160 and 190 ºC at a constant shear rate of 1000 s^{-1}, (Figure 3. 16) is 73.2 kJ/mol. This value is relatively high compared to those previously reported. For example, for extruded Ni-YSZ feedstocks E_a values were in the range of 27-39 kJ/mol for powder loadings of 55 to 65 vol. %. However, a similar activation energy than that obtained for LTO was reported before for successful injection moulding of alumina using a powder loading of 55 vol. % (69.2 kJ/mol) [3]. This means that the LTO-feedstock prepared in this work is highly sensitive to temperature changes. Thus, as the feedstock comes out of the nozzle, the temperature decreases and consequently the viscosity increases, leading to optimal shape retention. If the viscosity does not increase quickly, the cross-section of the extruded material could be reduced leading to a geometry distortion. For this reason, a high activation energy is beneficial for the process.

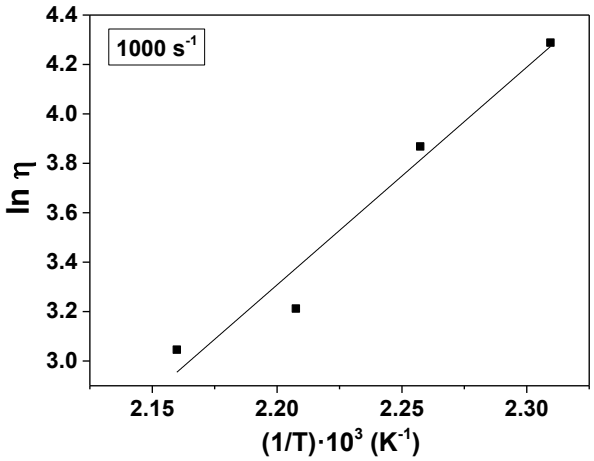

Figure 3. 16. Linear fit for the activation energy calculation of the optimized LTO feedstock.

3.4.2.2. Extrusion and green pieces

Based on torque measurements and the rheological characterization, the feedstock with 55 vol. % of powder loading was selected as the optimum for powder extrusion moulding. Therefore, larger quantities of feedstock were prepared in a twin-screw extruder. Inspection of the feedstock was performed by SEM in order to check the distribution of the powder and the binder (see Figure 3. 17). In the BSE image, the bright parts correspond to LTO while the dark zones represent the binder. LTO particles are embedded in the binder which is homogeneously distributed through the material. SEM inspection was carried out in different fractions of the same feedstock and analogous images were observed, which confirms the good homogeneity of the mixture.

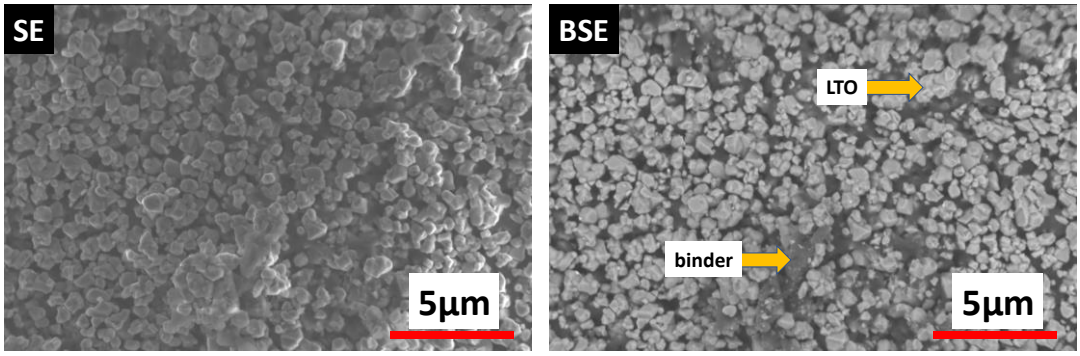

Figure 3. 17. SEM images of 55 vol. % LTO feedstock using SE and BSE detectors.

Extrusion moulding allowed obtaining the so-called green layers of 0.5 and 1 mm of thickness. The temperature profile along the barrel was optimized to obtain defect-free samples. From the feeding area to the nozzle, four resistors were programmed at 170, 175, 185 and 155 ºC, respectively. 185 ºC was the maximum programmed temperature to avoid binder degradation. The last resistor, placed adjacent to the nozzle, was found to be of critical importance to achieve the desired film geometry. As mentioned before, in vertical extrusion, a reduction of the cross-section of the film may happen associated to a low viscosity of the feedstock when getting out of the nozzle. This defect is usually known as necking. In such a way, temperature and extrusion speed are important control parameters. On one side, the higher the temperature the lower the viscosity and the more probable is the necking to happen. Therefore, the temperature was gradually decreased along the extrusion barrel from 185 ºC in the feeding area to 155 ºC in the nozzle to minimize the necking. As calculated before, the feedstock has a very high activation energy (73.2 kJ/mol), so a fast cooling of the extruded layers would reduce substantially the viscosity of the extruded material and help it retain the geometry. Therefore, the samples were cooled down to room temperature by immersion in water just in the output of the nozzle in order to drastically

reduce the viscosity. Figure 3. 18-(a) includes an example of LTO green layers of 0.5 and 1 mm thickness and 6 cm length. Longer samples were not produced, as the collapse of the geometry happened. The first inspection of the layers showed flat pieces with good geometry retention and no macroscopic defects. The cross-section of a green LTO layer was further inspected by SEM (Figure 3. 18-(b)). Firstly, the dimensions of the cross-section were measured and, with respect to the nozzle dimensions (0.5 mm thickness and 6 mm width), a contraction of the extruded layer is observed. In addition, it is observed that the thickness of the layer considerably decreases from the centre of the piece to the extremes, from approximately 480 µm to 400 µm. These facts can be attributed to the fast cooling of the material coming out from the nozzle and being immersed in water, which provokes a contraction of the binder and, therefore, a reduction of the layer size. The anisotropic contraction of the thickness is attributed to the nozzle geometry, as the feedstock supports higher tension in the corners of the nozzle than in the centre zone. Thus, when this tension is released, a higher contraction is expected in the corners.

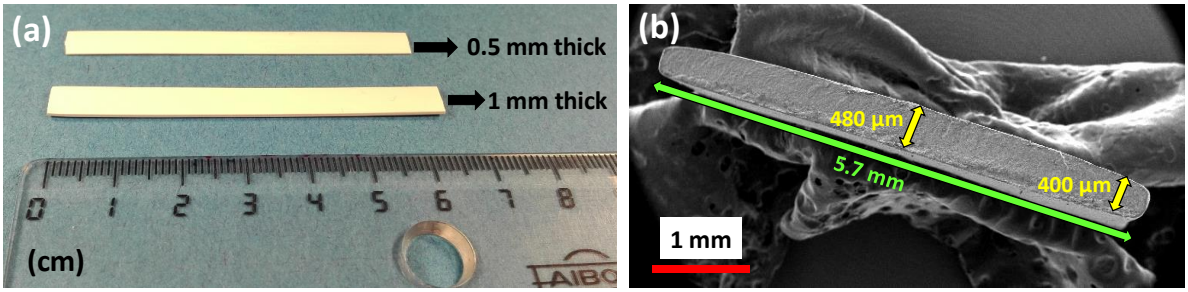

Figure 3. 18. (a) Picture 0.5 and 1 mm thickness LTO extruded layers. (b) SEM image of the cross-section of a 0.5 mm thickness LTO extruded layer.

3.4.2.3. Debinding

After the debinding step the so-called "brown" layers were obtained. As previously described, this step consisted of two parts: solvent debinding and thermal debinding.

In the solvent debinding step, the binder components with the smallest molecular weight, paraffin wax and stearic acid, are dissolved in n-heptane by immersion of the green part in order to create channels along the layer that accelerate the thermal decomposition of PP, decreasing the total debinding time. Thus, the immersion time and the temperature were optimized. Figure 3. 19 collects the weight percentage of PW and SA removed at different immersion times at 30 and 50 ºC. At both temperatures, it can be observed that the elimination of PW and SA increases with time. Moreover, during the first minutes, the removal rises very fast and then increases very slowly, remaining almost constant for the rest of the time. The maximum amount removed is 95 wt. %,

reached at 50 ºC. On the other hand, at 30 ºC the elimination of SA and PW was lower (87 wt. %). This difference is attributed to the increase of solubility of the components with the temperature.

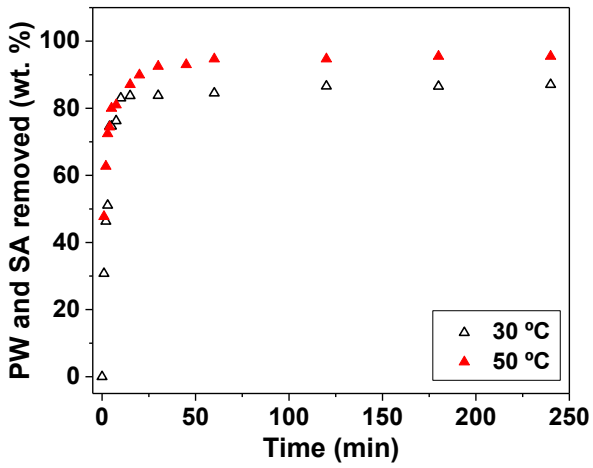

Figure 3. 19. PW and SA removal as a function of immersion time in n-heptane at 30 and 50 ºC.

In this manner, two mechanisms can be clearly distinguished according to a fast and slow removal of the soluble components. In a first stage, which occurs during the first minutes, the fast removal is attributed to the fact that the solvent is directly in contact with PW and SA. While the dissolution is occurring, a porous surface is being generated in the material. However, in the second stage, the removal is very slow, as the solvent penetrates the compact by the capillary effect and the components must diffuse out through the pores, which are longer as the removal increases, resulting in a slow process [36].

Shivashankar and German proposed a model to describe this process, based on the following equation [37]:

$$\ln\left(\frac{1}{F}\right) = \frac{D_e t \pi^2}{(\psi)^2} + K \qquad \text{Eq. 3.X}$$

where F is the fraction of the remaining soluble component, D_e is the interdiffusion coefficient of the soluble component and solvent, t is the solvent debinding time, K is a constant that counts for the change of mechanism during the removal and ψ is the effective length scale, which is given by the volume to surface area ratio of a compact and for a prismatic layer it is defined as:

$$\psi = \frac{HB(2L)}{2[HB + B(2L) + (2L)H]}$$

where $2L$, B and H are the thickness, width and length of the compact, respectively. It can be noticed that according to this geometrical factor, the higher the volume/surface ratio, the slower the removal is.

By representing $\frac{1}{F}$ versus the solvent debinding time t, the interdiffusion coefficient can be calculated for the two stages of the process. Thus, the interdiffusion coefficients of paraffin wax and n-heptane were calculated considering a geometrical factor ψ of 0.22 mm. Figure 3. 20 represents $\frac{1}{F}$ against the immersion time at 30 and 50 ºC and the linear fittings corresponding to the two different stages of the process. In both cases the behaviour is similar. A slope change is observed from low immersion times to longer times confirming that the process takes place in two steps. Moreover, the slope of the first part is clearly higher than the one of the second part, which indicates that the interdiffusion process is faster. Figure 3. 20 evidences that the mechanism change occurs earlier at 30 ºC (after 10 minutes) than at 50 ºC (after 20 minutes). This can be attributed to the better solubility of the paraffin wax in n-heptane with the temperature.

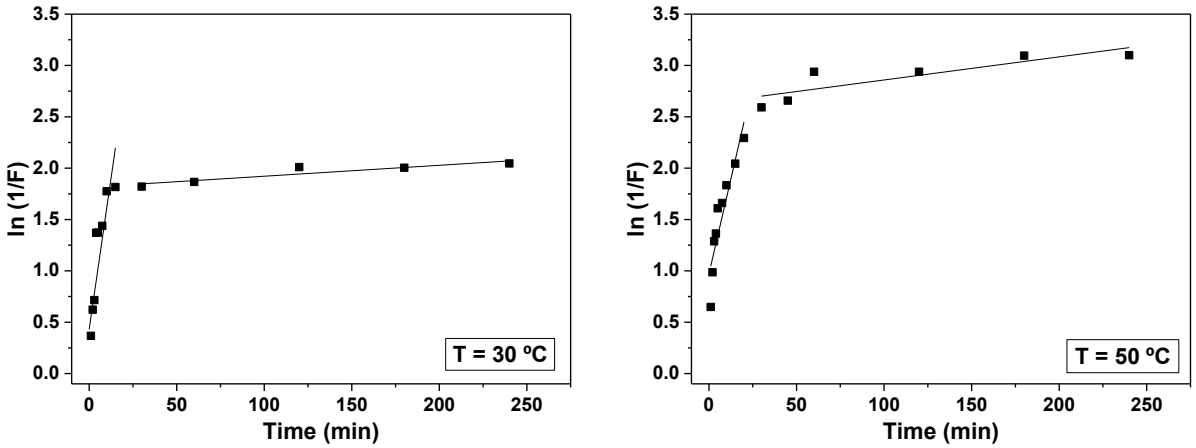

Figure 3. 20. Representation of $\frac{1}{F}$ *versus* solvent debinding time for LTO layers immersed in n-heptane at 30 and 50 ºC. The linear fitting in the two regions of the graphics are included.

The calculated interdiffusion coefficients for paraffin wax and n-heptane at both temperatures are collected in Table 3. 6. In the first stage, D_e is higher than in the second stage at both temperatures, as expected. As mentioned before, in the first stage the solvent is directly in contact with the wax, while in the second stage both the solvent and the dissolved component need to penetrate in and out through the created channels. Thus, the first stage is controlled by the dissolution of the components and the second one is controlled by the diffusion, which is a slower process. By comparing the calculated interdiffusion coefficients, during the first stage very similar

values were obtained at both temperatures. On the other hand, the coefficient is slightly higher in the second stage at 50 ºC than at 30 ºC, as the diffusion through the channels is favoured by the temperature.

Table 3. 6. Interdiffusion coefficients of stearic acid and paraffin wax in n-heptane in green LTO layers.

	D_e (cm²/s)	
	30 ºC	50 ºC
1st stage (*dissolution*)	$5.78 \cdot 10^{-8}$	$5.83 \cdot 10^{-8}$
2nd stage (*diffusion*)	$5.20 \cdot 10^{-10}$	$1.10 \cdot 10^{-9}$

Thus, the immersion in n-heptane was carried out at 50 ºC for 1 h to ensure the maximum removal of paraffin wax and stearic acid.

The following thermal debinding, which completely degrades the rest of the binder, was then performed. As SA and PW degradation starts around 200 ºC, a first step was programmed by heating to 200 ºC, using a heating rate of 5 ºC/min. Then, to degrade PP, the samples were heating to 450 ºC, using a heating rate of 1 ºC/min. The samples were kept at 450 ºC for 1 h to ensure the complete PP decomposition. The designed thermal debinding has a total time of approximately 8 h (Figure 3. 21). This cycle was used for three separated batches of samples using three different atmospheres: oxidant (air), inert (N_2) and reducing (Ar/H_2).

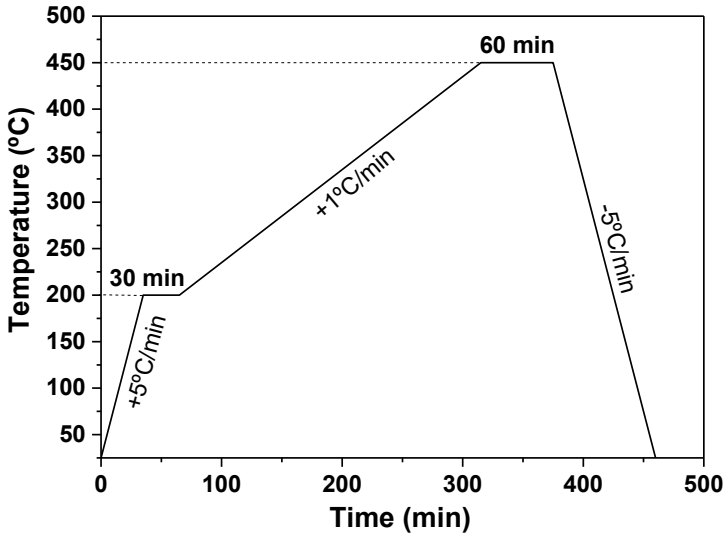

Figure 3. 21. Debinding thermal cycle for green extruded electrodes.

After the debinding process, the brown electrodes were inspected by SEM. The images of Figure 3. 22 show a homogenously distributed LTO powder with high porosity due to the lack of binder. In the image corresponding to BSE, no polymer residues were observed.

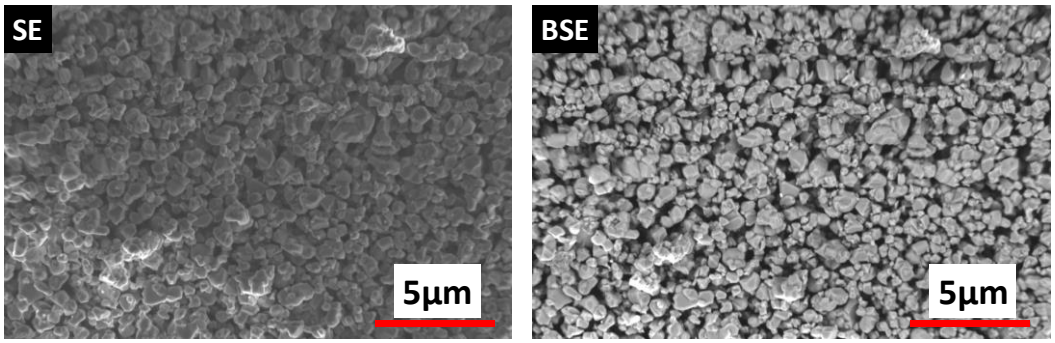

Figure 3. 22. SEM images of LTO brown electrodes after the thermal debinding under Ar/H_2 and using SE and BSE detectors.

As mentioned before, the poor electronic conductivity and low ionic lithium diffusion in LTO are a major problem that can compromise the electrochemical performance of the electrode. Thus, covering LTO particles with conductive carbon is a useful approach for overcoming this problem. By using an inert or reducing atmosphere during the debinding step, incomplete polymer degradation may occur leaving some residual carbon in the material. The carbon content of samples treated in the debinding process under air, N_2 and Ar/H_2 was measured and the results are shown in Figure 3. 23. In all the cases, some carbon was detected, and the highest carbon content (determined by elemental analysis), of approximately 0.32 wt. %, was obtained under Ar/H_2.

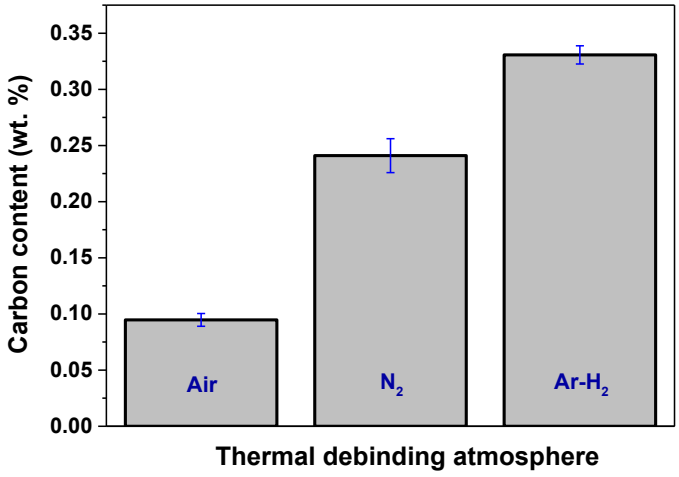

Figure 3. 23. Carbon content of LTO samples after debinding under air, N_2 and Ar/H_2.

3.4.2.4. Sintering

LTO samples were sintered at temperatures between 900 and 1100 ºC under the same atmosphere used during the thermal debinding (air, N_2 and Ar/H_2). A slow heating rate (2 ºC/min) was used in order to avoid the presence of any crack, defect or bending of the layers. Firstly, the density of the sintered parts was measured by the Archimedes method and the porosity was evaluated by Helium pycnometry and SEM. Then, the effect of sintering temperature and atmosphere in the composition was evaluated by means of XRD. Colour changes are evident between the samples treated in air/N_2 and those sintered under Ar/H_2 reducing atmosphere, as shown in Figure 3. 24. The materials treated under a reducing atmosphere presented a dark-violet colour. Thus, elemental carbon analysis was performed to determine the carbon content of the samples. Moreover, as Ti^{3+} compounds typically present a characteristic dark-violet colour [38], XPS measurements were carried out in order to determine the possible Ti^{4+} reduction.

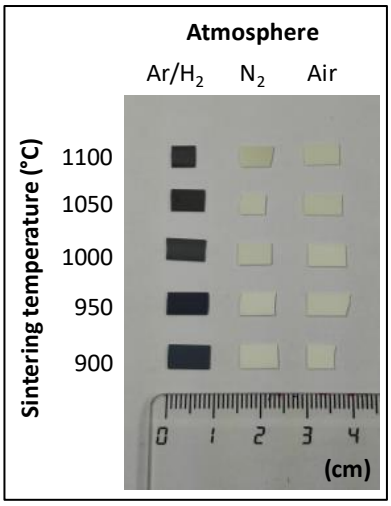

Figure 3. 24. LTO samples sintered at temperatures between 900 and 1100 ºC and under air, N_2 or Ar/H_2 atmosphere.

3.4.2.4.1. Density and shrinkage

The Archimedes density of samples sintered between 900 and 1100 ºC in different atmospheres is shown in Figure 3. 25. A similar tendency in the density variation with the sintering temperature is observed for the three atmospheres. The density increases with temperature from 900 to 950 ºC, temperature at which the maximum density is already reached (84 % of the theoretical density). From 950 to 1100 ºC the density remains basically constant.

Helium pycnometry experiments were performed in samples from 900 to 1100 ºC sintered in air. In all the cases the obtained values were 3.48 $\pm$ 0.02 g/cm^3, very close to the theoretical

density 3.47 ± 0.01 g/cm^3 (which is the pycnometry density of the starting LTO powder). This is an indicator that the helium gas is flowing through all the material by interconnected pores and negligible close porosity is detected. Thus, according to the average density value obtained for sintering temperatures between 950 and 1100 ºC (84 %), the total porosity is 16 %.

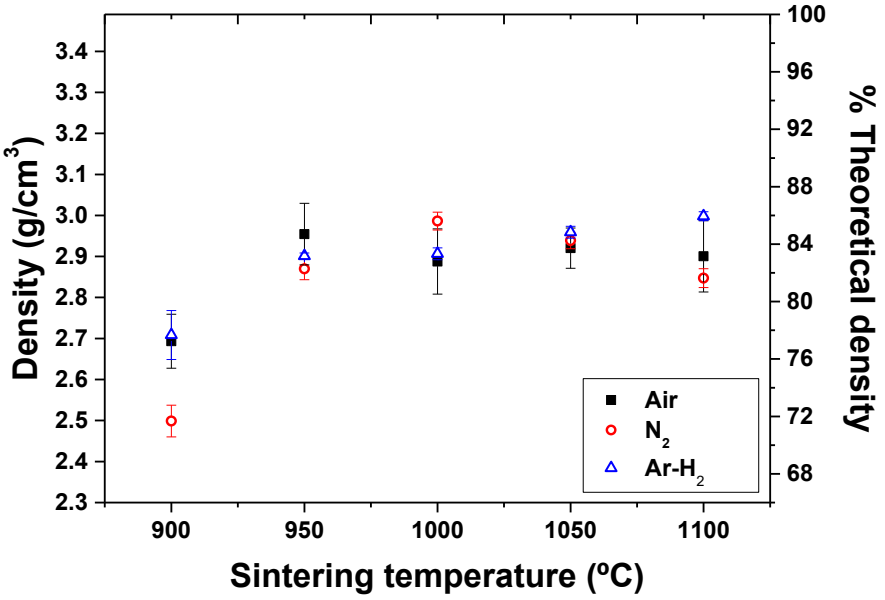

Figure 3. 25. Density of extruded LTO samples sintered at different temperatures under air, N_2 and Ar/H_2.

These results are in good agreement with the microstructure of the materials, as can be seen in the SEM images for samples sintered in Ar/H_2 included in Figure 3. 26. At 900 ºC the particles are highly packed, and no particle growth is observed compared to the starting LTO powder, confirming that the porosity is very high and density does not significantly change. However, by increasing the temperature to 1000 ºC, the grain size becomes larger and the porosity decreases, corresponding to a contraction of the material. From 1000 to 1100 ºC the grain size increases. The porous decrease in number but increase in size, so the total porosity remains almost constant.

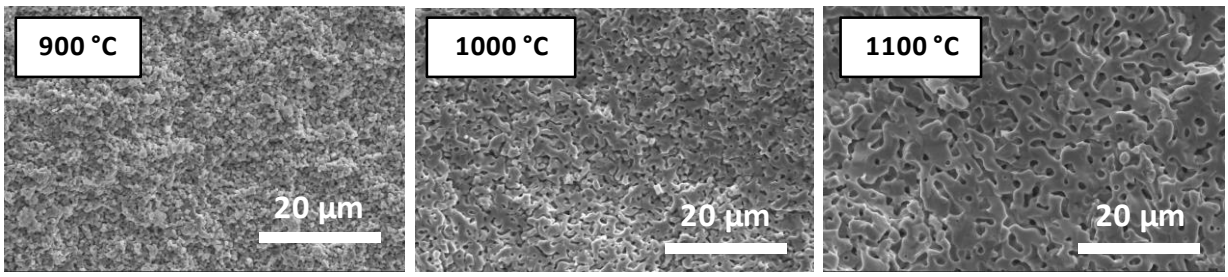

Figure 3. 26. SEM images of materials sintered in Ar/H_2 at different temperatures are included in the plot.

In batteries, electrodes porosity is an important feature that directly affects the electrochemical performance of the device. High porosity is usually desired for the easy electrolyte infiltration through the compact material and hence wet the maximum electrode surface for an efficient Li exchange between the liquid and the solid.

The cross-section of sintered samples was also characterized by SEM. An example is shown in Figure 3. 27. For all sintering temperatures and in all the atmospheres it is observed that the thickness of the layer is not homogeneous, as observed before in green LTO layers (see Figure 3. 18-(b)). As expected, the shape is maintained when sintering. In order to avoid high standard deviation in the shrinkage results, the thickness was always measured in the centre of the layer.

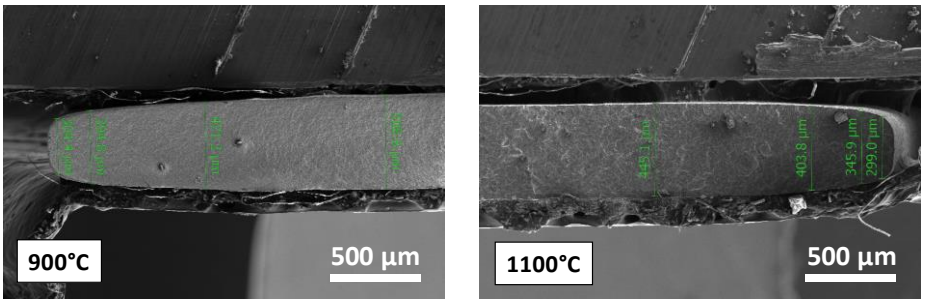

Figure 3. 27. SEM Cross-section images of LTO layers sintered at 900 ºC (left) and 1100 ºC (right) under Ar/H_2.

The shrinkage of extruded LTO materials with respect to the green parts is plotted in Figure 3. 28 as a function of the sintering temperature and atmosphere. In all the cases the shrinkage evolution with the temperature is very similar. A maximum contraction between 10 and 12 % is reached in each measured magnitude and a maximum total volume contraction of 40 % was calculated for all the atmospheres.

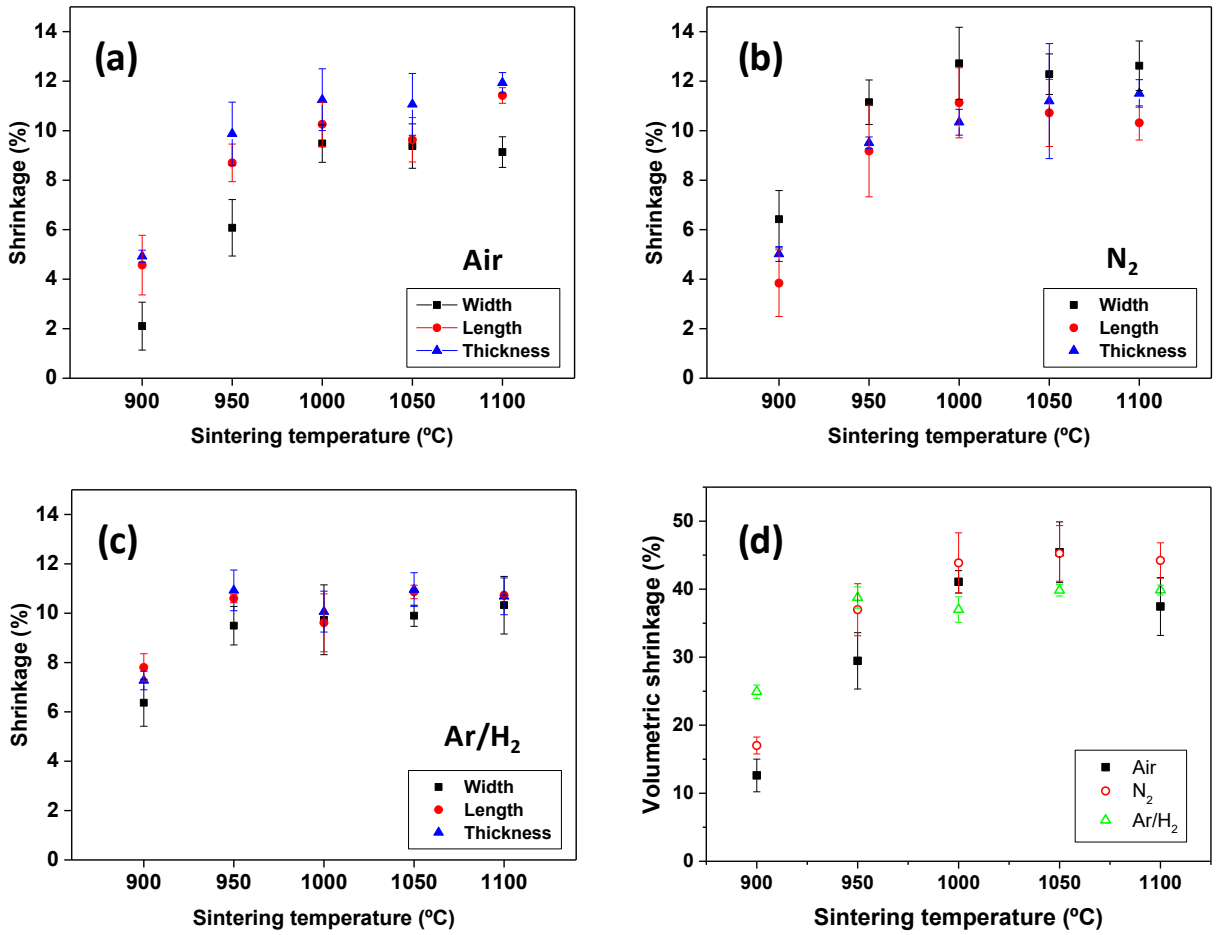

Figure 3. 28. Shrinkage variation of width, length and thickness of the extruded LTO samples prepared under (a) air, (b) N_2 and (c) Ar/H_2 as a function of the sintering temperature. The volumetric shrinkage is shown in (d).

The pore distribution was also analysed by SEM, by looking at higher magnifications of the sample cross-section. The maximum sintering temperature (1100 ºC) was selected for a better identification of the pores. The porosity was evaluated along the samples thickness. Figure 3. 29. shows a representation of the examined area. Several areas were examined, and the presented images are displayed as representative examples of the entire sample. The porosity was found to be homogeneously distributed over the full surface and no significant change in their size distribution was detected.

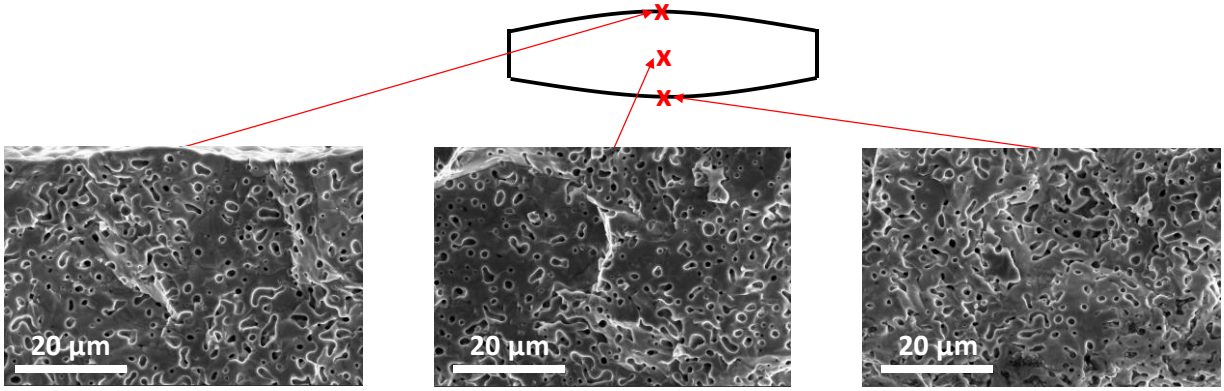

Figure 3. 29. SEM images from the inside of a LTO sample in three different points sintered at 1100 ºC in air.

3.4.2.4.2. X-Ray diffraction

Sintered LTO electrodes were studied by X-ray diffraction. According to the Li_2O-TiO_2 phase diagram in air, firstly proposed by West *et al.* [39], the spinel $Li_4Ti_5O_{12}$ decomposes at 1015 ± 5 ºC to meta-titanate (Li_2TiO_3) and ramsdellite ($Li_2Ti_3O_7$) (see Figure 3. 30). As in this work LTO layers were sintered from 900 to 1100 ºC, LTO decomposition is expected to occur at the highest sintering temperatures. Moreover, the different atmospheres employed (air, N_2 and Ar/H_2) may also affect the formation of secondary phases. Thus, the effect of temperature and atmosphere in the electrode composition was analysed by means of powder X-ray diffraction.

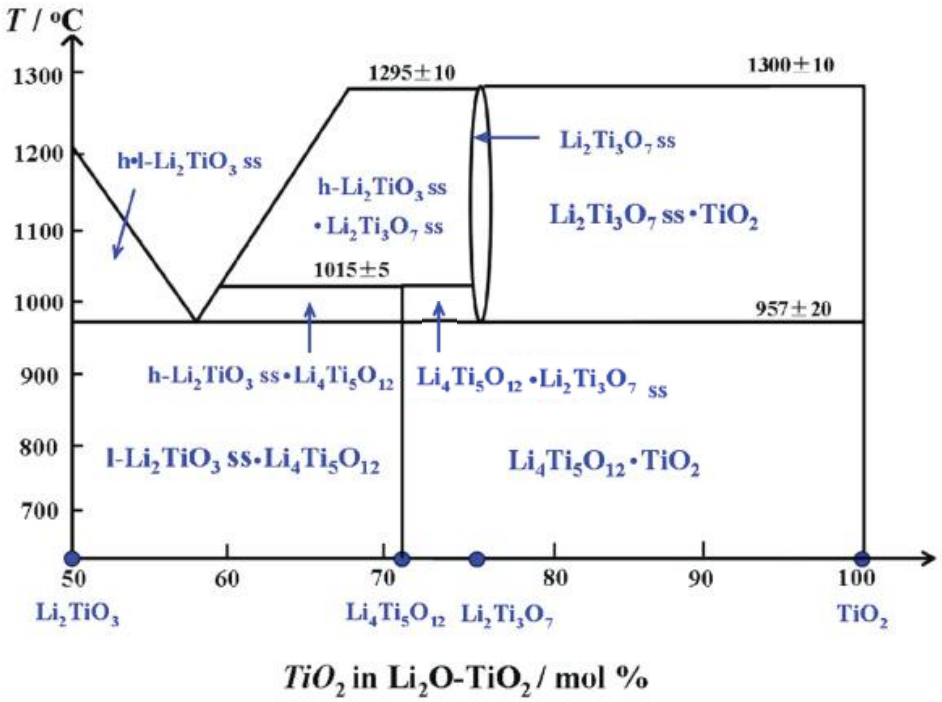

Figure 3. 30. Li_2O-TiO_2 phase diagram. Image taken from [40].

In Figure 3. 31 the XRD patterns of LTO electrodes sintered at different temperatures are collected in three different separated graphs according to the sintering atmosphere. The starting LTO powder XRD pattern is also represented as reference. Firstly, it can be observed that the patterns obtained for electrodes sintered in air and N_2 are very similar. In all the cases the main phase is identified as LTO. Only the sample sintered in air at 1100 ºC presents an additional peak with low intensity (< 10 %) at 2θ = 20.06 º identified as ramsdellite. On the other hand, in Ar/H_2, the presence of secondary phases is observed from 1000 to 1100 ºC. The main peaks identified as ramsdellite are marked as (*) in the diffractograms. However, the identification of meta-titanate needs a deeper inspection of the XRD patterns. Li_2TiO_3 crystallizes in a rock salt structure and, as well as $Li_4Ti_5O_{12}$. The structure is based on a cubic close packing of oxide ions, and titanium occupies octahedral positions in both materials, resulting in similar diffractograms with peaks overlapping at several 2θ values. Thus, the two phases cannot be easily discriminated. As the sintering temperature increases, the ramsdellite content decreases, while the meta-titanate content increases. This is in good agreement with the relative intensity of the highest intensity peaks of both meta-titanate and ramsdellite at 2θ around 18 and 20 º, respectively.

To sum up, XRD results suggest that no significant decomposition occurs in LTO electrodes sintered in oxidant or inert atmospheres in the studied temperature range but, in reducing atmosphere, 950 ºC is the maximum temperature at which no decomposition takes place. Moreover, given what previously discussed, and that decomposition must be avoided, a quantitative analysis of the decomposition products is not performed, as it is considered out of the scope of this study.

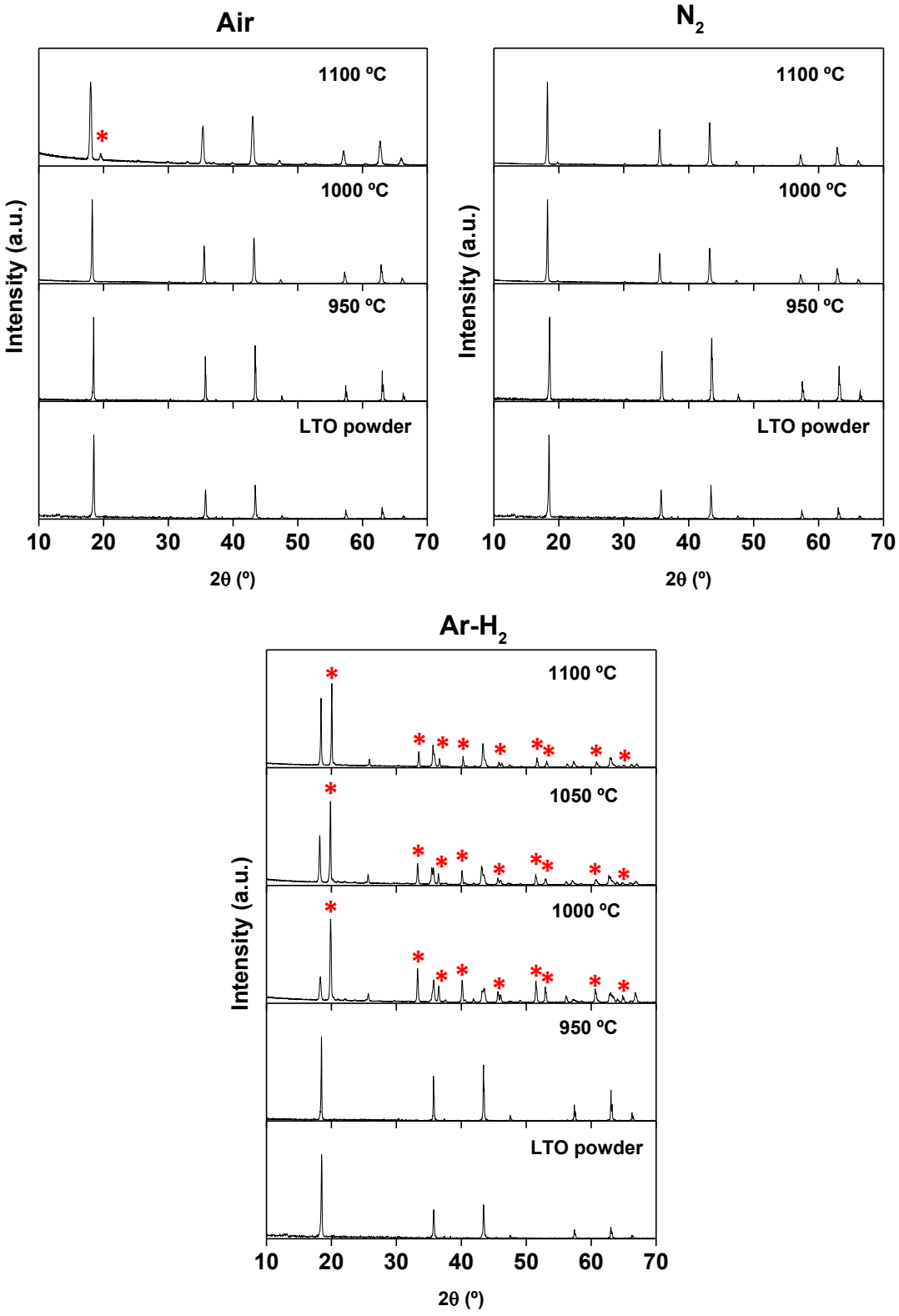

Figure 3. 31. Powder XRD patterns of sintered LTO from 1000 to 1100 ºC in air, N_2 and Ar/H_2. Ramsdellite peaks are marked as (*).

3.4.2.4.3. Carbon content and its distribution

The carbon content of the samples sintered at 950 ºC in air, N_2 and Ar/H_2 was measured by elemental analysis. The maximum content of carbon is found for the materials sintered under Ar/H_2, which is (0.14 ± 0.02) wt. %. The results indicate that under reducing atmosphere, some residual carbon coming from the binder decomposition remains in the electrodes.

On the other hand, for N_2 atmosphere a value of (0.05± 0.02) wt. % was measured. This unexpectable low carbon content could be attributed to the very small O_2 impurities in the N_2 gas flow used for sintering (< 10 ppm of O_2, according to the supplier) or to the not well sealed furnace. Eventually, negligible carbon (< 0.01 wt. %) was detected for the samples treated in air atmosphere, as expected from the carbon oxidation.

In this manner, the samples sintered at 950 ºC under Ar/H_2 reducing atmosphere were deeper investigated. Firstly, the carbon distribution was analysed by means of EDS mapping in a SEM microscope. As it can be observed in Figure 3. 32, the carbon is homogeneously distributed.

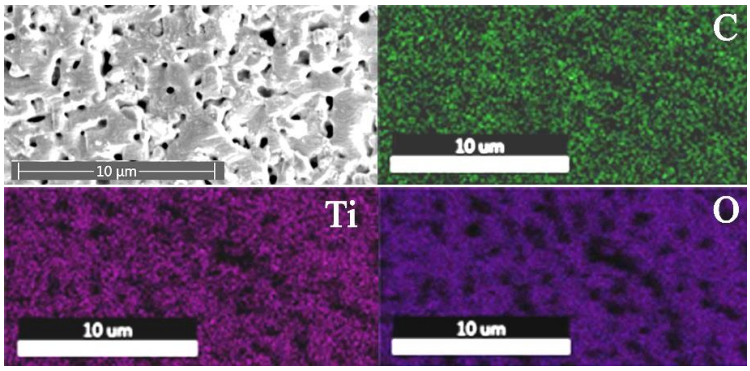

Figure 3. 32. EDS mapping of C, Ti and O of extruded LTO electrode sintered at 950 ºC under Ar/H_2.

By means of High Resolution-Transmission Electron Microscopy (HR-TEM), the carbon coating of LTO particles was analysed. In Figure 3. 33, a TEM image of the extruded sintered sample is shown and compared with the starting LTO powder. The micrographs suggest that an amorphous carbon layer of around 2 nm thickness homogeneously covers the LTO particles. Similar results were previously obtained by Y. Wang *et al.* [41] using polyaniline as carbon source and Ar/H_2 atmosphere (5 % H_2), in which the prepared LTO powder was covered with a carbon layer coming from the polymer pyrolysis. Moreover, during the heat treatments under Ar/H_2 atmosphere, as we will see later, Ti is reduced from Ti (IV) to Ti (III). Both carbon coating and presence of Ti^{3+}, improve electron conductivity. This is in agreement with other examples reported in the literature [42–44].

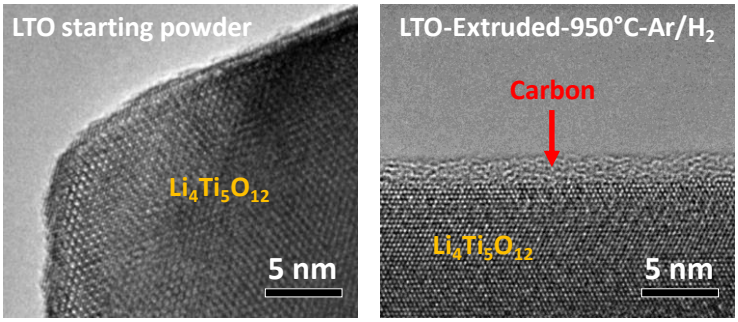

Figure 3. 33. TEM images of particles of starting LTO powder (left) and a LTO samples obtained by PEM sintered at 950 ºC under Ar/H_2.

3.4.2.4.4. X-Ray photoelectron spectroscopy

In order to study the effect of the reducing atmosphere on the oxidation state of Ti in LTO samples, X-ray photoelectron spectroscopy was conducted in two different extruded LTO samples sintered at 950 ºC in air and Ar/H_2. The measurements were carried out in the surface of the pieces and the fittings of the obtained results are shown in Figure 3. 34.

The spectra of the sample sintered in air shows a Ti 2p doublet with strong intensities at 464.4 and 458.7 eV, corresponding to Ti^{4+} and a less intense doublet at 462.7 and 457.1 eV for Ti^{3+} [45]. On the other hand, in the sample sintered in Ar/H_2 the signal identified as Ti^{3+} is predominant with respect to that of Ti^{4+}. Song *et al.* [46] reported a carbon-free LTO electrode prepared by conventional casting with good electrochemical performance. The good response of the electrode was explained by the presence of Ti^{3+}, which increases the electronic conductivity. Also, they monitored the colour of the electrode at different discharge and charge stages. The as-prepared electrode was white and as soon as some Li^+ is inserted the colour changed to bluish black. When the battery is full discharged, the electrode was completely black. They suggested that the progressive change from white to black could be related to the occupation of the 3d orbitals. This indicates that, despite the carbon coating improves the electrical conductivity of LTO particles, it is not mandatory for working in a battery. Similar conclusions were obtained previously by Zaghib *et al.* for very fast charge/discharge LTO//LFP batteries [47].

By fitting the XPS spectra, it was determined that the samples sintered in air present 87.4 % of Ti^{4+} respect to the total Ti, while a 12.6 % corresponds to Ti^{3+}. This result indicates that, even after sintering under an oxidant atmosphere, there is some Ti^{3+} in the material. On the other hand, the extruded samples sintered under Ar/H_2 has 2.7 wt. % of Ti^{4+} and 97.3 wt. % of Ti^{3+}, due to the reducing power of the H_2. It must be highlighted that XPS is a surface technique and, in this case,

the penetration of detectable photons is around 10 nm. This means that these results cannot be extrapolated to the whole sample and a homogeneous reduction along the material is uncertain.

Thus, by using the material sintered in reducing atmosphere, the discharge of the battery would not start from insulating $Li_4Ti_5O_{12}$ but from a more electron conductive material. Previous studies concluded that a reducing atmosphere improves the charge/discharge kinetics (reduced polarization) of the material, due to the Ti reduction [48].

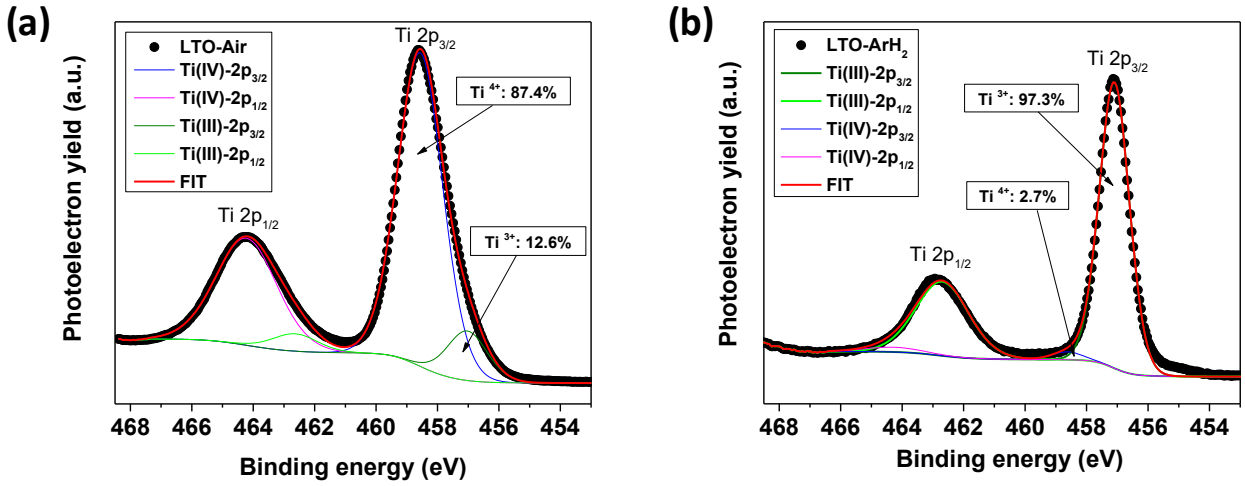

Figure 3. 34. XPS curves for LTO samples sintered at 950 C in (a) air and (b) Ar/H_2.

3.4.2.4.5. Impedance spectroscopy

Impedance measurements of LTO electrodes sintered at 950 ºC under air, N_2 and Ar/H_2 were performed at room temperature in order to determine the conductivity of the different samples and to study the effect of the atmosphere in the impedance of the materials.

Figure 3. 35-(a) collects the Nyquist diagrams of samples prepared in air and N_2. The Nyquist plot in air shows a flattened semicircle with an associated capacitance of 4 pF in the top of the semicircle, which is attributed to the bulk resistance of the material. At lower frequencies, another semicircle can be guessed which, in principle, could be attributed to the grain boundary resistance. In the low frequency region, impedance follows a linear trend with a 45 º spike, corresponding to the diffusion in the electrode interphase with the gold electrode and characteristic of an ionic conductor with blocking electrodes. In the case of the Nyquist plot in N_2, an analogous response is observed, in which a more distorted semicircle with an associated capacitance of 3.5 pF appears at slightly higher impedance values and another semicircle seems to appear at lower frequencies, which could correspond to the grain boundary contribution. As expected, the

impedance of these samples is very high, as the typical conductivity value for LTO is reported to be around 10^{-7} S/cm [28,49].

On the other hand, the Nyquist diagram of the sample sintered under Ar/H_2 presents a different response (Figure 3. 35-(b)). Most of the data points overlap in a single point at the Z' axes intersection at $6.5 \cdot 10^3$ Ω·cm, which indicates typical response of an electronic resistor. At higher frequencies, a semicircle is intuited, which could correspond to a small capacitance contribution due to the ionic character of LTO. Moreover, the impedance of this sample is much lower than that of the samples prepared in air or N_2. The frequency dependent conductivity plot in Figure 3. 35-(c) shows that the conductivity of the sample sintered in Ar/H_2 is more than three times the conductivity of those materials sintered in air or N_2. This difference can be attributed to: *(i)* the residual carbon present in the sample prepared in a reducing atmosphere coming from the debinding treatment and/or *(ii)* the partial reduction of Ti^{4+} to Ti^{3+}. For a better understanding, the starting commercial LTO powder was pelletized by uniaxial pressing and sintered under reducing Ar/H_2 atmosphere at 950 ºC for 1 h in order to reproduce same sintering conditions than the extruded electrode. It is worth noting that the colour of the obtained pellet is dark-bluish, which may suggest that a partial reduction of Ti occurs. The frequency dependence of the conductivity of this pellet is compared in Figure 3. 35-(d) with the extruded sample. The conductivity of the uniaxially pressed material decays drastically compared with the extruded electrode. This result is unexpected, as it was reported before that the impedance of a reduced LTO sample can increase until ~10^{-5} S/cm due to Ti partial reduction [38]. However, it must be considered that the sintering temperature used leads to highly porous materials. Therefore, even if the bulk conductivity increases, the grain boundary impedance could be increasing, resulting in an overall decrease in conductivity. Thus, our result indicates that the high conductivity of the extruded sample is not only due to the partially reduced Ti but also to the residual carbon. This carbon coating could provide an interconnected pathway between the particles for electron motion, decreasing the grain boundary impedance associated to the porous microstructure. On the other side, the partial reduction of Ti contributes to the bulk conductivity of the material. In this manner, the overall conductivity of the material increases tremendously to ~ 10^{-4} S/cm. This result is of major importance as proves that carbon coated porous LTO electrodes with considerably improved electronic conductivity can be obtained by PEM and makes this process very attractive for the scalable production of LTO thick electrodes.

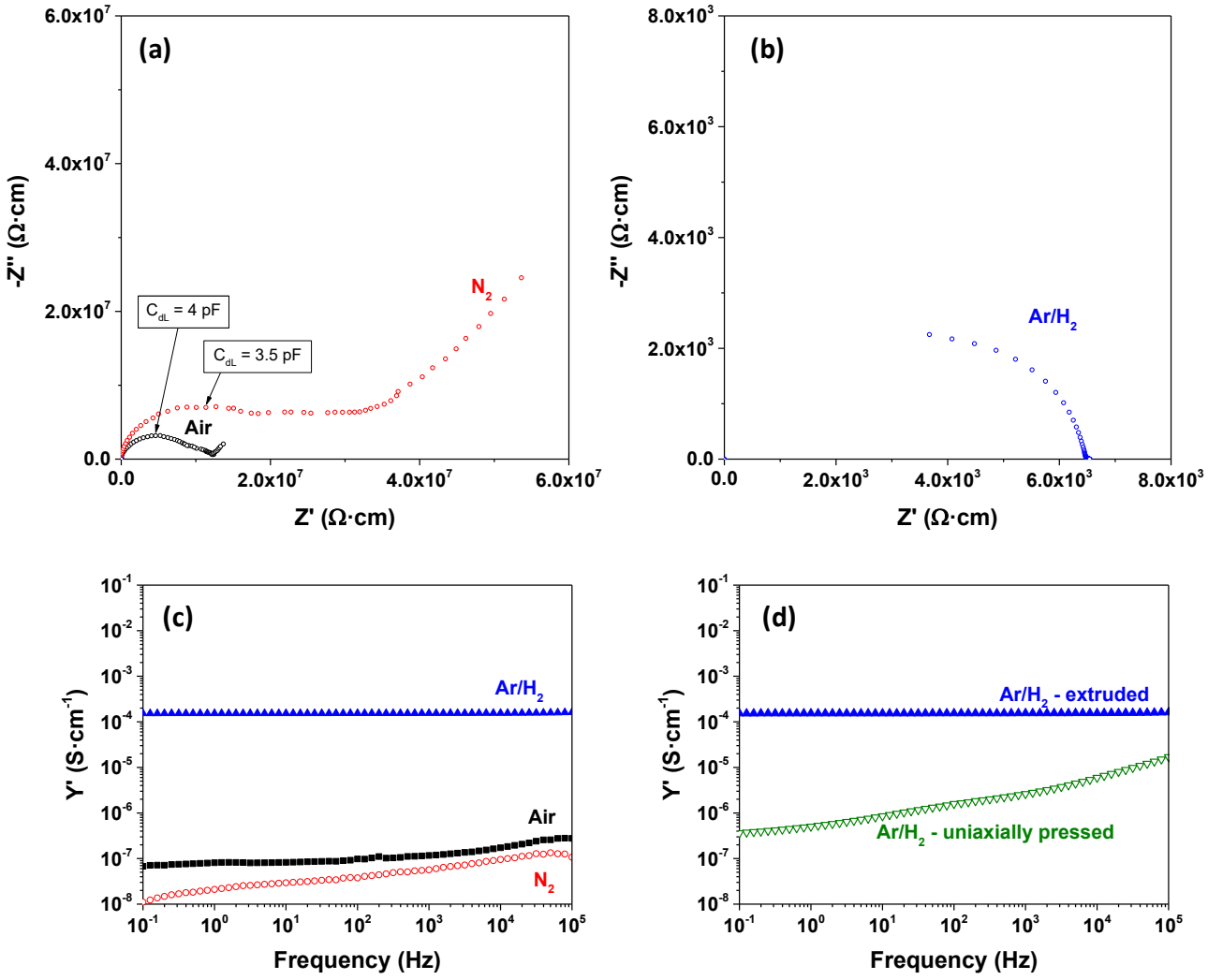

Figure 3. 35. Electrical response for LTO samples sintered at 950 ºC (a) Nyquist diagram air and N_2. (b) Nyquist diagram in Ar/H_2. (c) Frequency variation of the real part of the complex admittance in air, N_2 and Ar/H_2. (d) Frequency variation of the real part of the complex admittance in Ar/H_2 comparing extrusion and uniaxial pressing processes.

After impedance experiments it was concluded that the optimum extruded sample is that one sintered under Ar/H_2 as is the one with the highest conductivity. This material was therefore selected to be used as negative electrode in a Li-ion battery, hence its performance in Li/LTO half-cell was evaluated.

3.4.2.5. Application to lithium-ion batteries

The electrochemical performance of extruded electrodes sintered at 950 ºC in Ar/H_2 (labelled as LTO-extruded) was studied in lithium half cells [50]. In order to assess the advantages of these thick LTO-ceramic electrodes, their electrochemical performances are compared with those electrodes prepared by the conventional casting method from a mixture of the same commercial LTO powder used to elaborate the PEM samples (80 wt. %), carbon black (10 wt. %) and PVDF (10 wt. %) using the doctor-blade technique (labelled as LTO-composite). The maximum thickness reached for the composite electrodes without cracks and peeling off the current collector is 110 µm with an LTO active material loading of 9.4 mg/cm^2 of the electrode. On the other hand, the mass loading of the extruded electrode is 138 mg/cm^2. This value is huge compared to the composite reference electrode. It is reached due to *(1)* the lack of binder and extra carbon additives and *(2)* the relatively high density of the sintered material.

As the LTO-extruded anodes are additive-free and they have large thickness (475 µm) and, in order to minimize kinetic hindrances, it was decided to apply a low constant current of C/24 for the galvanostatic tests. In Figure 3. 36-(a), the discharge curves for the first charge-discharge cycle of LTO-extruded and LTO-composite electrodes are represented. In both cases the shape of the curves is comparable, displaying a flat *plateau* at approximately 1.5 V. The maximum discharge capacity is as high as 120 mA·h/g at the first cycle. The LTO-extruded average voltage (1.45 V vs. Li^+/Li) is close to that of the LTO-composite anode (1.53 V) and it remains almost constant, as for the composite electrode, during the discharge. The small polarization observed in the ceramic electrode with respect to the composite could be mainly attributed to the slow kinetics of the charge transfer process at the electrode surface, due to the very low carbon content in the electrode and the limited lithium diffusion in the thick electrode.

Electrode cyclability was evaluated at C/24. Figure 3. 36-(b) shows the discharge curves during the first 20 charge-discharge cycles. After 20 charge-discharge cycles, the thick ceramic electrode maintains relatively a flat *plateau* and no significant increase in polarization is observed. Figure 3. 36-(c) shows the specific capacity evolution during 20 cycles. The specific capacity only decreases from 119 to 107 mA·h/g which corresponds to a capacity retention of 90 %, a promising result giving that the extruded electrode does not contain any binder nor any conductive additive. No increase of specific capacity is observed when comparing the extruded electrode to the conventional one. However, it should be noted that the extruded negative electrodes' performance

is expected to be greatly improved as the process is optimised, and binders/additives are included in the formulation.

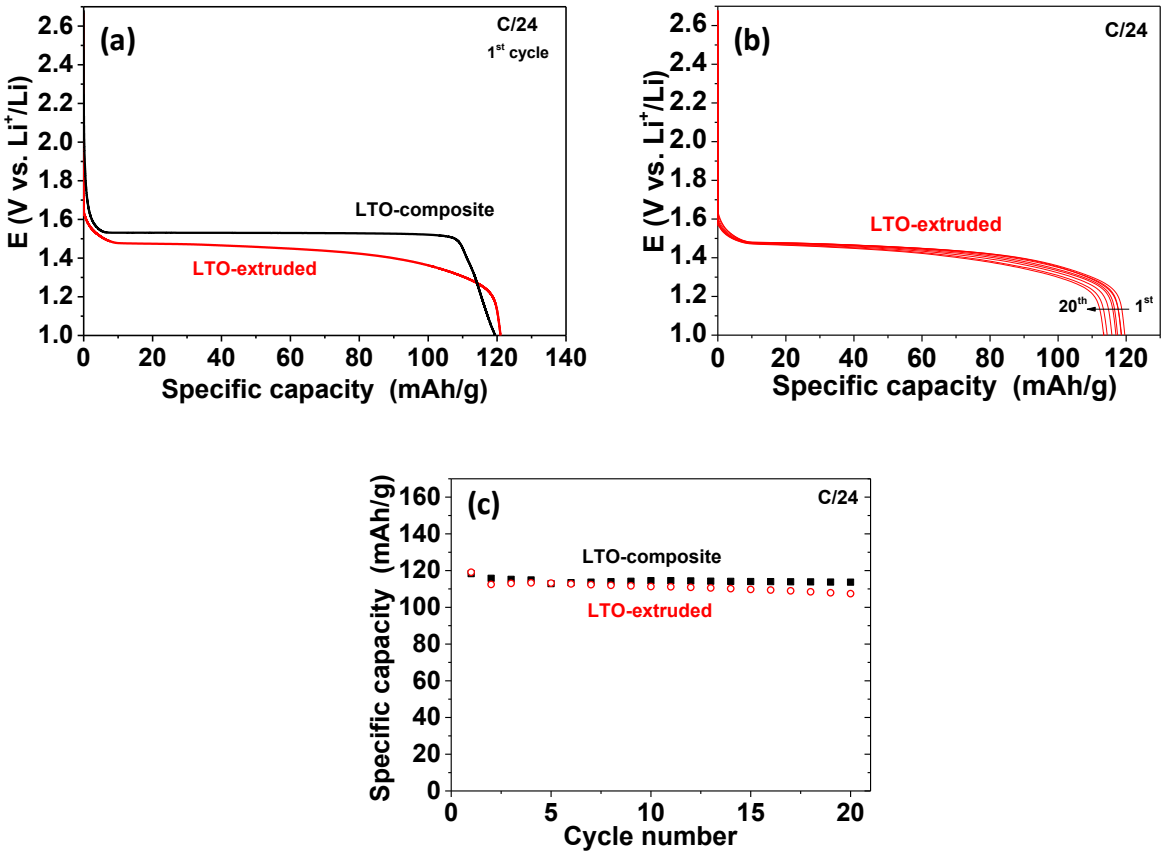

Figure 3. 36. (a) Discharge curves of the first cycle at C/24 for LTO-composite and LTO-extruded electrodes. (b) For the LTO-extruded electrode, discharge curves at C/24 for 20 cycles. (c) Capacity evolution as a function of cycle number at C/24 for LTO extruded (empty markers) and composite (full markers) electrodes.

3.4.2.5.1. Volumetric capacity and thickness effect

The reversible volumetric capacity of the LTO-extruded anode and the LTO-composite electrode, calculated according to their respective geometrical densities (2.9 and 1.1 g/cm^3), is shown in Figure 3. 37-(a) for 20 charge-discharge cycles. Interestingly, the volumetric capacity of the additive-free electrode is 310 mA·h/cm^3, almost 2.5 times higher than that of the LTO-composite electrode. The latter, 131 mA·h/cm^3, is calculated, as usual, from the electrode formulation without taking into account its swelling by the liquid electrolyte, which means that its actual capacity is lower than 131 mA·h/cm^3, while the LTO-extruded electrode volume is not modified by the electrolyte. This neat increase in volumetric capacity is ascribable to the higher density of the extruded electrode due to both the absence of additives and the sintering step.

The high cycling performance of the LTO-extruded electrode is also observed when higher charge/discharge currents of C/12 and C/8 are used (Figure 3. 37-(b)). When the current is increased at C/12, the reversible volumetric capacity (ca. 270 mA·h/cm^3) is slightly smaller (ca. 15 %). The loss in reversible capacity can be ascribed to kinetic limitations when high current densities are applied. On one side, the high thickness of the electrode hinders ion motion. On the other side, the low carbon content limits the distribution of high current densities. However, the cyclability at C/12 is better than at C/24. From the 2nd to the 20th cycle and from the 2nd to the 50th cycle, the LTO-extruded electrode retains 97.8 % and 88.7 % of its nominal capacity at C/12, respectively. Further increase of the rate to C/8 results in a more severe capacity loss with the reversible capacity being 130 mA·h/cm^3. It should be indicated that this value is similar to the volumetric capacity of the LTO-composite electrode recorded at a lower current of C/24 (Figure 3. 37-(a)). As for the other two rates tested, the cyclability at C/8 is also promising, with capacity retentions of 98.4 % after 20 cycles and 92.5 % at the end of the 30 cycles performed. In Figure 3. 37-(b), the evolution of the coulombic efficiency during cycling is also plotted. For all the rates tested, the coulombic efficiency values are very high, close to 100 % for every cycle.

The influence of the thickness on the electrochemical properties and on cycle life of the electrodes was also evaluated. For this study, an extruded LTO electrode, 850 µm thick, was used in a lithium half cell. Due to severe problems of cell polarization, mainly ascribed to the extremely high thickness of the ceramic electrode, the current intensity was decreased to a relatively very low value of C/50 for the galvanostatic test. Figure 3. 37-(c) collects the discharge/charge profiles for different cycles of the 850 µm thickness extruded anode. In spite of the extremely high thickness of the ceramic electrode and that it is additive-free, it was possible to reversibly insert/extract lithium in/from this electrode. However, an increase in thickness leads to a reduce reversible capacity, i.e. 90 mA·h/cm^3, much lower than that of the thinner (475 µm) LTO-extruded electrode (Figure 3. 37-(a)). This result is in agreement with previous studies reported in the literature which have shown that several electrochemical parameters such as capacity or cyclability notably decrease on increasing the electrode thickness, especially at high charge-discharge rates. For example, Singh *et al.* reported a capacity loss at C/2 due to kinetics limitations in NMC and graphite electrodes of 300 µm thickness [51]. On the other hand, Zhao *et al.* studied the effect of the electrode thickness on the electrochemical and thermal response of $LiMn_2O_4$ commercial lithium-ion batteries [52]. Apart from the diffusion limitations, high-thickness electrodes have more intense and uneven temperature distribution inside the electrode, especially at high C-rates.

This fact may cause capacity fading, lower power output and security risks between other problems.

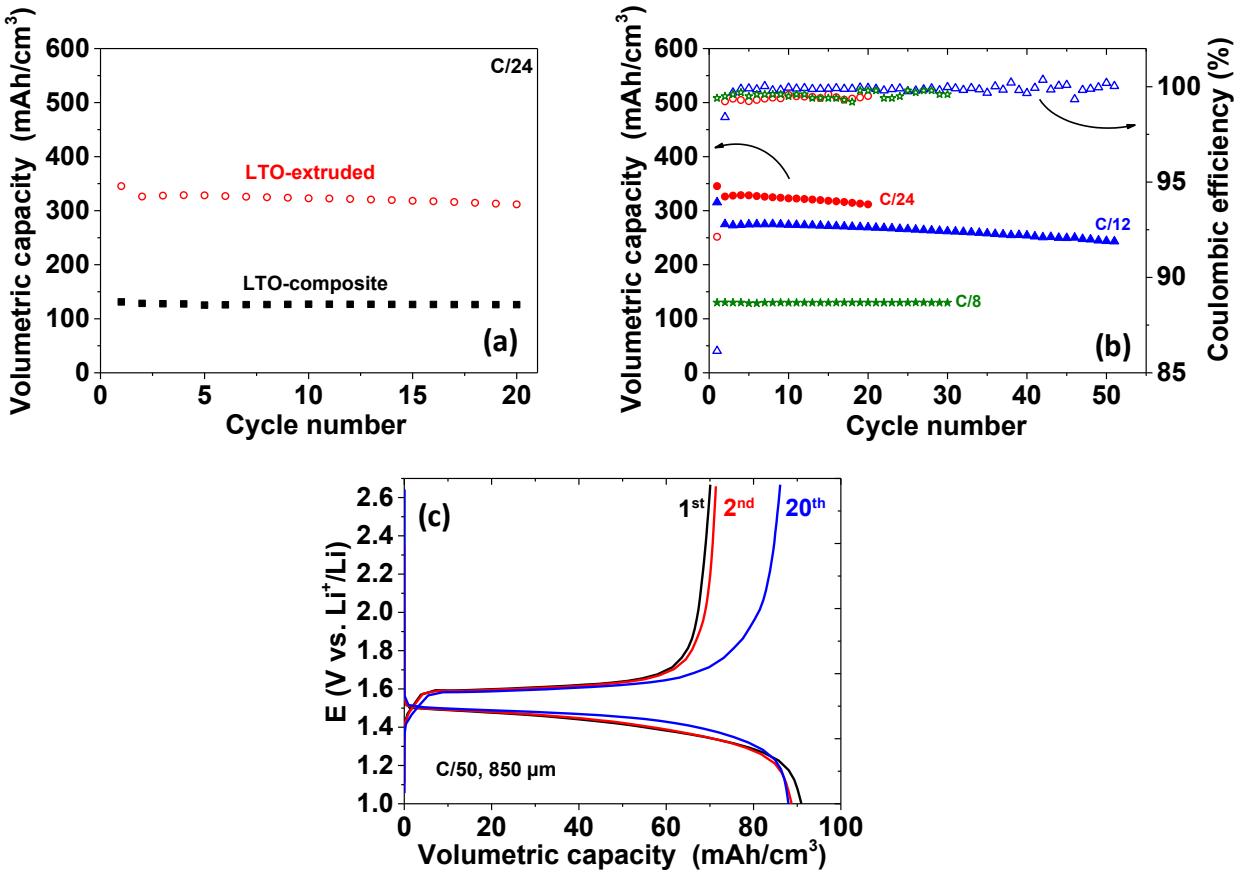

Figure 3. 37. (a) Evolution of volumetric discharge capacity vs. cycle number for additive-free LTO-extruded and LTO composite electrodes at C/24. (b) Evolution of volumetric discharge capacity vs. cycle number and coulombic efficiency for the LTO-extruded electrode registered at C/24, C/12 and C/8 rates. (c) Discharge/charge profiles of additive-free LTO extruded electrode of 850 µm thickness at C/50 rate.

3.4.2.5.2. Areal capacity

Regarding the areal capacity, the performance improvement is even much higher than the volumetric capacity gain, exceeding one order of magnitude, being 15.2 mA·h/cm^2 for the extruded electrode compared to 1.42 mA·h/cm^2 for the conventional electrode. In this case, in addition to the higher density, the greater thickness of the LTO-extruded electrode (475 *vs.* 110 µm) explains this outstanding improvement. It must be underlined again that the high thickness of the ceramic electrode together with the absence of binder permits getting a much larger LTO mass loading in the PEM electrode than in the conventional composite (138 vs. 9.4 mg/cm^2). All these results indicate that an effective percolation of the electrolyte into the bulk of the LTO-extruded electrode takes place. This result contrasts with the study of Suna *et al.*, who showed that a sintered

LTO electrode with 92 ± 11 µm thickness and a 7 % porosity had a very poor electrochemical response, only 1.5 mA·h/g at the very low rate of C/40 [53].

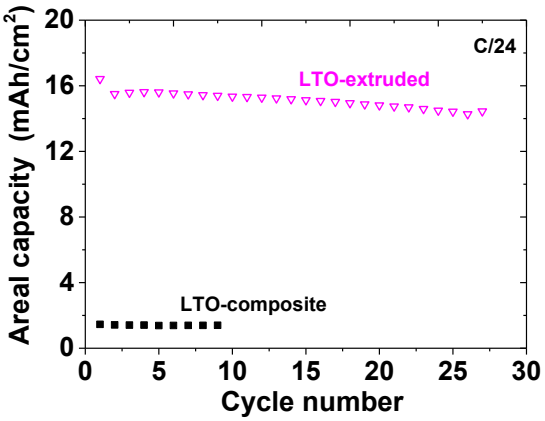

Figure 3. 38. Evolution of discharge areal capacity vs. cycle number for additive-free LTO-extruded and LTO-composite electrode at C/24.

The superior electrochemical response of our LTO-extruded electrodes is explained by their greater porosity (16 % as determined from the experimental/theoretical density ratio). This result is in agreement with the studies of Lai *et al.*, who reported that additive-free sintered $LiCoO_2$ cathodes made by uniaxial pressing with porosity between 13 and 30 % exhibited ultrahigh volumetric energy densities (from 350 to 650 W·h/l at C/3) [54].

In conclusion, the Powder extrusion moulding process allows obtaining LTO-ceramic electrodes that, due to the absence of additives and their high thickness, reaches volumetric and areal capacities much higher than a conventional LTO-composite electrode.

3.4.3. $LiFePO_4$ electrodes

3.4.3.1. Feedstock characterization

The prepared LFP feedstocks were characterized by means of torque, viscosity and density measurements. Their homogeneity was analysed and the Critical Powder Volume Concentration (CPVC) was estimated.

3.4.3.1.1. Torque measurements

Torque variation with time was used for estimating the homogeneity of the LFP feedstocks, using the same procedure than that carried out for LTO feedstocks. Figure 3. 39-(a) shows torque curves of feedstocks with different powder loadings. In all the cases, the steady-state torque is reached, and it increases with the powder loading due to a higher mixture viscosity. Figure 3. 39-(b) represents the variation of the steady-state (τ) with the powder loading. In the graph, two different regions are identified at low and high powder loadings and a linear fit of the points of each region reveals an abrupt slope change. Firstly, from 50 to 52.5 vol. % of LFP, a pronounced increase of torque occurs because of the increased powder loading in the mixture, indicating a higher viscosity. However, for powder loadings above 52.5 vol. %, the steady-state torque remains almost constant. This behaviour is totally unusual in powder-binder mixtures for PIM/PEM process, since generally the steady-state torque remains almost constant at low powder loadings and sharply increases above a certain value, as observed for the LTO feedstock prepared in this work as well as other ceramic and metal feedstocks previously prepared in our group such as austenitic-ferritic stainless steel [55], 430L stainless steel [12,15], Ni-YSZ [16,18] and alumina [7]. In the case of LFP feedstock, the steady-state increase at low powder loadings could be related with the fact that there is not enough binder to cover the surface of powder particles and a fraction of them are in contact with each other. Secondly, all the LFP particles are coated by a very thin carbon layer. This carbon coating acts as lubricant between particles reducing the friction and allowing to increase the powder loading without increasing the steady-state torque value. It is worth to note that, experimentally, in the case of the feedstock with a 58 vol. % of powder loading, the visual aspect is slightly different from the rest of the feedstocks prepared, observing clearly lack of powder coated by the polymer.

Compared to LTO feedstock, the steady-state torque values are considerably much higher. Specifically, for LFP feedstocks, τ varies between 3.78 and 8.62 N·m, while for LTO ones the variation was between 0.17 and 1.27 N·m. This difference could be attributed to different facts *(i)* particle size distribution of the starting materials. By comparing with the dataset resented in section

3.4.1.1.2., it is evident that LPF presented a higher content of small particles than LTO and less agglomerates. In previous studies, the torque value increased as the particle size decreased for an injected stainless steel powder [56], especially at high powder content (above 55 vol. %) which is in good agreement with our results. *(ii)* the carbon coating of LFP particles may hinder the adhesion between binder and powder, so some LFP particles are not covered by the binder, increasing the friction between each other and thus raising the registered torque.

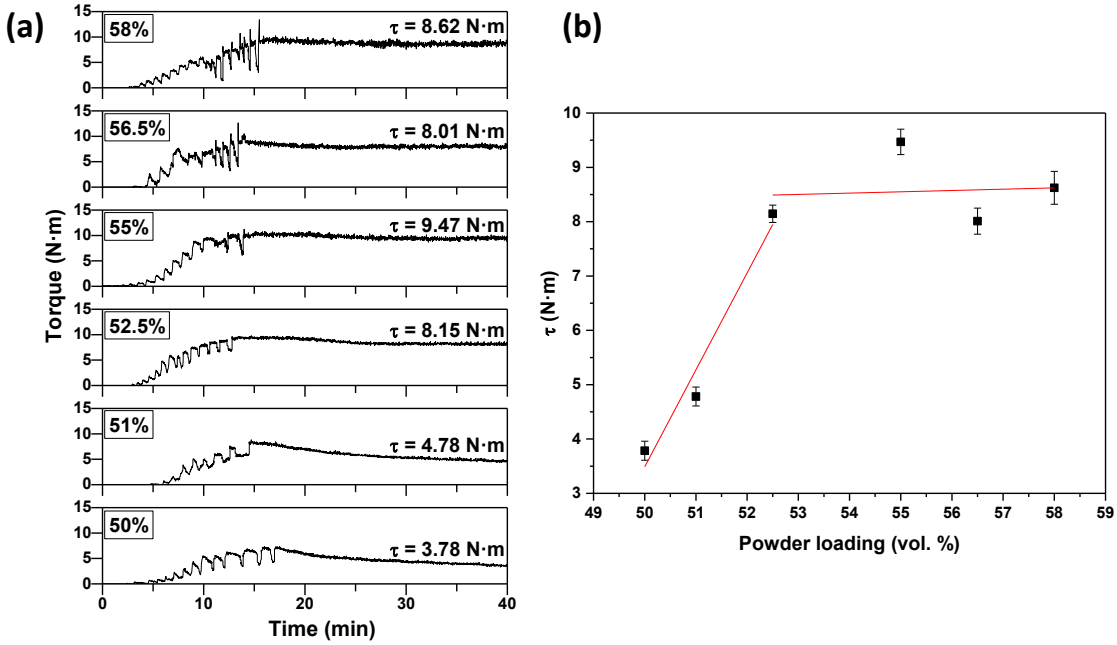

Figure 3. 39. (a) Torque against mixing time for mixtures with different LFP content and (b) steady-state toque (τ) variation with LFP powder loading.

3.4.3.1.2. Homogeneity

The homogeneity of the LFP feedstocks prepared in this work was analysed by viscosity and density measurements. Figure 3. 40-(a) shows viscosity values against time for feedstocks with powder loadings of 52.5 and 58 vol. % prepared in a rotor blade mixer. The measurements were carried out at the extrusion process temperature (180 ºC) and at a share rate of 1000 s^{-1}. As expected, the viscosity increases with the powder loading due to the higher friction between the powder particles. In both cases, a slight increase of viscosity was registered during the first 40 seconds of the experiment and trends to a constant value at longer times, which indicates a good homogeneity of the feedstocks.

On the other hand, the effect on viscosity of employing a twin-screw extruder in the mixing step was checked, and the viscosity variation with time for a feedstock with 55 vol. % of LFP was registered, as shows Figure 3. 40-(b). As a consequence of the higher shear rates encountered in

the twin-screw extruder compared with the rotor blade mixer, the viscosity shows a more constant value during the measurement time. Thus, in the case of LFP feedstocks, and contrary to LTO feedstocks, the use of either a rotor blade or a extruder leads to homogeneous mixtures.

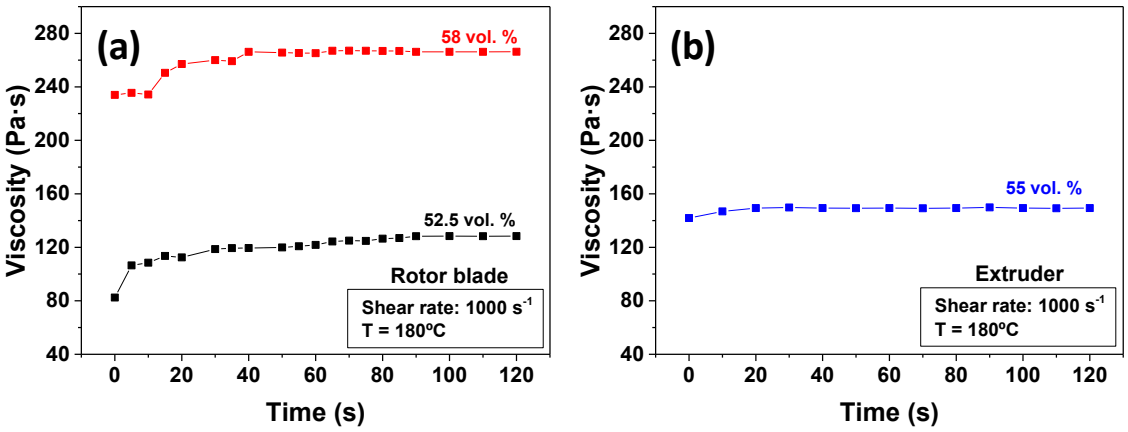

Figure 3. 40. Variation of viscosity with time for feedstocks with (a) 52.5 and 58 vol. % of LFP prepared in a rotor blade mixer and (b) 55 vol. % of LFP prepared in a twin-screw extruder.

The pycnometric density of the feedstock with 55 vol. % of powder prepared in the extruder, measured in three different fractions of the same mixture, was 2.362 ± 0.001 g/cm^3, while the theoretical density of the mixture is 2.369 g/cm^3. The results indicate that no compositional change occurred during processing and confirms a good feedstock homogeneity.

3.4.3.1.3. Rheological characterization

The rheological characterization of the prepared feedstocks was performed to determine their ability to be extruded. Figure 3. 41 shows the variation of the viscosity with the shear rate for four feedstock formulations. As expected, the viscosity increases with the powder loading, achieving the maximum viscosity for feedstock with 58 vol. %. All the samples display a pseudoplastic behaviour and all the viscosity values were lower than 1000 Pa·s between 100 and 2000 s^{-1}. As discussed for LTO feedstocks rheological characterization, these conditions are the most convenient for extrusion process.

The viscosity curves of the mixtures were fitted to the Ostwald and De Waele power law. The power law indexes were calculated from the slope of logarithmic plots of shear stress *versus* shear rate for feedstocks with different powder loadings in the shear rate range between 100 and 10000 s^{-1} (Figure 3. 41).

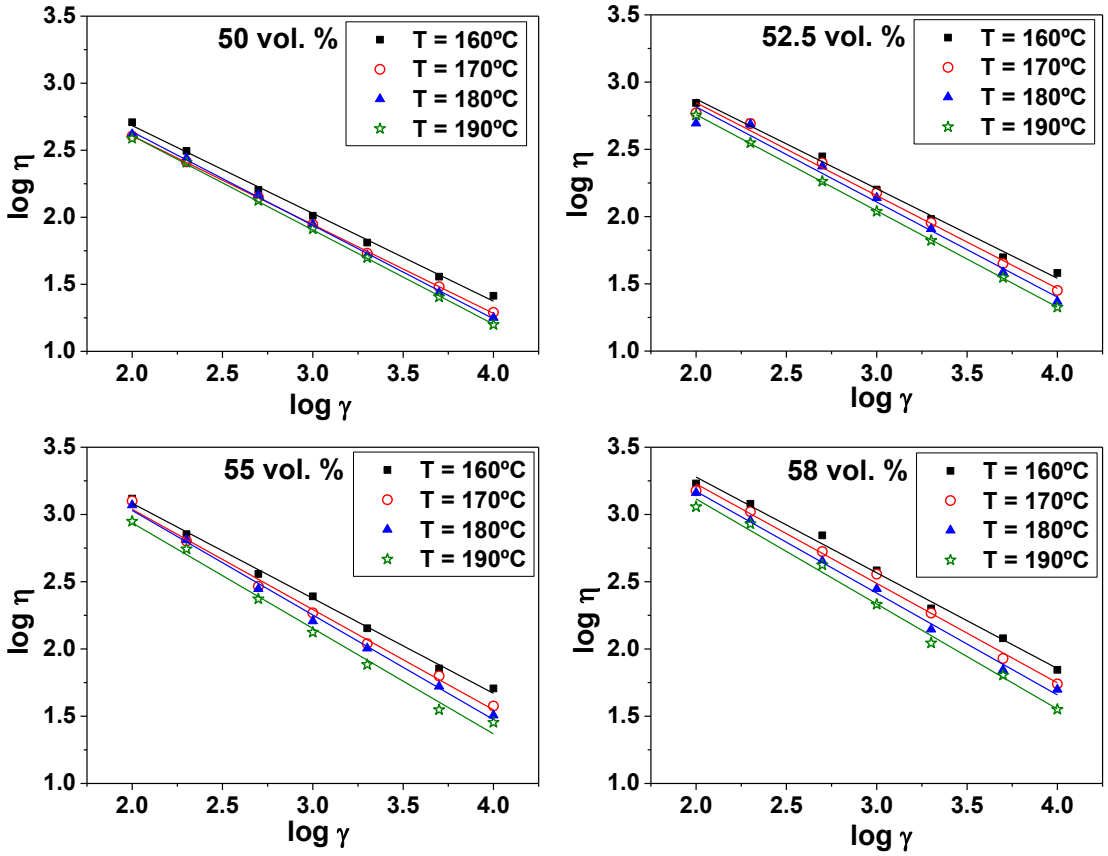

Figure 3. 41. Flow curves for LFP feedstocks with powder loadings of 50, 52.5, 55 and 58 vol. % at temperatures between 160 and 190 ºC.

In Table 3. 7 the power law indexes (n) are collected. The value of n decreases slightly with both the powder loading and the temperature, that is, the higher the powder loading and the temperature, the more pseudoplastic the feedstock is. This means that the polymer chains of the binder are more able to reorganize with high powder loadings during the moulding process and the feedstock is more sensitive to the shear rate at high processing temperatures. Comparing with LTO-feedstock prepared with similar binder formulation, the n value is lower (0.35-0.22 for LFP *vs.* 0.46-0.54 for LTO), being consequently more sensitive to shear rate. Moreover, similar values were obtained for injected YSZ [20] and extruded Ni-YSZ [18] electrolytes, in which the flow index were in the range 0.31-0.41 for YSZ and 0.17-0.30, respectively. In addition, in the case of Ni-YSZ, the flow index also decreased with the powder loading.

Table 3. 7. Power law index (n) and activation energy (E_a) of LFP feedstocks with different powder loads. The regression coefficient associated to the linear fit is given between brackets.

	n				E_a (kJ·mol^{-1})
Powder load (vol. %)	160 ºC	170 ºC	180 ºC	190 ºC	
50	0.35 (0.997)	0.34 (0.9997)	0.30 (0.9990)	0.30 (0.9994)	11.2
52.5	0.33 (0.994)	0.31 (0.991)	0.29 (0.98)	0.28 (0.9999)	20.0
55	0.29 (0.996)	0.25 (0.993)	0.22 (0.996)	0.22 (0.991)	33.1
58	0.29 (0.993)	0.26 (0.993)	0.24 (0.996)	0.22 (0.992)	33.1

Otherwise, as expected, the viscosity of all the feedstocks decreases with the temperature (Figure 3. 41), following the same behaviour than LTO feedstocks. E_a was calculated from the slope of plots of the logarithmic viscosity against temperature (Figure 3. 42) considering the viscosity values at a shear rate of 1000 s^{-1}. It is observed that the activation energy increases with the powder loading. This is explained by the different thermal expansion coefficients of powder and binder [1]. For feedstocks with lower powder loading, the ceramic particles are less close and there is less friction between them. Thus, a temperature rise produces a thermal expansion of the binder, increasing the distance between particles and decreasing their friction, facilitating the flow and, therefore, decreasing the viscosity. However, this effect is not as marked as in a feedstock with higher powder content in which the particles are much closer. A small increase in temperature contributes to decrease the friction between the particles facilitating the flow. Therefore, the effect of temperature on the viscosity in feedstocks with high powder loadings is greater, that is, the activation energy increases with the powder content [57].

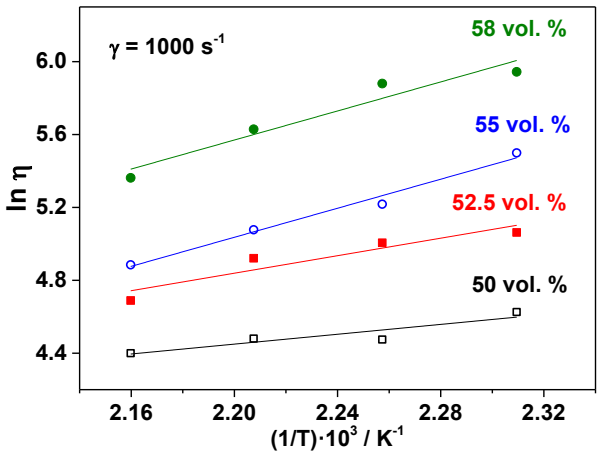

Figure 3. 42. Variation of viscosity with temperature for the different feedstocks. The data are adjusted following a linear fit according to an Arrhenius-type equation.

During vertical extrusion, a feedstock with a high activation energy is desired for rapidly increasing the viscosity when it exits from the nozzle and the temperature decreases. Therefore, the feedstock with the highest activation energy would be the most suitable for PEM, which are those with powder loadings of 55 and 58 vol. %. Moreover, their activation energies (33.1 kJ/mol in both cases) are similar to others reported before in our group for extruded Ni-YSZ solid electrolytes (27.4 kJ/mol for a feedstock with 55 vol. % of powder) [18]. Compared to LTO feedstock, previously described in this Chapter, the activation energy of LFP-feedstock is approximately half than that of LTO ($E_{a\ (LTO,\ 55\ vol.\ \%)}$ = 73.2 kJ/mol). Thus, LFP feedstock would be expected to be less viscous after moulded and more susceptible of suffering deformation. However, the more pseudoplastic behaviour (lower index flow values) of LFP compared to LTO leads to a greater increase of the viscosity when the shear rate ceases, and geometry is well retained. Thus, it can be concluded that the pseudoplastic character of the feedstock is more influent than its activation energy.

On the other hand, in terms of powder loading and temperature, the highest possible powder loading and the highest temperature would be the most convenient conditions for PEM [58], provided that the viscosity achieve values lower than 1000 Pa·s at a shear rate equal or higher than 100 s^{-1} [59]. Also, high powder loadings present the highest activation energies. Consequently, 55 and 58 vol. % would be the most convenient powder loadings. Between them, we decided to select a powder loading of 55 vol. %, which is the most conservative value considering that the viscosity is close to 1000 Pa·s at 100 s^{-1} for both feedstocks and in order to minimize the wear of the extrusion tools. Therefore, the selected feedstock was prepared in a twin-screw extruder.

3.4.3.2. Extrusion and green pieces

Before extrusion, a microstructural inspection of the selected feedstock (55 vol. % powder loading) was performed by SEM in order to analyse the quality of powder/binder dispersion. Figure 3. 43 shows SEM images of the feedstock. LFP particles, with higher molecular weight than the binder, were observed as bright particles, while darker parts corresponded to the binder. In any case, the powder was found to be well distributed in the polymer matrix, showing a good microstructural homogeneity.

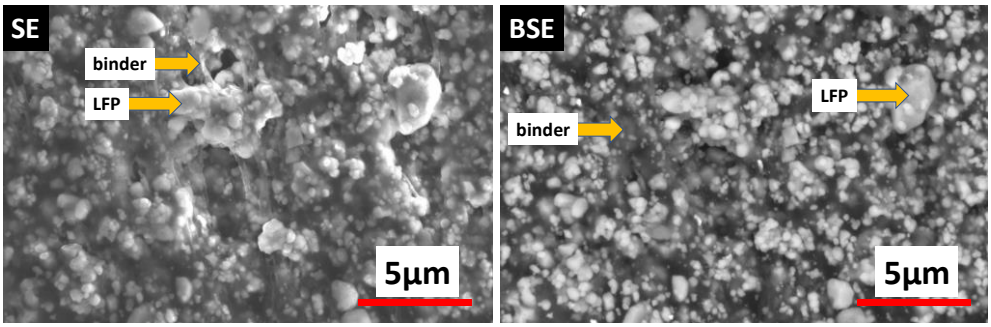

Figure 3. 43. SEM images of 55 vol. % LFP feedstock using SE and BSE detectors.

LFP green layers were obtained by extrusion moulding using a single screw extruder. The thickness of the extruded layers was 0.5 mm, while the width slightly decreased from 6 mm to 5.8 mm. Nevertheless, this contraction was homogeneous along the layer. The temperature profile of the barrel was optimized at 175/178/182/185ºC. Comparing to the programmed temperatures for extruding LTO (170, 175, 185 and 155 ºC), the temperature for LFP extrusion are, in general, higher than those for LTO. LFP feedstock presents higher viscosity than LTO for shear rates between 100 and 1000 s^{-1}, so higher temperatures were needed for the material to flow properly through the extruder.

It is to be noted that very long LFP layers were obtained, as can be seen in the picture of Figure 3. 44 (a). In fact, the extruder layers were extruded continuously and uninterruptedly at a constant screw speed of 10 mm^{-1}. This fact becomes important for industrial applications, as it leads to reduced processing time and cost. The reason for this behaviour has to do with the remarkable pseudoplastic behaviour of LFP feedstock. Thus, when the shear rate becomes zero at the end of the nozzle, the viscosity decreases drastically. The relatively high activation energy of the feedstock also contributes to increase the viscosity when the temperature decreases after extruding. Consequently, an excellent geometrical retention was achieved, as reveals the cross-section image of an extruded LFP layer in Figure 3. 44-(b). Comparing to LTO green layers (see Figure 3. 18-(b)), it can be observed that LFP layers are more homogeneous along the cross-section perimeter.

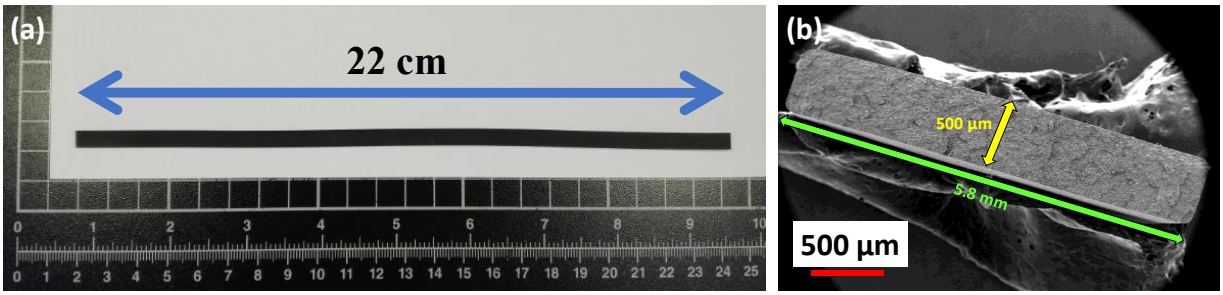

Figure 3. 44. (a) Picture of a 0.5 mm thickness LFP extruded layer. (b) SEM image of the cross-section of a 0.5 mm thickness LFP extruded layer.

3.4.3.3. Debinding

The debinding process for LFP green layers was based on the previously optimized debinding process of LTO layers (see section 3.4.2.3), as the binder composition and content are equal for both LTO and LFP green layers. Thus, the solvent debinding conditions were 50 ºC temperature and an immersion time of 1 h. However, the removal of SA and PW was calculated at different immersion times, as shows Figure 3. 45-(a). During the first minutes, the removed weight percentage of the soluble components increases drastically, and after 20 minutes a complete removal is reached.

In order to calculate the interdiffusion coefficients of the dissolution process, the model proposed by Shivashankar and German (previously explained for LTO debinding) was employed [37]. Thus, the representation of $\frac{1}{F}$ *versus* the solvent debinding time t (geometrical factor $\psi = 0.22$ mm) is plotted in Figure 3. 45-(b). During the first 5 minutes, the debinding rate is higher, leading to a loss of 92 wt. %, which means that the first stage is controlled by the dissolution of the soluble components while the second stage is governed by diffusion. This is coherent with the inclination of the slopes corresponding to the linear fittings of the points of each region.

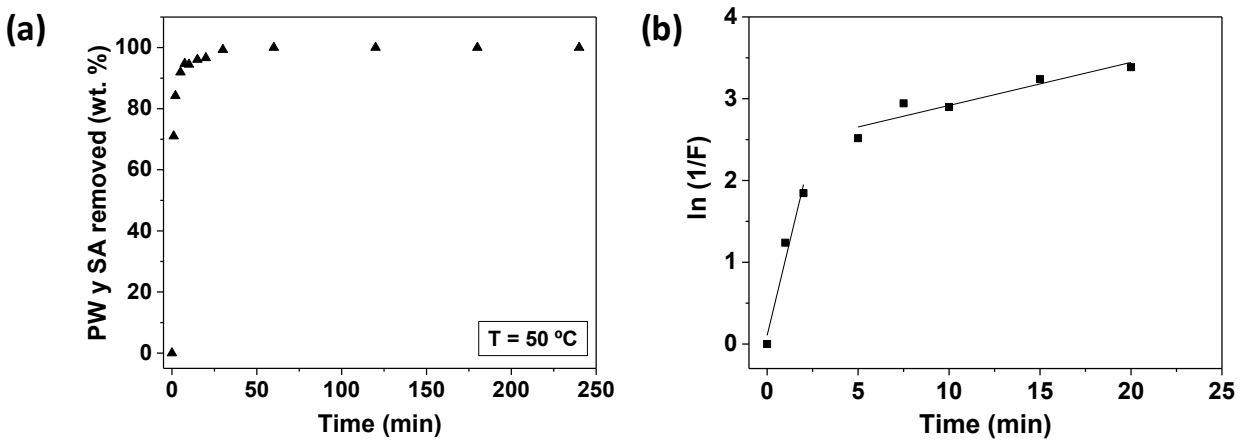

Figure 3. 45. For LFP green layers (a) PW and SA removal as a function of immersion time in n-heptane at 50 ºC and (b) representation of $\frac{1}{F}$ *versus* solvent debinding time at 50 ºC. The linear fittings in the two regions of the graphics are included.

The interdiffusion coefficients of the dissolution-controlled and diffusion-controlled stages are calculated and are compared with those of LTO in Table 3. 8. As expected, the coefficient for the first stage is higher than the one for the second stage, as the dissolution is a faster process than diffusion. By comparing the results for LTO and LFP at 50 ºC, it must be noticed that the interdiffusion coefficients are higher for LPF in both stages, which means that the solvent debinding process is faster in LFP layers than in LTO ones. This could indicate that the adhesion between the binder and the powder is stronger for the LTO feedstock probably due to the absence of a carbon coating around the ceramic particles.

Table 3. 8. Interdiffusion coefficients of stearic acid and paraffin wax in n-heptane in green LTO and LFP layers.

	D_e (cm^2/s)		
	LTO		**LFP**
	30 ºC	50 ºC	50 ºC
1st stage	$5.78 \cdot 10^{-8}$	$5.83 \cdot 10^{-8}$	$4.53 \cdot 10^{-7}$
2nd stage	$5.20 \cdot 10^{-10}$	$1.10 \cdot 10^{-9}$	$2.58 \cdot 10^{-8}$

The completed removal of SA and PW was checked by comparing DSC curves of the green LFP layers before and after the immersion. As can be observed in Figure 3. 46, before the solvent debinding, three endothermic peaks were obtained. The two peaks at low temperatures (44 and 60 °C) were assigned to the paraffin wax melting. These two peaks are not observed in the curve obtained for the material after the solvent debinding, so it can be concluded that the paraffin wax was eliminated. The endothermic peak corresponding to the melting of the SA is not detected

probably due to the low amount of this compound in the layer. On the other hand, a peak appears at 151 °C before the debinding process and at 164 °C after the n-heptane immersion. Both signals are related to the endothermic melting process of polypropylene. The shift of the peak is attributed to the plasticizer effect of paraffin wax in polypropylene.

After solvent debinding, a thermal cycle was carried out in order to degrade the remaining PP in the binder. As the same binder is used for preparing LFP and LTO feedstocks, the same thermal debinding cycle of LTO was used for LFP layers.

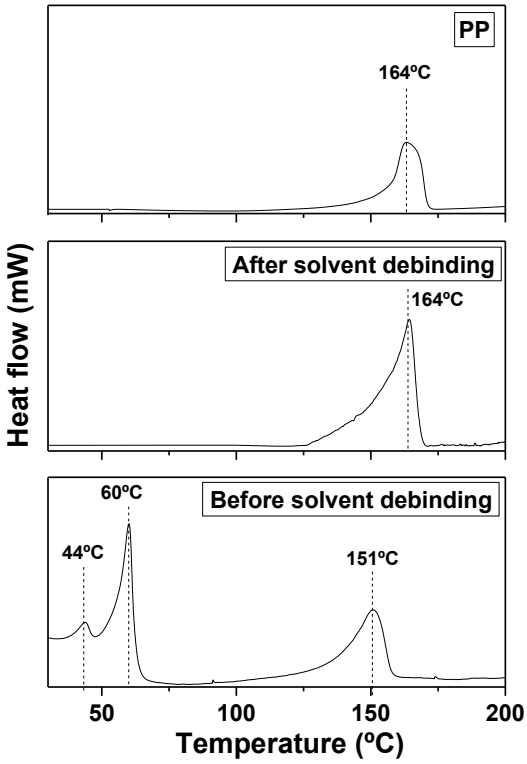

Figure 3. 46. DSC curves for pristine polypropylene and green LFP layer before and after 1 h immersion in n-heptane at 50 ºC.

All thermal treatments were performed under N_2 atmosphere to prevent Fe^{2+} oxidation and carbon combustion. Elemental analysis of five different samples after debinding (carbon content (2.10 ± 0.03) wt. %) confirmed that the carbon content is not only maintained, but also increased in comparison with the starting LFP powder ((1.7 ± 0.01) wt. %). This fact is explained by the incomplete decomposition of the PP, which leaves some residual carbon in the material. Eventually, the absence of polymer after the debinding step was verified by SEM, as can be observed in Figure 3. 47. The powder was homogeneously distributed, and a with high porosity is expected due to the absence of binder.

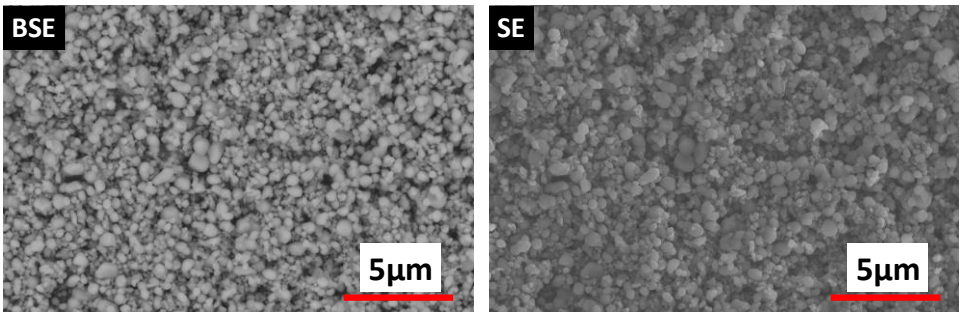

Figure 3. 47. SEM images of LFP brown electrodes after the debinding under N_2 and using SE and BSE detectors.

3.4.3.4. Sintering

LFP brown parts were sintered at temperatures between 550 and 850 ºC for 2 hours. Analogously to LTO, a slow heating rate (2 ºC/min) was used for preventing the bending of the layers. The density of the materials was determined by the Archimedes method, helium pycnometry and SEM images. On the other hand, the structure and composition were determined by XRD. Elemental carbon analysis was carried out to confirm the retention of the initial carbon content and TEM was employed to check the preservation of the carbon coating. Finally, the conductivity was evaluated by IS.

3.4.3.4.1. Density and shrinkage

The density of the sintered materials was measured by the Archimedes method and resulted to be practically the same for all sintering temperatures, with an average value of 65 % with respect to the theoretical one, as illustrated in Figure 3. 48-(a). In addition, helium pycnometric density was measured and in all cases the density value was 3.58 ± 0.01 g/cm^3, very close to the theoretical one (3.57 ± 0.01 g/cm^3). This indicates that all the porosity in the material is open and, thus, the porosity of the electrode can be calculated as the difference between the theoretical density and the density measured by Archimedes, resulting in a total porosity of 35 %.

The geometry of the electrodes was retained after sintering and, contrary to LTO electrodes, a constant thickness of 0.5 mm was measured along the layer (Figure 3. 48-(b)). As mentioned before, this good geometry retention has to do with the strong pseudoplastic behaviour of the feedstock, which allows increasing quickly the viscosity of the feedstock when it comes out of the nozzle.

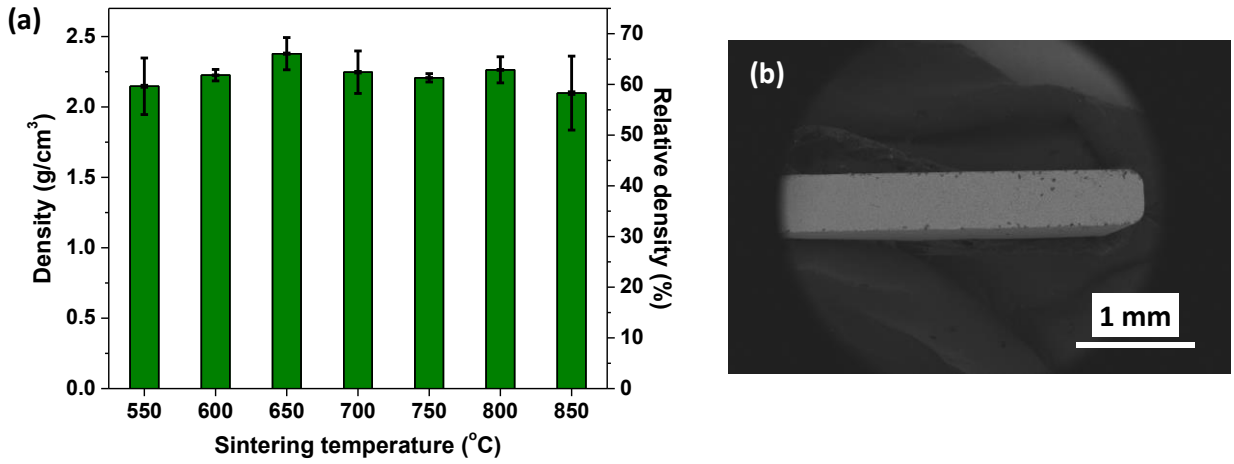

Figure 3. 48. (a) Density and relative density values for extruded LFP electrodes sintered between 550 and 850 ºC. (b) Cross-section SEM image of sintered LFP electrode at 650 ºC.

The microstructure of extruded LFP electrodes sintered between 550 and 850 ºC are shown in Figure 3. 49 and compared with the starting LFP powder as reference. The microstructure of the extruded samples sintered at different temperatures is very similar, presenting a high porosity. However, from 750 ºC to 800 ºC a small grain growth is observed and at 850 ºC bigger grains are clearly seen. Nevertheless, below 750 ºC negligible variation was observed in the particle size of the extruded materials compared to the starting LFP powder, which is in good agreement with the constant density values measured at different sintering temperatures. The lack of sintering of LFP particles can be explained by the presence of the carbon coating. Lin *et al.* compared the effect of carbon coating on the microstructure of LFP particles prepared by sol-gel method. They found much larger particles and density in the sample without carbon. On the other hand, the samples with carbon presented very high porosity and small particle size [60]. In the case of the high thickness extruded LFP electrodes, high porosity is necessary to achieve the liquid electrolyte infiltration into the pores and enable all the active material participate in the electrochemical reactions. Moreover, small particles are preferred to larger ones, due to high surface area favouring the contact with electrolyte and lithium diffusion will be shorter during the discharge-charge process and the specific surface area will be higher.

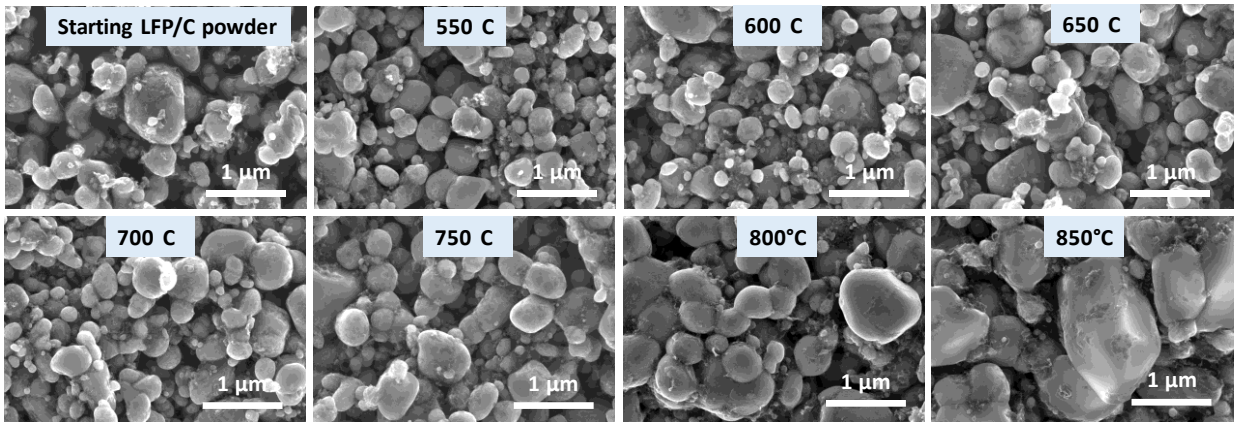

Figure 3. 49. SEM images of starting LFP powder and extruded LFP electrodes sintered between 550 and 850 ºC.

3.4.3.4.2. X-ray diffraction

XRD experiments were performed for the extruded layers sintered at temperatures between 550 and 850 ºC and compared with the diffraction pattern of the commercial LFP powder (Figure 3. 50). For sintering temperatures between 550 and 800 ºC, the diffraction peaks of the patterns are assigned to $LiFePO_4$ and no evidence of any secondary phase was detected. However, at 850 ºC, the main diffraction peak of a secondary phase is observed and identified as iron phosphide Fe_2P, (JCPDS #89-3680). In addition, as it can be observed in the SEM image of Figure 3. 50-(b), small particles with bright contrast are clearly distinguished in BSE micrograph of samples sintered at 850 ºC, indicating the presence of segregated secondary phase. EDS analysis of this bright particles indicate that Fe/P atomic ratio is 1.95 which is compatible with Fe_2P phase as revealed also by XRD. On the other hand, darker particles Fe/P atomic ratio was 1.03, which corresponds to LFP.

Iron phosphide segregation during LFP sintering commonly occurs in presence of carbon and in inert atmosphere at high sintering temperatures (> 700 ºC), and it is attributed to the reducing character of the carbon [61,62]. The presence of iron phosphides can improve the electronic conductivity of LFP electrodes due to the metallic nature of iron phosphides [63]. Lin *et al.* studied the influence of the presence of iron phosphides (FeP, Fe_2P, Fe_3P) in the electrochemical performance of LFP electrodes. They concluded that a suitable amount of these compounds (~ 3.7 wt. %) favours the reaction kinetics and the high rate performance of the electrode. However, high quantity (~ 16 wt. %) slows the kinetics and leads to poor electrochemical performance, as iron phosphides are not electrochemically active toward Li insertion/deinsertion [49]. In this context, even if the presence of an appropriate amount of Fe_2P could be beneficial for the electrochemical response of the electrode, it is out of the scope of this

work to include this variable. Moreover, above 850 ºC the particle growth observed by SEM could be detrimental for the material, reducing the specific surface area and probably damaging the carbon coating. Thus, sintering temperatures above 850 ºC will be avoided.

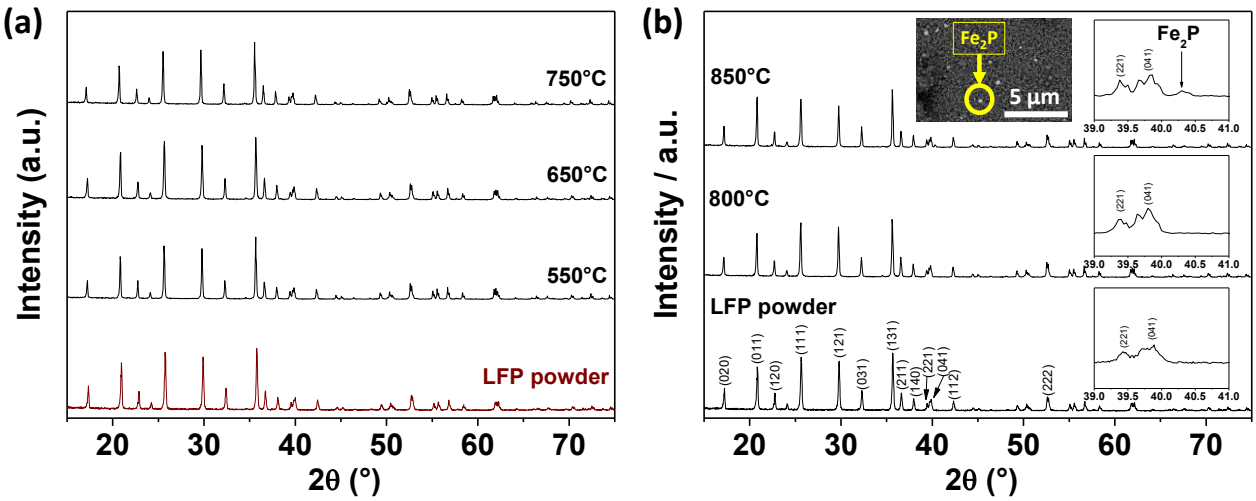

Figure 3. 50. (a) XRD diffraction patterns of starting LFP powder and extruded LFP electrodes sintered under N_2 at (a) 550, 650 and 750 °C and (b) at 800 and 850 °C. Fe_2P secondary phase is marked in the figure inset as (↓). A SEM image of extruded LFP electrode sintered at 850 ºC is also included.

3.4.3.4.3. Carbon content and distribution

Elemental carbon analysis was performed in the sintered electrodes. Figure 3. 51 shows the results from the elemental analysis of samples sintered at different temperatures. The carbon content of the commercial LFP powder and the brown material are also included in the representation. As explained before, the carbon content increases from 1.7 wt.% (commercial LFP powder) to 2.1 wt.% after debinding due to the incomplete PP decomposition. Then, the materials are sintered at different temperatures and, as observed in Figure 3. 51, the same carbon content measured after debinding is obtained. This means that during the sintering process no carbon loss occurs.

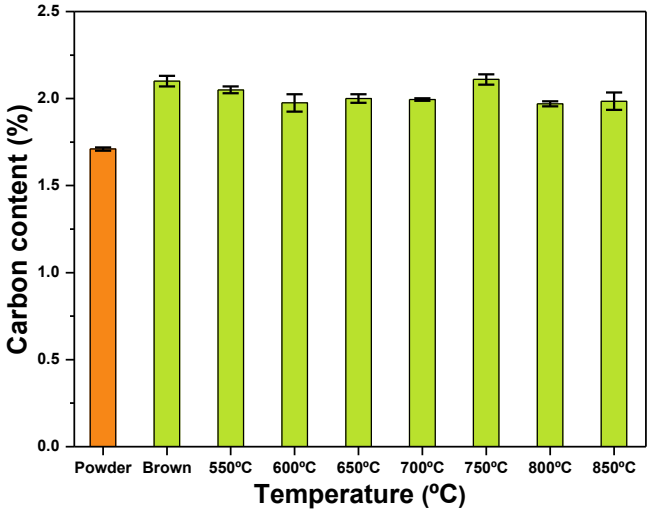

Figure 3. 51. Carbon content of commercial LFP powder ("powder"), LFP samples after the debinding ("brown") and LFP electrodes sintered from 550 to 850 ºC.

HR-TEM images of a particle of starting LFP powder and a particle of extruded LFP layer sintered at 650 °C are compared in Figure 3. 52. In both cases, crystalline $LiFePO_4$ is well distinguished from the amorphous carbon layer, which covers the ceramic particle. The carbon coating was homogeneous in both cases and its thickness was ~3 nm. The thickness of the electrode carbon coating is usually minimized in order to reduce the inactive carbon content. Carbon coatings of just ~2 nm thickness homogeneously distributed were reported to be sufficient for achieving high electronic conductivity and good electrochemical performance [64]. The results evidence that the carbon coating is preserved during the extrusion process and that it has an adequate thickness.

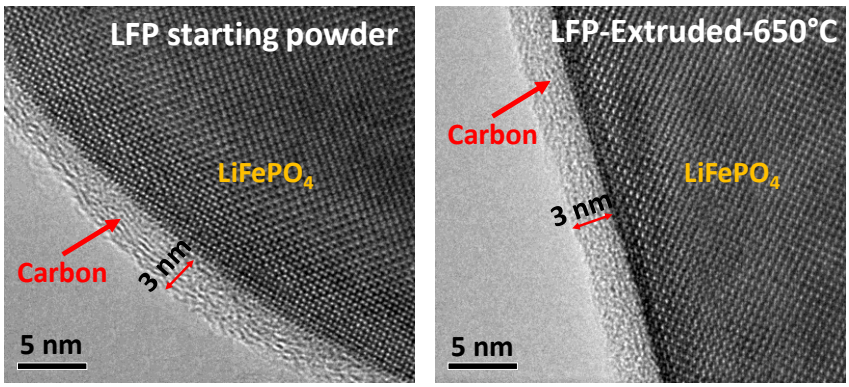

Figure 3. 52. HR-TEM images of a particle of starting LFP powder (left) and extruded LFP electrode sintered at 650 ºC (right).

3.4.3.4.4. Impedance spectroscopy

The impedance of a sintered LFP electrode (sintering temperature 800 ºC) was measured by IS in order to check the conductivity of the material. For that, gold blocking electrodes were employed, and the measurement was performed in the frequency range between 0.1 Hz and 10 MHz with an input signal amplitude of 100 mV. The obtained Nyquist plot for the impedance and real admittance (Y') as a function of the frequency are collected in Figure 3. 53.

In the Nyquist diagram (Figure 3. 53-(a)) most of the data points are in the intersection with the abscissa axis at ~ 70 Ω·cm, indicating an electronic conductor behaviour. The admittance response at variable frequency (Figure 3. 53-(b)), shows a DC *plateau* at $1.4 \cdot 10^{-2}$ S/cm in all the frequency range. Thus, the electrode behaves as a pure resistor and no ionic contribution is detected but probably masked by the electronic contribution.

The high electronic conductivity of the electrode can be attributed to the carbon content of the material (2.1 wt. %) and to the homogeneous carbon coating of the particles, previously observed by TEM. Therefore, the LFP particles are electrically connected, leading to a continuous pathway for electron motion through the material. This is very important for a good electrochemical response of the cathode in a lithium-ion battery, as ensures that all the LFP particles participate in the charge transfer reactions during the charge and discharge of the battery.

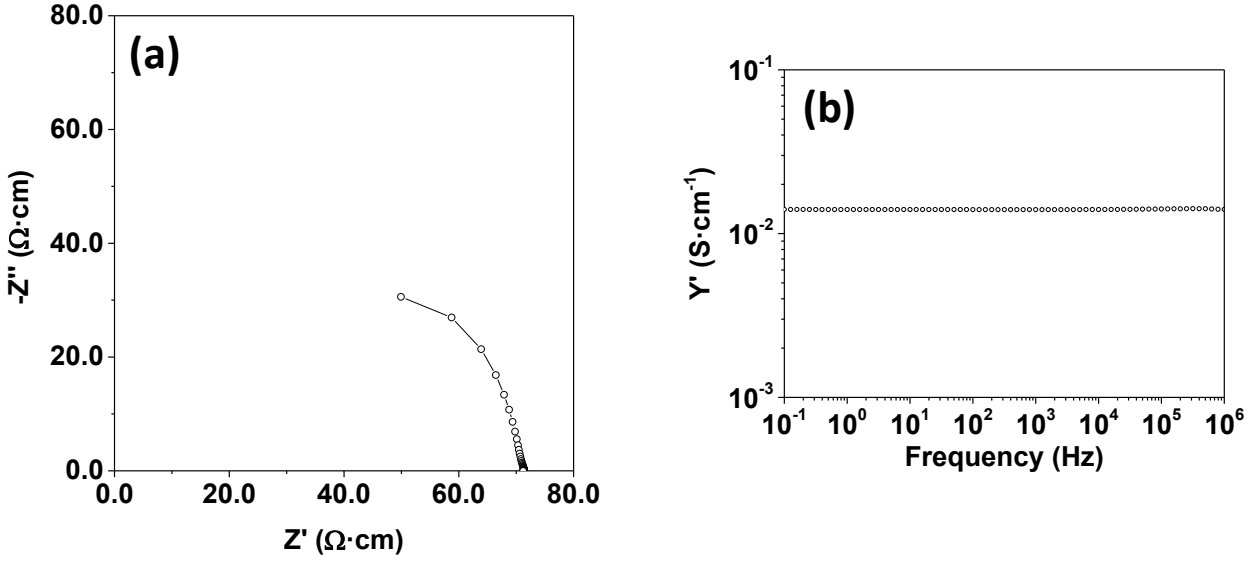

Figure 3. 53. For an extruded LFP electrode sintered at 650 ºC (a) Nyquist plot for complex impedance and (b) real admittance (Y') for variable frequency.

3.4.3.5. Application to lithium-ion batteries

The electrochemical performance of sintered LFP samples (labelled as LFP-extruded) was analysed by means of chronopotentiometry and compared with a composite electrode used as reference (labelled as LFP-composite), using lithium half cells. The influence of the processing and the sample thickness on the electrochemical activity of the cathodes was evaluated. Furthermore, the effect of the electrolyte viscosity, the sintering temperature and the cut-off voltage on the electrodes capacity was studied. Eventually, the impedance of a sintered electrode was studied at different discharge states of the battery.

3.4.3.5.1. Electrochemical performance dependence on processing and on samples thickness

In order to check the influence of PEM on the LFP powder, an extruded sample sintered at 600 ºC was grinded in an agate mortar and its electrochemical performance was tested as composite electrode and compared with that of the conventional LFP powder, used as the reference electrode. In both cases the LFP-composite electrodes were prepared using a mixture of active powder and additives. The ratio between these additives and active material was the same in both electrodes: 80 wt. % of active material, 7.5 wt. % of acetylene black, 7.5 wt. % of graphite and 5 wt. % of Teflon. Figure 3. 54-(a) shows the corresponding charge/discharge curves for the first cycle at a low C rate (C/20). Both samples exhibit a flat voltage *plateau* at 3.48 and 3.39 V for the charge and discharge, respectively. Moreover, a similar low hysteresis is observed. Both materials have a reversible capacity of 162 $mA \cdot h \cdot g^{-1}$, corresponding to a lithium uptake of 0.95 Li per $LiFePO_4$, and display similar cycling behaviour (Figure 3. 54-(b)) confirming again that the manufacturing process, here proposed, does not modify the original characteristic of the starting powders.

Figure 3. 54-(c) depicts the typical charge-discharge curves, achieved respectively at C/20 and C/100 for an LFP-extruded electrode sintered at 600 ºC. The shape of the curve is basically the same than that of the conventional composite electrodes prepared with the starting powder (Figure 3. 54-(a)). A reversible gravimetric specific capacity of about 170 $mA \cdot h \cdot g^{-1}$, close to the theoretical one, is obtained. This suggests that most of the active material in the 0.5 mm thickness electrode is electrochemically active. While the lithiation process carried out at C/100 takes place at a potential value close to the composite electrodes ones, the charge process at C/20 indicates the existence of a slight polarization phenomenon (3.55 V instead of 3.48 V vs. Li^+/Li) probably due to a much lower carbon content compared to composite electrode and to the higher thickness of the extruded material.

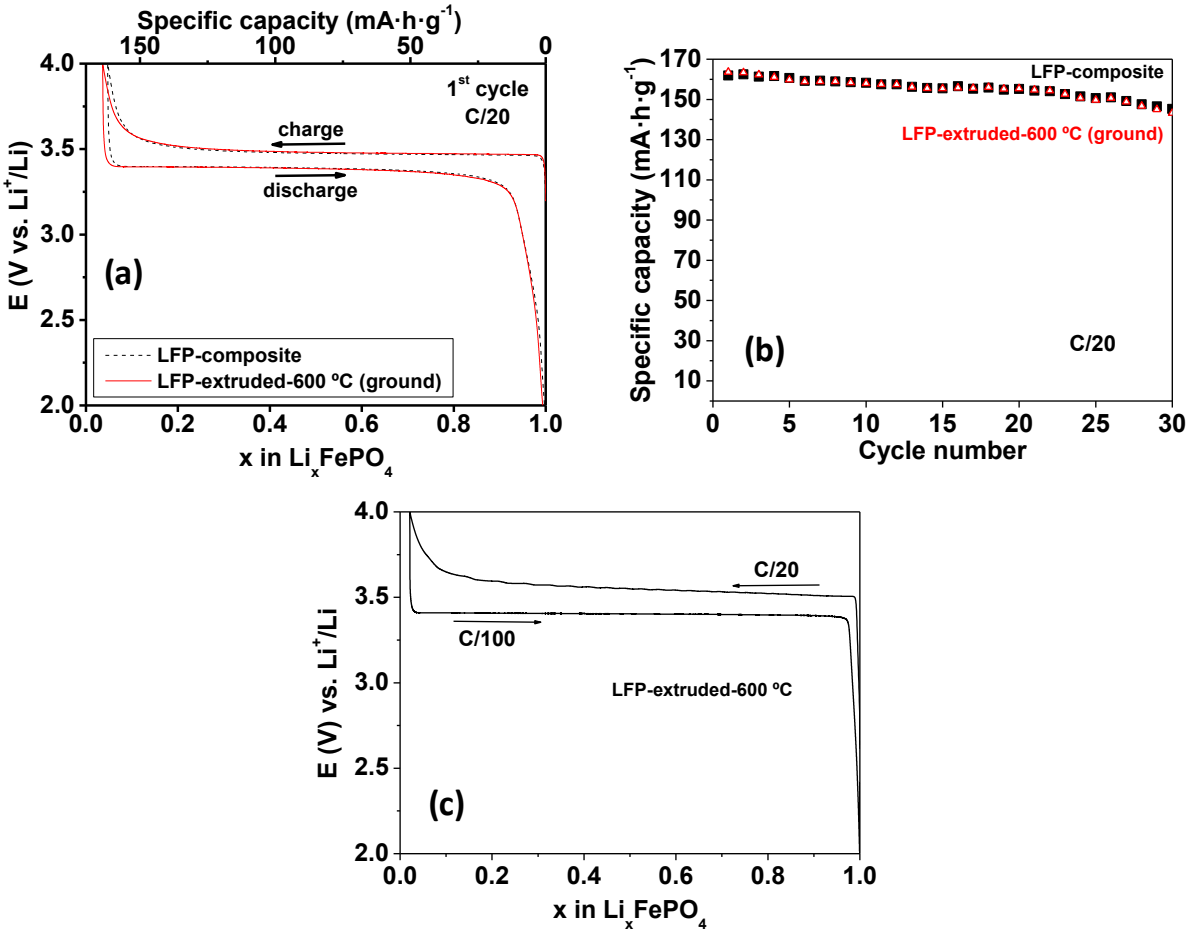

Figure 3. 54. (a) Charge/discharge first cycles registered at C/20 in 1M $LiClO_4$ in PC for the starting LFP powder electrode (dashed black curve) and for a ground-600°C extruded LFP powder electrode (full red curve). (b) Capacity evolution as a function of cycle number at C/20 for a ground-600 ºC extruded LFP powder electrode (empty markers) and for the starting powder composite LFP electrode (full markers). (c) First charge (C/20) and discharge (C/100) curves registered in PC/$LiClO_4$ 1 mol L^{-1} for a 600°C extruded LFP 0.5 mm thick electrode.

This hypothesis is confirmed by the evolution of the cycling curves as the C rate increases (Figure 3. 55-(a)). The hysteresis between charge and discharge rises from 340 mV to 900 mV while C rate increases from C/10 to C/2. Because of this, the system reaches the upper cut-off voltage before the end of the charge process. Hence, the higher the C rate the lower the efficiency of the charge that drastically impacts the recovered available capacities (118, 94 and 10 mA·h/g for respectively C/10, C/5 and C/2). Besides, at C rates exceeding C/2, the polarization of the electrode is so high that no capacity is achieved.

By reducing the sample thickness to 0.3 mm (Figure 3. 55-(b)), obtained by polishing the 0.5 mm thickness electrode, electrode kinetics are markedly improved. At C/10, the capacity increases (from 118 to 138 mA·h/g) and the polarization decreases (from 330 to 280 mV). At higher C rates, while the hysteresis remains about the same, capacity values are also significantly improved (112 mA·h/g at C/5 and 41 mA·h/g at C/2).

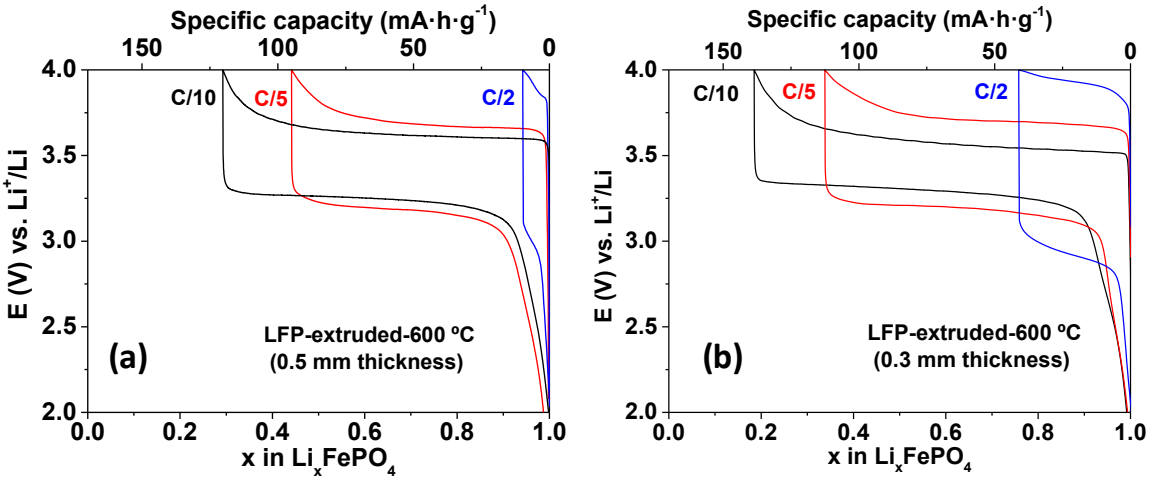

Figure 3. 55. Charge/discharge curves registered in 1M $LiClO_4$ in PC at C/10 (black), C/5 (red) and C/2 (blue) with a (a) 0.5 mm thickness and a (b) 0.3 mm thickness LFP-extruded-600ºC electrodes.

3.4.3.5.2. Dependence of LFP-extruded electrodes performances on electrolyte viscosity

Besides unoptimized electronic contacts in these extruded electrodes, another limitation might arise from their unoptimized impregnation with the electrolyte, especially as their thickness increases. In order to assess the dependence on LFP-extruded electrode performances on their wetting by the electrolyte, we have compared two electrolytes. The cycling curves presented so far have been recorded using a molar solution of $LiClO_4$ in propylene carbonate (PC). This solvent has, at 25°C, a viscosity higher than the usual electrolytes based on mixtures of carbonates [23]. For these reasons, we have tested the electrochemical performances of our extruded electrodes in a molar solution of $LiClO_4$ in a mixture of propylene carbonate (PC), ethylene carbonate (EC) and dimethyl carbonate (DMC) (1/1/1 in volume).

Figure 3. 56-(a) clearly depicts the advantages of using the ternary electrolyte. Higher capacities than with the PC electrolyte (see Figure 3. 55-(a)) are reached, with an improvement of 30 – 50 %. For the lowest C rates, values comparable to those obtained with the LFP-composite electrode are obtained (156 and 137 mA·h/g compared to 158 and 146 mA·h/g respectively at C/10 and C/5). However, as soon as the current densities exceed C/2, this ternary electrolyte does not enable the decrease in polarization and available capacities, although improved, always remain lower than those obtained in the case of the LFP-composite electrode. As a conclusion, a decrease in the viscosity of the electrolyte led to improved performances that we ascribe to a better penetration of the electrolyte and to a decreased polarization, improving the rate capability of the

0.5 mm thick extruded material. In this way, all the experiments that follow were carried out using the ternary electrode (1 M $LiClO_4$ in PC/EC/DMC).

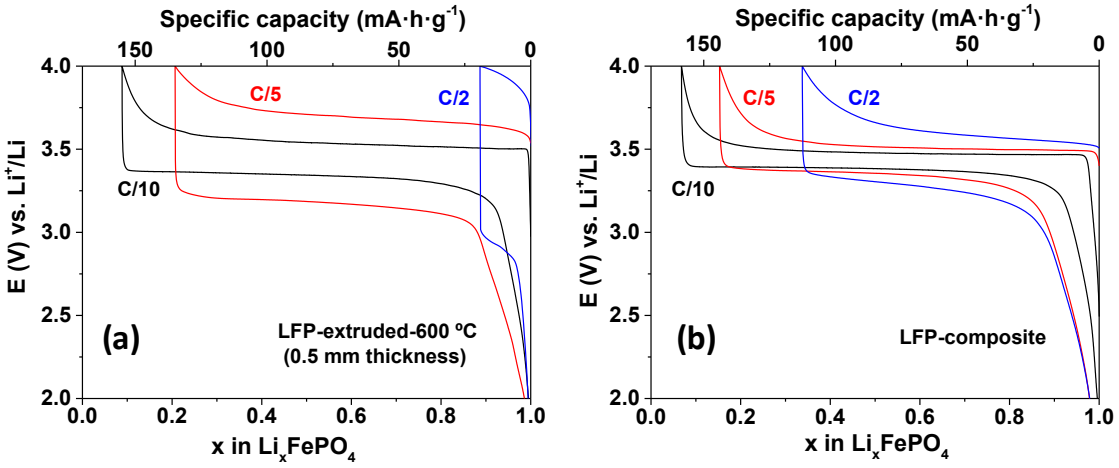

Figure 3. 56. Charge/discharge curves registered in 1M $LiClO_4$ in PC/EC/DMC for (a) a 0.5 mm thickness LFP-extruded-600°C electrode and for (b) an LFP-composite electrode at C/10 (black), C/5 (red) and C/2 (blue).

3.4.3.5.3. Dependence of LFP-extruded electrodes performances on the sintering temperature

The effect of the sintering temperature of extruded electrodes on electrochemical performances has also been studied. Cycling curves registered at C/5 for different sintering temperatures are shown in Figure 3. 57-(a). The lowest temperature of 550 °C leads to a limited capacity of 120 mA·h/g at C/5, against 130 mA·h/g and more for 600-650 °C. A higher polarization is also observed (about 850 mV against 600 mV for 600 and 650 °C, respectively). When the sintering temperature is fixed at 750 °C, polarization is quite the same as those observed for 600 or 650 °C while the capacity is lower, comparable to the capacity obtained for 550 °C. On contrary, the electrode sintered at the highest temperature of 850 °C is unable to deliver any capacity.

These results can be correlated to the electrodes morphologies previously discussed. Indeed, SEM images (Figure 3. 49) highlighted that in the case of 850 °C, the biggest particle size was obtained. This large grain size could make the carbon coating thinner or heterogeneous, so that the continuous pathway for electronic conduction could be interrupted, worsening the electrochemical response of the electrode. The larger LFP grain size also has a detrimental effect on the kinetics of lithium transport since the length of diffusion pathway increases. Moreover, the XRD pattern indicated the presence of Fe_2P in the electrode sintered at 850 °C (see Figure 3. 50) that is known to be non-active for lithium insertion/extraction.

On the other hand, at C/5, between all the extruded electrodes, the one sintered at 650 °C presented the highest capacity values. However, at C/2 the extruded materials presented very low capacity associated to high polarization (Figure 3. 57-(b)). Hence the sample sintered at 650 °C was selected as the one with the best electrochemical response at low C rates (C/10 and C/5) and was used for further characterizations.

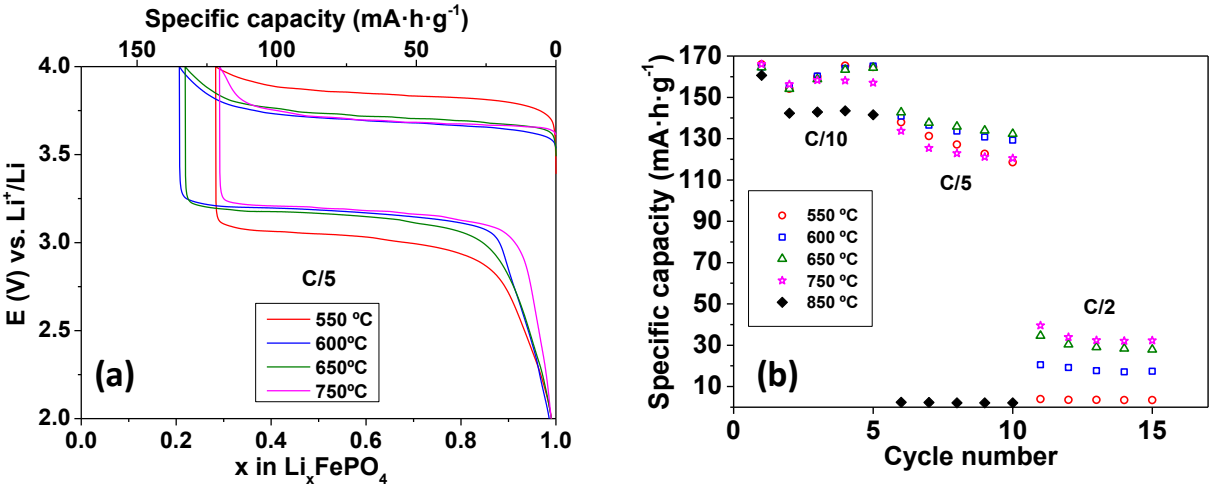

Figure 3. 57. Influence of sintering temperature for 0.5 mm thickness LFP-extruded electrodes in 1M $LiClO_4$ in PC/EC/DMC on (a) the shape of cycling curves registered at C/5 and on (b) rate capability.

As the self-supported LFP-extruded electrodes present capacities comparable to those obtained with LFP-composite electrodes (at C/10), cycle life of the two electrode formulations (LFP-extruded and LFP-composite) was evaluated. The results are reported in Figure 3. 58-(a). Clearly, at this moderate C rate, both methods allow to reach the same performances, indicating the good mechanical stability of the extruded electrode over at least 20 cycles. Moreover, the coulombic efficiency of the extruded electrode is always higher than 95 %, slightly higher than the composite one.

The capacity of the extruded and composite electrodes referred to the total mass of the electrode is represented in Figure 3. 58-(b). Due to the absence of additives and binder in the extruded electrode, the gravimetric capacity increases ~25 %.

On the other hand, the areal capacity evolution, calculated considering the mass loading of the electrodes, is plotted in Figure 3. 58-(c). It is noticeable that areal capacity is greatly enhanced. Indeed, with values between 12 and 14 $mA \cdot h \cdot cm^{-2}$, it is about 4 times higher than the composite one.

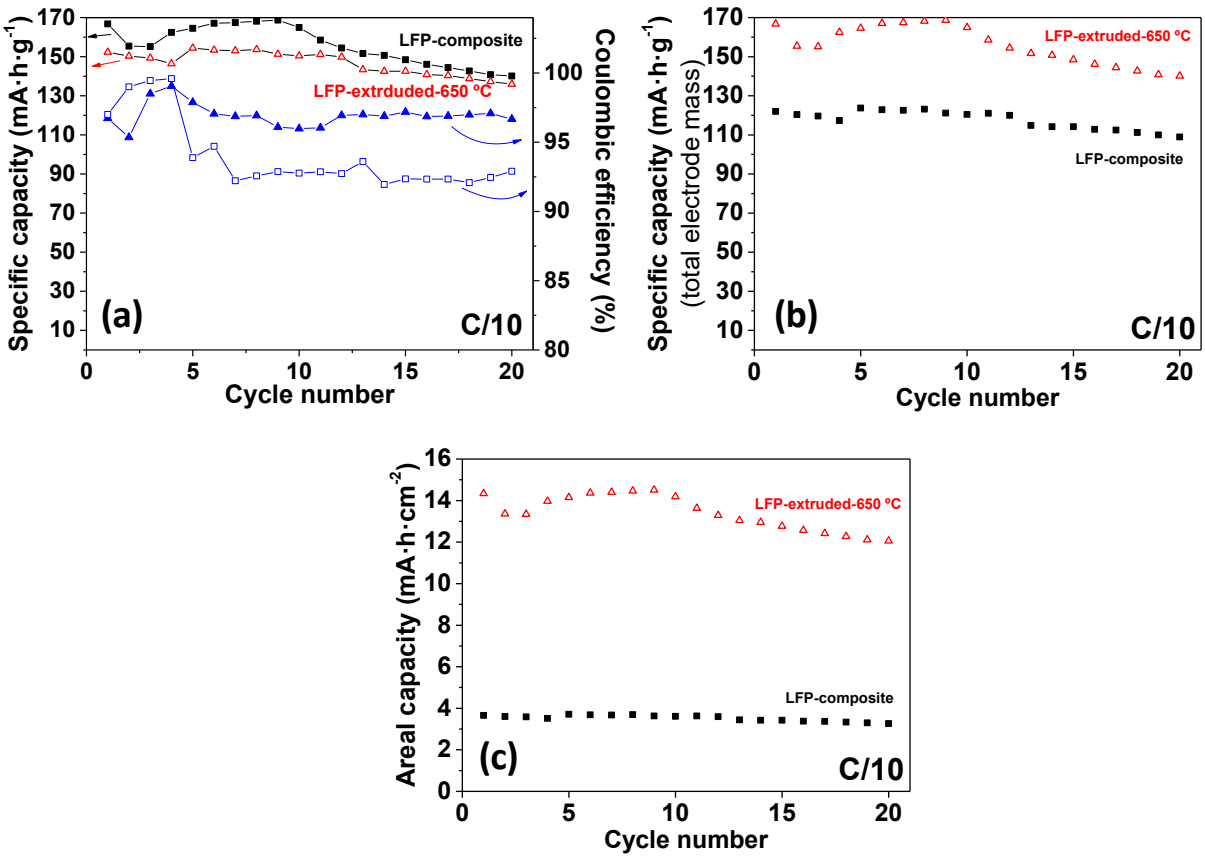

Figure 3. 58. (a) Specific capacity, (b) specific capacity referred to the total electrode mass and (c) areal capacity evolution as a function of cycle number at C/10 in 1M $LiClO_4$ in PC/EC/DMC for a 0.5 mm thickness LFP-extruded-650 °C electrode (empty red markers) and for a LFP-composite electrode (full black markers).

3.4.3.5.4. Cut-off voltage

As already mentioned, the intrinsic polarization observed in the extruded electrodes, impede the charge process at 4 V, especially at C/2. Hence, a higher oxidation voltage as new upper limit could allow to complete the charge process at C/2 and then to enhance the recovered capacity. To get a qualitative idea of the voltage limits that can be applied to the electrolyte, different density currents were applied to an electrolyte solution of $LiClO_4$ 1M in PC:EC:DMC (1:1:1 vol. %) into a coin cell, using a stainless-steel spacer and a lithium metal disc as working and negative electrodes, respectively. Figure 3. 59 shows the evolution of the potential with the time for different C rates. Around 4.7 V, a constant potential value is registered, which indicates a very significant electrolyte decomposition. In this manner, it was decided to limit the voltage to 4.5 V in order to limit the electrolyte decomposition.

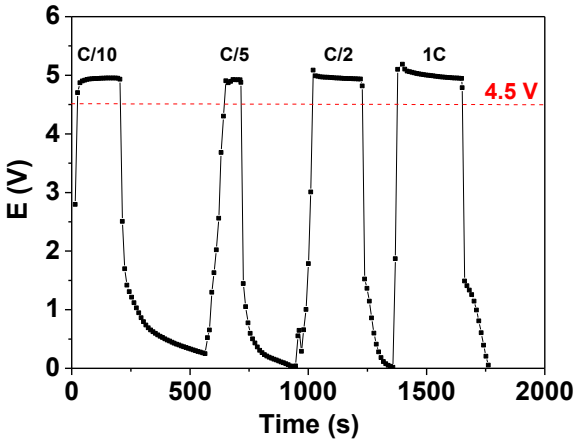

Figure 3. 59. Chronopotentiometry of an electrolyte solution of $LiClO_4$ 1M in PC:EC:DMC (1:1:1 vol. %) at different current densities for reduction and oxidation.

The rate capability of extruded 650 ºC electrodes in the enlarged 4.5 V - 2 V potential window is reported in Figure 3. 60-(b) with some of the corresponding typical cycling curves selected for C/10, C/5 and C/2. The results are compared with those achieved in the previous 4V-2V range reported Figure 3. 60-(a). For moderate C rates (C/10), no significant change in the capacity value around 165 mA·h/g is observed. However, for C/5 the capacity already increases from 138 to 156 mA·h/g. At C/2 more than twice the capacity is obtained in the extended potential range with 82 mA·h/g against about 35 mA·h/g.

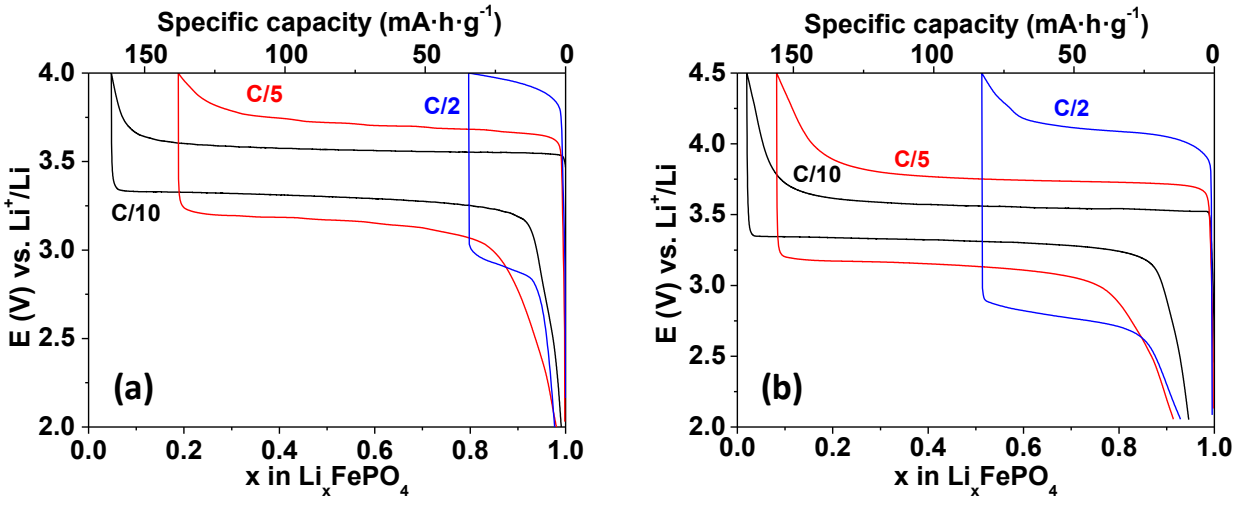

Figure 3. 60. Charge/discharge curves registered in 1M $LiClO_4$ in PC/EC/DMC with a 0.5 mm thickness LFP-extruded-650°C at C/10 (black), C/5 (red) and C/2 (blue) (a) between 2.0 V and 4.0 V and (b) between 2.0 V and 4.5 V.

3.4.3.5.5. Impedance spectroscopy

A study by IS has been carried out in a three electrodes cell, on a 0.5 mm thickness LFP-extruded-650 °C electrode, for different lithium contents in Li_xFePO_4 (with x = 0, 0.2, 0.5, 0.9 and 1). The measurements have been carried out during the second cycle. The corresponding Nyquist diagrams are represented in Figure 3. 61-(a). Such diagrams are typical of insertion compounds [65]. They all exhibit different contributions characterized by (see inset): *(1)* the electrolyte resistance R_{elec}, given by the intercept of the abscissa and the starting point of a semicircle at high frequencies; *(2)* a well-defined semicircle at high frequencies corresponding to the charge transfer resistance R_{CT}; *(3)* a Warburg region for diffusion process at medium frequencies, characterized by a 45 º line with respect to the real axis; *(4)* a quasi-vertical line ascribed to the finite diffusion at low frequencies. All these characteristic values have been determined and compared to those obtained in the case of the LFP-composite electrode, which contains exactly the same amount of active material (13.7 mg in both electrodes). At first, it can be noticed that the electrolyte resistance is comparable for both electrodes. This point is interesting because discards a possible poor contact between our self-supported electrode and the current collector due to its rigidity, hypothesis that could have explained the huge polarization observed and already discussed as soon as the C rate increases.

About the charge transfer resistance, a quite stable value of 250 Ω is obtained for $0 \leq x < 1$. It is a little bit higher for x = 1 with 282 Ω but all these values are higher, by one order of magnitude, than for the LFP-composite electrode (see Table 3. 9). This indicates a slower kinetics for the electron transfer in the extruded electrode than in the composite one, and such a discrepancy could be related with the lower carbon content in the extruded sample (2.1 wt. % against 16.7 wt. % in the composite electrode). This fact is in agreement with the evolution of the total impedance |Z| of the extruded electrode (Figure 3. 61-(b)) much higher by a factor 4, than the composite one, whatever the x value in composite. This well illustrates the difference in the electrode technology used in both cases.

Table 3. 9. Frequency at the top of the semi-circle, charge-transfer resistance and double layer capacity of for LFP-composite and LFP-extruded-650 ºC electrodes at different x values.

Electrode	x in Li_xFePO_4	f_{max} (Hz)	R_{ct} (Ω)	C_{dL} (µF)
LFP-composite	1	100.16	34	48
	0.9			
	0.5			
	0.2			
	0			
LFP-extruded	1	10.00	282	56
	0.9	12.60	251	50
	0.5			
	0.2			
	0	12.60	255	49

Besides, the characteristic frequency at the top of the semicircle (f_{max} according to the scheme Figure 3. 61-(a) inset) is in both cases independent of the lithium content in the material, being about 100 Hz for the LFP-composite electrode and close to 10 Hz for the extruded one. It is possible to deduce the double layer capacitance (C_{DL}) from this frequency and the charge transfer resistance, using the relation:

$$C_{DL} = \frac{1}{2\pi R_{CT} f_{max}}$$

The same capacitance is found, 48 µF and 50 µF for the composite electrode and for the extruded electrode, respectively. This indicates that the electroactive surface areas are equivalent for the same involved active material mass (13.7 mg) while geometrical areas are very different (ratio composite/extruded ≈ 3). This finding justifies that capacities close to the theoretical one are achieved with this kind of additive-free electrode where all the LFP grains take part to the electrochemical lithium extraction-insertion. The additive-free electrode obtained by PEM technology proposed here with our extruded LFP homogeneously and quantitatively works.

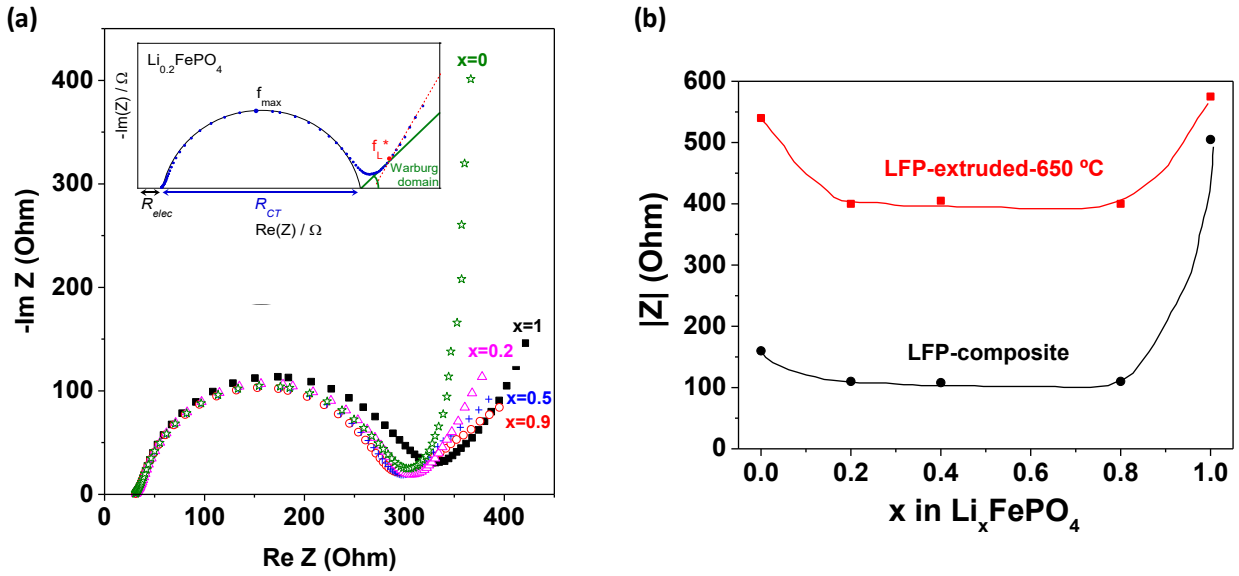

Figure 3. 61. (a) Nyquist diagrams of an LFP-extruded-650 °C electrode (S = 0.4 cm²) for different charge states. (b) Comparison of total impedance |Z| between LFP-composite electrode and LFP-extruded-650 °C electrode for different charge states.

The Warburg domain can be exploited over the composition range $0.2 \leq x \leq 0.9$, with the following equation [65]:

$$D_{Li} = \left(\frac{V_M}{\sqrt{2}\, n\, F\, S} \times \frac{dE}{dx} \times \frac{1}{A_s} \right)^2$$

where V_M is the molar volume of the compound (44.8 cm^3/mol); n the number of electron; S is the geometric surface area of the electrode (S = 0.4 cm^2); $\frac{dE}{dx}$ is the slope, at fixed x, of the curve E = f(x) (Figure 3. 54-(c)) that corresponds to the equilibrium potential composition curve and A_s the slope of the line obtained by representing Re (Z) as a function of $\frac{1}{\sqrt{\omega}}$ corresponding to the Warburg region.

For the extruded electrode, lithium diffusion coefficient around 5·10-12 cm^2/s is found in the $0.2 \leq x \leq 0.9$ composition range. The $\frac{dE}{dx}$ slope value is $8.9 \cdot 10^{-2}$ V in this range of composition corresponding to the biphasic domain where $LiFePO_4$ and $FePO_4$ coexist. It is also possible to use the limiting frequency f_L*, defined by the intercept between the Warburg line and the quasi vertical line, as illustrated in the inset Figure 3. 61-(a) using the following equation:

$$2\pi \cdot f_L^* = \frac{D_{Li}}{L^2}$$

in which L is the maximum length of the diffusion pathway corresponding to half the grain size (100 nm). Very close D_{Li} values are obtained ($8 \cdot 10^{-12}$ cm^2/s for x = 0.2 and x = 1). Higher D_{Li} values by one order of magnitude are found in the case of the starting LFP powder. We think this apparent difference in the lithium diffusion kinetics is not to be related to an intrinsic property of the LFP material but rather reflects the electrode technology used in each case.

3.4.4. Design of a lithium-ion battery with extruded $Li_4Ti_5O_{12}$ and $LiFePO_4$ electrodes

To complete the electrochemical characterization of the additive-free electrodes, an LTO-extruded/LFP-extruded Li-ion cell configuration was characterized [66]. In that way, the cell configuration is more realistic than a lithium half-cell (using lithium as negative electrode) and the result could be better compared with commercial systems.

Extruded LTO and LFP electrodes, sintered at 950 ºC in Ar/H_2 and 800 ºC in N_2, respectively, were selected as anode and cathode for the LTO/LFP full cell. The characteristics of the additive-free, LTO and LFP ceramic electrodes produced by PEM process are given in Table 3. 10. The density of the LTO and LFP electrodes, measured by Archimedes method, is 2.7 g cm^{-3} (77 % of theoretical density), and 2.3 g cm^{-3} (64 % of theoretical density), respectively. After sintering, the LTO and LFP electrodes contained 0.14 and 2.03 wt. % of carbon, respectively. The mass loading was 110 mg cm^{-2} for LTO and 90 mg cm^{-2} for LFP.

Table 3. 10. Characteristics of extruded LTO and LFP electrodes.

Electrode	Carbon content (wt. %)	Density (g/cm^3)	Porosity (%)	Mass loading (mg/cm^2)
LTO	0.14	2.7	23	110
LFP	2.03	2.3	36	90

A three-electrode configuration was selected for preparing the LTO/LFP full cell. Before measuring the electrochemical performance of the full cell, Li/LTO and Li/LFP half cells were evaluated by galvanostatic tests in order to check that this configuration is appropriate for the thick electrodes. Figure 3. 62 and Figure 3. 63 show, respectively, the electrochemical response of Li/LTO and Li/LFP half cells, employing a thin sputtered gold coating as current collector. The voltage vs. capacity profiles of selected charge-discharge cycles of the Li/LTO half cell are reported in Figure 3. 62-(a). A flat *plateau* around 1.55 V is observed. The average voltage of cell

is only slightly lower than the theoretical value, indicating similar polarization than that previously obtained in two-electrode configurations (coin cells). During the first discharge of the LTO half cell, a capacity of 143 mA·h/g is recorded. The comparison with the following delithiation cycle evidences the first cycle irreversible capacity to be only about 5.7 mA·h/g, with a relatively high coulombic efficiency (96 %) compared with commercial graphite electrodes of 90-94 % [67]. Furthermore, the voltage profiles at C/12 rate upon both the charge and discharge are practically overlapping, indicating for the high reversibility of the lithium insertion process in the following cycles. Also, a good capacity retention at 10th cycle is achieved (~101 mA·h/g, corresponding to 60 % of the nominal capacity) while the coulombic efficiency is as high as 99.7 % (Figure 3. 62-(b)). It is important to note that the capacity reached after 15 cycles at C/12 is similar to that obtained at C/24 using a two-electrodes configuration. Thus, this three-electrodes configuration seems to be more appropriate for the cell performance. These results are extremely promising considering the use of lithium metal as the counter electrode, which introduces unstable decomposition products in the electrolyte by direct chemical reactions.

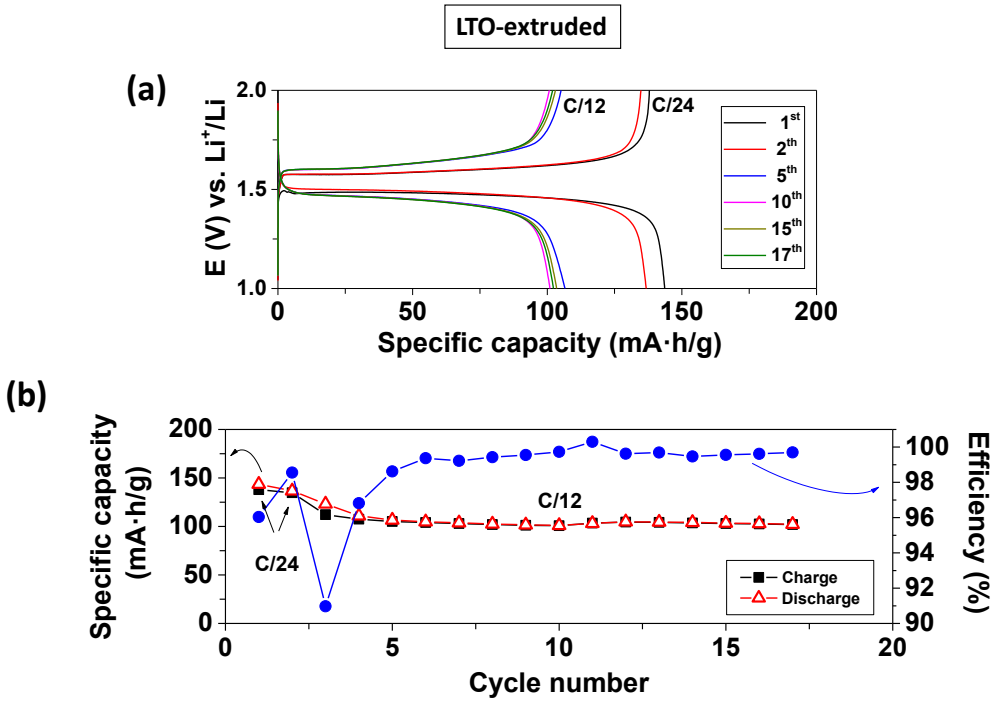

Figure 3. 62. Performance of Li/LTO-extruded half-cell in 1M $LiPF_6$ in EC:DMC (1:1, in weight). 1st and 2nd cycles at C/24 and the following at C/12. (a) Voltage vs. capacity profiles of Li/LTO at 20 ºC. (b) Specific capacity retention and coulombic efficiency upon cycling of Li/LTO-extruded.

In Figure 3. 63-(a) the voltage profiles of some selected charge-discharge cycles of the Li/LFP-extruded half cell are displayed, showing the characteristic features of LFP upon delithiation (charge) and following lithiation (discharge), i.e., a rather flat voltage *plateau* around

3.4 V. In the first cycle (C/24 rate) a discharge capacity of 142 mA·h/g is observed. Even under increasing the current density (C/12), the discharge capacity (see the 7th cycle) still reaches 123 mA·h/g, with a coulombic efficiency close to 98 % (Figure 3. 63-(b)).

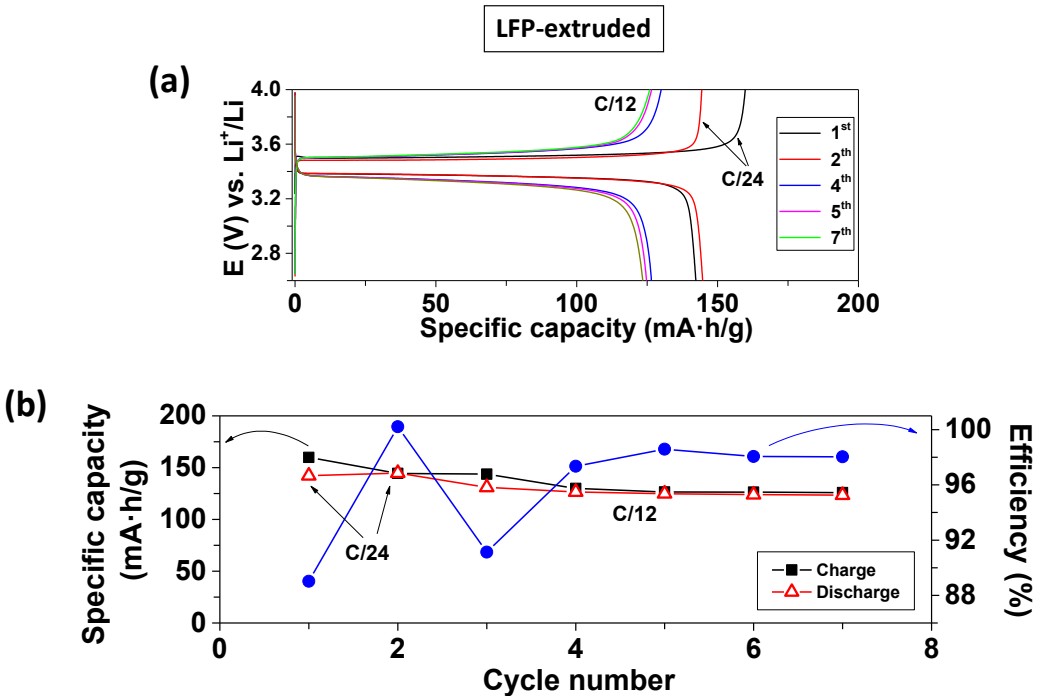

Figure 3. 63. Performance of Li/LFP-extruded half cell in 1M $LiPF_6$ in EC:DMC (1:1, in weight). 1st and 2nd cycles at C/24 and the following at C/12. (a) Voltage vs. capacity profiles of Li/LFP at 20 °C. (b) Specific capacity retention and coulombic efficiency upon cycling of Li/LFP-extruded.

The performance of the LTO-extruded/LFP-extruded lithium-ion cell upon charge-discharge tests is illustrated in Figure 3. 64. Selected cell voltage profiles are shown in Figure 3. 64-(a) while Figure 3. 64-(b) shows the capacity retention upon long-term testing carried out at two different rates, C/24 and C/12. The flat charge-discharge profiles are centred in 1.9 V. The cell delivers an initial discharge capacity of about 148 mA·h/g, which decreases, after 50 cycles, to ca. 112 mA·h/g, still corresponding to a volumetric capacity of 257 mA·h/cm^3.

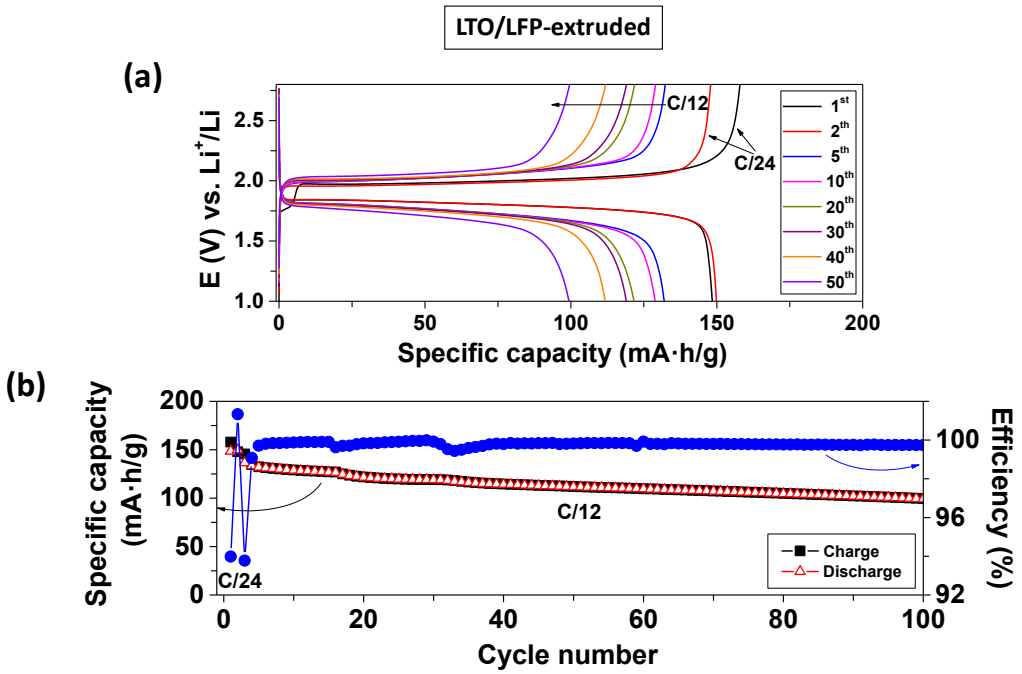

Figure 3. 64. Performance of LTO/LFP LIB in 1M $LiPF_6$ in EC:DMC (1:1 in weight). 1st and 2nd cycle at C/24 and the following at C/12. (a) Voltage *vs.* capacity profiles at 20 ºC. (b) Specific capacity retention and coulombic efficiency under cycling (the specific capacity is referred to the LFP cathode).

In summary, the electrochemical performance of the LIB composed of LTO and LFP thick self-supported extruded electrodes with a mass loading of ~100 mg/cm^2 opens the door to develop a new generation of safe LIB with high volumetric and areal capacities. The proposed manufacturing procedure of the thick, additive-free electrodes is easily scalable, allowing for the fast-commercial development of this new generation of high performance LIBs.

3.5. CONCLUSIONS

In this investigation, the optimization of the powder extrusion moulding of LTO and LFP thick layers as electrodes for lithium-ion batteries has been successfully developed. For that, a thermoplastic binder system with composition PP/PW/SA (50, 46, 4 vol. %) and LTO and LFP commercial powder were employed. The different steps of the process were optimized, and the main conclusions are summarized:

- In the mixing step, the powder loading of the LTO and LFP feedstocks was optimized using torque measurements and feedstocks with a powder loading of 55 vol. % for both materials were successfully processed. By capillary rheology it was determined that the selected mixtures presented a pseudoplastic behaviour and a viscosity lower than 1000 Pa·s, being suitable for extrusion moulding. In general terms, LFP feedstocks presented higher viscosity and more pseudoplastic behaviour than LTO ones. This could be attributed to the LFP powder carbon coating.

- During the extrusion step, the LFP layers were cooled down in air, while the LTO ones were cooled down in water (immersion), due to the lower pseudoplastic behaviour of the LTO feedstock. After extrusion, defect-free green layers of approximately 0.5/1 mm thickness, 6 mm width and different length were obtained. The microstructure of the green layers reveals a homogenous distribution of the powder in the binder.

- The removal of the paraffin wax by dissolution in n-heptane was studied in the green layers. For LFP layers, a complete removal was obtained after 1 h of immersion at 50 ºC. On contrary, for LTO layers the removal was incomplete (84 wt. %). The elimination of the rest of the binder was carried out in both cases by a thermal treatment, obtaining defect-free brown layers.

- The effect of the sintering temperature (900-1100 ºC) and sintering atmosphere (air, N_2 or Ar/H_2) in LTO electrodes were investigated in terms of composition, microstructure and electrical properties. On the other side, the effect of the sintering temperature (550-850 ºC) was studied in LFP electrodes in N_2 atmosphere. Eventually, sintered LTO and LFP were tested together in a full-cell. The main conclusions regarding to each material are specified as follows:

LTO-extruded electrodes

The density variation with the sintering temperature follows the same tendency for the three sintering atmospheres. The maximum density, already reached at 950 ºC, is 84 % and the total

open porosity is 16 %. The inspection of the electrodes by SEM revealed a homogeneous porous distribution. This porosity is necessary for the electrolyte penetration into the thick electrode in the lithium cell.

By XRD, high purity LTO is identified when oxidant or inert sintering atmospheres are used. However, in reducing atmosphere, 950 ºC is the maximum temperature without LTO decomposition. For this reason, 950 ºC was selected as the optimum sintering temperature in Ar/H_2 atmosphere.

As a consequence of an incomplete binder decomposition, some residual carbon was detected in electrodes sintered in inert and reducing atmospheres. The carbon content was higher in Ar/H_2 (0.14 ± 0.02 wt. %) than in N_2 (0.05 ± 0.02 wt. %) for electrodes sintered at 950 ºC. HR-TEM images reveals the presence of a homogeneous carbon coating of approximately 2 nm thickness in electrodes sintered in Ar/H_2. Moreover, the used of XPS allowed identify a partial reduction of Ti^{4+} to T^{3+} in those electrodes sintered in the reducing atmosphere. This, together with the presence of conductive carbon, suggests that this electrode could be the most appropriate for battery applications.

Impedance spectroscopy measurements confirmed that the maximum conductivity is reached when Ar/H_2 atmosphere is used. In this manner, the LTO electrode sintered at 950 ºC in Ar/H_2 was selected for battery tests.

The LTO-extruded electrode was tested during 20 cycles at C/24. The additive-free electrode reaches the same specific capacity than LTO-composite electrode, which means that all the active material in the extruded layer is inserting and extracting lithium. This is attributed to the interconnected porosity of the electrode, which allows the electrolyte to soak all the LTO particles. Furthermore, and as a consequence of LTO being a zero-strain insertion material, the sintered ceramic electrode retains its shape after intercalation/deintercalation cycles. It explains its remarkable cycling performance, with a 90 % of capacity retention after 20 cycles at C/24 and 88.7 % and 92.5 % after 30 cycles at C/12 and C/8, respectively.

The absence of additives maximizes the active material powder content in the electrode. As a direct consequence of this latter feature, the volumetric discharge capacity of the LTO-extruded electrode (310 $mA \cdot h/cm^3$ at C/24) is almost three times higher than that of the LTO-composite electrode (131 $mA \cdot h/cm^3$) prepared by conventional casting. This result is explained by the higher density of LTO-extruded electrode and its additive-free nature. Moreover, due to the

absence of additives and especially due to the very high thickness of our LTO-extruded electrode, the areal capacity (15.2 mA·h/cm^2) exceeds by more than one order of magnitude that of the LTO-composite electrode (1.42 mA·h/cm^2).

LFP-extruded electrodes

The density of the electrodes sintered at different temperatures is very similar and reached the maximum value of 65 %. The total open porosity is 35 % and the porous microstructure of the samples was confirmed by SEM images.

For sintering temperatures higher than 800 ºC, the segregation of Fe_2P was identified by XRD. This phase is non active for Li insertion/deinsertion.

The carbon elemental analysis revealed an increase of the carbon content from the initial LFP powder (1.7 wt. %) to the sintered electrodes (2.1 wt. %). This means that *(i)* the use of an inert-N_2 sintering atmosphere resulted successful for preventing oxidation of the LFP carbon coating and *(ii)* some residual carbon results from the incomplete binder elimination. TEM was used to confirm the preservation of the homogeneous carbon coating of ~ 3 nm after sintering.

The total conductivity of the electrode was measured by IS resulting in ~ 10^{-2} S/cm. This relatively high conductivity is attributed to the percolative and conductive carbon coating previously observed.

The LFP-extruded electrodes (0.5 mm thickness) were tested in lithium half cells and the effect of processing, electrode thickness, electrolyte viscosity and sintering temperature were investigated. It was confirmed that the manufacturing process does not affect the characteristics of the original powder. However, an increase in the electrode polarization was detected from C/10 to C/2, which can be strongly limited using thinner electrodes. The decrease in the electrolyte viscosity led to a better electrolyte penetration and decreases the polarization, improving the rate capability of the 0.5 mm thickness extruded electrode. The electrolyte 1 M $LiClO_4$ in PC/EC/DMC (1/1/1 in volume) was used for further investigations.

The highest capacity values were obtained for the LFP-extruded electrode sintered at 650 ºC. Over 20 cycles at C/10 the electrode reaches same performance than the LFP-composite electrode, indicating the good mechanical stability of the extruded material. However, due to the absence of additives and binder, the gravimetric capacity is increased by a 25 % compared to the composite electrode. Furthermore, the increase in the areal capacity is even more significant, reaching 14

$mA \cdot h/cm^2$, which is approximately 4 times the areal capacity of the composite electrode used as reference. It must be highlighted that, with roughly the same thickness, the extruded LFP demonstrates improved cycling performances compared to LTO.

LTO-extruded/LFP-extruded lithium-ion battery

A LIB using sintered LTO and LFP extruded electrodes as anode and cathode, respectively, was tested. The large mass loading of the electrodes (~100 mg/cm^2) lead to high areal (> 13 $mA \cdot h/cm^2$) and volumetric (340 $mA \cdot h/cm^3$) capacities. Thus, the manufacturing of thick additive-free ceramic electrodes by powder extrusion moulding pavs the way to a new generation of high performance LIBs.

3.6. BIBLIOGRAPHY

[1] G. R.M., B. A., Injection Molding of Metals and Ceramics, Princeton NJ: Metal Powder Industries Federation, 1997.

[2] F. Händle, ed., Extrusion in ceramics, Springer, Mühlacker, 2007.

[3] W.W. Yang, K.Y. Yang, M.H. Hon, Effects of PEG molecular weights on rheological behavior of alumina injection molding feedstocks, Mater. Chem. Phys. 78 (2002) 416–424. doi:10.1016/S0254-0584(02)00203-1.

[4] W. Ostwald, Speed function of viscosity of disperse systems I, Kolloid-Zeitschrift. 36 (1925) 99–117.

[5] A. de Waele, Viscometry and plastometry, J. Oil Colour Chem. Assoc. 6 (1923) 33–69.

[6] P. Thomas-Vielma, A. Cervera, B. Levenfeld, A. Várez, Production of alumina parts by powder injection molding with a binder system based on high density polyethylene, J. Eur. Ceram. Soc. 28 (2008) 763–771. doi:10.1016/j.jeurceramsoc.2007.08.004.

[7] P. Thomas, B. Levenfeld, A. Várez, Production of Alumina Microparts by Powder Injection Molding, Int. J. Appl. Ceram. Technol. 8 (2011) 617–626. doi:10.1111/j.1744-7402.2009.02471.x.

[8] C. Barry, M. Grant, Ceramic materials- Sienice and Engineering, 2nd ed., Springer, New York, 2013.

[9] M.W. Barsoum, Fundamentals of ceramics, Institue of Physics Publishing, Bristol and Philadelphia, 2003.

[10] J. Zhou, B. Huang, E. Wu, Extrusion moulding of hard-metal powder using a novel binder system, J. Mater. Process. Technol. 137 (2003) 21–24. doi:10.1016/S0924-0136(02)01058-0.

[11] W. Liu, Q. Cai, Y. Ma, Q. Huang, J. Zhang, Fabrication of 93W-Ni-Fe alloy large-diameter rods by powder extrusion molding, Int. J. Refract. Met. Hard Mater. 42 (2014) 233–239. doi:10.1016/j.ijrmhm.2013.09.011.

[12] M.E. Sotomayor, B. Levenfeld, A. Várez, Powder extrusion moulding of 430L stainless steel thin tubes for porous metal supported SOFCs Powder extrusion moulding of 430L stainless steel thin tubes for porous metal supported SOFCs, Powder Metall. 54 (2016) 103–107. doi:10.1179/003258909X12502679013693.

[13] Y. Fangli, W. Huanrui, Y. Jianfeng, G. Jiqiang, Effects of organic additives on microstructure and mechanical properties of porous Si_3N_4 ceramics, Bull. Mater. Sci. 33 (2011) 285–291. doi:10.1179/174367611x12989099028692.

[14] M. Trunec, Fabrication of zirconia- and ceria-based thin-wall tubes by thermoplastic extrusion, J. Eur. Ceram. Soc. 24 (2004) 645–651. doi:10.1016/S0955-2219(03)00258-9.

[15] M.E. Sotomayor, L.M. Ospina, B. Levenfeld, A. Várez, Characterization of 430L porous supports obtained by powder extrusion moulding for their application in solid oxide fuel cells, Mater. Charact. 86 (2013) 108–115. doi:10.1016/j.matchar.2013.09.020.

[16] H. Monzón, M.A. Laguna-Bercero, A. Larrea, B.I. Arias, A. Várez, B. Levenfeld, Design of industrially scalable microtubular solid oxide fuel cells based on an extruded support, in: Int. J. Hydrogen Energy, 2014: pp. 5470–5476. doi:10.1016/j.ijhydene.2014.01.010.

[17] M.E. Sotomayor, B.I. Arias-Serrano, J. Ciruelos, A. Várez, B. Levenfeld, Porous Ni-YSZ planar anodes by powder extrusion moulding employing PMMA as pore former, Powder Metall. 59 (2016). doi:10.1080/00325899.2016.1207919.

[18] B.I. Arias-Serrano, M.E. Sotomayor, A. Várez, B. Levenfeld, H. Monzón, M.A. Laguna-Bercero, A. Larrea, High-performance Ni-YSZ thin-walled microtubes for anode-supported solid oxide fuel cells obtained by powder extrusion moulding, RSC Adv. 6 (2016) 19007–19015. doi:10.1039/c5ra28183k.

[19] J.M. Amarilla, B. Levenfeld, M.E. Sotomayor, A. Varez, J.-Y. Sanchez, W. Bucheli, ES2633149-A1, ES2633149-B2, 2016; WO2017158223-A1, 2017. https://patents.google.com/patent/US20190173083A1/en?oq=varez+and+amarilla, n.d.

[20] T. Jardiel, M.E. Sotomayor, B. Levenfeld, A. Várez, Optimization of the processing of 8-YSZ powder by powder injection molding for SOFC electrolytes, Int. J. Appl. Ceram. Technol. 5 (2008) 574–581. doi:10.1111/j.1744-7402.2008.02286.x.

[21] J. Janardhana Reddy, N. Ravi, M. Vijayakumar, A simple model for viscosity of powder injection moulding mixes with binder content above powder critical binder volume concentration, J. Eur. Ceram. Soc. 20 (2000) 2183–2190. doi:10.1016/S0955-2219(00)00096-0.

[22] Y. Wang, Y. Wang, E. Hosono, K. Wang, H. Zhou, The design of a $LiFePO_4$/carbon nanocomposite with a core-shell structure and its synthesis by an in situ polymerization restriction method, Angew. Chemie - Int. Ed. 47 (2008) 7461–7465. doi:10.1002/anie.200802539.

[23] R. Dominko, M. Bele, M. Gaberscek, M. Remskar, D. Hanzel, S. Pejovnik, J. Jamnik, Impact of the Carbon Coating Thickness on the Electrochemical Performance of $LiFePO_4$/C Composites, J. Electrochem. Soc. 152 (2005) A607–A610. doi:10.1149/1.1860492.

[24] Z. Wang, G. Chen, J. Xu, Z. Lv, W. Yang, Synthesis and electrochemical performances of $Li_4Ti_{4.95}Al_{0.05}O_{12}$/C as anode material for lithium-ion batteries, J. Phys. Chem. Solids. 72 (2011) 773–778. doi:10.1016/j.jpcs.2011.03.013.

[25] J. Lin, C. Hsu, H. Ho, S. Wu, Sol – gel synthesis of aluminum doped lithium titanate anode material for lithium ion batteries, Electrochim. Acta. 87 (2013) 126–132. doi:10.1016/j.electacta.2012.08.128.

[26] S. Huang, Z. Wen, X. Zhu, Z. Lin, Preparation and Electrochemical Performance of Spinel-Type Compounds $Li_4Al_yTi_{5-y}O_{12}$ (y=0, 0.10, 0.15, 0.25), J. Electrochem. Soc. 152 (2005) A186–A190. doi:10.1149/1.1833315.

[27] J. Rodríguez-Carvajal, Fullprof Program: Rietveld Pattern Matching Analysis of Powder Patterns, Grenoble, ILL, 1990, Phiysica B. 192 (1993) 55–69.

[28] I.A. Leonidov, O.N. Leonidova, L.A. Perelyaeva, R.F. Samigullina, S.A. Kovyazina, M. V Patrakeev, Structure , Ionic Conduction , and Phase Transformations in Lithium Titanate $Li_4Ti_5O_{12}$, Phys. Solid State. 45 (2003) 2183–2188.

[29] G. Rousse, L. Le, P.J. Verne, Magnetic Structures of the Triphylite $LiFePO_4$ and of Its Delithiated Form $FePO_4$, Chem. Mater. 15 (2003) 4082–4090. doi:10.1021/cm0300462.

[30] T.-F. Yi, S.-Y. Yang, Y. Xie, Recent advances of $Li_4Ti_5O_{12}$ as a promising next generation anode material for high power lithium-ion batteries, J. Mater. Chem. A. 3 (2015) 5750–5777. doi:10.1039/C4TA06882C.

[31] H. Zhao, Y. Li, Z. Zhu, J. Lin, Z. Tian, R. Wang, Structural and Electrochemical Characteristics of $Li_{4-x}K_xTi_5O_{12}$ as Anode Material for Lithium-Ion Batteries, Chinese J. Inorg. Chem. 53 (2008) 7079–7083. doi:10.1016/j.electacta.2008.05.038.

[32] M.S. Islam, D.J. Driscoll, C.A.J. Fisher, P.R. Slater, Atomic-scale investigation of defects, dopants, and lithium transport in the $LiFePO_4$ olivine-type battery material, Chem. Mater. 17 (2005) 5085–5092. doi:10.1021/cm050999v.

[33] A. Genovese, G. Amarasinghe, M. Glewis, D. Mainwaring, R.A. Shanks, Crystallisation, melting, recrystallisation and polymorphism of n-eicosane for application as a phase change material, Thermochim. Acta. 443 (2006) 235–244. doi:10.1016/j.tca.2006.02.008.

[34] J.S. Han, C.W. Gal, J.M. Park, S.J. Park, Powder injection molding of PNN-PMN-PZN doped low temperature sintering PZT ceramics, J. Manuf. Process. 28 (2017) 235–242. doi:10.1016/j.jmapro.2017.06.008.

[35] I. Manas-Zloczower, Mixing and compounding of polymers: Theory and Practice, 2nd editio, Hanser, Munich, 2009.

[36] S. Eroglu, H.I. Bakan, Solvent debinding kinetics and sintered properties of injection moulded 316L stainless steel powder, Powder Metall. 48 (2005) 329–332. doi:10.1179/174329005X66782.

[37] T.S. Shivashankar, R.M. German, Effective Length Scale for Predicting Solvent-Debinding Times of Components Produced by Powder Injection Molding, J. Am. Ceram. Soc. 82 (1999) 1146–1152. doi:10.1111/j.1151-2916.1999.tb01888.x.

[38] J. Wolfenstine, U. Lee, J.L. Allen, Electrical conductivity and rate-capability of $Li_4Ti_5O_{12}$ as a function of heat-treatment atmosphere, J. Power Sources. 154 (2006) 287–289. doi:10.1016/j.jpowsour.2005.12.044.

[39] G. Izquierdo, A.R. West, Phase equilibria in the system Li_2O-TiO_2, Mater. Res. Bull. 15 (1980) 1655–1660.

[40] G.-N. Zhu, L. Chen, Y.-G. Wang, C.-X. Wang, R.-C. Che, Y.-Y. Xia, Binary $Li_4Ti_5O_{12}$-$Li_2Ti_3O_7$ Nanocomposite as an Anode Material for Li-Ion Batteries, Adv. Funct. Mater. 23 (2012) 640–647. doi:10.1002/adfm.201201741.

[41] Y. Wang, H. Liu, K. Wang, H. Eiji, Y. Wang, H. Zhou, Synthesis and electrochemical performance of nano-sized $Li_4Ti_5O_{12}$ with double surface modification of Ti(III) and carbon, J. Mater. Chem. 19 (2009) 6789–6795. doi:10.1039/b908025b.

[42] Y. Zhao, C. Wu, J. Li, L. Guan, Long cycling life of Li_2MnSiO_4 lithium battery cathodes under the double protection from carbon coating and graphene network, J. Mater. Chem. A. 1 (2013) 3856–3859. doi:10.1039/c3ta01521a.

[43] S.L. Chou, J.Z. Wang, C. Zhong, M.M. Rahman, H.K. Liu, S.X. Dou, A facile route to carbon-coated SnO_2 nanoparticles combined with a new binder for enhanced cyclability of Li-ion rechargeable batteries, Electrochim. Acta. 54 (2009) 7519–7524. doi:10.1016/j.electacta.2009.08.006.

[44] J. Liu, T.J. Richardson, X. Song, L. Yang, T.E. Conry, M.M. Doeff, Spherical nanoporous $LiCoPO_4$/C composites as high performance cathode materials for rechargeable lithium-ion batteries, J. Mater. Chem. 21 (2011) 9984. doi:10.1039/c1jm10793c.

[45] M.C. Biesinger, L.W.M. Lau, A.R. Gerson, R.S.C. Smart, Resolving surface chemical states in XPS analysis of first row transition metals, oxides and hydroxides: Cr, Mn, Fe, Co and Ni, Appl. Surf. Sci. 257 (2010) 887–898. doi:10.1016/j.apsusc.2010.10.051.

[46] M.S. Song, A. Benayad, Y.M. Choi, K.S. Park, Does $Li_4Ti_5O_{12}$ need carbon in lithium ion batteries? Carbon-free electrode with exceptionally high electrode capacity, Chem. Commun. 48 (2012) 516–518. doi:10.1039/c1cc16462g.

[47] K. Zaghib, M. Dontigny, A. Guerfi, P. Charest, I. Rodrigues, A. Mauger, C.M. Julien, Safe and fast-charging Li-ion battery with long shelf life for power applications, J. Power Sources. 196 (2011) 3949–3954. doi:10.1016/j.jpowsour.2010.11.093.

[48] W.T. Li, T. Yuan, W. Zhang, J. Ma, C. Zhang, Y.S. He, X.Z. Liao, Z.F. Ma, Influence of lithium precursors and calcination atmospheres on graphene sheets-modified nano-$Li_4Ti_5O_{12}$ anode material, J. Power Sources. 285 (2015) 51–62. doi:10.1016/j.jpowsour.2015.02.021.

[49] M. Wilkening, R. Amade, W. Iwaniak, P. Heitjans, Ultraslow Li diffusion in spinel-type structured $Li_4Ti_5O_{12}$ - A comparison of results from solid state NMR and impedance spectroscopy, Phys. Chem. Chem. Phys. 9 (2007) 1239–1246. doi:10.1039/b616269j.

[50] M.E. Sotomayor, C. de la Torre-Gamarra, W. Bucheli, J.M. Amarilla, A. Varez, B. Levenfeld, J.-Y. Sanchez, Additive-free $Li_4Ti_5O_{12}$ thick electrodes for Li-ion batteries with high electrochemical performance, J. Mater. Chem. A. 6 (2018) 5952–5961. doi:10.1039/C7TA10683A.

[51] M. Singh, J. Kaiser, H. Hahn, Thick Electrodes for High Energy Lithium Ion Batteries, J. Electrochem. Soc. 162 (2015) A1196–A1201. doi:10.1149/2.0401507jes.

[52] R. Zhao, J. Liu, J. Gu, The effects of electrode thickness on the electrochemical and thermal characteristics of lithium ion battery, Appl. Energy. 139 (2015) 220–229. doi:10.1016/j.apenergy.2014.11.051.

[53] L. Sun, N. Karanjgaokar, K. Sun, I. Chasiotis, W.C. Carter, S. Dillon, High-strength all-solid lithium ion electrodes based on $Li_4Ti_5O_{12}$, J. Power Sources. 196 (2011) 6507–6511. doi:10.1016/j.jpowsour.2011.03.045.

[54] W. Lai, C.K. Erdonmez, T.F. Marinis, C.K. Bjune, N.J. Dudney, F. Xu, R. Wartena, Y.M. Chiang, Ultrahigh-energy-density microbatteries enabled by new electrode architecture and micropackaging design, Adv. Mater. 22 (2010) E139–E144. doi:10.1002/adma.200903650.

[55] M.E. Sotomayor, B. Levenfeld, A. Várez, Powder injection moulding of premixed ferritic and austenitic stainless steel powders, Mater. Sci. Eng. A. 528 (2011) 3480–3488. doi:10.1016/j.msea.2011.01.038.

[56] M.E. Sotomayor, A. Várez, B. Levenfeld, Influence of powder particle size distribution on rheological properties of 316L powder injection moulding feedstocks, Powder Technol. 200 (2010) 30–36. doi:10.1016/j.powtec.2010.02.003.

[57] M. Khakbiz, A. Simchi, R. Bagheri, Investigation of rheological behaviour of 316L stainless steel-3 wt. % TiC powder injection moulding feedstock, Powder Metall. 48 (2005) 144–150. doi:10.1179/003258905X37747.

[58] Y. Li, L. Li, K.A. Khalil, Effect of powder loading on metal injection molding stainless steels,J.Mater.Process.Technol.183(2007) 432–439. doi:10.1016/j.jmatprotec.2006.10.039.

[59] B.C. Mutsuddy, Injection-Molding research paves way to ceramic engine parts, Ind. Res. Dev. 25 (1983) 76–80.

[60] Y. Lin, M.X. Gao, D. Zhu, Y.F. Liu, H.G. Pan, Effects of carbon coating and iron phosphides on the electrochemical properties of $LiFePO_4$/C, J. Power Sources. 184 (2008) 444–448. doi:10.1016/j.jpowsour.2008.03.026.

[61] S.-Y. Chung, J.T. Bloking, Y.-M. Chiang, Electronically conductive phospho-olivines as lithium storage electrodes, Nat. Mater. 1 (2002) 123–128. doi:10.1038/nmat732.

[62] Y. Xu, Y. Lu, L. Yan, Z. Yang, R. Yang, Synthesis and effect of forming Fe_2P phase on the physics and electrochemical properties of $LiFePO_4$/C materials, J. Power Sources. 160 (2006) 570–576. doi:10.1016/j.jpowsour.2006.01.042.

[63] P.S. Herle, B. Ellis, N. Coombs, L.F. Nazar, Nano-network electronic conduction in iron and nickel olivine phosphates, Nat. Mater. 3 (2004) 147–152. doi:10.1038/nmat1063.

[64] R. Tian, H. Liu, Y. Jiang, J. Chen, X. Tan, G. Liu, L. Zhang, X. Gu, Y. Guo, H. Wang, L. Sun, W. Chu, Drastically enhanced high-rate performance of carbon-coated $LiFePO_4$ nanorods using a green chemical vapor deposition (CVD) method for lithium ion battery: A selective carbon coating process, ACS Appl. Mater. Interfaces. 7 (2015) 11377–11386. doi:10.1021/acsami.5b01891.

[65] C. Ho, I.D. Raistrick, R.A. Huggins, Application of A-C Techniques to the Study of Lithium Diffusion in Tungsten Trioxide Thin Films, J. Electrochem. Soc. 127 (1980) 343–350. doi:10.1149/1.2129668.

[66] M.E. Sotomayor, C. de la Torre-Gamarra, B. Levenfeld, J.-Y. Sanchez, A. Varez, G.-T. Kim, A. Varzi, S. Passerini, Ultra-thick battery electrodes for high gravimetric and volumetric energy density Li-ion batteries, J. Power Sources. 437 (2019) 226923. doi:10.1016/j.jpowsour.2019.226923.

[67] Y. Jin, B. Zhu, Z. Lu, N. Liu, J. Zhu, Challenges and recent progress in the development of Si anodes for lithium-ion battery, Adv. Energy Mater. 7 (2017) 1–17. doi:10.1002/aenm.201700715.

Chapter 4

$Li_4Ti_5O_{12}$ ceramic electrodes manufactured by Tape Casting

4.1. INTRODUCTION TO THE TAPE CASTING PROCESS

The tape casting process, also known as doctor-blade, band casting or knife casting, is a very common manufacturing process for ceramic layers with a very constant thickness, usually in the range between 5 µm and a few millimetres. It was developed during the 1940s to produce piezoelectric materials, which is currently one of the most important applications of this process. Tape casting basically consists in casting a fluid suspension of a ceramic powder (called slurry or slip) on a polymer or glass surface. Then, the solvent is evaporated, and the obtained film can be cut with the desired dimensions. The organic components are thermally removed in a debinding step and subsequently the film is sintered. The versatility and simplicity of this process make it very useful for industrial applications [1,2].

4.1.1. Slurry components

The slurry is a mixture of different components: ceramic powder, binder, plasticizer, deflocculant and solvent. The proportion in which they are combined is crucial for obtaining a layer with appropriate mechanical properties and good homogeneity.

4.1.1.1. Powder characteristics

The characteristics of the initial powder, such as particle size, distribution and morphology, play an important role on the sintered microstructure and final properties of the casted and sintered tapes.

In order to achieve a high packing of the powder particles, small particle size is usually desired. However, the smaller the particles the higher the surface area and, consequently, more additives concentration is needed, which can provoke defects in the materials during the debinding and sintering steps. For example, Besendörfer *et al.* used three different batches of a powder with average particle sizes (d_{50}) of 1.8, 2.4 and 3.0 µm to study their effect in the shrinkage of a commercial ceramic and they concluded that the higher the particle size the higher the shrinkage anisotropy [3]. Furthermore, the particle size and its distribution also have an important effect on the final layer characteristics. Das *el al.* prepared alumina membrane filters by tape casting using different particle sizes of d_{50} between 0.2 and 1.5 µm and they obtained that not only the initial particle size was critical in the pore properties of the membrane, but also the particle size distribution. As expected, they observed that the lower the particle size, the lower the pore size as

a consequence of a higher packing of the particles. Moreover, the narrower the particle size distribution is, the more uniform the pores are distributed in the final layer [4].

On the other hand, the particle shape of the initial powder affects to different parameters during the process. For example, slurries with spherical particles present lower viscosities than those with platelet shaped particles. Spherical particles lead to high packing densities as they allow easier particle rearrangement. On contrary, particles with specific shapes, such as rod-like particles, can produce orientation effects under the shear rate of the blade and thus produce non isotropic shrinkage [5].

4.1.1.2. Solvents

The selected solvent must dissolve the organic additives of the slurry (deflocculant, binder and plasticizers). On the other side, it must not react with the ceramic powder and should form a suspension of the powder in the homogeneous fluid. Solvents used in tape casting are classified as aqueous or organic.

Despite organic solvents can present toxicity, they can be selected in order to have low boiling point, low viscosity and high vapour pressure compared to aqueous solvents. Thus, the drying step is faster than in water and the total time of the process is reduced. Also, the low superficial tension of organic liquids reduces crack formation in the layer during their evaporation. Organic solvents also provide high solubilization of the organic additives, providing a homogeneous slurry after mixing. Furthermore, the low viscosity easies the casting of the slurry. Sometimes mixtures of solvents are used, such as azeotropic mixtures, which result in a decrease of the vapor pressure of the mixture compared with its separated components, letting the system dry faster at a given temperature. Also, both components evaporate as one, allowing a homogenous evaporation through all the mixture with no solvent composition changes [6]. For safety and health concerns, mixtures of alcohols are desired. Thus, one of the most common solvents is the azeotropic mixture of Methyl Ethyl Ketone (MEK) and Ethanol (Et) [7].

On the other hand, aqueous solvents present the advantages of being cheap, non-toxic and thermally stable. Thus, water-based tape casting is well developed for some materials, such as Al_2O_3 [8]. On contrary, complete water elimination from the cast layers is sometimes a big issue, especially in thick layers. Thus, only thin green layers are usually produced [9]. Moreover, some ceramics are unstable in presence of water, for example the Li-ion conductors $Li_{0.44}La_{0.52}TiO_3$ [10] and $Li_7La_3Zr_2O_{12}$ [11].

4.1.1.3. Deflocculants

The ceramic particles present a tendency to be in contact with each other due to Van der Waals forces. The most used method for avoiding agglomeration is using a deflocculant agent, which usually is a liquid that creates an electrical double layer around each particle generating a repulsion between the particles. When the repulsive force is higher than the attraction one, the suspension is stabilized.

The role of the deflocculant is to disperse the powder particles throughout the slurry and avoid agglomeration. In this manner, the slurry viscosity decreases, and the powder loading can be increased for improving the packing of the particles.

The most widely employed deflocculant is ether phosphate. Due to its high acidity, it ionizes and provides high positive charge to the particles surface, which favours the linkage to the organic molecules and hence, prevents the double layer repulsion. However, other compounds as oleic or stearic acid have been also successfully employed [7].

4.1.1.4. Binders and plasticizers

The binder/plasticizer system is critical for achieving the desired mechanical properties of the film in the green stage. The specific role of the plasticizer is to provide flexibility to the layer for an easy handling, while the binder must form a robust and consistent layer after solvent evaporation, permitting to store and to manipulate the material. The general requirements for selecting an appropriate binder are high effectivity at low concentrations, low glass transition temperature, easy burnout, no interference with solvent evaporation or trapped air and act as lubricant between particles. For cost considerations, it is always advisable to choose polymers that can be dissolved in an inexpensive and environmentally friendly solvent. Binders are usually polymers either natural or synthetic that form organic bridges between the ceramic particles. In general terms, polymers with long chains will contribute positively to achieve high strength and toughness. The most common binder used in tape casting is Poly Vinyl Butyral (PVB) and the most employed plasticizers are glycols and phthalates [12]. On the other hand, the plasticizer addition provokes a decrease in the binder glass transition temperature, as the movement of the polymer chains is enhanced, increasing the flexibility of the layer. Nevertheless, this is accompanied by a decrease in the layer strength. Thus, the relative concentration of binder and plasticizers must be properly adjusted.

The molecular weight of the polymer system affects the properties of the slurry and consequently of the cast layer. For example, the higher the molecular weight the higher the viscosity of the slurry, which leads to poor material dispersion in the layer, resulting in low density layers. Moreover, higher molecular weights lead to higher debinding temperatures, which increase the time and cost of the process [13].

4.1.2. Tape casting steps

The different steps involved in tape casting process are detailed below and can be followed in the scheme of Figure 4. 1

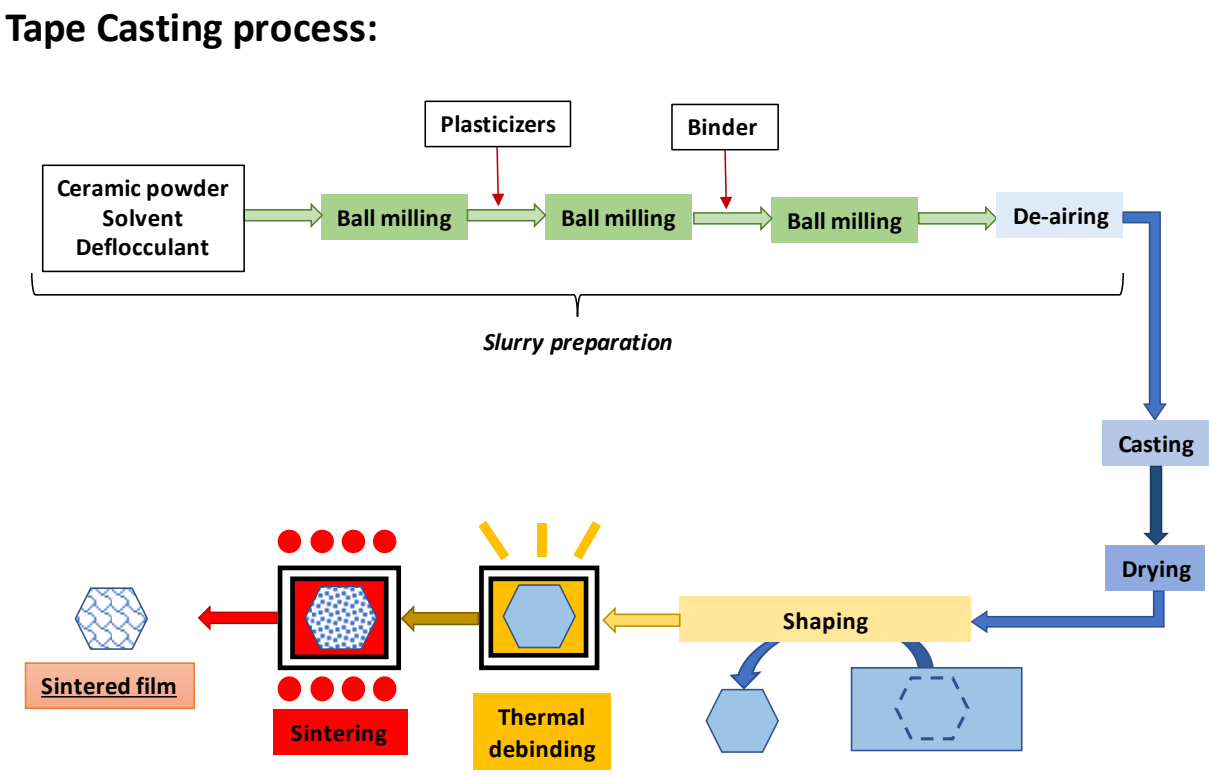

Figure 4. 1. Schematic representation of the tape casting process.

4.1.2.1. Slurry preparation

The slurry preparation, at a laboratory scale, starts with the mixing of the different components in a standard ceramic ball mill vessel. The use of ball milling favours the distribution of the different components in the mixture. In order to avoid competitive adsorption of polymers, the slurry can be prepared by a three-step slurry procedure. First, the deflocculant, solvent and ceramic powder are mixed and ball milled. As the role of the deflocculant is avoiding

agglomeration, it must be added in the initial phase of the milling step. Once the ceramic particles are homogeneously suspended in the solvent, the plasticizers are added, and subsequently in a third step, the binder is mixed to obtain the slurry. The next step is to remove any trapped air bubbles from the slurry, which can be carried out by simply stirring the mixture or by making little vacuum (600-700 mm Hg) for a few minutes.

4.1.2.2. Slurry rheological characterization

Once the slurry is prepared, rheology characterization tests are crucial to check the suitability of the mixture for tape casting, as they give insight into the slurry flow behaviour. Commonly, rheology experiments are carried out by measuring the slurry viscosity variation in a shear rate range. The presence of large polymer chains and anisotropic ceramic particles in the slurry generally does not follow the viscosity response against shear rate of Newtonian fluids. The viscosity is initially high due to the disorder of polymer and ceramic particles, which prevents the ceramic particle agglomerates. However, during casting, anisotropic components, such as rods-geometry particles orient toward the casting direction. In addition, polymer chains are disentangled, reducing the slurry viscosity and enable a steady flow. Thus, the viscosity decreases with the shear rate. When the slurry is out of the blade region the viscosity increases again allowing obtaining a film with preserved geometry. That is the reason why tape casting slurries usually present a pseudoplastic behaviour, an important requirement from the processing point of view. The rheological behaviour of tape casting slurries has been described by many different models, while the general tendency is that most of them have a power-law nature [14].

The viscosity of a slurry is strongly influenced by its composition. The proportion in which each component is added can be optimized by means of rheology experiments. In general terms, the higher the powder loading, the higher the viscosity. On the other hand, the presence of dispersants decreases the slurry viscosity [15]. Ceramic slurry viscosity values can be in the range 0.1-100 Pa·s in the shear rate range 0-200 s^{-1}, depending on the slurry formulation and composition [16].

4.1.2.3. Casting and drying

The casting of the slurry is usually carried out on a flat substrate like a glass or a polymer which is chosen based on the slurry composition for easing the removal of the dried tape from the carrier. The blade gap and the casting speed are controlled and play a key role in the final thickness of the layer. Thus, the higher the blade gap and the lower the casting speed, the higher the thickness

of the tape. Figure 4. 2. represents a scheme of the casting process. As previously mentioned, it is important to consider that, as the slurry is forced to pass under the blade, anisotropic ceramic particles and polymers will be orientated in the shear direction, which may provoke anisotropic shrinkage. Solvent evaporation is also an anisotropic process, as it only occurs at the top surface of the cast tape. This may difficult the manufacturing, especially for multilayer ceramics, in which the stack of the layers must be very precise. In general, the anisotropic shrinkage can be decreased by using higher blade gaps or lower casting speeds in order to decrease the shear rate or also by decreasing the powder loading [17].

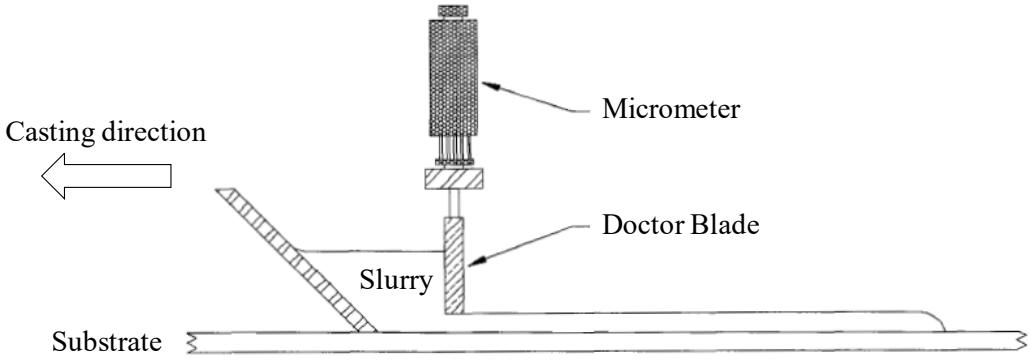

Figure 4. 2. Schematic representation of the casting step in doctor blade process. Adapted from reference [18].

4.1.2.4. Debinding and sintering

After drying, the cast tape is very flexible and can be easily cut in the desired geometry. The next step consists in removing completely the organic components of the layer and then sintering. For that, optimized thermal treatments, in which the degradation temperature of each component is considered, are used, employing slow heating rates to avoid defects [2]. Sintered cast layers can reach densities as high as 99 % with respect to the theoretical density [19].

4.1.3. Tape casting applications

Tape casting was originally developed in 1947 for the manufacturing of capacitors [20] and, some years later, in 1967, the production of Al_2O_3 thin films as substrates for circuits, devices and integrated circuits was patented [21]. The possibility of stacking layers previously metallized and interconnecting them led to a breakthrough in the manufacturing of multilayer ceramic circuits [22], which have been widely employed in the electronic industry.

Although initially it was the main motivation to produce materials for the conventional electronic industry, nowadays tape casting has become useful for the production of ceramic

materials with other applications, as piezoceramics for transducers for sensors [23], materials for photovoltaic solar cells [24], multilayer anode supported solid oxide fuel cells (SOFC) [25], SiC multilayers for thermal protection of spacecrafts [26] or phosphor ceramics for light emitting diodes (LED) [27].

Regarding to the application of tape casting to sintered materials for Li-ion batteries applications, Gao *et al.* recently reported the preparation of high density (99%) garnet-type $Li_{6.4}La_3Zr_{1.4}Ta_{0.6}O_{12}$ (LLZTO) solid electrolyte. The obtained layer presented high ionic conductivity ($5 \cdot 10^{-4}$ S/cm al 30 ºC) and was used for preparing an all-solid-state battery Li/LLZTO/$LiFePO_4$ with excellent cyclability at 60 ºC and 0.1 C [19]. On the other hand, Schiffmann *et al.* prepared green layers of $Li_4Ti_5O_{12}$ (120-140 µm thickness) and $Li_{0.33}La_{0.557}TiO_3$ (LLTO, 25-40 µm thickness) by tape casting which were stacked together and co-sintered. Despite the good cohesion between electrode and electrolyte, the measured conductivity of LTO was very low (~ 10^{-6} S/cm), which was in principle attributed to the phase transition of LTO due to the high sintering temperature (1100 ºC), which is necessary for sintering of LLTO [28].

4.2. OBJECTIVES

The aim of this investigation is to prepare thick $Li_4Ti_5O_{12}$ (LTO) ceramic electrodes by the tape casting process and test them in lithium half cells in order to obtain high energy density anodes for lithium-ion batteries.

The different steps of the tape casting of LTO will be optimized. The slurry components will be thermally characterized, and the slurry composition selected according to rheological measurements. After casting, a debinding and sintering thermal treatment will be designed. The debinding will be done according to the decomposition temperatures of the organic slurry components. The effect of the sintering temperature and atmosphere on the structural, microstructural and electrical properties of the electrodes will be studied. Finally, the tape casting LTO ceramic anodes will be tested in lithium-ion half cells.

4.3. EXPERIMENTAL

4.3.1. Materials

4.3.1.1. $Li_4Ti_5O_{12}$ powder

Commercial $Li_4Ti_5O_{12}$ (LTO) powder was provided by Linyi Gelon Lib Co. LTD. The as received powder was characterized by means of elemental carbon determination, particle size distribution analysis, scanning electron microscopy, transmission electron microscopy, energy dispersive spectroscopy, X-ray diffraction and pycnometric density. The results are discussed in Chapter 3, section 3.4.1.1. In summary, the LTO starting powder had negligible carbon content and presented a bimodal particle size distribution as a consequence of agglomeration of particles, with two volume % maximum, centred in 1 μm particle diameter and 200 μm particle diameter, approximately. This fact was confirmed by SEM. The presence of agglomerates is usually not desired for tape casting because, as mentioned before, it may provoke low packing densities and high shrinkage anisotropy. Anyhow, agglomerates are often eliminated during the liquid mixing [7]. Moreover, the EDS analysis revealed the presence of a small amount of aluminium in the powder composition, probably due to contamination from grinding process during powder manufacturing. Nevertheless, this contamination could be beneficial for conductivity of the material. Finally, XRD experiments confirmed the high purity and crystallinity of the commercial $Li_4Ti_5O_{12}$ powder.

For tape casting, it results also interesting to study the stability of the $Li_4Ti_5O_{12}$ powder in water in order to check the possibility of using an aqueous solvent for preparing the slurry. For that, and in order to identify possible reactions between the ceramic powder and water, LTO powder was immersed in distilled water and the change of the pH with the time was measured separately for solutions of 60 ml of H_2O with different amounts of commercial LTO powder (5, 125, 250 and 500 mg).

The results, which are collected in Figure 4. 3, show the pH evolution with the immersion time during 24 h and during the first 15 minutes (figure inset) for different amounts of LTO powder. In all the cases, the pH increases immediately after the powder addition indicating a raise in the OH^- concentration. Even when a very small mass of powder (5 mg) is added, an increase of the pH is registered. In less than 2 min (see Figure 4. 3-inset), the pH increases from the initial pH of water (pH = 6.5) to a maximum pH value of 10.5. After 15 min the pH stabilizes and remains constant until 24 h.

The increase of the pH is explained by the exchange of Li^+ ions from LTO by H^+ from water according to the following reaction:

$$Li_4Ti_5O_{12} + x\ H_2O \rightarrow H_xLi_{4-x}Ti_5O_{12} + x\ Li^+ + x\ OH^-$$

Similar behaviour was previously reported for Li-garnets [29,30] and perovskites [10,31]. Regarding to the Li^+/H^+ exchange in the spinel $Li_4Ti_5O_{12}$, Simon *et al.* studied the proton exchange for LTO in acidic solutions and observed a decrease in the capacity of the LTO electrode when the ion exchange increases [32]. However, in our case, the Li^+/H^+ exchange reaction takes place in pure water and it is observed that no high proton concentration is needed for the exchange reaction to occur.

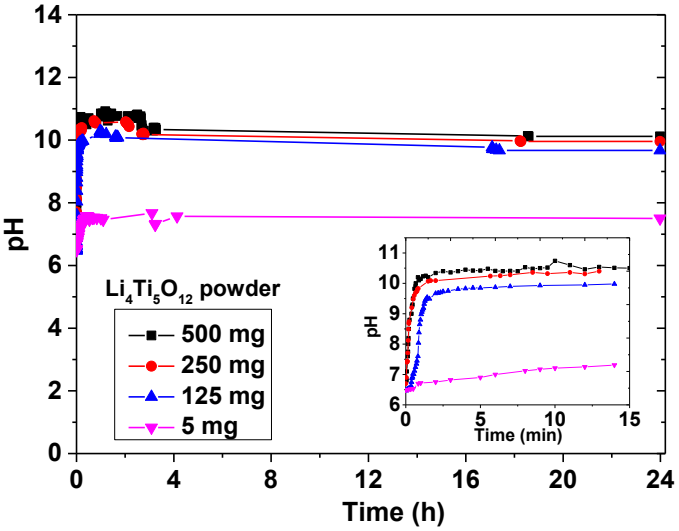

Figure 4. 3. pH evolution with time for different amounts of commercial $Li_4Ti_5O_{12}$ powder.

From the obtained results, it can be concluded that exposure to water must be avoided during the processing of LTO thick electrodes by tape casting in order to prevent Li^+/H^+ exchange, as the electrochemical properties of the final material can be damage. Thus, an organic solvent should be selected for the slurry preparation.

4.3.1.2. Binder system

In order to prepare a suitable slurry for the tape casting process, $Li_4Ti_5O_{12}$ powder was mixed with different components. The selection of these components was done according to previous studies in which titanate zirconate lead (PZT) films were successfully prepared by doctor blade process [33].

As *deflocculant agent*, Butyl Phosphate (BP), (Merck, mixture of mono and di esters, boiling point 145 ºC) was employed. The mono ester is composed by a hydrocarbon chain with a phosphate group in its extreme, while the di ester has two hydrocarbon chains and the phosphate group is between them. This structure justifies the polar character and therefore the high affinity for the powder surface.

On the other hand, the composition selected for the *solvent* was methyl ethyl ketone (MEK)-ethanol (EtOH) (0.49-0.5). This mixture is an azeotrope at normal conditions of temperature and pressure (20 ºC and 1 atm, supposed as working laboratory conditions) and has a boiling point of 75 ºC [34].

Regarding to the *plasticizers*, Poly Ethylene Glycol (PEG) (molecular weight 10000, Fluka) and Benzyl Butyl Phthalate (BBP) (Sigma-Aldrich, 98%, boiling point 370 ºC) were used.

Eventually, Polyvinyl butyral (PVB) (Sigma-Aldrich) was used as *binder*, as it presents rigid groups that contribute to the robustness of the film.

The molecular structure of the deflocculant, plasticizers and binder is represented in Figure 4. 4.

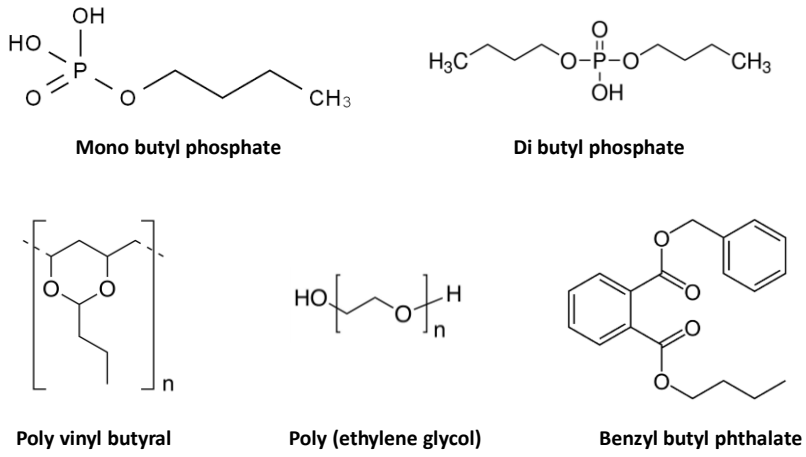

Figure 4. 4. Molecular structure of the components employed for the slurry.

4.3.2. Production of $Li_4Ti_5O_{12}$ ceramic electrodes by tape casting

The steps followed for the preparation of sintered LTO thick layers for lithium-ion batteries electrodes by tape casting is described in this section. The strategy for obtaining additive-free thick anodes with the desired performances is based on the elimination of the binder and subsequent sintering, analogously to that followed for producing LTO-extruded electrodes (Chapter 3). Thus,

the atmosphere used during the debinding and sintering steps is critical and was optimized to allow preserving some carbon from the binder decomposition and to avoid adding extra conductive carbon.

4.3.2.1. Slurry preparation

The composition of the slurry was optimized to obtain a homogeneous and mechanically stable film. For preparing a slurry, the deflocculant BP, the solvent MEK-ET and the LTO powder were firstly mixed in a 250 mL zirconia vessel for 10 min. The suspension was ball milled at 500 r.p.m. using zirconia balls of 5 mm diameter. The weight ratio powder/balls was 10/1. Then, the plasticizers BBP and PEG were added to the vessel and the mixture was ball milled for another 10 min at 500 r.p.m. Eventually, the binder PVB was added and the resultant mixture was ball milled again for 15 min at 250 r.p.m. After milling, the mixture was de-aired under vacuum for 2 min to remove possible air bubbles retained inside the slurry.

4.3.2.2. Casting and drying

Tape casting was performed on a Mylar® substrate foil employing a blade of 750 µm gap height and a constant casting speed of 60 $cm \cdot min^{-1}$. After casting, the green layers were dried at room temperature for 24 hours in air and subsequently cut with the desired dimensions.

4.3.2.3. Debinding and sintering

Debinding and sintering were carried out in a two-step thermal treatment. First, a thermal debinding until 500 ºC was designed based in the boiling point and decomposition temperature of the different slurry components. Secondly, the samples were sintered at 900, 950, 1000,1050 and 1100 °C for 1h and cooled down to room temperature. The thermal treatment was performed in a horizontal tubular furnace Carbolite STF 15/75/450 with controlled gas flow of air, N_2 or Ar/H_2 (5 vol. % H_2).

4.3.3. Electrochemical performance of LTO electrodes obtained by tape casting

The electrochemical properties of the additive-free LTO electrodes were evaluated by chronopotentiometry in two-electrode Swagelock cells. The samples size was between 0.2 and 0.6 cm^2 and the mass loading between approximately 50 and 67 mg/cm^2. For comparison, conventional composite electrodes with 80 wt. % of the same commercial $Li_4Ti_5O_{12}$ as active material, 10 wt. % of carbon black (TIMREX Super-P) as conductive additive and 10 wt. % of

polyvinylidene fluoride (PVDF) as binder were processed by conventional doctor-blade procedure. Composite electrodes with maximum thicknesses of ca. 120 μm and active material loading close to 9.5 mg/cm^2 were prepared without cracks and well attached to the copper current collector.

The cells were assembled in a dry glove box MBraun Labmaster (< 0.1 ppm H_2O) filled with argon, using a lithium foil as negative and reference electrode. A fiberglass separator (Whatman BSF80) soaked with 0.3 ml of the electrolyte (1M $LiPF_6$ in EC:DMC (1:1 in volume) supplied by UBE) was used for battery tests.

The galvanostatic cycling tests were performed with a Biologic VMP3 multichannel tester at C/20 (8.75 mA·g^{-1}) constant current, in the potential range from 2.7 to 1.0 V and at a temperature of 30 ºC.

4.4. RESULTS

4.4.1. Tape casting process optimization

4.4.1.1. Optimization of the slurry composition and casting

The powder ceramic content of the slurry influences the basic characteristics of the green cast layers, like density, thickness (contraction) and microstructure. The density is expected to increase with the solid content as the amount of organic additives decreases and the ceramic particles can establish a more cohesive network. On the other hand, the contraction of the casted layers during drying decreases with the amount of LTO powder. Therefore, not only the casting conditions determine the thickness of the sintered ceramic layers, but also the ceramic powder content. In this work, both high density and high thickness are desired for producing high areal and volumetric capacities additive-free LTO electrodes. Thus, the slurry was optimized in order to reach the maximum possible LTO content. For that, slurries with different compositions were prepared. Table 4. 1 collects the relative weight amounts of the components of the prepared slurries. The solid content of the slurry was progressively increased from 45 wt.% to 55 wt. % while the solvent, plasticizers and binder were decreased. The maximum solid content reached was 55 wt. %.

Table 4. 1. Composition of the different prepared LTO slurries.

Component	Test 1	Test 2	Test 3
	wt. (%)		
LTO (active material)	45.0	50.0	55.0
BP (Deflocculant)	0.1	0.1	0.1
MEK-Et (Solvent)	43.8	41.1	38.4
PEG (Plasticizer)	0.7	0.6	0.5
BBP (Plasticizer)	1.4	1.2	1.0
PVB (Binder)	9.0	7.0	5.0

The slurry rheology is a critical parameter in tape casting. High viscosities allow a good geometrical retention in the casted layer. Besides that, a slurry must present a pseudoplastic behavior, that is, the viscosity must decrease when the slurry is forced to high shear rates flowing under the blade and increase when the shear rate decreases. Thus, the evolution of the viscosity

with the shear rate was measured for the different slurries in the shear rate range between 0 and 200 s^{-1}, as shows Figure 4. 5. It is observed that the viscosity increases with the relative amount of LTO powder. This is the expected behavior, as the increase of the powder content hinders the movement of the polymeric chains. The slurry with the highest powder content (55 wt. %) slightly decreases its viscosity with the shear rate from ~ 700 mPa·s to ~ 500 mPa·s, showing a pseudoplastic behavior. This indicates that at low shear rates, which simulates the first stage of the tape casting process, the shear stress increases due to the internal resistance caused by the disentanglement of the polymer chains and the splitting of particle agglomerates. Further application of shear stress results in the flow of the slurry without obstacles and, hence decreasing the viscosity. On contrary, the slurries with lower powder content (45 and 50 wt. %) present an almost constant viscosity in the shear rate range (Newtonian behavior).

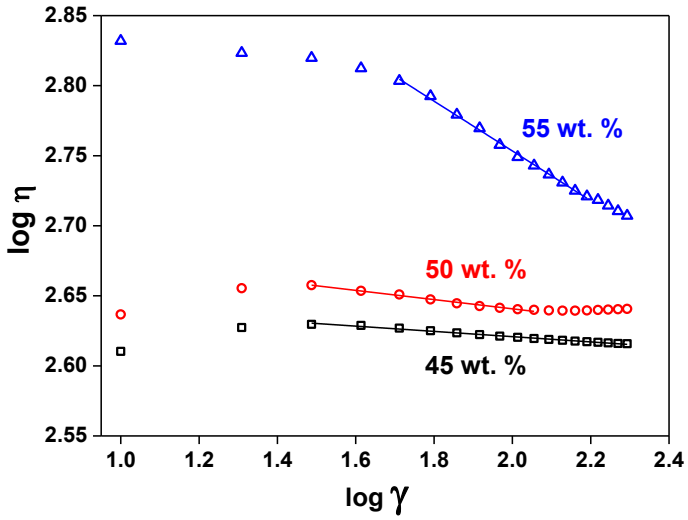

Figure 4. 5. Viscosity curves for LTO slurries with 45, 50 and 55 wt. % of LTO powder.

The flow behavior of a slurry can be described according to different rheological models based on the dependence of the viscosity with the shear rate. Between them, the most common used one is the Ostwald and de Waele power law model, which follows the following equation [14]:

$$\eta = k\,\dot{\gamma}^{n-1}$$

where η is the viscosity, k is the consistency index, $\dot{\gamma}$ is the shear rate and n is the power law index. If n is equal to one, the fluid behaves as a Newtonian fluid. When n is less than one, the fluid is pseudoplastic and the lower n is, the more pseudoplastic the fluid is.

The power law index for the slurries with different powder loading was obtained. For that, the linear regression of the logarithmic representation of the viscosity *versus* the shear rate was calculated in the shear rate range that follows the power law model. Figure 4. 6 collects the curves for each powder loading with their corresponding linear fittings.

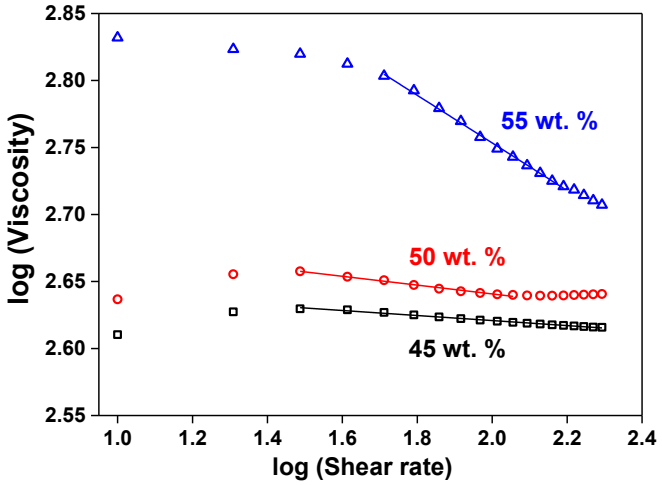

Figure 4. 6. Fittings of the linear regression of the logarithmic representation of viscosity against shear rate for slurries with 40, 45 and 50 wt. % of LTO.

The calculated power law indexes are collected in Table 4. 2. In all cases, n is lower than 1, which means that all the slurries present a pseudoplastic behavior. However, the slurry with the highest powder loading (55 wt. %) presents the lowest power law index, which indicates that is the most pseudoplastic fluid. On the other hand, for 45 and 50 wt. % of LTO, n is very close to 1, which shows the poor pseudoplastic character of the slurries and their *quasi*-Newtonian behavior. Marani *et al.* also reported a decrease in the power law index with the powder loading from 0.97 to 0.78 for ceria-gadolinium oxide tape casting slurries [35].

Table 4. 2. Power law index for slurries with different powder loadings. The regression coefficients of the linear fittings are also indicated in brackets.

LTO content (wt. %)	n
55	0.82 (0.997)
50	0.97 (0.98)
45	0.98 (0.99)

According to the rheological characterization, the slurry with 55 wt. % of LTO is the most pseudoplastic fluid, so it would be the most appropriate for tape casting. Furthermore, in order to obtain ceramics with higher mechanical properties, higher powder loading is also the most convenient.

The three slurries were casted using the same blade gap (750 µm) and the thickness of the dry layer was measured. As shows Table 4. 3, the thickness of the green layer increases with the LTO content as a consequence of the lower solvent content in the slurry. In all cases, homogeneous layers were obtained, and no visual defects were observed.

Table 4. 3. Effect of the LTO powder content in the thickness of green LTO layers.

LTO content (wt. %)	Thickness (µm)
45	148 ± 16
50	185 ± 13
55	276 ± 36

It can be appreciated that the difference between the blade gap and the thickness of the green layers is very large. This is attributed to the relative high volume percentage of solvent in the slurry compared to the LTO powder (see Table 4. 4). Thus, after the evaporation of the solvent, a contraction of approximately 63 % is expected, which is in good agreement with the thickness measured for the green layer with 55 wt. % (shown in Table 4. 3).

Table 4. 4. Relative weight and volume compositions of an LTO slurry.

Component	wt. % in slurry	vol. % in slurry*
LTO	55.0	26.0
BP	0.1	0.2
MEK-Et	38.4	63.2
PEG	0.5	0.8
BBP	1.0	1.6
PVB	5.0	8.2

*For the equivalence to vol. %, the mixing rule was used considering a density of 3.49 $g \cdot cm^{-3}$ for LTO and 1 $g \cdot cm^{-3}$ for the rest of the components.

The fact that the higher thickness was obtained for the slurry with 55 wt.% of LTO together with the pseudoplastic behavior of this mixture, made this composition the one of choice for preparing thick LTO layers by tape casting.

4.4.1.2. Thermal treatments

The debinding and sintering of the casted layers was carried out in a two-step thermal cycle. Firstly, the elimination of the organic components (debinding) was designed according to their decomposition temperature. In order to determine the decomposition temperature range of the solid organic components of the slurry (PEG and PVB), thermogravimetric analysis was performed heating at 10 ºC/min from 30 to 500 ºC in air. Figure 4. 7-(a) and (b) collects the thermograms of PEG and PVB, respectively. In both cases, a single weight loss is observed. The temperature at which the weight loss starts and ends was estimated from the curves and marked as T_1 and T_2, respectively, in the thermogravimetric curves. The degradation of PEG occurs at lower temperature than that of PVB due to the lower molecular weight of PEG compared to PVB. On the other hand, the boiling point of the liquid components of the slurry was considered. Table 4. 5 summarizes decomposition temperature ranges of the solid and boiling points of the liquid components of the slurry.

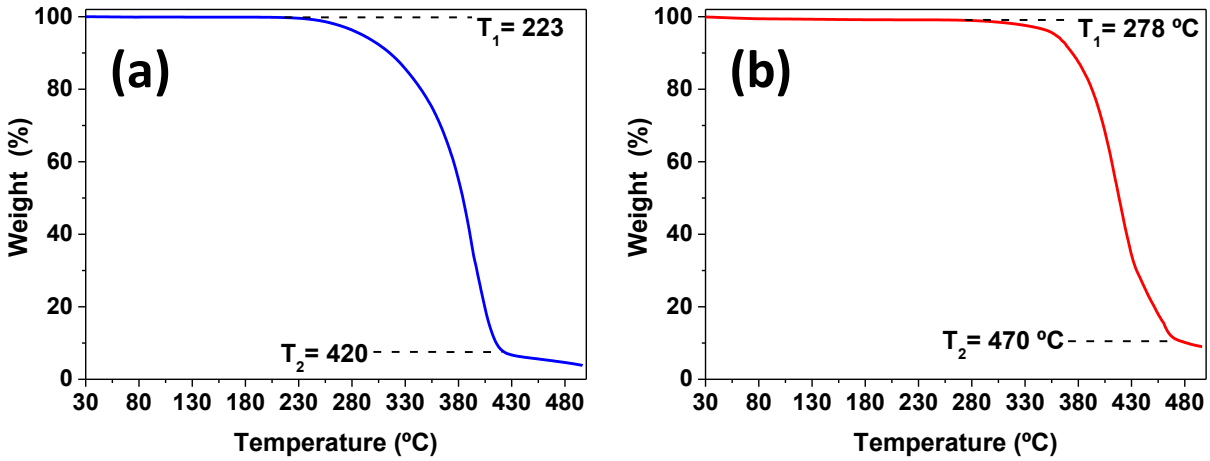

Figure 4. 7. Thermogravimetric curve of (a) PEG-10000 and (b) PVB.

Table 4. 5. Decomposition temperatures ranges (solids) and boiling points (liquids) of the organic slurry components for preparing LTO thick electrodes by tape casting.

Solid compounds	Decomposition temperature range (ºC)
Poly Ethylene Glycol-10000 (PEG)	223-420
Poly Vinyl Butyral (PVB)	278-470

Liquid compounds	Boiling point (ºC)
Butyl Phosphate (BP)	145*
Methyl Ethyl Ketone-Ethanol (MEK-EtOH)**	75 [34]
Benzyl Butyl Phthalate (BBP)	370*

* Taken from the supplier specifications (Merck for BP and Sigma-Aldrich for BBP).

** This component is supposed to have been completely eliminated during the drying step. However, as possible traces may remain in the green layer, the elimination of the remain solvent may be considered.

During the debinding, while the temperature is increased, the elimination of possible traces of MEK-Et (remaining from the drying step) should occur first, followed by the evaporation of BP. However, the temperatures at which PEG, PVB and BBP are eliminated overlap between 223 and 470 ºC. Thus, in order to optimize the thermal treatment and to identify the different mass losses corresponded to each component, a thermogravimetric analysis of a green layer was carried out from 30 to 600 ºC. The resulting thermogravimetric curve is shown in Figure 4. 8. Firstly, from 30 to 155 ºC, a very small mass loss (< 0.05 %) is detected, which can be attributed to the partial elimination of BP (boiling point = 145 ºC) or solvent traces evaporation. Then, three main mass losses are observed in the plot, which temperature ranges are indicated at the bottom of the figure. In the first one, between 155 and 280 ºC, the mass loss could be attributed to some remaining BP or MEK-Et and to the decomposition of PEG, which starts at 223 ºC. A second mass loss is observed between 280 and 370 ºC and during this temperature range PEG continues decomposing while PVB decompositions starts at 278 ºC. The third mass loss is identified between 370 and 470 ºC. The starting temperature of this weight loss corresponds to the boiling point of BBP. Eventually, from 470 to 500 ºC no mass loss is detected, which indicates that the complete elimination of PEG, PVB and BBP finished at 470 ºC.

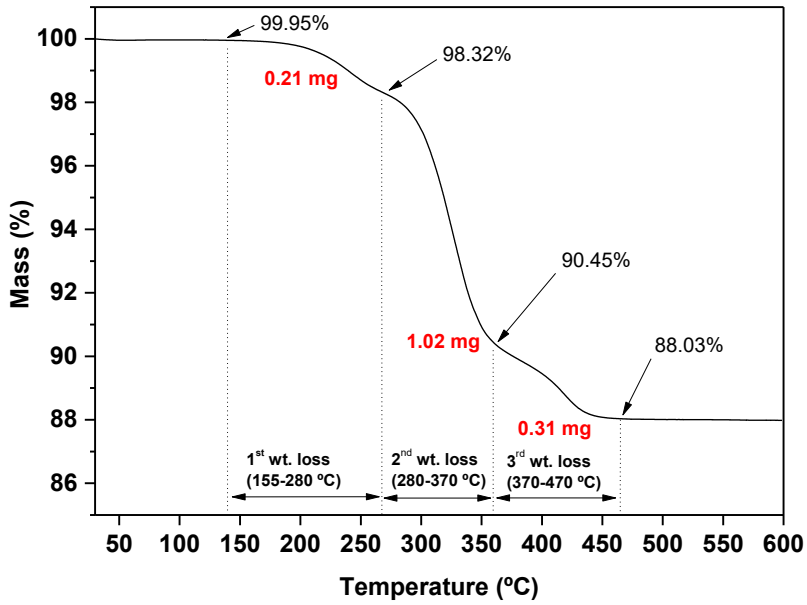

Figure 4. 8. Thermogravimetric curve of a tape casting LTO-green layer with 55 wt. % of LTO. The thermogravimetric analysis was carried out in air.

For a better understanding, the mass of each component in the green layer, considering the solvent was completely evaporated during the drying step, was calculated (see Table 4. 6). First, it must be highlighted that, if all the solvent (MEK-Et) had already been evaporated, the mass % after the elimination of the rest of the components at 500 ºC should be ~ 89 %, corresponding to the LTO wt. % in the green layer. However, the experimental value (88 %) is slightly lower than expected which indicates that part of the solvent was not fully eliminated. As can be seen in Figure 4. 8, the first mass loss is 0.21 mg. This mass is higher than that corresponding to the elimination of BP (0.03 mg) and PEG (0.10 mg), which confirms that some solvent must have been evaporated in this temperature range. Then, the second and third mass losses (total of 1.33 mg), are coherent with the elimination of the remaining PEG (less than 0.10 mg) and the complete removal of BBP and PVB (total mass 1.26 mg). Because the different decompositions overlap, it is very difficult to determine with precision the decomposition temperature range of each component. Anyhow, the results are in good agreement with the slurry composition.

Table 4. 6. Relative compositions of LTO slurry and green layer. The first column indicates the nominal composition of the prepared slurry. The second column was recalculated considering that no solvent remains in the green layer. The third column indicates the mass of each component of the green part measured in the thermogravimetric analysis.

Component	wt. % in slurry	wt. % in green layer	mass (mg) in green layer
LTO	55.0	89.3	11.58
BP	0.1	0.2	0.03
MEK-Et	38.4	0	0
PEG	0.5	0.8	0.10
BBP	1.0	1.6	0.21
PVB	5.0	8.1	1.05

According to these results, the debinding and sintering thermal treatment was designed. As different mass losses were detected in the green layer until 470 ºC, it was decided to heat up to 500 ºC and maintain this temperature for 1 hour to ensure the complete removal of the organic components. A slow heating rate was programmed to gradually remove the different compounds and avoid defects in the layer. Two different heating rates were used in the first step (0.5 and 1 ºC/min) and, once the organics are eliminated, the heating speed can be accelerated, so a speed of 2 ºC/min was selected for the sintering. The inspection of the sintered layers revealed no defects for any of the heating rates used during the debinding. In this manner, the fastest rate (1 ºC/min) was selected in order to minimize the total time of the thermal treatment. Separated LTO layers were sintered at 900, 950, 1000, 1050 and 1100 ºC for 1 h in three different atmospheres (air, N_2 and Ar/H_2 (5 vol. % H_2)) and cooled down to room temperature. As an example, the thermal treatment for a sintering temperature of 1100 ºC is illustrated in Figure 4. 9, being the total time of the treatment ~ 18 hours.

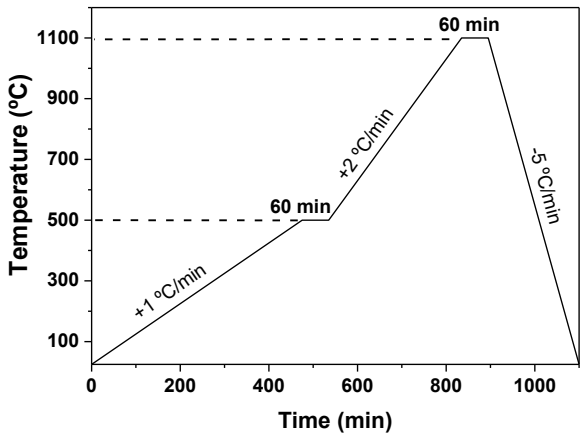

Figure 4. 9. Debinding and sintering thermal cycle for green cast LTO electrodes.

After sintering, it was observed that the colour of the materials changed with the sintering atmosphere. The color of the layers sintered under N_2 or Ar/H_2 was dark grey, while that sintered in air was white (see Figure 4. 10). Analogous results were obtained for LTO anodes obtained by powder extrusion moulding, as discussed previously in Chapter 3 (section 3.4.2.4). Thus, the color difference could indicate that *(i)* inert and reducing atmospheres prevent for the total degradation of the organics, leaving some residual carbon in the material and/or *(ii)* the use of a reducing atmosphere results in a material with a dark-bluish color, most probably due to the partial reduction of Ti^{4+} to Ti^{3+}.

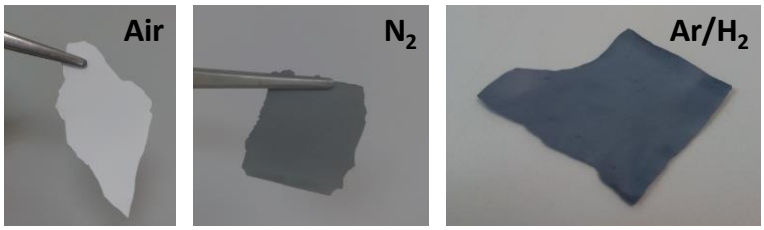

Figure 4. 10. Pictures of LTO layers after sintering at 1050 ºC in air, N_2 and Ar/H_2.

On the other hand, the placement of the layers in the substrate (alumina crucible) inside the furnace resulted very important for the final properties of the sintered materials and affected the color homogeneity of the layers. In the case of oxidant atmosphere, by placing the green layer on a fiber glass inside an alumina crucible, the sintered material did not maintain its geometry and buckled (Figure 4. 11-(a)). However, if the layer was placed on a flat surface, with a porous alumina piece on top for favoring gas evacuation, a flat and defect-free layer was obtained (Figure 4. 11-(b)).

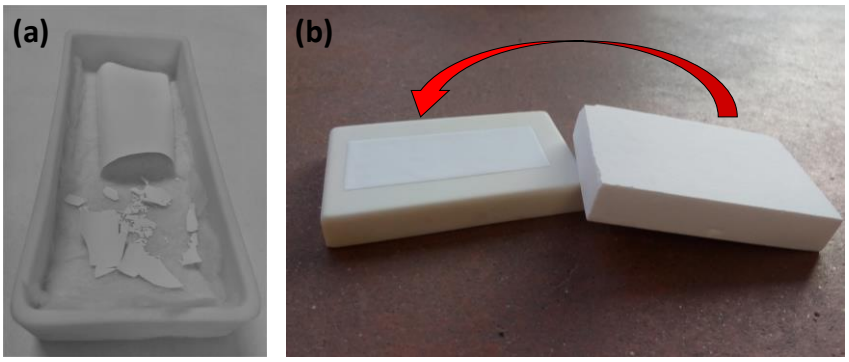

Figure 4. 11. Sintered LTO layers using two different set-up (a) green layer placed on a glass-fiber inside an alumina crucible and (b) green layer placed on an alumina crucible with an alumina porous piece located on top.

Nevertheless, when an inert or reducing gas (N_2 or Ar/H_2) was used during the thermal treatment, a different configuration was necessary, as the gas must be in contact with all the layer surface to avoid the oxidation of the material. Thus, several configurations were tried. One of them consisted in stacking LTO layers spaced with alumina pieces for the gas to flow in between (Figure 4. 12-(a)). However, this configuration resulted in the structure collapse and formation of cracks in the layers (Figure 4. 12-(b)).

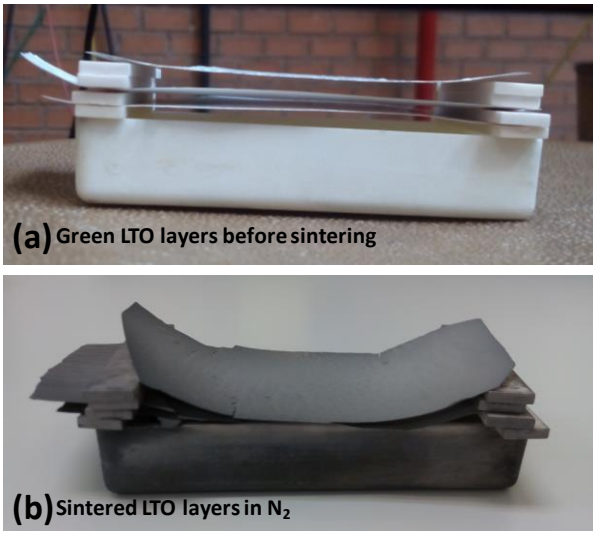

Figure 4. 12. Stack-configuration of LTO layers spaced with alumina pieces (a) before sintering and (b) after sintering under N_2.

The best configuration was found by placing the LTO layer vertically in the alumina crucible (Figure 4. 13-(a)). After sintering, a flat LTO layer was obtained (Figure 4. 13-(b)) and, no cracks or defects were found. Moreover, the part of the layer covered by the alumina pieces presented a light grey color due to partial oxidation of the material. However, the part in contact with the gas flow had a dark grey color (Figure 4. 13-(c)).

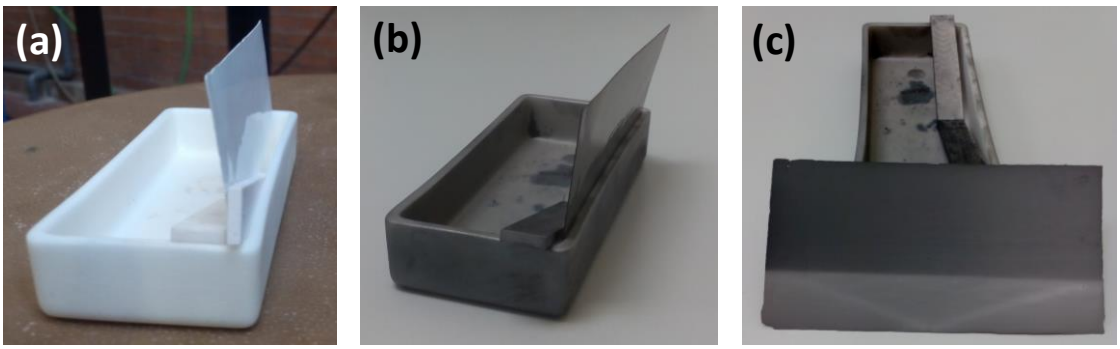

Figure 4. 13. Tape casting LTO layers before (a) and after sintering under N_2 (b), (c).

Consequently, for producing sintered LTO binder-free electrodes in N_2 or Ar/H_2 the layers were placed vertically in an alumina crucible, while when an oxidant atmosphere was used the best configuration resulted from placing the layer in a flat surface with a porous alumina piece on the top.

4.4.2. Sintering

4.4.2.1. Density and shrinkage

Density and porosity are very important features for an electrode and they directly affect the electrochemical performances of the battery. Thus, high density leads to higher volumetric capacity while high porosity is desired for favouring electrolyte penetration and to maximize the electrolyte-electrode interface for successful lithium exchange. It is therefore important to analyse the effect of the sintering temperature in the densification and microstructure of the LTO anodes. For that, density measurements as well as SEM images were used to optimize the sintering temperature.

The density evolution with the sintering temperature between 900 and 1100 ºC in air, N_2 and Ar/H_2 measured by the Archimedes method is represented in Figure 4. 14-(a). In general, the density increases with the sintering temperature. For all the sintering temperatures, the density is higher in air than in N_2 or Ar/H_2. Thus, the highest densities were achieved for samples sintered in air, increasing progressively with the sintering temperature from 78 to 92 % of the theoretical density (3.47 g/cm^3) in the sintering temperature range. On the other side, the same tendency is observed for samples sintered in N_2 and Ar/H_2; the density increases from 900 to 1050 ºC, and then remains almost constant until 1100 ºC. The maximum density reached in N_2 and Ar/H_2 is approximately 75 % of the theoretical density. The difference in density between the samples sintered in distinct atmospheres could be attributed to the carbon coating, which may difficult the sintering process. On contrary, air atmosphere lead to a higher densification.

By comparing these results with those obtained for extruded sintered layers (Chapter 3, section 3.4.2.4.1) it can be observed that the maximum density reached in air is higher by tape casting (92 %) than by extrusion (84 %). This could be due to the different thickness of the layers (typically 250 µm for TC and 500 µm for PEM). However, as mention in the introduction of this chapter, tape casting process usually leads to very significant relative densities (up to 99 %), commonly higher than those obtained by PEM. On the other hand, the maximum density reached after sintering in N_2 and Ar/H_2 is 75 % for tape casting layers and 84 % for extruded layers. The

lower density obtained for the tape casting layers could be attributed to a higher carbon content of the extruded samples, which hinders the sintering process. The carbon content of extruded and tape casting layers will be compared later (section 4.4.2.3).

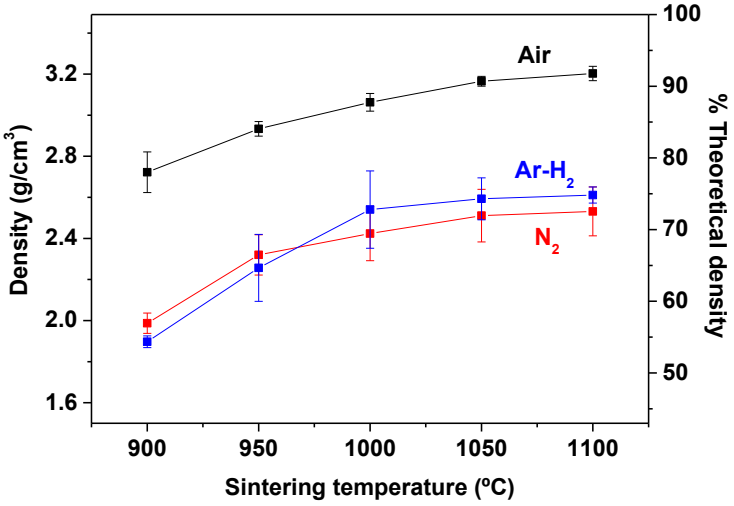

Figure 4. 14. Density of cast LTO layers sintered at different temperatures in air, N_2 and Ar/H_2.

In addition, helium pycnometric measurements of different sintered materials resulted in density values close to the theoretical one. This fact confirms the interconnection between the porous inside the material and allows calculating the open porosity directly as the difference between the theoretical density and the density measured by the Archimedes method. Thus, for example, at 1100 ºC, the open porosity in air is 8 %, while in N_2 and Ar/H_2 is 27 and 25 %, respectively.

In order to analyse the morphology and porosity of the LTO sintered layers, scanning electron microscopy was employed. The evolution of the microstructure with sintering temperature under different atmospheres is shown in Figure 4. 15. In samples sintered in air, the grain size increases with the sintering temperature and the porosity of the material is progressively reduced. Thus, at 900 ºC the grain size is very similar to that of the starting LTO commercial powder, while at 1100 ºC bigger grains can be observed. This is in good agreement with the density, which increases progressively with sintering temperature from 900 to 1100 ºC (Figure 4. 14). On the other hand, for samples sintered in N_2 and Ar/H_2 atmospheres, an increase in the grain size is detected from 900 to 1000 ºC, with the corresponding porosity reduction. However, from 1000 to 1100 ºC no densification can be seen in the images. This is in agreement with the density measurements, as from 1000 to 1100 ºC the density in N_2 and Ar/H_2 increases a little and small density changes are difficult to detect by SEM. In this manner, by comparing the images at 1100

ºC, it can be observed that the densification in air is much significant than in the other atmospheres, which is in good agreement with the Archimedes density measurements, in which the relative densities are 92 % in air and 75 % in N_2 and Ar/H_2.

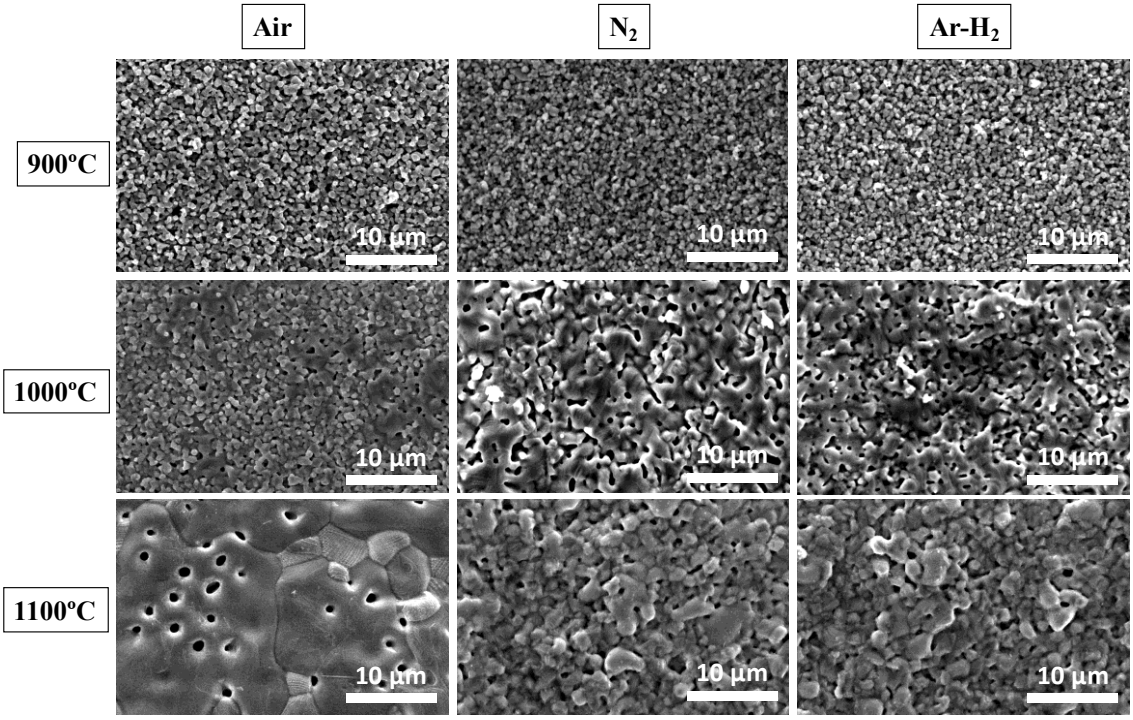

Figure 4. 15. SEM images of sintered LTO layers under air, N_2 and Ar/H_2 from 900 to 1100 ºC. Secondary electrons detector was employed in all the cases.

Moreover, the shrinkage of the layers during sintering is an important parameter that conditions the reproducibility of the process. It is especially critical when irregular-shape powder particles are used, as anisotropic shrinkage can be obtained as a consequence of the alignment of the solid particles in the casting direction when shear forces act during the casting process [32]. In such a way, the shrinkage of the LTO layers sintered in air at different temperatures was measured in (1x1) cm^2 green samples. The contraction was measured along the three dimensions of the samples: thickness, casting direction (Length 1) and direction perpendicular to the casting (Length 2). The results, plotted in Figure 4. 16, indicate an increase of the shrinkage with the sintering temperature, presenting the same tendency than the corresponding densification curve.

For N_2 and Ar/H_2 atmospheres, shrinkage measurements were not carried out as it was difficult to obtained reproducible flat layers.

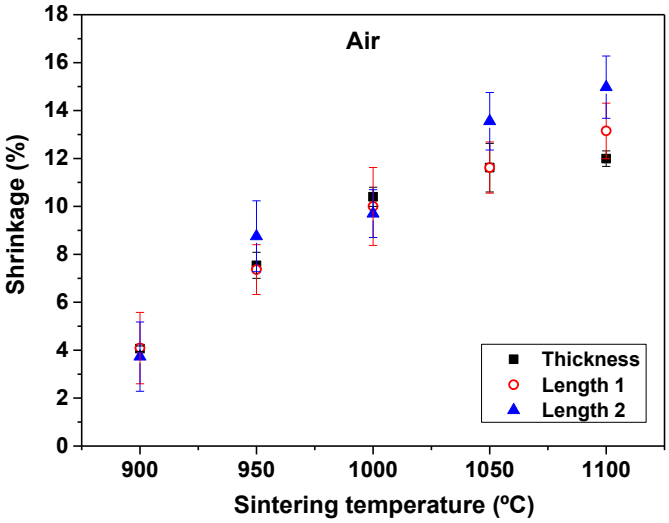

Figure 4. 16. Shrinkage variation of thickness, length in the casting direction (Length 1) and length perpendicular to the casting direction (Length 2) of LTO layers sintered at different temperatures in air.

4.4.2.2. X-ray diffraction

It was previously observed for extruded LTO electrodes (see Chapter 3), that LTO decomposes when sintering above 950 ºC in Ar/H_2 atmosphere. For this reason, the effect of the sintering atmosphere and sintering temperature on the composition of tape casting LTO electrodes was also studied by X-Ray Diffraction experiments.

Figure 4. 17 collects the XRD patterns of different batches of LTO layers sintered at different temperatures in air, N_2 and Ar/H_2. In all cases, for sintering temperatures below 1000 ºC, the XRD patterns only present the main peaks of $Li_4Ti_5O_{12}$. However, at higher sintering temperatures some extra peaks corresponding to the main diffraction peaks of ramsdellite, marked as (*), appear in the diffractogram. These extra peaks are the same independently of the sintering atmosphere. As mentioned before, according to the Li_2O-TiO_2 phase diagram in air proposed by West *et al.* [36] (see Figure 3.30), LTO decomposes in $Li_2Ti_3O_7$ and Li_2TiO_3 at approximately 1015 ºC. In our case, LTO decomposes following the mentioned phase diagram and the temperature at which the decomposition starts and the relative intensity of the main peaks of the secondary phases depend on the sintering atmosphere. Thus, LTO decomposition occurs at 1050 ºC in air and N_2 and at 1000 ºC in Ar/H_2. Moreover, the relative intensity of the main diffraction peaks suggests that LTO decomposition is more significant in Ar/H_2 and N_2 compared to air. Thus, it can be concluded that 1000 ºC is the maximum sintering temperature without LTO decomposition in air and N_2, while for Ar/H_2 is 950 ºC.

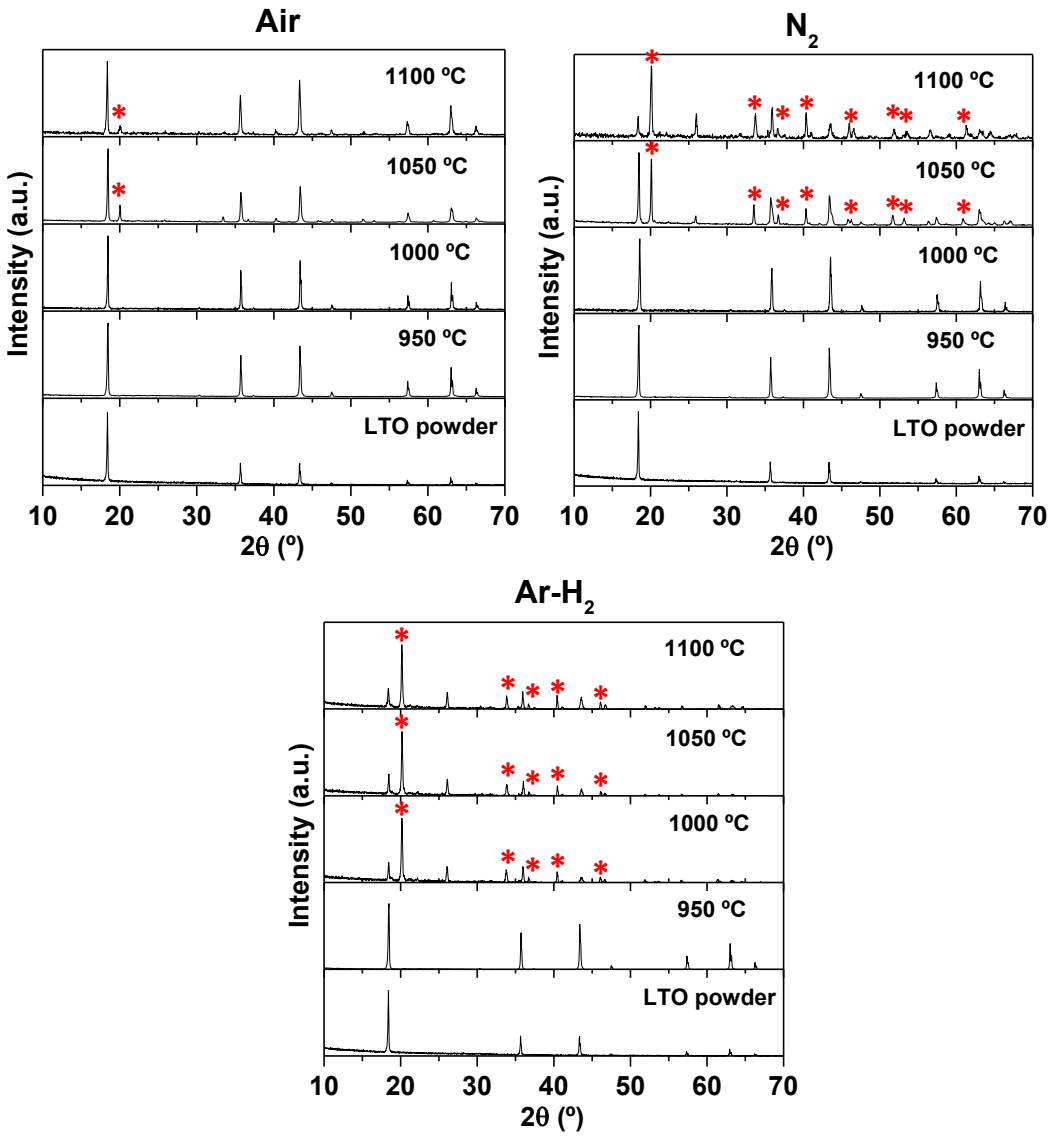

Figure 4. 17. XRD patterns of LTO layers sintered at different temperatures in air, N_2 and Ar/H_2. Ramsdellite ($Li_2Ti_3O_7$) peaks are marked as (*).

4.4.2.3. Carbon content

The effect of the sintering temperature in the carbon content was studied in samples sintered in different atmospheres at 950 and 1050 ºC. The results of the carbon elemental analysis are collected in Table 4. 7 and compared to those obtained in powder extrusion moulding (Chapter 3). It can be seen how the inert and reducing atmosphere leave some residual carbon in the sintered layers. This is attributed to a partial decomposition of the organic components of the slurry. On contrary, in air, negligible carbon content was detected, which confirms the total elimination of the organics in this atmosphere. In addition, no significant differences in the amount of carbon were detected between samples sintered at 950 ºC and 1050 C.

Table 4. 7. Carbon content of tape casting LTO layers sintered at 950 and 1050 ºC and extruded LTO layers sintered at 950 ºC, in air, N_2 and Ar/H_2.

	Carbon content (wt. %)		
	Tape casting		Powder extrusion moulding
Sintering atmosphere	**950 ºC**	**1050 ºC**	**950 ºC**
Air	0.02 ± 0.01	0.03 ± 0.01	< 0.01
N_2	0.24 ± 0.03	0.23 ± 0.02	0.05± 0.02
Ar/H_2	0.34 ± 0.02	0.38 ± 0.01	0.14 ± 0.02

According to these results, Ar/H_2 would be the most convenient atmosphere, as the carbon content is the highest, so a higher conductivity of the electrode is expected. Nonetheless, the distribution of the carbon around the LTO particles is crucial to obtain a homogeneous distribution of the current density through the active material and reach electronic percolation along the electrode.

Thus, the carbon distribution was studied in a sample sintered at 1050 ºC in different atmospheres by means of HR-TEM. Figure 4. 18, collects the images corresponding to particles of LTO layers sintered in air (left images), N_2 (central images) and Ar/H_2 (right images). First, in the image of the particle sintered in air, the crystalline planes of LTO are clearly observed, confirming the high crystallinity of the material. On the other hand, in samples sintered in inert and reducing atmospheres, a coating is clearly identified around the LTO particles, which corresponds to amorphous carbon due to its typical contrast [37]. Thus, in N_2, a carbon coating of approximately 2-3.5 nm is observed, while in Ar/H_2 the carbon coating is around 1-1.7 nm. However, it was expected to find a thicker carbon layer in the reducing atmosphere, as the total carbon content is higher than in N_2 (Table 4. 7). This difference can be attributed to the segregation of carbon agglomerates located between the particles in Ar/H_2, which retain part of the carbon, as observed in the image of Ar/H_2 particle (top) in Figure 4. 18. Same comparison can be done between an LTO-extruded electrode sintered in Ar/H_2 and a tape casting LTO-ceramic layer. Despite the higher carbon content of the tape casting electrode (0.38 wt. % vs. 0.14 wt. % of the extruded anode) it presents a thinner carbon coating (1-1.7 nm vs. 2 nm for the extruded anode) as the homogeneity of this coating is lower in the tape casting material.

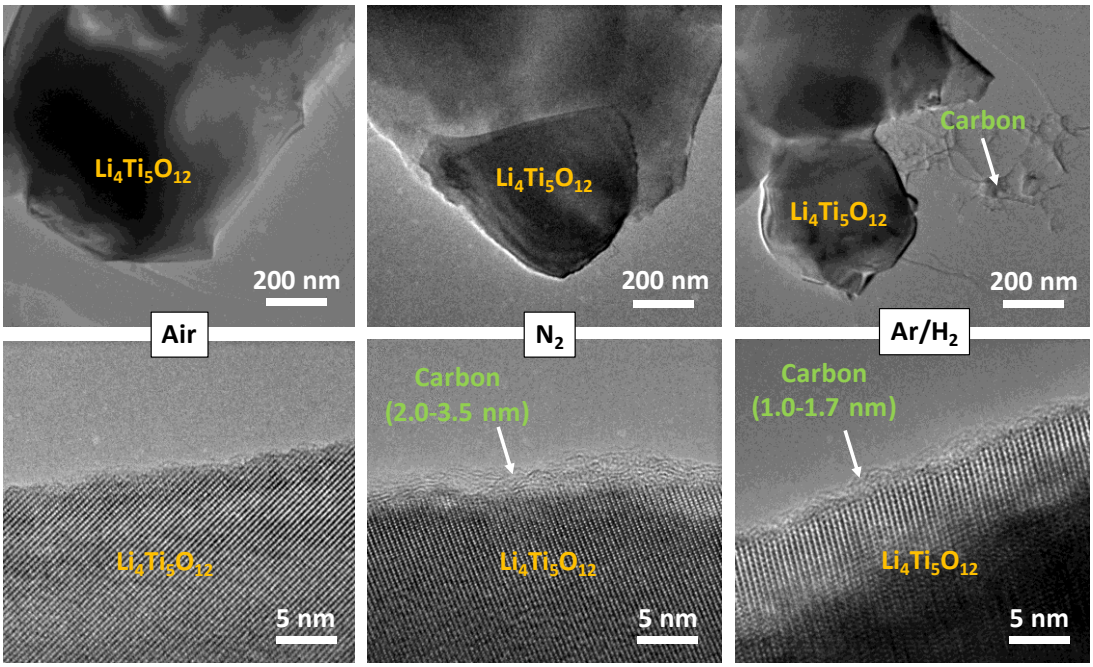

Figure 4. 18. HR-TEM images of different LTO particles from tape casting layers sintered in air (a) and Ar/H_2 (b, c) at 1050 ºC.

The presence of a carbon coating in particles sintered in inert and reducing atmospheres is in good agreement with the fact that the densification of this material is lower than those sintered in air. Thus, the carbon coating may make more difficult the sintering process.

According to the inspection of the HR-TEM images, it can be concluded that N_2 and Ar/H_2 are the most convenient atmospheres for obtaining LTO layers in terms of carbon content and distribution.

4.4.2.4. Impedance spectroscopy

In order to check the overall conductivity of the electrodes, the impedance of LTO layers sintered at 950 and 1050 ºC in different atmospheres was measured by IS. The measurement was performed in the frequency range 0.1-10 MHz with an input signal amplitude of 100 mV using gold blocking electrodes. In these experiments, the total conductivity was estimated without discriminating between electronic and ionic conductivities. However, ionic contribution to the impedance is expected to be much higher than the electronic one, considering the very high thickness of the materials.

The admittance response at variable frequencies is plotted in Figure 4. 19 for the electrode sintered at (a) 950 ºC (b) 1050 ºC in air, N_2 and Ar/H_2. The corresponding Nyquist impedance plots can be found in Supplementary information-Figure S4.1 and Figure S4.2).

First, it can be observed that for both sintering temperatures and atmosphere (air and N_2) the response is similar. This indicates that the presence of carbon in both samples does not contribute to the conductivity. However, considering that the detected carbon is conductor, this could indicate that there is no electron percolation in the material, even if a homogeneous carbon coating was observed by TEM. Moreover, the high impedance is attributed to the low ionic conductivity of LTO sintered in air, previously reported in the literature. More specifically, Schiffmann *et al.* [28] measured the conductivity of LTO layers prepared by tape casting (thickness ~130 µm) in air at 900 and 1050 ºC, and obtained values of approximately 10^{-7} S/cm, similar to those measured in this work.

On the other hand, the conductivity for the electrodes sintered in Ar/H_2 is more than twice the conductivity of those sintered in oxidizing or inert atmosphere. This conductivity increase could be attributed to *(i)* the effect of the reducing atmosphere in the composition of the electrode because of the partial reduction of Ti^{4+} to Ti^{3+} and/or *(ii)* the conductive residual carbon coming from the incomplete decomposition of the binder, which content is higher than in air or N_2.

For further understanding, the starting commercial LTO powder was uniaxial pressed in a pellet and sintered in Ar/H_2 at 950 ºC for 1 h. First, the colour of the sintered pellet was dark-bluish, indicating the partial reduction of Ti^{4+}. The frequency dependence of the conductivity of this material is displayed in Figure 4. 19-(c). The conductivity is several orders of magnitude lower than the sample obtained by tape casting and sintered at the same temperature in the same sintering atmosphere, indicating that the residual carbon coming from the thermal decomposition of the binder is crucial for obtaining good electrical performances, in addition to the partial reduction of Ti^{4+}. As there is no carbon in the pellet and the grain boundaries are large (due to poor sintering), no charge transfer occurs between the LTO particles and a high impedance is measured. From this result it can be concluded that both the presence of the carbon coating and the reduction of the Ti are necessary for the material to increase its conductivity.

These results are analogous to those obtained for LTO-extruded electrodes (see Chapter 3-section 3.4.2.4.5). However, in the case of the LTO extruded sample the conductivity reached in Ar/H_2 (~ 10^{-4} $S \cdot cm^{-1}$) is higher than the conductivity of the electrodes prepared by tape casting ($5 \cdot 10^{-5}$ $S \cdot cm^{-1}$ for 950 ºC and $2 \cdot 10^{-5}$ $S \cdot cm^{-1}$ for 1050 ºC). This result may be a consequence of the thinner carbon coating created after tape casting (1-1.7 nm) compared to Powder Extrusion Moulding (2 nm), which limits the electronic conductivity. Furthermore, the higher density of the extruded LTO electrodes (84 %) compared to the tape casting LTO ones (75 %) in N_2 and Ar/H_2 may be also the reason for the higher conductivity of the extruded anode.

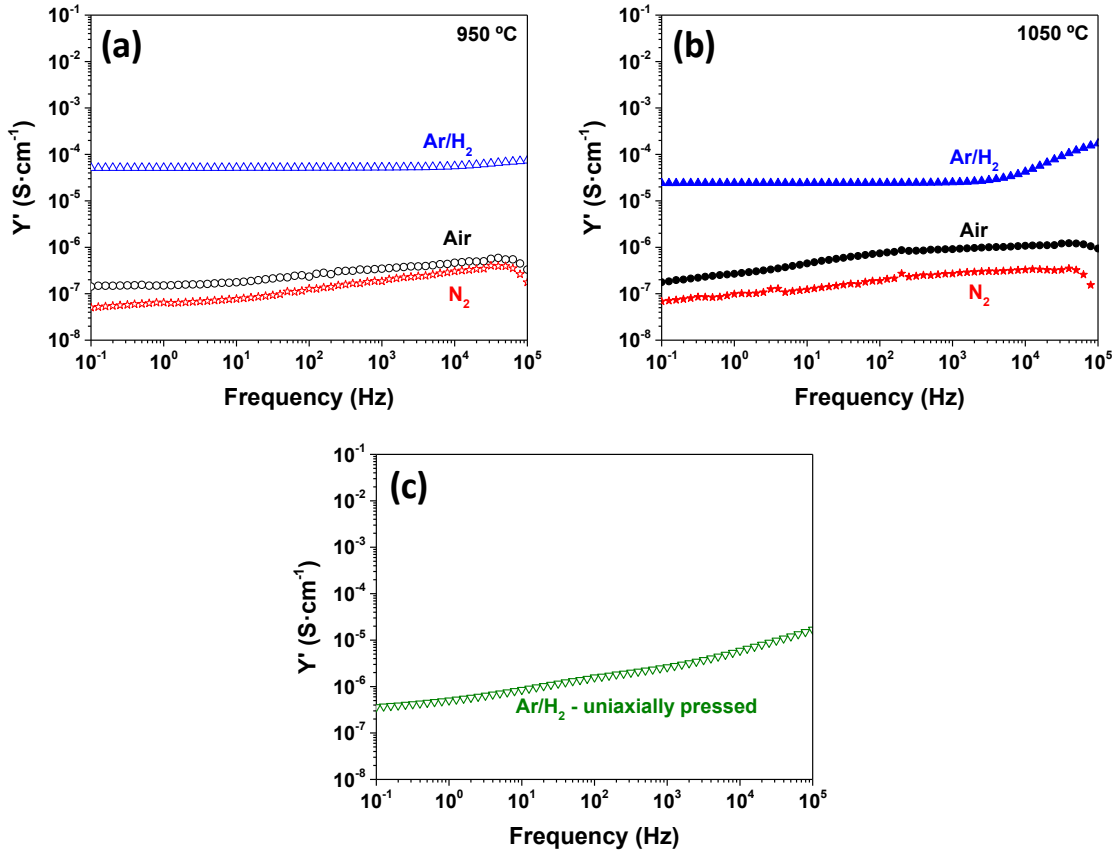

Figure 4. 19. Admittance curves for LTO-tape casting ceramic electrodes sintered at 950 ºC (a) and 1050 ºC (b) in different atmospheres and for an uniaxially pressed commercial powder LTO pellet sintered in Ar/H₂ at 950 ºC for 1 h (c).

In conclusion, the layers sintered in Ar/H_2 present the highest conductivity, due to a combination between the non-percolative carbon coating and the partially reduced LTO conductions, being the most appropriate for working as anodes. The measured conductivity, however, is relatively low compared to commercial composite LTO electrodes (> 10 S/cm), in which higher content (5-10 wt. %) of super conductive carbon is added [38]. This means that it is expected that the tape casting LTO ceramic electrode could distribute only low current densities in charge-discharge battery cycles.

4.4.3. Electrochemical performance of tape casting $Li_4Ti_5O_{12}$ ceramic electrodes

Electrochemical characteristics of the selected LTO ceramic electrodes, more specifically those sintered at 950 and 1050 ºC under Ar/H_2 (labelled as LTO-TC-950ºC and LTO-TC-1050ºC, respectively), were studied by galvanostatic cycling at 30ºC. The electrochemical properties of the cast ceramic electrodes are compared with a reference conventional electrode (labelled as LTO-

composite), prepared also by doctor blade technique but using a mixture of the same commercial LTO powder used for tape casting (80 wt. %), carbon black (10 wt. %) and PVdF (10 wt. %).

The specifications of the selected tape casting ceramic electrodes and the composite electrode are summarized in Table 4. 8.

Table 4. 8. Characteristics of tape casting LTO electrodes and LTO-composite electrode.

Electrode	Active material mass (mg)	Area (cm^2)	Mass loading (mg/cm^2)	Thickness (cm)	Density (g/cm^3)	Porosity (%)
LTO-Composite	10.6	1.13	9.42	0.0120	0.77	----
LTO-TC-950ºC	27.7	0.56	49.46	0.0240	2.05	35
LTO-TC-1050ºC	14.6	0.22	66.59	0.0276	2.40	25

4.4.3.1. Sintering temperature effect on the electrochemical properties of LTO ceramic electrodes

Figure 4. 20-(a) shows the cell potential evolution with the specific capacity for LTO-TC-950ºC and LTO-composite electrodes registered during the discharge of the first cycle. For the ceramic electrode, a very flat *plateau* developed at ca. 1.483 V in discharge is observed. The shape is similar to the LTO-composite electrode, and those usually reported for spinel $Li_4Ti_5O_{12}$-based anodes [37]. The slightly lower discharge voltage compared to that of the reference electrode (~1.530 V), indicates that kinetic limitations are a little higher for the ceramic electrode. This result is remarkable considering that LTO-TC-950ºC ceramic electrode is additive-free and has very high thickness (240 µm). As well, it must be highlighted that the specific capacity of LTO-TC-950ºC (143 $mA{\cdot}h{\cdot}g^{-1}$) is close to that of the LTO-composite (151 $mA{\cdot}h{\cdot}g^{-1}$). The slightly lower capacity delivers for the thick ceramic electrode is justified by its low polarization.

The cyclability of the cast electrode was studied at C/20 during 15 charge/discharge cycles. Figure 4. 20-(b) collects a selection of charge and discharge curves from the first to the fifteenth cycle for both LTO-TC-950ºC and LTO-composite. The first remarkable result is the high cyclability, which is strongly favoured by *(1)* the LTO-spinel is a zero-strain insertion electrode; the cubic cell parameter changes less than 0.2 % during the Li^+-insertion/extraction reactions [39] and *(2)* the relatively high working voltage avoids the electrolyte decomposition. The shape of the charge-discharge curves is maintained during the cycles and no polarization increase is observed.

However, the capacity decreases from 143 $mA \cdot h \cdot g^{-1}$ in the first cycle to 120 $mA \cdot h \cdot g^{-1}$ in the fifteenth cycle, as shows Figure 4. 20-(c). The variation of the coulombic efficiency during cycling is also displayed in the figure and the capacity values are compared to those of the reference electrode (LTO-composite). From the third cycle, coulombic efficiency values are very high, being > 99 % for every cycle. This result shows that degradation reactions of the electrolyte on the LTO all-ceramic electrode are negligible. The lower capacity values of the LTO-TC electrode compared to the LTO-composite one can be attributed, as mentioned before, to the slightly larger polarization of the binder-free thick anodes. This polarization can be related to *(i)* the high thickness of the ceramic, which increases the impedance for the ionic diffusion through the electrode and *(ii)* the very low carbon content (~ 0.38 wt. %) that hinders the current density distribution within the electrode volume. However, the high porosity of the material (25 %) allows reaching a good permeability of the liquid electrolyte, permitting the lithium insertion/extraction in all the active material.

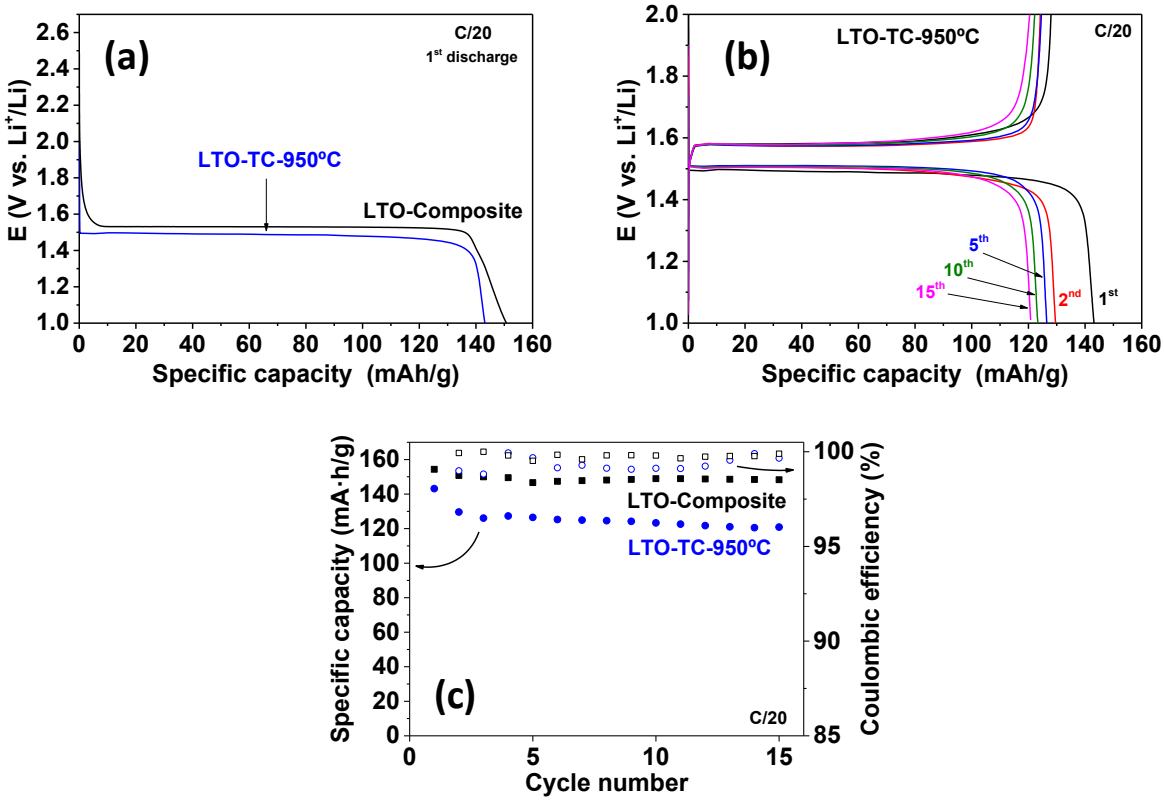

Figure 4. 20. (a) Discharge curves during the first charge-discharge cycle at C/20 for the LTO-TC electrode sintered at 950 ºC and for the LTO-composite electrode. (b) Selection of charge-discharge cycles at C/20 for the LTO-TC electrode sintered at 950 ºC. (c) Comparison of the cyclability at C/20 during 15 cycles of the LTO-TC electrode (sintering temperature 950 ºC) and the LTO-composite electrode.

On the other hand, the electrochemical properties of the LTO layer sintered at 1050 ºC were studied. The discharge curve of the first discharge-charge cycle of LTO-TC-1050ºC is compared with LTO-composite in Figure 4. 21-(a). Two main differences can be clearly appreciated: *(1)* the shape profiles of the discharge curves are clearly different and *(2)* the capacity of the LTO-TC electrode is lower than that of the composite one.

Firstly, the change in the profile shape indicates that the active material of both electrodes is not the same, which is in good agreement with the X-ray data which showed that, at 1050 ºC in Ar/H_2, $Li_4Ti_5O_{12}$ decomposes into ramsdellite ($Li_2Ti_3O_7$) and meta-titanate (Li_2TiO_3), being ramsdellite the majority phase (Figure 4.17). Previous studies of LTO-$Li_2Ti_3O_7$ composites reported that the shape of the charge-discharge curve of the composite is given by the characteristic shape of the charge-discharge curves of both LTO and ramsdellite [40,41]. In order to verify this behaviour, we studied the electrochemical response of LTO, ramsdellite and an LTO-$Li_2Ti_3O_7$ (50:50 wt.) composite (see Supplementary information-Figure S4.3-(a)). The charge-discharge profile of LTO shows a flat potential *plateau* at 1.55 V. On the other hand, the corresponding ramsdellite profile displays a progressive decrease in the discharge potential (Supplementary information-Figure S4.3-(b)). The composite charge-discharge curve (Supplementary information-Figure S4.3-(c)) shows a mixture of both ramsdellite and LTO profiles, presenting a discharge potential decrease followed by a flat *plateau* at 1.55 V and a final potential decay. These experiments confirm the results obtained in the literature.

On other side, the low specific capacity of the electrode (130 mA·h/g compared to the theoretical specific capacity of ramsdellite, 235 mA·h/g) can be explained by the presence of Li_2TiO_3. As previously deduced from XRD results, Li_2TiO_3 is present in the material. As Li^+ ion insertion and extraction process in Li_2TiO_3 is irreversible, the mass corresponding to Li_2TiO_3 in the tape casting electrode is electrochemically inactive, decreasing the total specific capacity of the anode. However, it must be highlighted that Li_2TiO_3 improves the rate capability and cyclability of composite LTO-Li_2TiO_3 electrodes [42,43], which may explain the excellent cyclability of the composite electrode prepared in this work (LTO-TC-1050ºC).

Thus, in contrast with LTO-TC-950ºC, the shape of the discharge profile for LTO-TC-1050ºC is not flat, having a small slope. It is observed that the cell voltage progressively decreases upon Li-insertion, and two slopes between 2 V-1.5 V and 1.4 V-1.3 V are clearly defined. This result indicates that the lithium insertion into LTO-TC-1050ºC takes place in at least two stages. In fact,

several stages during Li^+-insertion/extraction into/from ramsdellite $Li_2Ti_3O_7$ electrodes have been previously reported [44–47].

The cyclability of the electrode was measured at C/20. For all cycles, the sloping shape of the profiles, as well as the cell voltage evolution are very close (Figure 4. 21-(b)). These results evidence the high reversibility of the Li^+ insertion/extraction into/from the LTO-TC-1050ºC electrode. The capacity retention over 19 cycles is very high, as shown in Figure 4. 21-(c). High cyclability was reported for conventional composite electrodes with ramsdellite $Li_2Ti_3O_7$ as active anode material [48]. However, despite the good cyclability of LTO-TC-1050ºC, the specific capacity obtained for this material is much lower than the theoretical one (235 mA·h/g). Apart from the presence of Li_2TiO_3, the possible reasons for this capacity loss may be: *(i)* the high impedance associate to the large electrode thickness, *(ii)* the low carbon content of the sample (0.38 ± 0.01 wt. %) compared to conventional composite electrodes, which lead to a poor current density distribution and *(iii)* the relative high particle size of the material compared to samples sintered at lower temperatures (see Figure 4. 15), which can decrease the specific surface area for the lithium insertion/extraction.

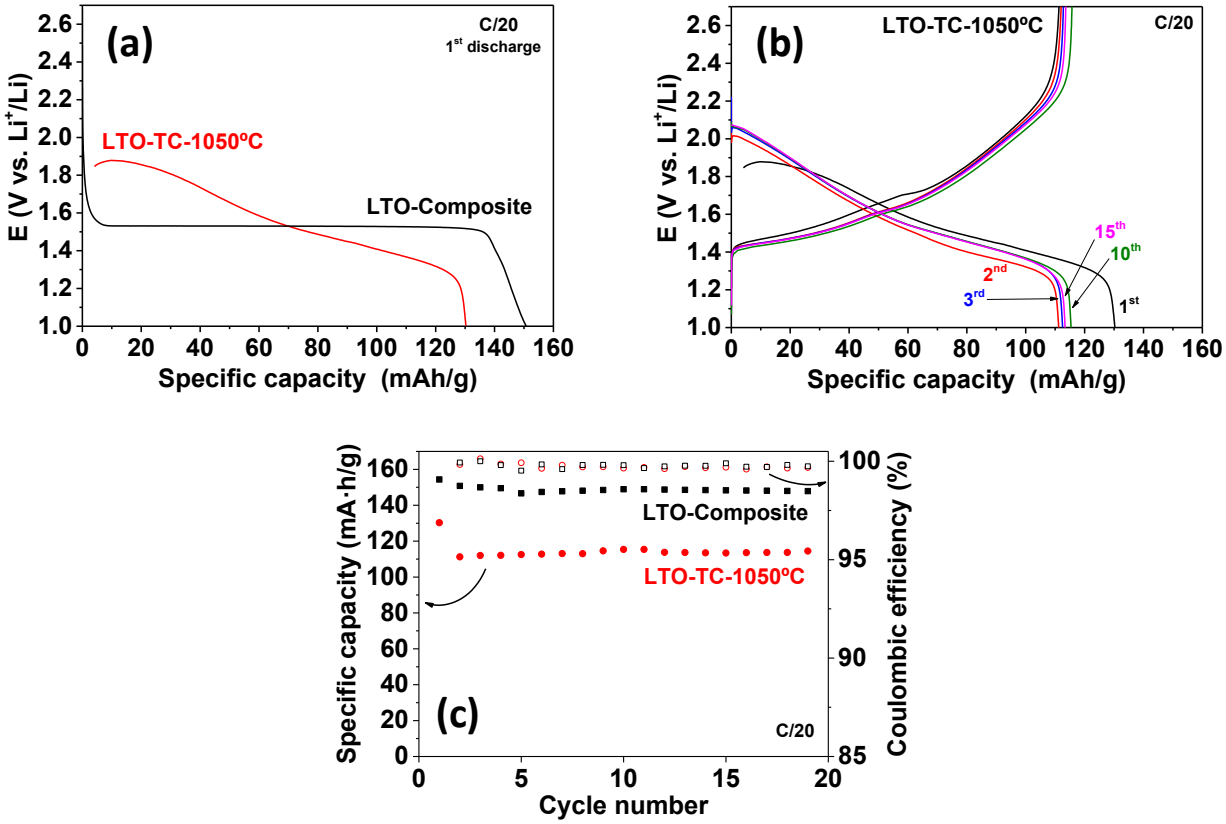

Figure 4. 21. (a) Discharge curves during the first charge-discharge cycle at C/20 for the cast LTO electrode sintered at 1050 ºC and for the LTO-composite electrode. (b) Selection of charge-discharge cycles at C/20 for the LTO cast electrode sintered at 1050 ºC. (c) Comparison of the cyclability at C/20 of the LTO cast electrode (sintering temperature 1050 ºC) and the LTO-composite electrode.

4.4.3.2. Areal and volumetric capacities of LTO cast ceramic electrodes

Electrodes with high volumetric and areal capacities are currently very appealing, especially in applications for which the size is a key parameter [49]. As it is evidenced in Figure 4. 22, the volumetric capacity of both LTO-TC-950ºC and LTO-TC-1050ºC is notably higher (more than twice) than those of the conventional LTO-composite. These outstanding volumetric capacity values are ascribable to the higher density of the TC-ceramic anodes (2.05 and 2.40 g/cm^3 for LTO-TC-950ºC and LTO-TC-1050ºC, respectively) and the absence of additives and to the sintering step.

When the areal capacity is analysed, the improvement is even greater, more than 3 times for LTO-TC-950ºC and more than 4 times for LTO-TC-1050ºC than the conventional LTO-composite electrode used as reference. For this electrochemical parameter, in addition to the higher density, the greater thickness of the LTO-ceramic anodes (240, 276 µm for LTO-TC-950ºC and LTO-TC-1050ºC, respectively vs. 120 µm for LTO-composite) with higher active LTO-loading (49.46 and 66.59 mg/cm^2 for LTO-TC-950ºC and LTO-TC-1050ºC, respectively vs. 9.42 mg/cm^2 for LTO-composite) account for this outstanding improvement. Previous papers reported that, for additive-free electrodes with large thickness, an appropriate porosity is necessary to have electrochemical activity [49–51]. Thus, the remarkable electrochemical response of the tape casting LTO electrodes show an effective percolation of the electrolyte into the bulk of electrode, which is favoured by the porosity of the electrodes processed by tape casting (35 % for LTO-TC-950ºC and 25 % LTO-TC-1050ºC).

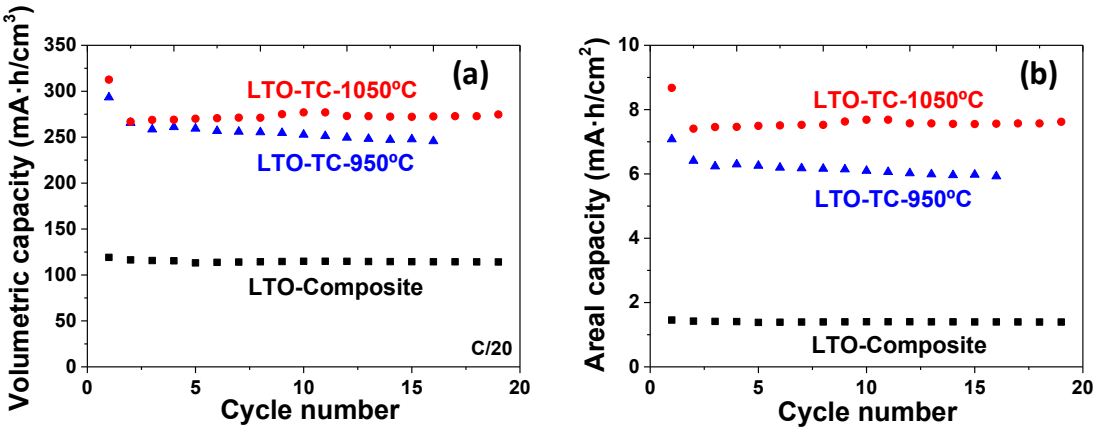

Figure 4. 22. Volumetric capacity (a) and areal capacity (b) during cycling at C/20 for tape casting LTO electrodes sintered at 950 and 1050 ºC and for the reference LTO-composite.

4.5. CONCLUSIONS

In this chapter, binder free and self-supported LTO-ceramic electrodes were successfully manufactured by the tape casting process. The different steps involved in the process were optimized, the structural and electrical properties of the sintered LTO ceramic electrodes were investigated and the optimized electrodes were tested in lithium half cells.

The slurry composition was optimized and an LTO powder loading of 55 wt. % was selected because this slurry presents the most significant pseudoplastic behaviour (power law index of 0.82). By using a doctor-blade gap of 750 μm and a casting speed of 60 $cm \cdot min^{-1}$, LTO-green layers of thickness 276 ± 36 μm were successfully obtained. The thermal debinding was optimized considering the decomposition temperatures of the different binder components and sintering was subsequently carried out, obtaining defect-free LTO ceramic layers.

Samples sintered in air achieved higher densities (92 %) than those sintered in inert or reducing atmospheres (75 %) such as N_2 and Ar/H_2. The porosity of the electrodes was confirmed by their morphology inspection by SEM. Consequently, inert and reducing sintering atmospheres are more appropriated for producing a porous electrode which favours the electrolyte penetration.

By XRD, the decomposition of LTO in ramsdellite and meta-titanate was identified for sintering temperatures higher than 950 ºC in all the sintering atmospheres. It was observed that the amount of meta-titanate increases with the sintering temperature.

The visual inspection of the sintered materials revealed that the location of the green layers in the alumina substrate is crucial to ensure a good contact between the gas and the LTO layer and affects the properties of the sintered materials. The dark colour of the electrodes sintered in inert and reducing atmospheres suggests the presence of carbon. This was confirmed by using elemental carbon analysis, resulting in a carbon content of approximately 0.24 wt. % for samples sintered in N_2 and between 0.34 and 0.38 wt. % for those sintered in Ar/H_2. Furthermore, by TEM, a conductive carbon coating between 1 and 3.5 nm thickness was observed around the LTO particles. On the other hand, the partial reduction of Ti^{4+} due to the Ar/H_2 explains the bluish colour observed in the layers.

Impedance spectroscopy showed that due to a combination between the non-percolative carbon coating and the partially reduced LTO conductions, electrodes sintered in Ar/H_2 present the highest conductivities ($2 \cdot 10^{-5}$-$5 \cdot 10^{-5}$ S/cm), being the most appropriate for working as anodes.

However, electrodes sintered in air and N_2 presents lower conductivity (~ 10^{-8} S/cm), on principle, not enough for battery applications.

The electrodes sintered in Ar/H_2 at 950 ºC presented a specific capacity in the first discharge at C/20 of 143 mA·h/g, only slightly lower to that of the composite reference electrode (151 mA·h/g). After 15 cycles, the capacity retention was 84 %. Thus, despite its high thickness (240 μm) and the low carbon content, the electrodes have a remarkably good electrochemical performance. In the case of the ceramic electrode sintered at 1050 ºC in Ar/H_2, the specific capacity in the first discharge at C/20 is 130 mA·h/g. This relatively low capacity is mainly attributed to the presence of the electrochemically inactive Li_2TiO_3 formed during sintering. Nonetheless, from the 2nd to the 19th cycle the capacity retention is close to 100 %.

When the volumetric and areal capacities are analysed, an outstanding improvement compared with the conventional composite electrode is found. The ceramic electrodes present a volumetric capacity between 250 and 275 mA·g/cm^3, which is more than twice than that of the reference electrode. The reason for this improvement is attributed to *(i)* the high densities of the ceramic-electrodes (2.05-2.40 g/cm^3) and *(ii)* the lack of additives, which reduces the inactive material in the electrode formulation. In the case of areal capacities, the improvement is even major, reaching 6 mA·h/cm^2 and almost 8 mA·h/cm^2 for the electrodes sintered at 950 and 1050 ºC, respectively, compared to the composite electrode (1.5 mA·h/cm^2). These outstanding areal capacity values are ascribable, in addition to the high densities and absence of additives, to the large thickness of the ceramic electrodes.

4.6. BIBLIOGRAPHY

[1] C. Barry, M. Grant, Ceramic materials- Sienice and Engineering, 2nd ed., Springer, New York, 2013.

[2] R.E. Mistler, The principles of tape casting and tape casting applications, in: Ceram. Process., Springer Science & Business Media, 2011: pp. 147–173.

[3] G. Besendörfer, A. Roosen, Particle shape and size effects on anisotropic shrinkage in tape-cast ceramic layers, J. Am. Ceram. Soc. 91 (2008) 2514–2520. doi:10.1111/j.1551-2916.2008.02510.x.

[4] N. Das, H.S. Maiti, Ceramic membrane by tape casting and sol-gel coating for microfiltration and ultrafiltration application, J. Phys. Chem. Solids. 70 (2009) 1395–1400. doi:10.1016/j.jpcs.2009.08.016.

[5] A. Heunisch, A. Dellert, A. Roosen, Effect of powder, binder and process parameters on anisotropic shrinkage in tape cast ceramic products, J. Eur. Ceram. Soc. 30 (2010) 3397–3406. doi:10.1016/j.jeurceramsoc.2010.08.012.

[6] R. Moreno, J. Requena, Introducción al colaje de cinta, Bol. Soc. Esp. Ceram. Vidr. 31 (1992) 99–108.

[7] R. Moreno, The Role of Slip Additives in Tape-Casting Technology: Part I-Solvents and Dispersants, Am. Ceram. Soc. Bull. 71 (1992) 1521–1531.

[8] J. Luo, R. Eitel, Aqueous tape casting of Al_2O_3 for multilayer co-fired ceramic based microfluidic chips with translucent windows, Ceram. Int. 44 (2018) 3488–3491. doi:10.1016/j.ceramint.2017.11.076.

[9] D. Hotza, P. Greil, Review: aqueous tape casting of ceramic powders, Mater. Sci. Eng. A. A202 (1995) 206–217. doi:10.1016/0921-5093(95)09785-6.

[10] T. Durán, E. Climent-Pascual, M.T. Pérez-Prior, B. Levenfeld, A. Varez, I. Sobrados, J. Sanz, Aqueous and non-aqueous Li^+/H^+ ion exchange in $Li_{0.44}La_{0.52}TiO_3$ perovskite, Adv. Powder Technol. 28 (2017) 514–520. doi:10.1016/j.apt.2016.10.020.

[11] G. Larraz, A. Orera, M.L. Sanjuán, Cubic phases of garnet-type $Li_7La_3Zr_2O_{12}$: the role of hydration, J. Mater. Chem. A. 1 (2013) 11419–11428. doi:10.1039/c3ta11996c.

[12] R. Moreno, The Role of Slip Additives in Tape Casting Technology, Part II-Binders and Plasticizers, Am. Ceram. Soc. Bull. 71(11) (1992) 1647–57.

[13] J.-K. Song, J.-H. Park, H.-S. Lee, K.-W. Chung, W.-S. Um, M.-S. Kang, Effect of polymer molecular weight variations on PZT slip for tape casting, J. Eur. Ceram. Soc. 20 (2002) 685–688. doi:10.1016/s0955-2219(99)00198-3.

[14] M. Jabbari, R. Bulatova, A.I.Y. Tok, C.R.H. Bahl, E. Mitsoulis, J.H. Hattel, Ceramic tape casting: A review of current methods and trends with emphasis on rheological behaviour and flow analysis, Mater. Sci. Eng. B. 212 (2016) 39–61. doi:10.1016/j.mseb.2016.07.011.

[15] Q. Dong, T. Zhu, Z. Xie, Y. Han, D. An, Optimization of the tape casting slurries for high-quality zirconia substrates, Ceram. Int. 43 (2017) 16943–16949. doi:10.1016/j.ceramint.2017.09.099.

[16] Y. Duan, J. Zhang, X. Li, Y. Shi, J. Xie, D. Jiang, Optimization of the tape casting process for the development of high performance silicon nitride substrate, Int. J. Appl. Ceram. Technol. 14 (2017) 712–718. doi:10.1111/ijac.12679.

[17] P.M. Raj, W.R. Cannon, Anisotropic Shrinkage in Tape-Cast Alumina: Role of Processing Parameters and Particle Shape, J. Am. Ceram. Soc. 82 (1999) 2619–2625. doi:10.1111/j.1151-2916.1999.tb02132.x.

[18] R.E. Mistler, E.R. Twiname, Tape Casting. Theory and practice., American Ceramic Society, Westerville, 2000.

[19] K. Gao, M. He, Y. Li, Y. Zhang, J. Gao, X. Li, Z. Cui, Z. Zhan, T. Zhang, Preparation of high-density garnet thin sheet electrolytes for all-solid-state Li-Metal batteries by tape-casting technique, J. Alloys Compd. 791 (2019) 923–928. doi:10.1016/j.jallcom.2019.03.409.

[20] G.N. Howatt, R.G. Breckenridge, J.M. Brownlow, Fabrication of thin ceramic sheets for capacitors, J. Am. Ceram. Soc. 30 (1947) 237–242.

[21] H.W. Stetson, W.J. Gyurk, Alumina Substrates, 3698923, 1967.

[22] B. Schwartz, Review of multilayer ceramics for microelectronic packaging, J. Phys. Chem. Solids. 45 (1984) 1051–1068. doi:10.1016/0022-3697(84)90048-9.

[23] A.D. Moriana, S. Zhang, Lead-free textured piezoceramics using tape casting: A review, J. Mater. 4 (2018) 277–303. doi:10.1016/j.jmat.2018.09.006.

[24] A. Basak, H. Deka, A. Mondal, U.P. Singh, Effect of Substrate on the Structural, Optical and Electrical Properties of CuSnS Thin Films Prepared by Doctor Blade Method, Mater. Today Proc. 4 (2017) 12529–12535. doi:10.1016/j.matpr.2017.10.056.

[25] X. Chen, W. Ni, X. Du, Z. Sun, T. Zhu, Q. Zhong, M. Han, Electrochemical property of multi-layer anode supported solid oxide fuel cell fabricated through sequential tape-casting and co-firing, J. Mater. Sci. Technol. 35 (2019) 695–701. doi:10.1016/j.jmst.2018.10.015.

[26] W.S. Yang, L. Fuso, S. Biamino, D. Vasquez, C.V. Bolivar, P. Fino, C. Badini, Fabrication of short carbon fibre reinforced SiC multilayer composites by tape casting, Ceram. Int. 38 (2012) 1011–1018. doi:10.1016/j.ceramint.2011.08.024.

[27] J. Chen, H. Lan, Y. Cao, Z. Deng, Z. Liu, F. Tang, W. Guo, Application of composite phosphor ceramics by tape-casting in white light-emitting diodes, J. Alloys Compd. 709 (2017) 267–271. doi:10.1016/j.jallcom.2017.03.034.

[28] N. Schiffmann, F. Schröckert, E.C. Bucharsky, K.G. Schell, M.J. Hoffmann, Development and characterization of half-cells based on thin solid state ionic conductors for Li-ion batteries, Solid State Ionics. 333 (2019) 66–71. doi:10.1016/j.ssi.2019.01.020.

[29] L. Truong, V. Thangadurai, Soft-chemistry of garnet-type $Li_{5+x}Ba_xLa_{3-x}Nb_2O_{12}$ (x = 0, 0.5, 1): Reversible $H^+ \leftrightarrow Li^+$ ion-exchange reaction and their X-ray, ^7Li MAS NMR, IR, and AC impedance spectroscopy characterization, Chem. Mater. 23 (2011) 3970–3977. doi:10.1021/cm2015127.

[30] C. Liu, K. Rui, C. Shen, M.E. Badding, G. Zhang, Z. Wen, Reversible ion exchange and structural stability of garnet-type Nb-doped $Li_7La_3Zr_2O_{12}$ in water for applications in lithium batteries, J. Power Sources. 282 (2015) 286–293. doi:10.1016/j.jpowsour.2015.02.050.

[31] A. Boulant, P. Maury, J. Buzare, O. Bohnke, Efficient Ion Exchange of H+ for Li+ in $(Li_{0.30}La_{0.57}0_{0.13})TiO_3$ Perovskite in Water: Protons As a Probe for Li Location, Chem. Mater. 21 (2009) 2209–2217.

[32] D.R. Simon, E.M. Kelder, M. Wagemaker, F.M. Mulder, J. Schoonman, Characterization of proton exchanged $Li_4Ti_5O_{12}$ spinel material, Solid State Ionics. 177 (2006) 2759–2768. doi:10.1016/j.ssi.2006.03.057.

[33] E. Solera, T. Jardiel, M. Villegas, J.F. Fernández, Influencia de las diferentes etapas de procesamiento sobre la microestructura de dispositivos multicapa basados en PZT, Boletín La Soc. Española Cerámica y Vidr. 41 (2002) 166–170. doi:10.3989/cyv.2002.v41.i1.717.

[34] N.F. Martínez, E. Lladosa, M. Burguet, J.B. Montón, Isobaric vapour–liquid equilibria for binary systems of 2-butanone with ethanol, 1-propanol, and 2-propanol at 20 and 101.3kPa, Fluid Phase Equilib. 270 (2008) 62–68. doi:10.1016/j.fluid.2008.06.004.

[35] D. Marani, V. Esposito, B.R. Sudireddy, J.J. Bentzen, P.S. Jørgensen, D.W. Ni, F. Teocoli, R. Kiebach, Enhanced densification of thin tape cast Ceria-Gadolinium Oxide (CGO) layers by rheological optimization of slurries, Ceram. Int. 43 (2017) 5647–5653. doi:10.1016/j.ceramint.2017.01.098.

[36] G. Izquierdo, A.R. West, Phase equilibria in the system Li_2O-TiO_2, Mater. Res. Bull. 15 (1980) 1655–1660.

[37] B. Zhao, R. Ran, M. Liu, Z. Shao, A comprehensive review of $Li_4Ti_5O_{12}$-based electrodes for lithium-ion batteries: The latest advancements and future perspectives, Mater. Sci. Engeenering R. 98 (2015) 1–71. doi:10.1099/00221287-128-9-2165.

[38] K. Wang, Y. Wu, S. Luo, X. He, J. Wang, K. Jiang, S. Fan, Hybrid super-aligned carbon nanotube/carbon black conductive networks: A strategy to improve both electrical conductivity and capacity for lithium ion batteries, J. Power Sources. 233 (2013) 209–215. doi:10.1016/j.jpowsour.2013.01.102.

[39] T. Ohzuku, Zero-Strain Insertion Material of $Li[Li_{1/3}Ti_{5/3}]O_4$ for Rechargeable Lithium Cells, J. Electrochem. Soc. 142 (1995) 1431. doi:10.1149/1.2048592.

[40] G.-N. Zhu, L. Chen, Y.-G. Wang, C.-X. Wang, R.-C. Che, Y.-Y. Xia, Binary $Li_4Ti_5O_{12}$-$Li_2Ti_3O_7$ Nanocomposite as an Anode Material for Li-Ion Batteries, Adv. Funct. Mater. 23 (2012) 640–647. doi:10.1002/adfm.201201741.

[41] C. Villevieille, M. Van Thournout, J. Scoyer, C. Tessier, J. Olivier-Fourcade, J.C. Jumas, L. Monconduit, Carbon modified $Li_2Ti_3O_7$ ramsdellite electrode for Li-ion batteries, Electrochim. Acta. 55 (2010) 7080–7084. doi:10.1016/j.electacta.2010.06.052.

[42] Y. Wang, A. Zhou, X. Dai, L. Feng, J. Lie, J. Li, Solid-state synthesis of submicron-sized $Li_4Ti_5O_{12}/Li_2TiO_3$ composites with rich grain boundaries for lithium ion batteries, J. Power Sources. 266 (2014) 114–120. doi:10.1016/j.jpowsour.2014.05.002.

[43] H.S. Bhatti, D.H. Anjum, S. Ullah, B. Ahmed, A. Habib, A. Karim, S.K. Hasanain, Electrochemical characteristics and Li+ ion intercalation kinetics of dual-phase $Li_4Ti_5O_{12}/Li_2TiO_3$ composite in the voltage range 0-3 v, J. Phys. Chem. C. 120 (2016) 9553–9561. doi:10.1021/acs.jpcc.5b12114.

[44] M.E.A. y de Dompablo, E. Morán, A. Várez, F. García-Alvarado, Electrochemical lithium intercalation in $Li_2Ti_3O_7$-ramsdellite structure, Mater. Res. Bull. 32 (1997) 993–1001. doi:https://doi.org/10.1016/S0025-5408(97)00080-9.

[45] W. Ra, M. Nakayama, W. Cho, M. Wakihara, Y. Uchimoto, Electronic and local structural changes in $Li_{2+x}Ti_3O_7$ ramsdellite compounds upon electrochemical Li-ion insertion reactions by X-ray absorption spectroscopy, Phys. Chem. Chem. Phys. 8 (2006) 882–889. doi:10.1039/b512740h.

[46] R.K.B. Gover, J.R. Tolchard, H. Tukamoto, T. Murai, J.T.S. Irvine, Investigation of Ramsdellite Titanates as Possible New Negative Electrode Materials for Li Batteries, J. Electrochem. Soc. 146 (1999) 4348–4353. doi:10.1149/1.1392641.

[47] W. Cho, T. Kashiwagi, W. Ra, M. Nakayama, M. Wakihara, Y. Kobayashi, H. Miyashiro, Relationship between electrochemical behavior and Li/vacancy arrangement in ramsdellite type $Li_{2+x}Ti_3O_7$, Electrochim. Acta. 54 (2009) 1842–1850. doi:10.1016/j.electacta.2008.10.021.

[48] X. Gan, G. Yang, Y. Yao, Y. Dai, Synthesis of spinel $Li_4Ti_5O_{12}$–ramsdellite $Li_2Ti_3O_7$ composites under vacuum and their electrochemical properties, J. Alloys Compd. 637 (2015) 178–182. doi:10.1016/j.jallcom.2015.02.183.

[49] W. Lai, C.K. Erdonmez, T.F. Marinis, C.K. Bjune, N.J. Dudney, F. Xu, R. Wartena, Y.M. Chiang, Ultrahigh-energy-density microbatteries enabled by new electrode architecture and micropackaging design, Adv. Mater. 22 (2010) E139–E144. doi:10.1002/adma.200903650.

[50] L. Sun, N. Karanjgaokar, K. Sun, I. Chasiotis, W.C. Carter, S. Dillon, High-strength all-solid lithium ion electrodes based on $Li_4Ti_5O_{12}$, J. Power Sources. 196 (2011) 6507–6511. doi:10.1016/j.jpowsour.2011.03.045.

[51] M.E. Sotomayor, C. de la Torre-Gamarra, W. Bucheli, J.M. Amarilla, A. Varez, B. Levenfeld, J.-Y. Sanchez, Additive-free $Li_4Ti_5O_{12}$ thick electrodes for Li-ion batteries with high electrochemical performance, J. Mater. Chem. A. 6 (2018) 5952–5961. doi:10.1039/C7TA10683A.

General conclusions

In this Thesis, Powder Extrusion Moulding (PEM) and Tape Casting (TC) processes were optimized for the obtention of thick electrodes. Thus, LTO and LFP electrodes of ~500 μm thickness were prepared by PEM and LTO electrodes of ~250 μm thickness were obtained by TC. The additive-free electrodes were successfully tested in lithium half cells and finally a lithium-ion battery was designed using extruded LTO and LFP electrodes as anode and cathode, respectively.

Despite the very high thickness of the ceramic electrodes, they exhibit a very good electrochemical performance at relatively low C-rates (between C/10 and C/24), being very similar to those of the conventional composite electrodes used as reference. This unexpected result is reached thanks to the high porosity of the electrodes (between 16 and 25 % for LTO and 35 % for LFP), which permits the penetration of the liquid electrolyte into the thick material, hence allowing all the active material to be available for the electrochemical reaction during charging/discharging. Table 5. 1 summarizes the main electrochemical properties of the electrodes obtained in this work. Due to the high density of the electrodes and to the lack of binders and extra additives, the volumetric capacity of the thick electrodes was double or even triple the capacity of the composite electrodes, reaching more than 300 $mA \cdot h/cm^3$ for the extruded electrodes. The increase is even higher in the case of the areal capacity, not only because the lack of additives and high density but also to the much higher thickness of the electrodes compared to conventional ones. It can be observed that the extruded electrodes present higher areal and volumetric capacity than those prepared by tape casting, which is due to the higher thickness and density of the PEM-electrodes. Obviously, the higher the thickness, the higher the capacity per area unit. However, diffusion limitations force the use of relatively low current densities.

Thus, extruded LTO and LFP electrodes were selected as anode and cathode, respectively, for designing a high energy density lithium-ion battery (LIB). The results obtained from the electrochemical characterization show that the cell reached a volumetric of 257 $mA \cdot h/cm^3$ after 50 cycles at C/12, which correspond to an energy density of approximately 488 $W \cdot h/l$. This energy density could be increased at lower C-rates. This is an excellent result considering the high thickness of the electrodes and the very low amount of carbon.

Table 5. 1. Characteristics and main electrochemical properties of the additive-free LTO and LFP electrodes prepared in this work.

Cell	C-rate, cycle number	Specific capacity (mA·h/g)	Mass loading (mg/cm^2)	Thickness (µm)	Areal capacity ($mA·h/cm^2$)	Electrode density (g/cm^3)	Volumetric capacity (mA·h/l)
Li/LTO-extruded	C/24, 20th	107	138	475	14.7	2.9	310.3
Li/LFPO-extruded	C/10, 20th	140	86	500	12.0	2.3	322.0
Li/LTO-tape casting-950ºC	C/20, 15th	120	49.5	240	5.9	2.1	252.0
Li/LTO-tape casting-1050ºC	C/20, 15th	116	66.6	276	7.7	2.4	278.4

Both PEM and TC are presented as alternatives to conventional electrode manufacturing. They are both easily scalable processes by which, in principle, any ceramic electrode material could be prepared. In addition, commercial ceramic powders and binder compounds are used. Thus, this investigation opens the way for new research lines for obtaining other electrode compositions.

Despite being far from commercialization, different aspects must be considered for the transfer of PEM and TC to the battery industry, such as viability and difficulty of the process steps, energy cost, environmental impact and total process time. In both processes, similar time is expended in the thermal treatments. In PEM, the limiting time steps are mixing and extrusion in terms of time and cost. On the other hand, in tape casting drying the layers can consume relatively long time. However, the amount of material produced by PEM, even at laboratory scale, is larger than by TC, so PEM seems to be more cost-efficient.

Regarding environmental concerns, the main drawback of the TC process developed in this work is the use of flammable and volatile solvents, which require safety operation and specific collecting systems. In both TC and PEM, high-temperature furnaces are used during long times, which leads to a relatively high energy consumption and environmental impact. In the case of PEM technology, also high-power equipment, such as mixers and extruders, are employed. This equipment, besides the energy cost, require a moderate initial economical investment, which can be compensated by large production.

By PEM higher thickness electrodes (500 and 1000 μm) were obtained compared to TC (240-300 μm). In addition, by TC, difficulties were found to obtain flat layers (in N_2 and Ar-H_2 atmospheres), attributed to their position during the thermal treatments. This makes not possible produce TC-layers with a large area. On the other hand, the geometrical control of PEM materials was excellent, reaching high quality sintered electrodes.

Despite a liquid electrolyte were employed in all the tests, the additive-free thick electrodes approach could open the door to the design of novel high energy density all solid-state batteries. Thus, the high porosity of the electrodes can be used for designing new composite electrodes in which a solid electrolyte is infiltrated inside the porous.

To sum up, increasing areal capacity results is an efficient cost-cutting tool as it allows decreasing the surface of costly components as *(i)* current collectors *(ii)* macroporous separators and *(iii)* electrolyte volume. Process time is also saved, as the time for stacking electrodes and separators is reduced. In addition, the high porosity of the prepared electrodes reduces the time needed for the

electrolyte wetting. On the other hand, the absence of polymeric additives and solvent traces in the electrode composition increases the thermal stability and hence the battery safety.

A handicap of the thick electrodes is their limited ionic diffusion, which restricts the total conductivity and leads to a lower rate cyclability than conventional composite electrodes. Therefore, this Thesis should motivate further research as, in the future, the use of thick, cheap and safe electrodes and their batteries could be used for electric mobility, in which fast charging is required. Nevertheless, for certain stationary energy storage applications, in which only small and continuous current densities are needed, the thick electrode approach could be sufficient. Anyhow, contrary to conventional electrodes, thick ceramic electrodes are still in their initial research stage. Therefore, we believe that there are huge margins of progress given that an industrial scale-up is conceivable.

Supplementary information

Table S3. 1. Structural model used in refinements of cubic $Li_4Ti_5O_{12}$ and orthorhombic $LiFePO_4$.

$Li_4Ti_5O_{12}$		
Space group Fd-3m (nº 227)		
Atom	**Position**	**Atomic coordinates (x, y, z)**
Li1	8a	1/8, 1/8, 1/8
Li2	16d	1/2, 1/2, 1/2
Ti	16d	1/2, 1/2, 1/2
O	32e	x, x, x

$LiFePO_4$		
Space group Pnma (nº 62)		
Atom	**Position**	**Atomic coordinates (x, y, z)**
Li	4a	0, 0, 0
Fe	4c	x, 1/4, z
P	4c	x, 1/4, z
O1	4c	x, 1/4, z
O2	4c	x, 1/4, z
O3	8d	x, y, z

Table S3. 2. Structural refinement results of commercial $Li_4Ti_5O_{12}$ and $LiFePO_4$ powders from PDRX data.

$Li_4Ti_5O_{12}$	
a (Å)	8.33049(69)
O x	0.26986(29)
B_{Li1}	1.200(0)
B_{Li2}	0.628(2)
B_{Ti}	0.628(2)
B_{Al}	0.628(2)
B_O	1.842(6)
Reliability factors	
R_{Bragg}	13.8
R_F	15.2
R_p	15.2
$R\omega_p$	20.6
R_{exp}	12.68
χ^2	2.63

$LiFePO_4$	
a (Å)	10.32100(17)
b (Å)	6.00019(3)
c (Å)	4.68973(2)
Fe x	0.28326(14)
Fe z	0.97555(45)
P x	0.09501(31)
P z	0.41921(62)
O1 x	0.10158(71)
O1 z	0.74742(132)
O2 x	0.46202(82)
O2 z	0.20935(117)
O3 x	0.16618(54)
O3 y	0.04158(82)
O3 z	0.28444(79)
B_{Li}	1.300
B_{Fe}	0.685
B_P	0.538
B_{O1}	1.262
B_{O2}	1.262
B_{O3}	1.262
Reliability factors	
R_{Bragg}	6.73
R_F	4.82
R_p	16.3
$R\omega_p$	24.2
R_{exp}	15.46
χ^2	2.45

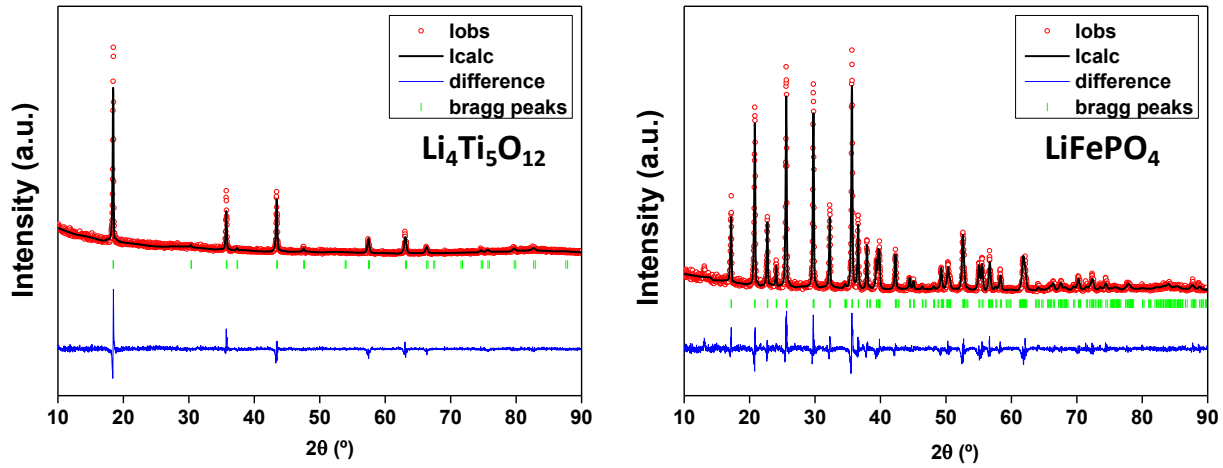

Figure S3. 1. Rietveld refinement of PXRD patterns of commercial $Li_4Ti_5O_{12}$ (left) and $LiFePO_4$ (right) samples. The experimental data is plotted as scattered circles and the solid line is a fit of calculated data. At the bottom of the graph, the difference between the calculated and measured data is given. Bragg positions are represented as vertical bars below the diffractograms.

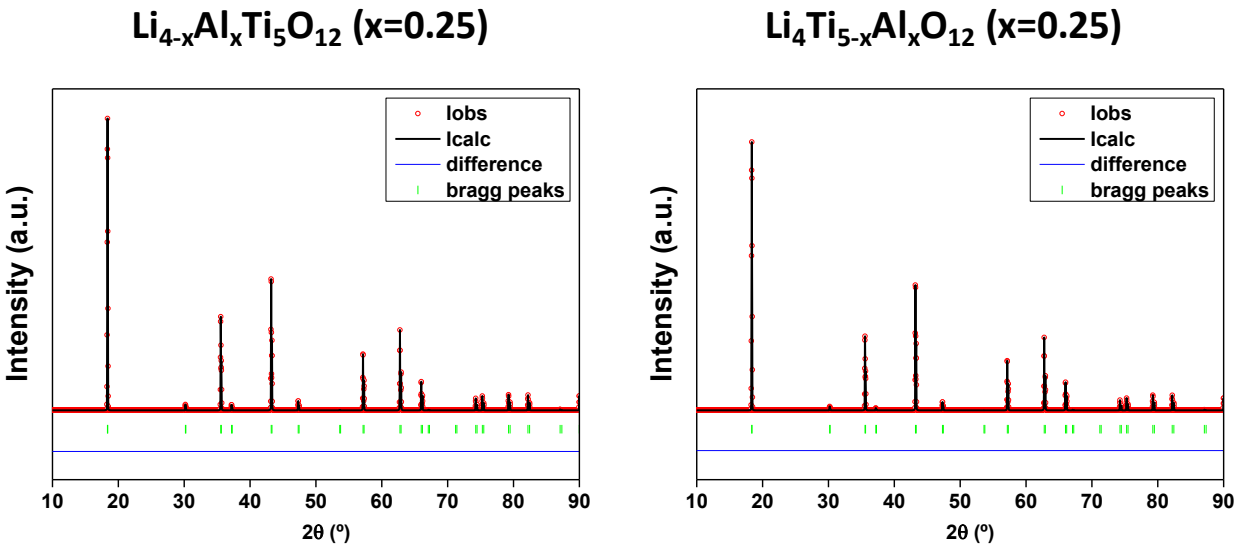

Figure S3. 2. Simulated XRD patterns for $Li_{4-x}Al_xTi_5O_{12}$ (x=0.25) (left) and $Li_4Ti_{5-x}Al_xO_{12}$ (x=0.25) (right).

Nyquist diagrams for tape casting LTO-ceramic anodes sintered at different atmospheres at 950 and 1050 ºC.

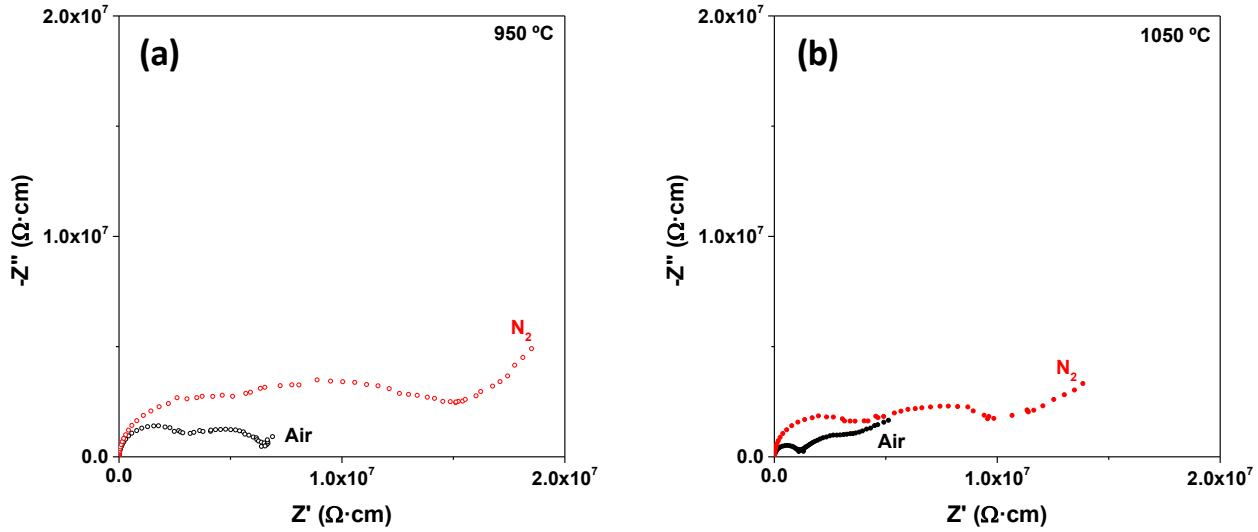

Figure S4. 1. Nyquist diagram for the impedance of tape casting LTO electrodes sintered in air and N_2 at (a) 950 ºC and (b) 1050 ºC.

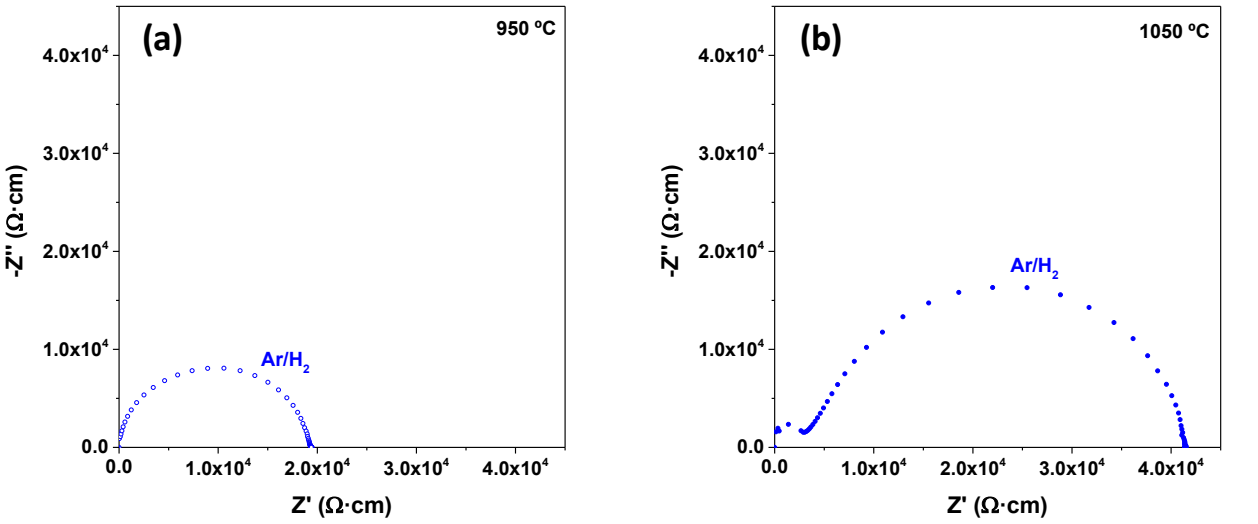

Figure S4. 2. Nyquist diagram for the impedance of tape casting LTO electrodes sintered in Ar-H_2 at (a) 950 ºC and (b) 1050 ºC.

Electrochemical response of LTO starting powder, ramsdellite powder and a LTO-ramsdellite composite.

- The electrodes were prepared by Doctor-blade process using 80 wt. % of active material, 10 wt. % of carbon black and 10 wt. % of PVdF.

- The LTO electrode was prepared using the same starting powder employed for the tape casting manufacturing of thick LTO layers.

- Ramsdellite powder was synthesised by conventional solid-state reaction using stoichiometric amounts of Li_2CO_3 (99,99%, Sigma-Aldrich), and TiO_2 (99,99%, Sigma-Aldrich). Raw materials were mixed in an agate mortar and the mixture was heated at 800ºC for 4 hours in alumina crucibles. Once cooled down to room temperature the mixture is grinded again in a mortar and pressed under 200 MPa using an isostatic press. Then, the prepared material is heated at 950 ºC for 2h and cooled down to room temperature. The formation of single phase $Li_2Ti_3O_7$ was confirmed by XRD (not shown here).

- The active material for the LTO-ramsdellite composite consisted in 50 wt.% commercial LTO powder and 50 wt. % synthesised ramsdellite powder.

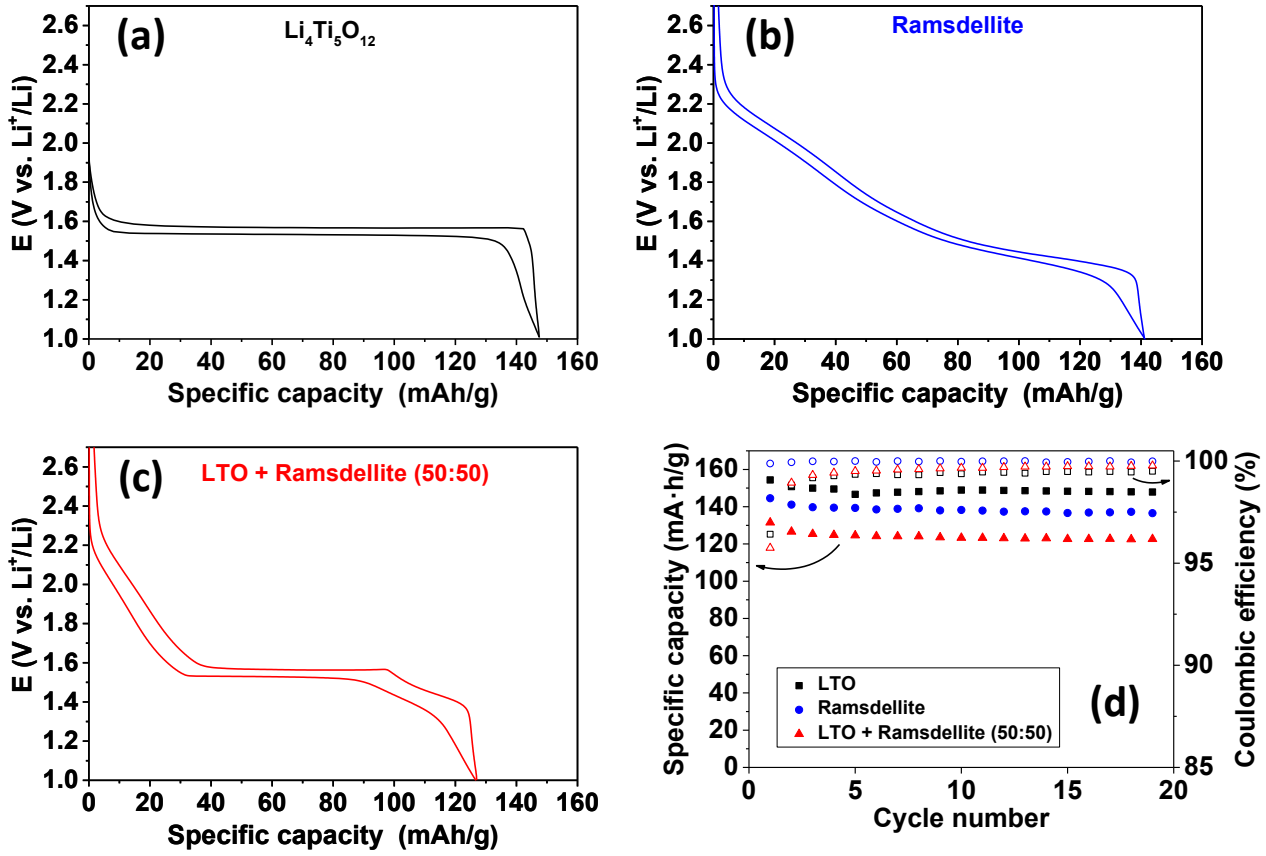

Figure S4. 3. Discharge-charge profiles at C/20 for (a) LTO powder-composite, (b) ramsdellite powder composite, (c) LTO powder-ramsdellite powder composite (50-50 wt. %). (d) Cyclability at C/20 of LTO, ramsdellite and LTO-ramsdellite composite.